

Monday Morning, November 10, 2014

2D Materials Focus Topic

Room: 310 - Session 2D+EM+NS+PS+SS+TF-MoM

2D Materials Growth and Processing

Moderator: Thomas Greber, University of Zurich

8:20am **2D+EM+NS+PS+SS+TF-MoM1 Exploring the Flatlands: Synthesis, Characterization and Engineering of Two-Dimensional Materials, Jun Lou**, Rice University **INVITED**

In this talk, we report the controlled vapor phase synthesis of MoS₂ atomic layers and elucidate a fundamental mechanism for the nucleation, growth, and grain boundary formation in its crystalline monolayers. The atomic structure and morphology of the grains and their boundaries in the polycrystalline molybdenum disulfide atomic layers are examined and first-principles calculations are applied to investigate their energy landscape. The electrical properties of the atomic layers are examined and the role of grain boundaries is evaluated. More importantly, if precise two-dimensional domains of graphene, h-BN and MoS₂ atomic layers can be seamlessly stitched together, in-plane heterostructures with interesting electronic applications could potentially be created. Here, we show that planar graphene/h-BN heterostructures can be formed by growing graphene in lithographically-patterned h-BN atomic layers. Our approach can create periodic arrangements of domains with size that ranging from tens of nanometers to millimeters. The resulting graphene/h-BN atomic layers can be peeled off from their growth substrate and transferred to various platforms including flexible substrate. Finally, we demonstrate how self-assembled monolayers with a variety of end termination chemistries can be utilized to tailor the physical properties of single-crystalline MoS₂ atomic-layers. Our data suggests that combined interface-related effects of charge transfer, built-in molecular polarities, varied densities of defects, and remote interfacial phonons strongly modify the electrical and optical properties of MoS₂, illustrating an engineering approach for local and universal property modulations in two-dimensional atomic-layers.

9:00am **2D+EM+NS+PS+SS+TF-MoM3 Influence of Substrate Orientation on the Growth of Graphene on Cu Single Crystals, Tyler Mowll**, University at Albany-SUNY, Z.R. Robinson, U.S. Naval Research Laboratory, P. Tyagi, E.W. Ong, C.A. Ventrice, Jr., University at Albany-SUNY

A systematic study of graphene growth on on-axis Cu(100) and Cu(111) single crystals oriented within 0.1° from the surface normal and a vicinal Cu(111) crystal oriented 5° off-axis has been performed. Initial attempts to grow graphene by heating each crystal to 900°C in UHV, followed by backfilling the chamber with C₂H₄ at pressures up to 5x10⁻³ Torr did not result in graphene formation on either the on-axis Cu(100) or on-axis Cu(111) surfaces. For the vicinal Cu(111) surface, epitaxial graphene was formed under the same growth conditions. By backfilling the chamber with C₂H₄ before heating to the growth temperature, epitaxial graphene was formed on both the on-axis Cu(100) and off-axis Cu(111) surfaces, but not the on-axis Cu(111) surface. By using an argon overpressure, epitaxial overlayers could be achieved on all three Cu substrates. These results indicate that the most catalytically active sites for the dissociation of ethylene are the step edges, followed by the Cu(100) terraces sites and the Cu(111) terrace sites. The need for an argon overpressure to form graphene the on-axis Cu(111) surface indicates that the Cu sublimation rate is higher than the graphene growth rate for this surface. This research was supported in part by the NSF (DMR-1006411).

9:20am **2D+EM+NS+PS+SS+TF-MoM4 Synthesis of Large Scale MoS₂-Graphene Heterostructures, Kathleen McCreary, A.T. Hanbicki, J. Robinson, B.T. Jonker**, Naval Research Laboratory

A rapidly progressing field involves the stacking of multiple two-dimensional materials to form heterostructures. These heterostructures have exhibited unique and interesting properties. For the most part, heterostructure devices are produced via mechanical exfoliation requiring the careful aligning and stacking of the individual 2D layered components. This tedious and time consuming process typically limits lateral dimensions to micron-scale devices. Chemical vapor deposition (CVD) has proven to be a useful tool in the production of graphene and has very recently been investigated as a means for the growth of other 2D materials such as MoS₂, MoSe₂, WS₂, WSe₂, and hexagonal boron nitride. Using a two-step CVD process we are able to synthesize MoS₂ on CVD grown graphene. AFM, Raman spectroscopy, and Photoluminescence spectroscopy of the MoS₂-graphene heterostructure show a uniform and continuous film on the cm scale.

9:40am **2D+EM+NS+PS+SS+TF-MoM5 Growth of 2D MoS₂ Films by Magnetron Sputtering, Andrey Voevodin**, Air Force Research Laboratory, C. Muratore, University of Dayton, J.J. Hu, Air Force Research Laboratory/UDRI, B. Wang, M.A. Haque, Pennsylvania State University, J.E. Bultman, M.L. Jespersion, Air Force Research Laboratory/UDRI, P.J. Shamberger, Texas A&M University, R. Stevenson, Air Force Research Laboratory, A. Waite, Air Force Research Laboratory/UTC, M.E. McConney, R. Smith, Air Force Research Laboratory

Growth of two dimensional (2D) MoS₂ and similar materials over large areas is a critical pre-requisite for seamless integration of next-generation van der Waals heterostructures into novel devices. Typical preparation approaches with chemical or mechanical exfoliation lack scalability and uniformity over appreciable areas (>1 mm) and chemical vapor deposition processes require high substrate temperatures. We developed few-layer MoS₂ growth under non-equilibrium magnetron sputtering conditions selected to minimize the MoS₂ nucleation density and maximize 2D growth of individual crystals [1]. In this process, the thermodynamically driven tendency to form islands is accomplished by maximizing atomic mobility through the control of incident flux kinetic energies, densities, and arriving angle to the substrate while avoiding defect formation (i.e., vacancy creation by sputtering of S atoms). Amorphous SiO₂, crystalline (0001) oriented Al₂O₃, and (002) oriented graphite substrates were used to grow few monolayer thick MoS₂ films. Continuous 2D MoS₂ films were produced over 4 cm² areas. They were composed of nano-scale domains with strong chemical binding between domain boundaries, allowing lift-off from the substrate and electronic transport measurements with contact separation on the order of centimeters. Their characteristics were similar to few-layer MoS₂ films produced by exfoliation with a direct band gap in thin samples of approximately 1.9 eV from photoluminescence spectra. The electron mobility measured for as-grown MoS₂ films was very strongly dependent on film thickness and substrate choice.

[1] "Continuous ultra-thin MoS₂ films grown by low-temperature physical vapor deposition", C. Muratore, J.J. Hu, B. Wang, M.A. Haque, J.E. Bultman, M. L. Jespersion, P.J. Shamberger, A.A. Voevodin, Applied Physics Letters (2014) in press.

10:00am **2D+EM+NS+PS+SS+TF-MoM6 Formation of Graphene on the C-face of SiC{0001}: Experiment and Theory, Jun Li, G. He, M. Widom, R.M. Feenstra**, Carnegie Mellon University

There are two {0001} surfaces of SiC, the (0001) surface known as the "Si-face", and the (000-1) surface or "C-face". The formation of graphene (by heating the SiC to 1100 – 1600 °C in various gaseous environments) has been studied for both surfaces, although it is much better understood on the Si-face. In that case, an intermediate C-rich layer, or "buffer layer" forms between the graphene and the SiC crystal. This buffer layer has 6√3x6√3-R30° symmetry; its structure is well established,¹ and it acts as a template for the formation of subsequent graphene layers. In contrast, graphene formation on the C-face is much less well understood. More than one interface structure between the graphene and the SiC has been observed,^{2,3} and, with one notable exception,⁴ the quality of the graphene formed on the C-face is generally lower than that for the Si-face.

In this work we provide new experimental and theoretical results that allow us to understand graphene formation on the C-face of SiC. Experimentally, by heating the SiC in a disilane environment, we map out the phase diagram of different surface and interface structures that form on the SiC as a function of disilane pressure and sample temperature. New surface structures that develop just prior to the graphene formation are observed. With additional heating, graphene forms on the surface, but some remnant of the surface structure prior to the graphene formation is believed to persist at the graphene/SiC interface. From first-principles theory, we find that the hydrogen in the disilane environment plays a critical role in the surface/interface structures that form. Experimentally, for disilane pressures below 5x10⁻⁵ Torr, we find a 2x2 surface structure forming prior to graphene formation. From theory we identify this structure as consisting of a silicon adatom together with a carbon restatom on the surface, with H-termination of those atoms being possible but not necessary. At higher disilane pressures we observe a 4x4 structure, and we identify that as consisting of a lower density of Si adatoms than the 2x2, now with at least some of the adatoms and restatoms being H-terminated. With graphene formation, this structure converts to the observed √43x√43-R± 7.6° interface structure. At higher disilane pressures we theoretically predict the formation of a surface consisting simply of H-terminated carbon restatoms. Experiments are underway to observe that surface, along with subsequent graphene formation on the surface.

(1) Y. Qi et al., PRL **105**, 085502 (2010).

- (2) F. Hiebel et al., PRB **78**, 153412 (2008).
 (3) N. Srivastava et al., PRB **85**, 041404 (2012).
 (4) W. A. de Heer et al., PNAS **108**, 16900 (2011).

10:40am **2D+EM+NS+PS+SS+TF-MoM8 Graphene on Hexagonal Boron Nitride Heterostacks Grown by UHV-CVD on Metal Surfaces**, *Juerg Osterwalder, S. Roth, A. Hemmi*, University of Zurich, Switzerland, *F. Matsui, Nara Institute of Science and Technology, Japan, T. Greber*, University of Zurich, Switzerland **INVITED**

Chemical vapor deposition (CVD) performed under ultra-high vacuum conditions on single-crystal metal surfaces enables the growth of large-area and high-quality graphene and hexagonal boron nitride (h-BN) single layers. We explore the CVD parameter space of precursor pressure and temperature in order to go beyond the self-saturating single-layer growth, or to grow heterostacks of the two materials. Formed layers are characterized structurally by LEED, STM and x-ray photoelectron diffraction. On Cu(111) a graphene layer could be grown on a pre-deposited single layer of h-BN when using 3-pentanone as a precursor at a pressure of 2.2 mbar and a substrate temperature of 1100 K [1]. On Rh(111) the same procedure leads to incorporation of carbon into the metal surface layers, while a graphene layer is formed only upon a second high-pressure dose [2]. In both cases the heterostructures show clearly the stacking sequence and structural and ARPES signatures of graphene on h-BN but are far from defect-free.

[1] S. Roth et al., Nano Lett. **13**, 2668 (2013).

[2] S. Roth, PhD Thesis, Department of Physics, University of Zurich (2013).

11:20am **2D+EM+NS+PS+SS+TF-MoM10 Kinetics of Monolayer Graphene Growth by Carbon Segregation on Pd(111)**, *Abbas Ebnonnasir, H.S. Mok, Y. Murata*, University of California at Los Angeles, *S. Nie, K.F. McCarty*, Sandia National Laboratories, *C.V. Ciobanu*, Colorado School of Mines, *S. Kodambaka*, University of California at Los Angeles

In this research, using in situ low-energy electron microscopy and density functional theory calculations, we elucidate the growth kinetics of monolayer graphene on single-crystalline Pd(111). In our experiments, carbon saturated Pd(111) samples were cooled down from 900 °C to segregate carbon on the surface in the form of graphene. Upon cooling the substrate, graphene nucleation begins on bare Pd surface and continues to occur during graphene growth. Measurements of graphene growth rates and Pd surface work functions along with DFT calculations establish that this continued nucleation is due to increasing C adatom concentration on the Pd surface with time. We attribute this anomalous phenomenon to a large barrier for attachment of C adatoms to graphene coupled with a strong binding of the non-graphitic C to the Pd surface.

Electronic Materials and Processing

Room: 314 - Session EM+MI+NS-MoM

Complex Oxides and Their Interfaces

Moderator: Jessica Hilton, Mantis Deposition, Lisa M. Porter, Carnegie Mellon University

8:20am **EM+MI+NS-MoM1 Emergent Phenomena at Complex Oxide Interfaces**, *Susanne Stemmer*, University of California at Santa Barbara **INVITED**

Two-dimensional electron gases (2DEGs) at interfaces between two insulating oxides have attracted significant attention because they can exhibit unique properties, such as strong electron correlations, superconductivity, and magnetism. In this presentation, we will discuss properties arising from strong electron correlations in narrow quantum wells of the band insulator SrTiO₃, sandwiched between Mott insulating rare earth titanates, SmTiO₃ and GdTiO₃, respectively. These quantum wells exhibit very high sheet electron high-densities, of approximately 1 electron per planar unit cell of the quantum well. We demonstrate electron correlation effects due to short-range Coulomb interactions, including mass enhancement, interface-induced magnetism in the electron gas, and a transition to a correlated insulator at the lowest thickness in quantum wells bound by ferrimagnetic GdTiO₃. We show that the metal-insulator transition is coupled with the sudden onset of structural distortions in the quantum well. In contrast, quantum wells bound by antiferromagnetic SmTiO₃ exhibit almost no structural distortions, incipient antiferromagnetism, no metal-insulator transition, and non-Fermi liquid behavior. We will discuss the implications of the results in the context of two-dimensional electron correlation physics.

This work was performed in collaboration with Clayton Jackson, Pouya Moetakef, Jack Zhang, Jinwoo Hwang, Leon Balents, and Jim Allen.

9:00am **EM+MI+NS-MoM3 Atomic and Electronic Structure of the Ferroelectric BaTiO₃-Ge (001) Interface**, *Kurt Fredrickson*, The University of Texas at Austin, *P. Ponath, A.B. Posadas*, University of Texas at Austin, *M.R. McCartney, T. Aoki, D.J. Smith*, Arizona State University, *A.A. Demkov*, University of Texas at Austin

In this study, we demonstrate the epitaxial growth of BaTiO₃ on Ge(001) by molecular beam epitaxy using a thin Zintl template buffer layer. A combination of density functional theory, atomic-resolution electron microscopy and *in situ* photoemission spectroscopy is used to investigate the electronic properties and atomic structure of the BaTiO₃/Ge interface. Aberration-corrected scanning transmission electron micrographs reveal that the Ge(001) 2x1 surface reconstruction remains intact during the subsequent BaTiO₃ growth, thereby enabling a choice to be made between several theoretically predicted interface structures. The measured valence band offset of 2.7 eV matches well with the theoretical value of 2.5 eV based on the model structure for an in-plane-polarized interface. The agreement between the calculated and measured band offsets, which is highly sensitive to the detailed atomic arrangement, indicates that the most likely BaTiO₃/Ge(001) interface structure has been identified.

9:20am **EM+MI+NS-MoM4 Strain-Controlled Stoichiometry Variations in CaMnO₃ Epitaxial Thin Films**, *Rajeswari Kolagani, G. Yong, Z. Warecki, C. Stumpf, D. Schaefer, P. Sharma, C. Hart, A. Burger*, Towson University

CaMnO₃ is a material of interest for application in novel energy technologies such as thermoelectric power generation, and as a photo catalyst for hydrogen energy storage. We are currently investigating the properties of epitaxial thin films of CaMnO₃ (CMO) and its electron doped derivatives towards tuning material properties that enable these applications. Oxygen stoichiometry and its effect on structural and electronic properties are key variables in optimizing thin films of these materials. We will present our studies of CMO thin films grown epitaxially by Pulsed Laser Deposition on several compatible oxide substrates with varying degrees of tensile and compressive lattice mismatch. Lattice mismatch results in the distortion of the unit cell symmetry from cubic to tetragonal. In hole-doped rare earth manganites such as La_{0.7}CaMnO₃, tensile as well as compressive lattice mismatch strain is known to cause a suppression of the insulator-metal transition, leading to an increase in electrical resistivity. In contrast, our studies of the structural and electrical properties of CMO thin films indicate that tensile strain causes a pronounced decrease in the electrical resistivity. The strained films have an expanded out of plane lattice parameter which is consistent with reduced oxygen stoichiometry. These results indicate that the tensile strain causes CMO thin films to be more susceptible to the formation of oxygen vacancies, thus reducing electrical resistivity. This is in agreement with recent theoretical predictions correlating strain and oxygen vacancies, where tensile strain induced in-plane expansion of the unit cell is shown to favor oxygen deficiency. The potential for employing lattice mismatch strain for tuning film composition has important implications for technological applications. We will present our detailed investigations of the correlation of strain and oxygen stoichiometry in CaMnO_{3-d} and related manganite compositions, employing high resolution X-ray diffraction, temperature dependent resistivity measurements, and characterization of the film surface morphology using atomic force microscopy.

9:40am **EM+MI+NS-MoM5 Controlling Complex Oxide Chemistry to Enable Advanced Dielectric, Ferroelectric, and Electronic Applications**, *Lane Martin*, University of California, Berkeley **INVITED**

Current and next-generation advanced functional materials are testing our ability to produce high-quality, complex materials with ever increasing precision. Particular interest has been given to candidate complex oxide materials which present a diverse range of material properties and functionality not easily produced in other classes of materials. The ultimate integration and utilization of these materials, however, will require that we can carefully and deterministically balance the intrinsic phenomena of interest in these materials with a knowledge of the potential extrinsic effects that can arise from defects which result from our inability to produce these complex materials with the precision we desire. This is made more challenging by the fact that these complex oxide systems are prone to and can accommodate large densities of point defects through a range of internal compensation mechanisms. In this presentation, we will explore the interrelationship between the complex oxide growth process, the chemical nature of these complex materials, the resulting structure and strain evolution, and the ultimate effect on properties in a range of prototypical complex oxide materials. We will explore these interrelationships in model systems including the classic dielectric materials SrTiO₃ and LaAlO₃, highly-controlled heterointerfaces that exhibit exotic physics including the

LaAlO₃/SrTiO₃ system, and ferroic systems such as BaTiO₃ and others. In this context, we will demonstrate routes by which we can deterministically utilize the tendency for these materials to form point defects to enhance epitaxial thin film strain, developing new modalities of strain control of thin-film materials that go beyond traditional lattice mismatch effects, and how the combination of epitaxial strain and defects in materials can be used to enhance performance, independently tune susceptibilities, and provide new insights into the nature of these complex materials. For instance, in BaTiO₃ we will illustrate how one can couple epitaxial strain to defect structures to provide an additional out-of-plane strain component that can dramatically enhance ordering temperatures and will explore the use of compositionally-graded heterostructures to further extend what can be done with epitaxial strain to manipulate dielectric, ferroelectric, and electronic properties of materials.

10:40am **EM+MI+NS-MoM8 Monolithic Integration of Epitaxial BaTiO₃ on Si and SiGe for Ferroelectric Devices**, *L. Mazet, R. Bachelet, G. Saint-Girons*, Institut des Nanotechnologies de Lyon (INL) - CNRS - ECL, France, *D. Albertini, B. Gautier*, Institut des Nanotechnologies de Lyon (INL) - CNRS - INSA de Lyon, France, *M.M. Frank, J. Jordan-Sweet, I. Lauer, V. Narayanan*, IBM T.J. Watson Research Center, *M. Hych, S. Schamm-Chardon*, CEMES - CNRS - Université de Toulouse, France, *Catherine Dubourdieu*, Institut des Nanotechnologies de Lyon (INL) - CNRS - ECL, France

INVITED

Ferroelectric oxides integrated on a semiconductor substrate are of particular interest for various applications such as memory or logic devices, electro-optic devices or as piezoelectric materials for sensors and actuators. Among the ferroelectric compounds, BaTiO₃ is an attractive candidate for large-scale applications compared to Pb- or Bi-based oxides. It is a well-known perovskite largely studied for its dielectric, piezoelectric and ferroelectric properties.

In this talk, I will briefly review the challenges associated with the monolithic integration of crystalline complex oxides on a semiconductor and more particularly with the integration of ferroelectrics. Molecular Beam Epitaxy (MBE) provides unique advantages to precisely construct, almost atom by atom, the oxide/semiconductor interface.

I will then present an experimental work on the epitaxy of BaTiO₃ thin films (1.2 - 20 nm) on silicon and Si_{1-x}Ge_x substrates. Films are grown by MBE, in the thickness range of 1.2-20 nm. Different growth conditions such as temperature and oxygen pressure are explored to optimize the BaTiO₃ film quality and to minimize the SiO₂ interfacial layer regrowth between Si and the SrTiO₃ buffer layer. The surface quality is monitored *in-situ* by reflection high-energy electron diffraction (RHEED) and *ex-situ* by X-ray reflectometry (XRR) and atomic force microscopy (AFM). The crystalline structure is studied by conventional and synchrotron X-ray diffraction. It is also investigated at the nanoscale using advanced transmission electron microscopy techniques. Strain maps determined with high precision (0.05%), 5 nm spatial resolution and with a large field of view (1 μm) using dark field electron holography will be discussed for selected samples. The crystalline domain orientations (*c*- versus *a*-domains) will be discussed with respect to the growth conditions and thickness. The ferroelectric properties are investigated by piezoresponse force microscopy (PFM). Ferroelectric films are obtained in optimized conditions that will be discussed. Ultrathin films of few monolayers are investigated to determine the onset of ferroelectricity.

I will conclude with ongoing perspectives on the integration of such heterostructures in new field-effect devices for low power logic applications.

11:20am **EM+MI+NS-MoM10 The Surface Study of Hexagonal LuFeO₃ Multiferroic Thin Films**, *Shi Cao, X.S. Xu, T. Paudel, E.Y. Tsymbal, P.A. Dowben*, University of Nebraska-Lincoln

The surface properties of hexagonal LuFeO₃ thin film have been studied by ultra-high vacuum based characterization technologies such as X-ray/ultraviolet photoemission spectroscopy (XPS/UPS), inverse photoemission spectroscopy (IPES) and XMCD-PEEM. Hexagonal LuFeO₃ is a stable multiferroic at room temperature with potential magneto-electric properties. The application of this material in voltage controlled magnetic devices depends very significantly on the interface composition and interface magnetism. The angle resolved XPS shows the possible iron-rich termination and the oxygen deficiency due to the sensitivity of the surface to the of sample preparation methods. The combined UPS and IPES allow us to infer that this multiferroic oxide, LuFeO₃, has a band gap about 2.35eV. All these characterizations are consistent with the density function theory calculations of the surface and bulk band structure.

11:40am **EM+MI+NS-MoM11 Integration of Ferroelectric Perovskites on Ge(001) by ALD: A Case Study of BaTiO₃**, *Thong Ngo, M.D. McDaniel, S.N. Chopra, J.G. Ekerdt, A.B. Posadas, A.A. Demkov*, The University of Texas at Austin

Germanium, which exhibits higher hole and electron mobilities than silicon, might become a candidate to replace silicon as a channel material in a field effect transistor (FET) beyond the 3D FET generation. Unlike Si, when the high-κ dielectrics are integrated on Ge, the chemical instability of GeO₂ is an advantage. Moreover, the instability of GeO₂ also enables epitaxial functional oxides on Ge. Crystalline perovskites can be high-κ insulating, with many also being ferromagnetic, ferroelectric, multiferroic, or superconducting. This wide range of properties, combined with possibilities for lattice match to Ge(001), allows for multi-functional oxides to be engineered on Ge(001).

Epitaxial integration of ferroelectric barium titanate, BaTiO₃ (BTO), on Ge has attracted much attention due to the low lattice mismatch between Ge(001) and BTO (0.25% above Curie temperature, T_c = 120 °C). The efforts to epitaxially integrate ferroelectric BTO on Ge(001) have been demonstrated using molecular beam epitaxy (MBE) by several groups. However, for device manufacturing applications, atomic layer deposition (ALD) has advantages over MBE due to its high step coverage, significantly low thermal budget, scalability, and low cost.

We demonstrate an all-chemical route to epitaxially integrate BTO directly on Ge(001). Amorphous BTO films were grown on the 2×1 reconstructed, clean Ge(001) surface at 225 °C using ALD. Barium bis(triisopropylcyclopentadienyl), titanium tetrakisopropoxide, and water were employed as co-reactants. The films become highly crystalline after a vacuum anneal at 600–700 °C. In-situ x-ray photoelectron spectroscopy confirms the stoichiometry of the BTO films with no detectable GeOx formation or carbon incorporation. In-situ reflection high energy electron diffraction (RHEED) shows high order of BTO film crystallinity after vacuum annealing. X-ray diffraction (XRD) is used to determine the crystallinity and the orientation of BTO films. Electrical characterization, including capacitance-voltage, leakage current, interface trap density, and piezoresponse force microscopy measurements will also be performed to explore the high-κ insulating and ferroelectric properties of BTO films on Ge(001). The integration of BTO films on Ge(001) by ALD is a promising method for fabricating a ferroelectric FET at production scale.

Nanometer-scale Science and Technology

Room: 304 - Session NS+SE-MoM

Delivering Energy and Mass at the Nanoscale

Moderator: Paul Sheehan, Naval Research Laboratory

8:20am **NS+SE-MoM1 Mechanical Properties of Polymer Systems Using Atomic Force Microscopy**, *Gregory Meyers*, The Dow Chemical Company

INVITED

Scanned probe microscopy (SPM) has had a long history at The Dow Chemical Company, beginning in the late 1980s when commercial scanning tunneling microscopes were just hitting the market. Since that time Dow has invested in internal and external collaborative efforts to drive and develop atomic force based technologies for property measurements of polymeric materials at nanometer length scales.

Our most cited early work described a unique phenomenon of surface wear of polystyrene thin films where the interaction of a sliding AFM tip lead to characteristic patterns that depended on the polymer molecular weight. Since that time work such as this has been studied in order to understand elastic, adhesive, and thermal properties of polymer coatings and films near rigid interfaces. Collaborations with NIST in the late 1990s provided our first attempts at quantifying mechanical properties at the nanoscale, combining knowledge gained from classical nanoindentation to the calibration of AFM systems for quantitative AFM based indentation. This work set the stage for a large scale effort in the latter 2000 time frame, funded by the NIST-ATP program in collaboration with Veeco Instruments (now Bruker-Nano). The objective of this program was to develop an AFM based platform for quantitative modulus measurements of polymers at sub 100 nm length scales, to provide better than 10% precision for polymer materials with bulk properties in the 10 MPa to 10 GPa range. As a result of this program, we now have quasistatic AFM based indentation capability that provides the most comprehensive suite of analytical models (elastic, elastic-plastic, and adhesive) to interpret material properties at these scales. Within the last few years the ability to map properties at high spatial resolution via high speed AFM indenting has been realized. A key consideration in all of the mechanical probing is the time scale over which the tip-surface interaction occurs and so we have looked to computational simulations with Purdue University to study the role of dissipative factors –

viscoelasticity and surface adhesion hysteresis – to help interpret our measurements.

9:00am **NS+SE-MoM3 Extension of Loss-Tangent Mode to Characterization of Materials' Stiffness and Damping**, *X. Yu, M. Tao, Nancy Burnham*, Worcester Polytechnic Institute

Viscoelastic materials are engineered and used in a variety of applications; however, it has been a great challenge to characterize their viscoelasticity at the nanoscale, at which the degradation and failure mechanisms often initiate. For linear viscoelastic materials, an atomic force microscopic (AFM) technique, loss-tangent mode, has been recently developed to fulfill this need [1]. The loss tangent of a material is expressed as the ratio of the lost energy (damping) over the stored energy (stiffness) and is claimed to be independent of the tip-sample contact area. Since this new mode was invented, only a few example materials have been studied. In this project, viscoelasticity of several different materials (i.e., asphalt binders [2], epoxy, silica tire, and graphite) were investigated using loss-tangent mode; the damping and stiffness terms were derived with easily measurable terms for a more detailed understanding of materials' viscoelasticity.

Results show that both free amplitude and set-point ratio affect the loss-tangent measurement. For all the examined materials, the loss tangent and damping decreased (power laws of -2.4 ± 1.1 and -2.1 ± 1.0 , respectively) with increasing free amplitude at constant set-point ratio, while stiffness increased (power law 0.32 ± 0.18). The loss tangent increased (power law 0.8 ± 0.5) with increasing set-point ratio at constant free amplitude; stiffness decreased more rapidly than damping (power laws of -1.75 ± 0.06 and -1.0 ± 0.4 , respectively). These trends might indicate that the loss tangent, as measured by AFM, is not independent of the tip-sample contact area. Computer simulation of loss-tangent mode is ongoing for explanation of these observations, in order to advance understanding of nanoscale viscoelastic measurements.

1. R. Proksch and D.G. Yablou, *Appl. Phys. Lett.* **100**, 073106 (2012)

2. X. Yu, N.A. Burnham, R.B. Mallick, M. Tao, *Fuel* **113**, 443 (2013)

9:40am **NS+SE-MoM5 Direct Mechanical Measurements of Viscoelasticity in Simple Liquids Using Vibrating Nanostructures**, *Matthew Pelton*, University of Maryland, Baltimore County, *D. Chakraborty*, University of Melbourne, Australia, *E. Malachosky, P. Guyot-Sionnest*, University of Chicago, *J.E. Sader*, University of Melbourne, Australia

Studies of acoustic vibrations in nanometer-scale particles can provide fundamental insights into the nanomechanical properties of nanoscale materials, and into the mechanical coupling between the nanoparticles and their environment. Metal nanoparticles allow for all-optical, non-contact measurements, using ultrafast laser pulses to generate and probe high-frequency acoustic vibrations. In early studies, the decay of the signal due to nanoparticle vibrations was dominated due to vibrations in nanoparticle size. By using highly uniform bipryamidal gold nanoparticles, we were able to overcome the effects of inhomogeneous damping and measure the rate at which the acoustic oscillations dissipate energy. Measurements in low-viscosity liquids such as water showed a strong "intrinsic" damping occurring within the nanoparticles themselves, and an environmental damping due to viscous coupling to the surrounding liquid. This fluid damping was described quantitatively using a parameter-free model.

In higher-viscosity liquids, however, the measured oscillation frequencies and damping rates deviate strongly and qualitatively from the predictions of this model. The deviations are explained quantitatively as arising from non-Newtonian effects in the liquid. The nanoparticles vibrate at very high frequencies (20 GHz), so that their vibration periods are comparable to the intrinsic relaxation times of the liquid. The structure-fluid interaction is thus dominated by viscoelastic effects. The observed viscoelasticity is not due to molecular confinement, but is a bulk continuum effect arising from the short time scale of vibration. This represents the first direct mechanical measurement of the intrinsic viscoelastic properties of simple bulk liquids, and opens a new paradigm for understanding extremely high frequency fluid mechanics, nanoscale sensing technologies, and biophysical processes.

10:00am **NS+SE-MoM6 Electronic and Optical Properties of Nanometer Sized Structures formed via Local Intercalated of Carbon in Layered Materials**, *Andrew Stollenwerk*, University of Northern Iowa

Electron beam radiation is often used to synthesize nanometer scale structures through lithographic techniques, direct altering of chemical bonds, or milling away material. We have recently demonstrated a new method to locally intercalate carbon with nanometer precision using the electron beam of a scanning electron microscope to break apart residual organics. This process was found to work only on layered materials such as topological insulators, novel superconductors, charge density wave materials, and graphite. Structurally, the incorporation of carbon raises the

height of the substrate from a few nanometers up to several hundred nanometers depending on the exposure time. While easily observable using atomic force microscopy, these features are effectively invisible to the scanning tunneling microscope at tunneling biases below approximately 0.75 V. Tunneling spectrum of these structures exhibit semiconducting properties with band gaps varying between 0.5 eV – 2.5 eV. This is in agreement with the broad-wavelength photoluminescence observed in the corresponding optical spectrum. Both of these results suggest that the carbon intercalates form nano-clusters with a wide distribution in the size and density.

10:40am **NS+SE-MoM8 Effects of Chemical Bonding on Heat Transfer Across Interfaces**, *Paul Braun, M. Losego, M. Grady, N. Sottos, D.G. Cahill*, University of Illinois at Urbana-Champaign **INVITED**

Interfaces often dictate heat flow in micro- and nanostructured systems. However, despite the growing importance of thermal management in micro- and nanoscale devices, a unified understanding of the atomic-scale structural features contributing to interfacial heat transport does not exist. Herein, we experimentally demonstrate a link between interfacial bonding character and thermal conductance at the atomic level. Our experimental system consists of a gold film transfer-printed to a self-assembled monolayer (SAM) with systematically varied termination chemistries. Using a combination of ultrafast pump-probe techniques (time-domain thermoreflectance, TDTR, and picosecond acoustics) and laser spallation experiments, we independently measure and correlate changes in bonding strength and heat flow at the gold-SAM interface. For example, we experimentally demonstrate that varying the density of covalent bonds within this single bonding layer modulates both interfacial stiffness and interfacial thermal conductance. We believe that this experimental system will enable future quantification of other interfacial phenomena and will be a critical tool to stimulate and validate new theories describing the mechanisms of interfacial heat transport. Ultimately, these findings will impact applications, including thermoelectric energy harvesting, microelectronics cooling, and spatial targeting for hyperthermal therapeutics.

11:20am **NS+SE-MoM10 Enhanced Thermal Transport at Covalently Functionalized Carbon Nanotube Array Interfaces to Oxide-forming and Noble Metals**, *S. Kaur*, Lawrence Berkeley National Laboratory, *N. Raravikar*, Intel Corporation, *B.A. Helms*, Lawrence Berkeley National Laboratory, *R. Prasher*, Sheetak, Inc., *D.Frank Ogletree*, Lawrence Berkeley National Laboratory

It has been more than a decade since the experimental demonstration that the thermal conductivity of carbon nanotubes can exceed that of diamond, which has the highest thermal conductivity among naturally existing materials. In spite of tremendous promise as a thermal material, results have been disappointing for practical thermal systems and applications based on nanotubes. The main culprit for the dramatic shortfall in the performance of nanotubes in practical systems is high thermal interface resistance between them and other components due to weak adhesion at the interface. We demonstrated a six-fold reduction in the thermal interface resistance between both oxide-forming and noble metal surfaces and vertically aligned multi-wall carbon nanotube arrays after bridging the interface with short, covalently-bonded organic molecules. Increased thermal transport was associated with a significant increase in interface mechanical adhesion [1]. Functionalized CNT thermal interfaces were shown to be stable in air for many months and resistant to thermal stress up to 180° C. We were also able to independently determine the intrinsic CNT interface resistance and the fraction of the CNT array contributing to thermal transport by performing multi-frequency time-domain thermo-reflectance (TDTR) measurements. Since our interface-functionalization method avoids destructive solution-phase processing, this development may lead to the practical integration of CNT arrays for thermal management in microelectronic devices

[1] "Enhanced thermal transport at covalently functionalized carbon nanotube array interfaces", Sumanjeet Kaur, Nachiket Raravikar, Brett A. Helms, Ravi Prasher & D. Frank Ogletree, *Nature Communications* **5** 3082 (2014) doi: 10.1038/ncomms4082

11:40am **NS+SE-MoM11 Desktop Nanofabrication with Cantilever-Free Scanning Probes**, *Keith A. Brown, D.J. Eichelsdoerfer, X. Liao, C.A. Mirkin*, Northwestern University

The availability of reliable nanofabrication methods has dictated the pace of progress in many areas of physics, materials science, electronics, and biotechnology. A major deficiency in these fields is our inability to simultaneously control the architecture of soft materials from macroscopic to nanoscopic length scales. Scanning probe instruments, such as the atomic force microscope, are promising platforms for nanofabrication because they provide direct access to the nanoscale. However, the central barrier to their

widespread use as lithographic instruments is throughput, as it is prohibitively slow to pattern large areas with a single nanoscale probe. To address this challenge, we explored a new architecture that utilizes a thin elastomeric film on a glass slide in lieu of cantilevers to enable the use of a massive array of probes in a simple format. Unfortunately, these cantilever-free probe arrays are passive duplication tools where each probe writes a copy of the same pattern. Here, we report on our recent advances in developing techniques for actuating individual probes in cantilever-free arrays and discuss the new scientific directions that these advances enable. Specifically, we present methods for both physically actuating cantilever-free probes using local heating and optically addressing probes that function as light valves for near-field photolithography, and find both to be capable of stitching together high resolution patterns that span multiple probes. These advances in nanofabrication have enabled new types of experiments, and in particular, we present recent progress in the combinatorial study of biochemical interactions and the high throughput fabrication of functional metamaterials using cantilever-free techniques. Taken together, these observations indicate that versatile desktop nanofabrication is possible using scanning probes and that these techniques can address the emerging challenges related to patterning soft materials.

2D Materials Focus Topic

Room: 310 - Session 2D+AS+EM+NS+SS-MoA

Dopants, Defects, and Interfaces in 2D Materials

Moderator: Jun Lou, Rice University

2:00pm **2D+AS+EM+NS+SS-MoA1 Cutting and Assembling 2 Nanometer Voids in Single Layer Hexagonal Boron Nitride**, *Thomas Greber, H.Y. Cun, M. Iannuzzi, A. Hemmi, J. Osterwalder*, University of Zurich, Switzerland **INVITED**

Argon implantation beneath hexagonal boron nitride nanomesh on Rh(111) [1] leads to the formation of vacancy and interstitial defects [2]. The nanomesh is a single layer of hexagonal boron nitride on Rh(111), where 13x13 h-BN units accommodate on 12x12 Rh unit cells. The resulting super-honeycomb has a lattice constant of 3.2 nm and consists in regions where the h-BN “wets” the Rh substrate (pores), and regions where h-BN is quasi freestanding (wires) [3].

The interstitial defects are called “nanotents”, where atoms are trapped beneath the ultimately thin “rainfly” made of a single layer of h-BN [2,4]. They are stable at room temperature and survive exposure to air.

The vacancy defects are sites where a boron or a nitrogen atom was kicked out by the Ar ion impact. If the implanted structures are annealed to 900 K the can-opener effect occurs: 2 nm h-BN-flakes or “lids” are cut out of the h-BN nanomesh and 2 nm voids form [2]. At higher temperatures the resulting voids may diffuse and assemble, due to their repulsive interaction, in a super-structure with some order, i.e., a nearest neighbor distance of about 15 nm. Near the disintegration temperature of the h-BN nanomesh we finally observe self-healing of the voids in the nanomesh, which we assign to their annihilation in larger holes in the structure.

The report bases on scanning tunneling microscopy, x-ray photoelectron spectroscopy, molecular dynamics and density functional theory calculations.

Financial support by the Swiss National Science Foundation and support by the EC under the Graphene Flagship (contract no. CNECT-ICT-604391) is gratefully acknowledged. We thank the Swiss National Supercomputer Centre (CSCS) for allocation of computer time.

[1] M. Corso et al. *Science*, 303 (2004) 217.

[2] H. Y. Cun et al. *Nano Letters* 13 (2013) 2098.

[3] S. Berner et al. *Angew. Chem. Int. Ed.* 46 (2007) 5115.

[4] H.Y. Cun et al. *ACS Nano* 8 (2014) 1014.

2:40pm **2D+AS+EM+NS+SS-MoA3 Engineering Structural Defects in Graphene Materials**, *Jeremy Robinson, M. Zhaludinov, J. Culbertson, C. Junkermier, P.E. Sheehan, T. Reinecke, A. Friedman*, Naval Research Laboratory

Graphene's atomic thinness makes it highly sensitive to surface adsorbates or defects within its carbon backbone. Aside from the known effects and impact on electronic properties, here we demonstrate the impact of defects on the mechanical properties and the response of mechanical resonators. In particular, once defects are formed in atomically-thin materials they can be quite mobile and form more complicated defect structures such as bi- or tetra-vacancy clusters. We execute experiments using mechanical drum resonators made from single- to multi- to many-layer graphene systems. We use both CVD grown graphene and reduced graphene oxide (rGO) films to capture a wide range of defect structures. By measuring the fundamental frequency response of the resonators (in the MHz range) we extract properties such as tension, quality factor, and modulus as a function of external manipulation [1]. For highly defective rGO films measuring 10-40nm thick, we can tune the frequency response by 500% and quality factor by 20x through laser annealing, which effectively rearranges defects throughout the film [1]. Alternatively, using graphene 1-4 layers thick, we find the resonator response is significantly more sensitive to the formation and annihilation of meta-stable defects, such as the tetra-vacancy structure. We will show how the defect mobility and resonator response changes with different energy photons and come to understand these differences based on calculated defect migration energies of different defects types in graphene.

[1] *Nano Letters* 12, 4212 (2012)

3:00pm **2D+AS+EM+NS+SS-MoA4 Graphene Cleaning using a Low Energy Ar Ion Beam**, *KiSeok Kim, G. Yeom*, Sungkyunkwan University, Republic of Korea

Recently, graphene has been widely investigated due to the superior electrical, mechanical, thermal, and chemical properties. Especially, CVD graphene which was grown on Cu foil and transferred to various substrates using PMMA has been used most widely due to the possible large area applications such as electronic devices for displays, semiconductors, etc. However, in order to apply the transferred CVD graphene to the various electronic device fabrication, PMMA residue on the graphene surface formed during the transfer process and lithography process needs to be completely removed without damage. Various methods have been investigated to remove the residue on the graphene surface such as current cleaning, heat treatment, chemical cleaning, etc. However, it is reported that these methods are not effective in removing the residue on graphene or not applicable to industry.

In this study, a controlled Ar ion beam has been used to effectively remove the PMMA residue on graphene surface. By controlling the Ar ion beam condition, the residue on graphene surface could be removed while minimizing the damage on the graphene surface. Especially, by lowering the Ar beam energy less than 10 eV, it was possible to effectively remove the PMMA residue without damaging the graphene. The removal of PMMA residue on the graphene surface could be identified using Raman Spectroscopy showing the red shift of 2D peak (2670 cm^{-1}) and blue shift of G peak (1580 cm^{-1}) in addition to the decrease of RMS roughness from 1.3nm to 0.3 nm using an AFM (Atomic Force Microscopy). The effectiveness of graphene cleaning was also confirmed by XPS (X-ray Photoelectron Spectroscopy), by the uniform deposition of ALD HfO_2 layer on the cleaned graphene surface, by measuring the electrical properties of deposited ALD HfO_2 , etc.

3:40pm **2D+AS+EM+NS+SS-MoA6 Electronic Structure Modification in van der Waals Heterostructures: Interlayer Hybridization in the Case of Graphene/MoS₂**, *Matthias Batzill, H. Coy-Diaz*, University of South Florida, *M.C. Asensio*, Synchrotron Soleil, France, *J. Avila*, Synchrotron Soleil

Artificial van der Waals heterostructures promise to combine materials with diverse properties. Simple mechanical stacking or conventional growth of molecular hetero-layers would enable fabrication of novel materials or device-structures with atomically precise interfaces. Because covalent bonding in these layered materials is limited to molecular-planes, interface interactions between dissimilar materials are expected to modify the properties of the individual layers only weakly. Here we prepare graphene/MoS₂ heterostructures by transferring CVD-grown graphene onto a MoS₂ substrate. It is shown that high quality interfaces between graphene and MoS₂ can be obtained by UHV annealing. The quality of the graphene is demonstrated by atomic resolution scanning tunneling microscopy of ultraflat graphene. The electronic structure of the interface between the polycrystalline graphene and a MoS₂ substrate is measured by angle resolved photoemission spectroscopy (ARPES) and nano-ARPES utilizing a focused photon beam at the SOLEIL synchrotron. We show that at the Fermi-level graphene exhibits a perfect, gapless and undoped Dirac-cone. However, in regions where the π -band of graphene overlaps with states of the MoS₂ substrate, opening of several band-gaps are observed. This demonstrates that the electronic properties in van der Waals heterostructures can be significantly modified by interlayer interaction and thus exemplifying opportunities for tuning materials properties of graphene and other 2D-materials by interfacing them with dissimilar van-der Waals materials.

4:00pm **2D+AS+EM+NS+SS-MoA7 Edge States and Exposure to Hydrogen of Silicon at the 2D Limit on Ag(111)**, *A.J. Mannix, B.T. Kiraly*, Argonne National Laboratory, *M.C. Hersam*, Northwestern University, *Nathan Guisinger*, Argonne National Laboratory

Chemical functionalization of atomically thin materials results in significant modifications to their electronic properties, which can be exploited in device applications. Compared to the chemical inertness of graphene, 2D silicon is expected to exhibit greater reactivity, and thus a greater amenability to chemical functionalization. Among potential functionalization chemistries, hydrogen termination is favored for its relative simplicity and proven efficacy with graphene and bulk Si surfaces. Using ultra-high vacuum (UHV) scanning tunneling microscopy (STM), we have studied the temperature-dependent effects of exposing 2D silicon platelets grown on Ag(111) to molecular and atomic hydrogen. At low doses, atomic hydrogen results in limited adsorption and temperature dependent etching. In the bulk, the formation of vacancies and extended

etch pits is observed. In addition, edge states can play a critical role in the electronic properties of 2D materials. We have also examined at the atomic-scale the edges of 2D silicon platelets.

4:20pm **2D+AS+EM+NS+SS-MoA8 Chlorine Trap-Doping for Transparent, Conductive, Thermally Stable and Damage-Free Graphene.** *Pham Viet Phuong, K.N. Kim, M.H. Jeon, K.S. Kim, G. Yeom*, Sungkyunkwan University, Republic of Korea

We propose a novel doping method of graphene by cyclic trap-doping with low energy chlorine adsorption. Low energy chlorine adsorption for graphene chlorination avoided defect (D-band) formation during doping by maintaining the π -bonding of the graphene, which affects conductivity. In addition, by trapping chlorine dopants between the graphene layers, the proposed doping method dramatically decreased the sheet resistance by ~88% at an optimized condition. Among the reported doping methods including chemical, plasma, photochemical methods etc., the proposed doping method is believed to be the most promising for producing graphene of extremely high transmittance, low sheet resistance, high thermal stability, and high flexibility for use in various flexible electronic devices. Results of angle resolved X-ray photoelectron spectroscopy (XPS), high-resolution transmission electron spectroscopy (HR-TEM), Raman spectroscopy, ultraviolet-Visible spectroscopy (UV-Vis) and sheet resistance, showed that this method is also non-destructive and controllable. The sheet resistance of the doped tri-layer graphene was 70 Ω /sq at 94% transmittance, which was maintained for more than 6.5 h at 230°C. Moreover, the defect intensity of graphene was not increased during the cyclic trap-doping.

4:40pm **2D+AS+EM+NS+SS-MoA9 Modification of Graphene by Neutral Beam Irradiation and Edge Structure Analysis.** *Takeru Okada, S. Samukawa*, Tohoku University, Japan

Since the discovery of single layer of Graphite, Graphene, a single layer of hexagonal carbon atoms, has attracted much attention and shown exciting specific properties. Graphene is a zero band gap semiconductor. Therefore band gap control is one of most important issue to apply for electronic device applications. In order to construct electronic devices with logic operation, both p- and n-type conduction and the control of the carrier density in an active channel are required. Doping with foreign atoms, such as N and B, has proven to be an effective way to modify the electronic properties of carbon related materials and extend their applications. In particular, nitrogen doping brings a carrier which could turn carbon nanotube into n-type semiconductors. It is also feasible to modify the electronic properties of Graphene. Although several doping methods have reported so far, process damages (defect generation) cause degradation of electronic properties.

In this paper, we introduce ultra-low damage neutral beam system which consists of a plasma and process chambers that are separated by a carbon aperture. Charged species and ultra-violet photon from the plasma can be effectively eliminated by the aperture. As a result, only the neutral beam arrives the surface of the sample at the substrate in the process chamber.

We used nitrogen gas for plasma generation and adopted multi-layer Graphene to investigate nitridation mechanism. Graphene multi-layer was irradiated by nitrogen neutral beam with controlled energy of 10 eV at room temperature. The surface modification was analyzed by x-ray photoelectron spectroscopy (XPS). XPS analysis indicated that the carbon atoms were substituted to nitrogen atom and atomic concentration of nitrogen reaches 15 %. Additionally, bonding state of C and N was found to depend on neutral beam irradiation time. Thus beam energy controlled neutral beam can selective nitridation of Graphene. Furthermore the doping density is estimated by Raman spectroscopy and result in 10^{12} [cm⁻²], which is enough to n-type doping of Graphene.

5:00pm **2D+AS+EM+NS+SS-MoA10 Growth Mechanism of Metal Clusters on a Graphene/Ru(0001) Template.** *Shixuan Du, L.Z. Zhang*, Chinese Academy of Sciences, *W. Hofer*, University of Liverpool, UK, *H.-J. Gao*, Chinese Academy of Sciences

Metal nano-clusters have attracted considerable interest because of the potential applications in catalysis and information storage. Due to the soft nature of epitaxial graphene and the lattice mismatch between graphene and metal substrates periodic moiré patterns can be formed. A graphene/metal template, moiré template, can be used to grow dispersed metal nano-clusters with controllable size and shape, or metal clusters with large size and metal layers. However, how intrinsic properties of metal atoms and the moiré template influence the selective adsorption and the growth mode of metal clusters is still open to debate. A general rule, predicting the morphology of metal nano-clusters on a G/metal surface, important to guide experimenters, is still missing. Using first-principles calculations combined with scanning tunneling microscopy experiments, we investigated the adsorption configurations, electronic structures and the corresponding growth mechanism of several transition metal (TM) atoms (Pt, Ru, Ir, Ti, Pd, Au,

Ag, and Cu) on a graphene/Ru(0001) moiré template (G/Ru(0001)) at low coverage. We find that Pt, Ru, Ir, and Ti selectively adsorb on the fcc region of G/Ru(0001) and form ordered dispersed metal nano-clusters. This behavior is due to the unoccupied *d* orbital of the TM atoms and the strong *sp*³ hybridization of carbon atoms in the fcc region of G/Ru(0001). Pd, Au, Ag, and Cu form nonselective structures because of the fully occupied *d* orbital. This mechanism can be extended to metals on a graphene/Rh(111) template. By using Pt as an example, we provide a layer by layer growth path for Pt nano-clusters in the fcc region of the G/Ru(0001). The simulations agree well with the experimental observations. Moreover, they also provide guidance for the selection of suitable metal atoms to form ordered dispersed metal nano-clusters on similar templates.

References:

1. L.Z. Zhang *et al.* Advanced Materials Interfaces, accepted.
2. Y. Pan *et al.* Applied Physics Letter, 95, 093106 (2009)

Biomaterial Interfaces

Room: 317 - Session BI+AS+NS-MoA

Bio/Nano Interfaces

Moderator: Patrick Koelsch, University of Washington

2:00pm **BI+AS+NS-MoA1 Controlling Bio/Nano Interface Response using Metal Oxide Atomic Layer Deposition: Zinc Oxide ALD Modifies how Human Lung Fibroblasts respond *In Vitro* to Multiwall Carbon Nanotubes.** *Erinn Dandley, A. Taylor, G.N. Parsons, J. Bonner*, North Carolina State University

Carbon nanotubes have been reported to cause pulmonary fibrosis in mice after inhalation exposure. When inhaled, multiwall carbon nanotubes (MWCNTs) activate macrophage inflammasomes and interleukin (IL)-1 β release, key cellular components of the innate immune response. Macrophages are the first line of defense that engulf and remove inhaled MWCNTs from the lungs. Macrophages are also a source of secreted osteopontin (OPN), which promotes tissue matrix remodeling and fibrosis. These responses may be triggered by the unique aspect ratio, aggregation or surface chemistry of MWCNTs. In previous studies, we explored atomic layer deposition (ALD) as a means to modify the surface functionality of MWCNTs and studied how the surface coating affected the toxic response of THP-1 cells, a widely used human monocyte/macrophage cell line, and primary peripheral blood monocytes (PBMCs) obtained from normal human donors. Compared to uncoated MWCNTs, we found that nanotubes with Al₂O₃ nanocoatings showed enhanced IL-1 β secretion and decreased OPN production in THP-1 cells and PBMCs, indicating that the coating enhances the innate immune response and decreases pro-fibrotic activity.

In this study we examined the effect of ALD ZnO coatings on the fibrogenic response in human lung fibroblast (HLFs) using mRNA expression and secretion of transforming growth factor (TGF)- β 1 and CXCL10, mediators that promote and deter fibrosis respectively. We find that the ALD ZnO layer thickness can be controlled down to ~5nm, and the thickness scaled directly with the number of ALD cycles, as observed by TEM. Thicker coatings inhibited MWCNT aggregation, and sonication allowed us to induce fiber fragmentation. In this way the ALD coating allowed us to independently adjust surface termination, fiber aggregation, and fiber aspect ratio, providing us a unique tool to examine how each of these factors influences cellular response. Initial results show that the ZnO coating significantly increased TGF- β 1 mRNA expression and stimulated a larger pro-fibrogenic response in HLFs compared to uncoated MWCNTs. Control experiments using ZnO nanoparticles also showed potent induction of TGF- β 1 mRNA in HLFs. Also, the response tends to correlate with extent of dispersion, and is nearly independent of MWCNT aspect ratio. These experiments show that nanoscale surface functionalization of nanoscale materials may help us gain better understanding of the mechanisms associated with toxicology of nanomaterials, and expand knowledge of biological response at nano/bio interfaces.

2:20pm **BI+AS+NS-MoA2 Mechanically Optimized Fe (III) Doped Silica Nanoshells as a Contrast Agent for Ultrasound Imaging and HIFU Therapy.** *James Wang, A. Liberman, R. Viveros, C. Barback, S.L. Blair, Z. Wu, R. Mattrey, W. Trogler, A.C. Kummel*, University of California at San Diego

Ultrasound (US) is a common medical imaging modality due to its flexibility, low-cost and therapeutic potential. 500 nm silica nanoshells were synthesized as a contrast agent to improve US imaging signal for better diagnostic performance. Iron (III) was included into the silica network to enhance the biodegradability of the silica nanoshells. Previously, ferric iron was shown to facilitate silica nanoshell biodegradation due to its strong

binding affinity with serum transferrin proteins. The removal of iron from the silica network by serum proteins fragments the nanoshells enabling effective biodegradation for *in vivo* applications. The silica nanoshells are filled with perfluorocarbon (PFC) vapor which expands and shatters the nanoshells during US irradiation. A mechanically weaker silica nanoshell increases US signal at lower power. A range of alkoxysilanes with selected R-groups such as long chain hydrocarbons, fluorinated carbon chains, fluorinated phenyl groups and vinyl groups were employed along with tetramethyl orthosilicate and iron (III) ethoxide in a modified sol-gel synthesis to create structural defects that alter the mechanical properties of the nanoshells. Monodispersed 500 nm polystyrene beads were used as a soft template during the reaction. The silica nanoparticles were calcined at 550 C to remove the polystyrene core and form hollow nanoshells. SEM and TEM showed that 500 nm silica nanoshells with different microstructures were synthesized incorporating alkoxysilanes with different R-groups. Formulations with higher concentrations of alkoxysilanes with large R-groups such as long chain hydrocarbons resulted in stronger *in vitro* contrast enhanced ultrasound (CEUS) signals due to the increase of structural voids that resulted in weaker shell strength. CEUS experiments demonstrated that mechanically weaker silica nanoshells exhibited longer signal life time and required a lower mechanical index (MI) for imaging. The high intensity focused ultrasound (HIFU) properties of the modified silica nanoshells were tested for potential therapeutic applications. Mechanically weaker silica nanoshells were shown *in vitro* to require a lower HIFU power to fracture which is consistent with safer HIFU therapy. By synthesizing strength tunable silica nanoshells as US contrast agents, it is possible to improve diagnostic US imaging performance in order to detect smaller tissue structures or early stage tumors. Additionally, mechanically weaker silica nanoshells may also increase the efficiency of HIFU enabling HIFU at lower US power and/or higher speed.

2:40pm **BI+AS+NS-MoA3 Synthesis, Functionalization, and Biological Imaging with Quantum Dots**, *Preston Snee*, University of Illinois at Chicago **INVITED**

Semiconductor quantum dots (QDs, or nanocrystals), are very bright chromophores that possess unlimited potentials in alternative energy generation and for biological sensing and imaging applications. Our group has made advances in the synthesis QDs to produce 100% efficient emitters; furthermore, we can dope the semiconductor with guest ions to alter the bandgap. We recently invented a method to dope each quantum dot with an exact number of guest ions, a feat that was previously considered impossible. As very bright fluorophores, quantum dots are ideal for biological imaging and sensing. Our first contribution in this regard was to develop methods of chemical and biological functionalization of water-soluble quantum dots as many existing methods either quenched the QDs or had very low reaction yields. We have circumvented these problems by synthesizing polymers which serve as QD functionalization reagents; the polymer – QD activated intermediate has increased stability and allows us to conjugate chemical and biological vectors to the nanocrystals with ~100% reaction yields. We use these methods to functionalize QDs with organic fluorophores that can report on the local chemical and biological environment. We have synthesized several ratiometric, or “self-calibrating” sensors, for pH, toxic metals, DNA, and proteins. In our recent work on protein sensing, we have developed an all optical method for sensing unlabeled proteins with a better detection limit than any currently existing technology. We have also circumvented the well-known problem of cyto cellular delivery of quantum dots into live, adherent cells.

3:40pm **BI+AS+NS-MoA6 Easynanofab: Fast, Simple, Combinatorial Routes to Reusable Plasmonically Active Gold Nanostructures Over Macroscopic Areas**, *A. Tsargorodskaya, O. El Zubir, Graham Leggett*, University of Sheffield, UK

Plasmonic effects associated with gold nanocrystals have attracted widespread interest for the interrogation of biological molecules. Existing approaches to fabrication of plasmonic nanostructures fall into two categories: high precision methods such as electron beam lithography that rely on complex, specialised infrastructure; and simple, low-cost methods such as colloidal lithography that offer limited capacity. Here, we describe a fast, simple method for the fabrication of re-usable, robust gold nanostructures over macroscopic (cm²) areas that provides enormous scope to control nanostructure morphology and dimensions, and which also uses only simple apparatus and requires no access to a clean-room. We have assembled a combinatorial library of over 200 different samples consisting of highly crystalline gold nanostructures that exhibit varying morphologies, dimensions and periodicities but yield intense plasmon bands. These structures enable the rapid identification of optimum substrates for the detection and analysis of biological targets, and provide a platform for exploring the relationship between particle morphology and optical properties. Self-assembled monolayers (SAMs) of alkythiolates on chromium-primed polycrystalline gold films are patterned using a Lloyd's

mirror interferometer and etched using mercaptoethylamine in ethanol in a rapid process. The use of a Cr adhesion layer facilitates the cleaning of specimens by immersion in piranha solution, enabling their repeated re-use without significant change in their absorbance spectra over two years. Annealing yields structures with a uniformly high degree of crystallinity that exhibit strong plasmon bands. Because of the ease with which nanoparticle morphology may be controlled using interferometric lithography (IL), it provides a convenient means to investigate the correlation between structural parameters (particle dimensions, spacing) and optical responses. The shift in the position of the plasmon band after site-specific attachment of histidine-tagged green fluorescent protein (His-GFP) and after adsorption of chlorophyll and bacteriochlorophyll was measured for a range of nanostructured films, enabling the rapid identification of structures that yielded the largest shifts. Strong resonant coupling was observed when light-harvesting membrane protein complexes from plants and bacteria were coupled to gold nanostructure arrays, yielding absorbance spectra that were very different from those of the clean gold nanostructures. This approach offers a simple route to the production of durable, reusable, macroscopic arrays of gold nanostructures with precisely controllable morphologies.

4:00pm **BI+AS+NS-MoA7 Impacts of Nanoparticle Synthesis Route, Structure and Serum Proteins on the Dispersion and Dissolution of Ag Nanoparticles in Biological Media**, *P. Munusamy, J.N. Smith, C. Liu, C.-M. Wang*, Pacific Northwest National Laboratory, *S. Chen*, Imperial College London, UK, *M.H. Engelhard*, Pacific Northwest National Laboratory, *A.E. Porter, M.P. Ryan*, Imperial College London, UK, *Donald Baer*, Pacific Northwest National Laboratory

The wide-spread use of silver nanoparticles in consumer products raises questions of environmental impact and toxicity. Because both silver particles, and silver ions formed by particle dissolution, may impact biological systems, it is important to understand the characteristics of silver nanoparticles as they are made and their stability and dissolution in the medium relevant to environmental and toxicological studies. Silver nanoparticles produced by different synthesis routes can have significantly varying physical and chemical characteristics. In this talk we will summarize the characterization and dissolution stability of three types of silver nanoparticles (20 nm particles synthesized with and without gold core (~7 nm) and 110 nm particles with gold core) in cell culture media with serum proteins: FBS10%/RPMI, the culture media used at Pacific Northwest National Laboratory for *in-vitro* toxicity studies. These nanoparticles were synthesized and prepared for biological study in aqueous solution. They were examined *in situ* using dynamic light scattering, zeta potential measurements and optical adsorption and *ex situ* with x-ray photoelectron spectroscopy and transmission electron microscopy. For the dissolution studies, concentrations of particles examined were varied from 1 µg/ml to 50 µg/ml, consistent with the range of concentrations typically used during *in-vitro* studies. Silver particles with gold cores had smaller crystallite size and higher apparent solubility than three different batches of pure ~ 20 nm silver particles. A simple dissolution model was found to describe the time variation of particle size and amount of dissolved silver for particle loadings above 9 µg/ml. The effective solubility product obtained from fitting the data was higher for the 20 nm particles with the gold core in comparison to the pure silver or 110 nm particles. The dissolution of silver nanoparticles was also found to be enhanced by presence of serum proteins contained in fetal bovine serum (FBS). In addition, the protocol of dispersion in cell culture medium was found to influence particle agglomeration and the rate of dissolution. In these measurements focusing on a 24 hour time point, we found that the structure of the silver nanoparticles can have a significant impact on the concentration of dissolved silver in media and thus the dosimetry to which cells would be exposed during *in vitro* studies.

This work has been supported by the NIEHS under Center grant U19 ES019544. Portions of this work were performed using EMSL, a national scientific user facility sponsored by the US Department of Energy, Biological and Environmental Research and located at PNNL.

4:20pm **BI+AS+NS-MoA8 Analysis of Protein Coated Nanoparticles by X-ray Photoelectron Spectroscopy and Solution-Based Particle Size Techniques**, *C. Minelli, Natalie Belsey, A.G. Shard*, National Physical Laboratory, UK

The attachment of proteins to nanoparticles' surface is of increasing interest in medicine for applications such as drug delivery and diagnostics. The unintentional acquisition of a protein corona from biological media is also important in determining the performance and potential toxicity of such particles. Understanding and refinement of the performance of nanoparticles of use in medical applications require accurate and quantitative characterisation of their protein interface. Our efforts are focussed upon developing measurement techniques to enable useful characterisation of this interface. In this study, three biomolecules of a range of sizes, shapes and

mechanism of interaction with gold surfaces, i.e. 16 AA peptide, BSA and IgG, were adsorbed to gold nanoparticles (10, 20, 40, 60 and 80 nm) and the shell thickness was measured in solution using dynamic light scattering (DLS) and differential centrifuge sedimentation (DCS). UV-visible spectrophotometry was used to monitor localised surface plasmon resonance (LSPR) shifts of the nanoparticles due to the acquisition of the protein shell. Combination of this information with thickness measurements allowed for an estimation of the protein shell refractive index and average number of biomolecules at the nanoparticle surface. X-ray photoelectron spectroscopy (XPS) analysis of the same nanoparticles deposited on a PTFE substrate enabled determination of the nanoparticle shell chemical composition and dehydrated thickness, from which the number of molecules at the nanoparticle surface was also estimated. Parallel characterisation of the nanoparticles in their colloidal form and in vacuum provided consistent results and the combination of the techniques revealed farther insight into molecular adsorption at nanoparticles' interfaces. The complementarity of the approaches also allowed for validation of the methods, which is important for their application to a wide range of nanoparticle types. For example, DLS and LSPR analysis are not suitable for dealing with aggregated samples, but XPS is, while XPS measurements of organic nanoparticles are challenging and liquid based techniques may be preferred.

4:40pm **BI+AS+NS-MoA9 Development of Nanofibrous Meshes as Smart Dressings for Chronic Wound Care, Martina Abrigo, P. Kingshott, S.L. McArthur**, Swinburne University of Technology, Australia
Diabetic, pressure, venous and arterial ulcers are a large social, economic and healthcare burden. These chronic non-healing wounds show delayed and incomplete healing processes exposing patients to high risk of infection. The design of wound dressings that combine the necessary morphological and physical requirements for wound healing with the value-added capability to address optimal cell responses and impair bacterial proliferation represents a major challenge in chronic wound care. Polymeric nanofibrous meshes fabricated through the electrospinning process are promising candidates as wound dressings due to their high surface area, micro-porosity and non-woven structure. In this study, the parameters of the electrospinning process (such as spinning rate and electric field intensity) were optimized to fabricate nanofibrous membrane in Polystyrene (M.W. 250.000). The morphological properties of the electrospun meshes were analysed by bright microscopy, three-dimensional optical profiler, Scanning Electron Microscopy (SEM) and Atomic Force Microscopy (AFM). Electrospun materials have been used as scaffolds for tissue engineering for a number of years, but there is surprisingly little literature on the interactions of fibres with bacteria. In order to understand microbial infiltration and control in wound dressings, a number of microbiological assays (MTT, MTS and live/dead) were completed using *E. Coli*, *P. Aeruginosa*, *S. Aureus* in an effort to understand how the morphological and structural properties of the electrospun meshes influence bacterial attachment, proliferation and growth.

5:00pm **BI+AS+NS-MoA10 Electrophoretic Stretching of Tethered DNA in Nanoslits, Jia-Wei Yeh, K. Szeto, H.G. Craighead**, Cornell University

We have investigated the field-extension of tethered DNA in nanoslits with slit heights ranging from 30 to 130 nm, and performed an analysis from an approximated modified worm-like chain (mWLC) field-extension relation. DNA molecules attached to microspheres were anchored at a micro-nanofluidic interface and the molecules electrophoretically extended. We demonstrated that both the DNA segmental correlation and equilibrium lengths increased as the slit height decreased. Furthermore, for extremely confined DNA where $h \leq 30$ nm, we observed reptation of the DNAs' contours within the nanoslit, a phenomena that may be induced by inhomogeneous surface charge distributions. This nano-confined system may have implications for single-molecule sensors on detecting and analyzing genetic, epigenetic markers, and related nanobiotechnological applications.

5:20pm **BI+AS+NS-MoA11 Measuring DNA Looping Pathways using Nanofluidic Manipulation, M. Roushan, Z. Azad, H. Wang, Robert Riehn**, NC State University

DNA performs a carefully choreographed ballet during the cell cycle. The organization is driven by the specific binding of proteins to form tertiary DNA-protein-DNA complexes. The search process that precedes the formation must overcome the challenge of very low effective mobility of genomic-sized DNA pieces in the dense cellular environment.

In this paper we will discuss a group of nanofluidic device that force two DNA molecules to either slide past each other in parallel, or cross over each other at a steep angle. Nanochannel cross-sections are 100×100 nm², and are hundreds of microns long. Because DNA is elongated through confinement,

loop with a length down to 2 kb can be directly observed in real time. Channels are made of fused silica, enabling single-molecule observation of both DNA and proteins. Because the effective concentration of DNA inside channels exceeds 1 mg/ml with the channel at the point of DNA-DNA contact, protein-mediated capture cross-sections are very high.

We will present analyses of different DNA-binding proteins that demonstrate that we can distinguish dense and sparse binding modes and the compensation of electrostatic DNA-DNA repulsion through protein binding. We further report the detection of long-lived tertiary complexes acting as a lock for looped DNA configurations, and the presence of very short-lived transient links. We further demonstrate a pathway for loop formation that is enhanced in nanochannel devices, and that may be important in a cellular context. By using precision hydrodynamic flows, we are able to measure free energies of the search process.

Energy Frontiers Focus Topic

Room: 315 - Session EN+EM+MN+NS+TR-MoA

Energy Harvesting with Nanostructures

Moderator: Phillip Christopher, University of California - Riverside

2:00pm **EN+EM+MN+NS+TR-MoA1 Optical Engineering for Colloidal Quantum Dot Photovoltaics, Susanna Thon**, Johns Hopkins University **INVITED**

The next generation of photovoltaics seeks to improve both efficiency and cost through the use of flexible platforms and new materials. Colloidal quantum dots (CQDs), semiconductor nanoparticles synthesized from solution, are a particularly attractive material for solar energy. The bandgap of films composed of arrays of CQDs can be tuned via the quantum confinement effect for tailored spectral utilization. The performance of CQD solar cells is currently limited by an absorption-extraction compromise, whereby photon absorption lengths in the near infrared regime exceed minority carrier diffusion lengths. I will review several photonic and optical engineering schemes aimed at overcoming this compromise. These include nanophotonic and geometric light trapping techniques, as well as jointly-tuned plasmonic-excitonic photovoltaics. Additionally, I will discuss how nanoscale engineering of CQDs and related materials can lead to emergent optical properties for building color-tuned optoelectronic films.

2:40pm **EN+EM+MN+NS+TR-MoA3 Energy Transfer from Nanocrystal Quantum Dots to Si Nanomembranes Monitored via Wavelength Dependent Photocurrent Response, Weina Peng, S. Sampat, S. Rupich, B. Anand, H. Nguyen, D. Taylor, Y. Gartstein, Y.J. Chabal, A. Malko**, University of Texas at Dallas

We report the observation of wavelength dependent photocurrent in thin silicon nanomembranes (75 nm) coupled to colloidal CdSe/ZnS nanocrystal quantum dots (NQDs). The measurement was performed on back-gated, FET-type thin Si structures, which are functionalized with self-assembled monolayer (SAM) of ester termination groups to prevent surface oxidation and the formation of surface defect states. A thin film of nanocrystals is drop casted on the surface and an increase of photocurrent, up to several hundred nA, are recorded as a function of excitation wavelength on NQD/SAM/Si devices vs. plain SAM/Si structures. Quantitative analysis of photocurrent vs. NQD absorption spectrum allows us to ascribe the observed photocurrents to the photoexcited NQD excitons transferred to the underlying Si substrate via non-radiative and radiative energy-transfer mechanisms¹.

¹H. M. Nguyen, O. Seitz, W. N. Peng, Y. N. Gartstein, Y. J. Chabal, and A. V. Malko, ACS Nano 6, 5574 (2012).

3:40pm **EN+EM+MN+NS+TR-MoA6 Triboelectric Nanogenerator - A New Energy Technology, ZhongLin Wang**, Georgia Institute of Technology **INVITED**

Triboelectrification is an effect that is known to each and every one probably ever since the ancient Greek time, but it is usually taken as a negative effect and is avoided in many technologies. We have recently invented a triboelectric nanogenerator (TENG) that is used to convert mechanical energy into electricity by a conjunction of triboelectrification and electrostatic induction. As for this power generation unit, in the inner circuit, a potential is created by the triboelectric effect due to the charge transfer between two thin organic/inorganic films that exhibit opposite tribo-polarity; in the outer circuit, electrons are driven to flow between two electrodes attached on the back sides of the films in order to balance the potential. Ever since the first report of the TENG in January 2012, the output power density of TENG has been improved for five orders of

magnitude within 12 months. The area power density reaches 500 W/m^2 , volume density reaches 490 kW/m^3 , and a conversion efficiency of $\sim 50\%$ has been demonstrated. The TENG can be applied to harvest all kind mechanical energy that is available but wasted in our daily life, such as human motion, walking, vibration, mechanical triggering, rotating tire, wind, flowing water and more. Alternatively, TENG can also be used as a self-powered sensor for actively detecting the static and dynamic processes arising from mechanical agitation using the voltage and current output signals of the TENG, respectively, with potential applications for touch pad and smart skin technologies. The TENG is possible not only for self-powered portable electronics, but also as a new energy technology with a potential of contributing to the world energy in the near future.

[1] Z.L. Wang "Trieboelectric Nanogenerators as New Energy Technology for Self-Powered Systems and as Active Mechanical and Chemical Sensors", ACS Nano 7 (2013) 9533-9557.

[2] G. Zhu, J. Chen, T. Zhang, Q. Jing, Z. L. Wang* "Radial-arrayed rotary electrification for high-performance triboelectric generator", Nature Communication, 5 (2014) 3456.

4:20pm EN+EM+MN+NS+TR-MoA8 **Conflicting Roles of Charge Traps in ETA Solar Cells: The CREM Point of View**, Hagai Cohen, Weizmann Institute of Science, Israel

The characterization of multi-interfacial devices commonly encounters critical difficulties due to the limited access of standard electrical probes to selected inner domains. In this respect, the XPS (x-ray photoelectron spectroscopy) based CREM (chemically resolved electrical measurements) [1] is a technique proposing particularly useful capabilities. Demonstration of internal junction fields evaluation has already been provided, as well as the direct measurement of layer-specific photovoltages in ETA (extremely thin absorber) solar cells.[2] However, the complex dynamics realized during charge separation in such cells has not yet been investigated thoroughly by CREM.

The present work focuses on this issue, showing conflicting roles of charge trap states and, specifically, their different expression under controllably varied conditions. Comparison with complementary characterization techniques is further discussed, demonstrating the unique insight provided by CREM for their interpretation.

References

1. H. Cohen, *Appl. Phys. Lett.* **85**, 1271 (2004).
2. Y. Itzhaik, G. Hodes, H. Cohen, *J. Phys. Chem. Lett.* **2**, 2872 (2011).

4:40pm EN+EM+MN+NS+TR-MoA9 **Understanding Morphological and Structural Effect on Organic Photovoltaic Devices from Plasmonic Particles using Advanced Characterization Techniques**, Nuradhika Herath, V. Lauter, J. Browning, Oak Ridge National Laboratory

Organic electronics have been under intense scientific interest in recent years because of their attractive properties such as low cost fabrication processes, ability to performance under low light, and flexibility. Major achievements are based on use of new conjugated polymer and small molecules in bulk heterojunction (BHJ) devices to increase the inner donor acceptor interfaces of fully functional devices such as organic photovoltaics (OPVs) and organic light emitting devices (OLEDs). Many strategies have been introduced to enhance the power conversion efficiency (PCE) of organic electronics. Among them, one of the most promising solutions to enhance the absorption and device efficiencies of OPVs is incorporation of various metal nanoparticles (NPs). Metallic NPs enhanced the efficiency of the devices through local surface plasmonic responses (LSPR). This phenomenon reduced the recombination level of geminate excitons and increases the exciton dissociations, which enhanced the photocurrent and fill factors of devices. However, metallic NPs blended within the active layer can act as polaron traps detracting the device performances. In this study, we investigate layer and interfacial structure of small molecule (SM), *p*-DTS(FBTTh₂) and fullerene, PC₇₀BM system incorporated with silver (Ag) NPs, using neutron reflectometry (NR), X-ray reflectometry and Atomic Force Microscopy (AFM). We present detailed composition changes with Ag NPs concentrations along the film depth to understand morphological and dynamical effects of BHJ devices incorporated with plasmonic particles. To complement and enhance the findings from NR, we report optical properties of the samples using UV-Visible absorption and Photoluminescence spectroscopy. Our findings provide unique information and clear insights into dynamics of plasmonic organic solar cells and their future applications for further enhancement of PCE.

This research was conducted at Spallation Neutron Source and at the Center for Nanophase Materials Sciences, which is sponsored at ORNL by the Scientific User Facilities Division, Office of Basic Energy Sciences, U.S. Department of Energy.

5:00pm EN+EM+MN+NS+TR-MoA10 **Doped TiO₂ Based Core-Shell Structures for High Efficiency Hybrid Solar Cells**, Jonas Weickert, J. Dorman, M. Noebels, M. Putnik, T. Pfadler, University of Konstanz, Germany, A. Wisnet, C. Scheu, LMU Munich, Germany, L. Schmidt-Mende, University of Konstanz, Germany

Hybrid solar cells, with an inorganic/organic interface for charge separation, have been extensively investigated in the past decade in order to replace the expensive Si based technology with an inexpensive alternative. Typically, these devices incorporate a mesoporous TiO₂ film which is decorated with dye molecules and filled with a hole transport polymer, for example P3HT, to conduct the electrons and holes, respectively. Recently, we have shown that the efficiency of nanowire based hybrid solar cells can be increased from $\sim 1.8\%$ to 2.5% through the formation of a Sn-doped TiO₂/TiO₂ core-shell device created via a hydrothermal growth and subsequent TiCl₄ treatment. However, this surface treatment presents difficulties in creating a crystalline conformal coating, limiting the control over the extent of coating and the crystallinity, directly affecting the charge injection from the polymer into the TiO₂ array. In this work, we directly deposit a controllable TiO₂ film through atomic layer deposition to conformally coat the nanowire arrays with various thicknesses. By changing the thickness and TiO₂ crystallinity, we are able to engineer the energy levels at the TiO₂-dye-P3HT interface due to the magnitude and position of the Fermi levels of the core and shell material, influencing the rate of charge injection and recombination. Furthermore, the crystallinity of the shell layer directly affects the amount of dye that can be absorbed on the surface of the nanostructures with a reduction in light absorption by roughly 30% from anatase to rutile TiO₂. Finally, a detailed mechanism will be proposed for the device performances based on the energy level alignment between the pinned Fermi-level TiO₂ structure and the HOMO of the P3HT resulting in a shifting open circuit voltage based on the crystal phases. Additionally, the core-shell structures are characterized with photovoltage decay and impedance spectroscopy measurements to study the charge transport and recombination across these various interfaces.

5:20pm EN+EM+MN+NS+TR-MoA11 **Stack Numbers Dependence of the Activation Energies for Carrier Escape from and Recombination in Strain-Balanced InGaAs/GaAsP MQW**, Atsuhiko Fukuyama, T. Ikari, K. Nishioka, T. Aihara, H. Suzuki, University of Miyazaki, Japan, H. Fujii, M. Sugiyama, Y. Nakano, The University of Tokyo, Japan

Fabrication of multiple quantum well (MQWs) in an absorption layer can extend the absorption region toward a longer wavelength and enhance the short-circuit current in the solar cells. However, MQWs function as recombination centers, leading to degradation in both open-circuit voltage and fill factor. We have already reported that the increase in stack number of QW causes the degradation of carrier collection efficiency [1]. In this study, we investigate the effects of stacks number on temperature dependences of the photoluminescence (PL), photothermal (PPT) and the surface photovoltage (SPV) signals. Although the photoexcited carriers in the barrier should relax by the radiative recombination (PL), carriers can thermally escape (SPV) or non-radiatively recombine (PPT) at the same time. Therefore, the latter two methodologies give us new insights for the carrier recombination and drift through the QW.

The present strain-balanced InGaAs/GaAsP MQWs absorption layer was composed of a 7.0-nm-thick In_{0.25}Ga_{0.75}As well and a 10.8-nm-thick GaAs_{0.66}P_{0.34} barrier. All layers were grown on an *n*-type GaAs substrate using metal-organic vapor phase epitaxy. We prepared different samples with MQW stack numbers of 10, 20, 30, and 40 in the *i*-region.

All PPT and SPV spectra showed three distinctive peaks followed by a step like function. They were decomposed into inter-subband transitions expressed by the two dimensional density of states for the QW and exciton peaks [2]. Although the PL intensity decreases with increasing the temperature, signals for PPT and SPV increases. We suppose two activation energies for the process: one is that for the carrier escape from the QW and another is for the non-radiative recombination in the QW. The three rate equations were built for PL, PPT and SPV and the temperature dependences are numerically fitted to estimate the two activation energies. As a result, we have estimated the activation energy for carrier escaping from the QW is constant as 70 meV for all samples with different stacks number. This is the same as the calculated barrier height. However, the activation energy for the non-radiative recombination increases from 6 to 49 meV for the sample with 10 and 40 stacks. This means that radiative recombination increases with increasing the stack number. The carriers thermally escape from the QW again relax into next well and may contribute to increase the radiative recombination.

[1] H. Fujii et al., *Jpn. J. Appl. Phys.* **51**, 10ND04 (2012).

[2] M. Kondow, A. Fukuyama, and T. Ikari et al., *Appl. Phys. Express* **2**, 041003 (2009).

Nanophotonics and Plasmonics**Moderator:** WeiDavid Wei, University of Florida**2:00pm NS+EN-MoA1 Sculpting the Flow of Light at the Nanoscale, Harry Atwater, California Institute of Technology INVITED**

Understanding the fundamental properties of plasmonic and dielectric materials in resonant subwavelength structures has fueled an explosion of interest in metamaterials and nanophotonic devices. In this seminar, we explore new directions for plasmonics by examining the relationship between plasmons and the electrochemical potential of the electron gas, and we discuss opportunities to observe quantum coherent states in plasmonic structures. Usually plasmons are described in a classical electromagnetic theory context, yet plasmons are fundamentally quantum excitations. Moreover, the carrier density and optical properties of plasmonic materials are typically fixed at the time of fabrication. Field effect tuning of the electrochemical potential in graphene nanoresonators enables the plasmon and phonon dispersion to be measured. Electrochemical and carrier density modulation in metals yields tunable resonances in metal nanostructures and reveals the plasmoelectric effect, a newly-discovered photoelectrochemical potential. By tuning the permittivity and index to near-zero values, expands the length scale over which coherent quantum emitter phenomena (e.g., concurrence, superradiance) can be observed in epsilon-near-zero media. Finally, we demonstrate entanglement or coherent superposition states of single plasmons using two plasmon-quantum interference in chip-based plasmon waveguide directional couplers.

Web resources:

<http://www.lmi.caltech.edu/><http://daedalus.caltech.edu/>**2:40pm NS+EN-MoA3 Patterning of Plasmonic Structures for Chiroptical Spectroscopy, Oded Rabin, A.P. Lawson, P.C. McAvoy, I.D. Mayergoyz, University of Maryland, College Park**

Fabrication of truly chiral nanostructures is a challenging process, often requiring multiple cycles of patterning, deposition and planarization. Planar and three dimensional plasmonic nanostructures were fabricated through focused ion beam (FIB) milling, electron beam lithography (EBL) patterning, and a combination thereof, achieving truly chiral nanoscale patterns in a single deposition step. Using computational modeling tools, the plasmon resonance spectra of the structures were predicted. We have combined our computational results and novel fabrication methods to achieve chiral plasmonic nanostructures with useful resonances in the visible and near infrared ranges of the EM spectrum. These substrates are promising for the selective manipulation of circularly polarized radiation at nanometer length scales.

3:00pm NS+EN-MoA4 Hot Electron Generation Enhanced by Carrier Multiplication Probed with a Graphene/TiO₂ Nanodiode, YoungKeun Lee, KAIST, Republic of Korea, H.K. Choi, ETRI, Republic of Korea, H. Lee, KAIST, Republic of Korea, J.S. Choi, ETRI, Republic of Korea, E. Hwang, Sungkyunkwan University, Republic of Korea, J.Y. Park, KAIST, Republic of Korea

Graphene has attracted intensive attention for viable applications such as energy conversion and optoelectronic devices. When photons hit the graphene, the photon energy can be transferred to hot carriers above the Fermi level from the valence band of the graphene before the photon energy is lost as heat. The efficiency of the conversion depends on the interaction of photons with electrons/holes in the system. In graphene without a bandgap, the process of energy relaxation consists of the Auger process (impact ionization), which leads to carrier multiplication. Here, we fabricated a graphene/TiO₂ nanodiode to investigate carrier multiplication by experimental detection and theoretical confirmation of hot electron amplification. Our findings indicate that carrier multiplication of the graphene based on the strong electron-electron interaction is highly efficient, compared with Au/TiO₂ at a given photon energy. Multiple generations of hot electrons can induce photocurrent, which suggests the possibility of feasible applications such as photovoltaics and photodetectors.

3:40pm NS+EN-MoA6 Doping Induced 1D Plasmons in Ag Monolayer Stripes on Si(557), Timo Lichtenstein, U. Krieg, C. Teegenkamp, H. Pfürir, Leibniz Universität Hannover, Germany

An efficient way to transfer energy, e.g. light, into an electronic system is by excitation of plasmons. Due to their flat and almost linear dispersion, allowing extreme confinement in a broad frequency range, and their natural function as wave guides 1D plasmons are particularly interesting.

As we show here for the system Ag adsorbed on Si(557), the interaction between adsorbate layers of transition metal atoms and strongly anisotropic surfaces can lead to various quasi-one-dimensional (1D) signatures, which, however, are not all necessarily metallic. Using low energy electron diffraction in combination with scanning tunneling microscopy and electron energy loss spectroscopy, we correlate the structure, determined by SPALEED and STM, with the properties of low dimensional collective excitations, as measured with momentum and energy resolving electron loss spectroscopy. Semiconducting structures with double periodicity along the chains are formed Ag coverages below 0.3 monolayers (ML). At higher coverages, the formation of wires with ($\sqrt{3}\times\sqrt{3}$) order sets in. Only these wires turn out to be metallic, as is evident from the appearance of plasmonic losses, which show 1D dispersion only along the wires. This 1D property even persists up to one monolayer, where a densely packed array of metallic ($\sqrt{3}\times\sqrt{3}$) stripes is formed. We show evidence that the metallic property is induced by an extrinsic doping process of excess Ag (or other) atoms localized at the step edges, which can be reversibly removed and added. With this system we were able to explicitly show that the 1D plasmon frequency depends on the electron density proportional to $\sqrt{n_e}$ also in the 1D case, and that the confinement of the electrons on the wires is also dependent on doping concentration.

4:00pm NS+EN-MoA7 Surface Plasmon-Mediated Gold Nanoparticle Deposition via Two Different Mechanisms, Jingjing Qiu*, W.D. Wei, University of Florida

Utilizing intrinsic surface properties to direct and control nanostructure growth on a large-scale surface is fundamentally interesting and holds great technological promise. We have developed a novel "bottom-up" approach to fabricating sub-15 nm Au nanoparticles on a nanostructured Ag surface via a chemical solution deposition by using localized surface plasmon resonance (SPR) excitation. Nanoparticle sizes were tunable between 3 to 10 nm by adjusting the deposition time utilizing the photothermal effects on a nanostructured Ag film surface. In addition, Au nanoparticles can be selectively deposited at the tip of a Ag bowtie nanostructure with the enhanced electric field.

4:20pm NS+EN-MoA8 Enhanced Light-Matter Interactions in Nanoparticle Arrays, Teri Odom, Northwestern University INVITED

Metal nanostructures concentrate optical fields into highly confined, nanoscale volumes that can be exploited in a wide range of applications. This talk will describe new ways to design arrays of strongly coupled nanoparticles and plasmonic hetero-oligomers that can exhibit extraordinary properties such as plasmon lasing and enhanced gas sensing. First, we will describe a new type of nanocavity based on arrays of metal nanoparticles. These structures support lattice plasmon modes that can be amplified and that can result in room-temperature lasing with directional beam emission. Second, we will focus on nanoparticle assemblies composed of more than one type of material. Hetero-oligomers composed of strong and weak plasmonic materials (Au-Pd dimers and trimers) showed unusual wavelength shifts when subjected to hydrogen gas. We performed detailed modeling to understand the near-field coupling responsible for these amplified light-matter interactions.

5:00pm NS+EN-MoA10 Plasmon-induced Current Enhancement at Nano-sized Metal-Oxide Interfaces, Jiechang Hou*, D.A. Bonnell, University of Pennsylvania

Nano-sized metal-oxide interfaces possess unique physical properties and offers new access to novel functionalities. We have shown that at the nanoscale the electronic properties of Au/SrTiO₃ interfaces are size and atomic structure dependent [1]. This size dependence of interface properties has consequences to related behavior, such as resistive switching [2]. Earlier we have shown that plasmon induced hot electrons can be extracted from Au nanoparticles into molecular devices [3]. Here we use Au nano-antennas/SrTiO₃ interfaces as a facile model system to study this phenomenon. The study combines nanofabrication, optical spectroscopies, field simulation and advanced scanning probe microscopy. The dependences of photocurrent on power density and temperature are quantified, and the mechanism of photocurrent enhancement is discussed. We believe that this study can improve the understanding of the mechanism of plasmon-induced current enhancement and facilitate the modern device design.

References:

- [1] J. Hou, S. S. Nonnenmann, W. Qin, D. A. Bonnell, *Appl. Phys. Lett.* **103**, 252106, 2013.
- [2] J. Hou, S. S. Nonnenmann, W. Qin, D. A. Bonnell, *Adv. Funct. Mater.* (2014). doi: 10.1002/adfm.201304121.

*** NSTD Student Award Finalist**

[3] D. Conklin, S. Nanayakkara, T. Park, M. F. Lagadec, J. T. Stecher, X. Chen, M. J. Therien, D. A. Bonnell, *ACS Nano* **7**, 4479 (2013).

5:20pm **NS+EN-MoA11 Extreme Tunability of Metal-Dielectric Multilayered Structures using Al-doped ZnO Grown by Atomic Layer Deposition**, *Jonathan Skuza, R.M. Mundle, K.C. Santiago*, Norfolk State University, *D.L. Lepkowski*, Louisiana State University, *A.K. Pradhan*, Norfolk State University

Plasmonic metamaterials have been a burgeoning area of research in recent years, where surface plasmon polaritons (SPPs) can manipulate light on the nanoscale. Typically, noble metals (e.g. Ag, Au) have been the key materials in this field of research, but suffer drawbacks (e.g. high loss) especially in the mid- and near-infrared (NIR) spectral ranges. Recently, wide bandgap semiconductors, such as Al-doped ZnO (AZO), have been shown to hold great potential in surpassing the tunability and flexibility of traditional noble metals in nanoplasmonic applications. Generally, these transparent conducting oxides have been extremely important for various optoelectronic applications due to the coexistence of high conductivity and high transparency, which can be tuned through doping. Recent studies have shown that these wide bandgap semiconductors, in particular AZO, are also efficient nanoplasmonic materials in the NIR due to their metallic behavior, strong confinement of SPPs, and low loss. AZO has been studied extensively using a multitude of deposition techniques, especially atomic layer deposition (ALD), which is particularly useful to grow uniform and conformal films with a high degree of thickness control on complex three-dimensional topographies because it is based on a binary sequence of self-limiting surface chemical reactions. Furthermore, the doping concentration can be precisely controlled by adjusting the ALD cycle ratios of the host and dopant materials, thus making ALD a unique and powerful method to deposit AZO into high aspect ratio structures for nanoplasmonic applications. Recently, it has been shown that ALD-grown AZO offers extreme tunability that can be utilized for many applications, including plasmonic components for epsilon-near-zero metamaterials. This extreme tunability is exploited here in metal-dielectric multilayered structures in order to manipulate and control light in subwavelength volumes for various optical applications.

Biomaterial Interfaces

Room: 317 - Session BI+AS+MN+NS-TuM

Biosensors

Moderator: Graham Leggett, University of Sheffield

8:20am **BI+AS+MN+NS-TuM2 An Inductive-Capacitive Sensor for Real-time Biofilm Growth Monitoring**, *Ekaterina Tolstaya, Y.W. Kim, S. Chu, K.D. Gerasopoulos, W.E. Bentley, R. Ghodssi*, University of Maryland, College Park

We present a real-time biofilm monitoring device based on inductive-capacitive (LC) sensing principles. Bacterial biofilms cause severe infectious diseases and environmental contamination. The bacterial biofilm's complex structure and composition, as well as its ability to exchange genetic information, result in a high tolerance for antimicrobial agents. As a result, established biofilms on implanted or external biomedical devices, such as catheters, are difficult to treat. Traditional antibiotic therapies for biofilm infections often require doses 500-5000 times larger than for non-biofilm infections [1]. Moreover, biofilm growth in environmental and industrial facilities causes contamination and corrosion of equipment due to the toxins generated by biofilms. Therefore, early detection of biofilm growth is critical to facilitate treatment of severe infections and prevent equipment contamination.

In this work, an LC sensor was fabricated using conventional lithography and metal deposition via E-beam evaporation (Cr/Au, 15 nm/200 nm) (Figure 1). The resonant frequency of the sensor was approximately 16 MHz in air at room temperature. A device sensitivity of 1140 Hz/dielectric was demonstrated using a known dielectric material (deionized water) (Figure 2). *Escherichia coli* W3110 biofilms were grown for 48 hours over the LC sensor and the resonant frequency of the sensor was measured every 80 seconds using a spectrum analyzer (Figure 3). As the biofilm grew over the device, an increase in the resonant frequency of the LC sensor was observed. This is due to the lower dielectric permittivity of the biofilm compared to that of the growth media (Luria Broth, $\epsilon \sim 80$), which results in decrease in the capacitance of the sensor. In control experiments with water and air as the media, a slight decrease in the resonant frequency was observed. The resonant frequency shift over time is in good agreement with the natural trend of biofilm growth (Figure 4) [2, 3]. The results validate the use of LC sensing for continuous monitoring of biofilm growth. This sensitive and reliable detection scheme, as well as the capability for flexible substrate integration and wireless interfacing, can serve as a foundation for the development of microsystems for real-time biofilm monitoring for both clinical and environmental applications.

8:40am **BI+AS+MN+NS-TuM3 The Interplay of Electrode Materials and Biomaterials in a Catechol-Modified Chitosan-Based Sensor for Clozapine Detection**, *Robert Dietrich, T.E. Winkler, H. Ben-Yoav, S.E. Chocron, E. Kim*, University of Maryland, College Park, *D.L. Kelly*, University of Maryland School of Medicine, *G.F. Payne, R. Ghodssi*, University of Maryland, College Park

We present a study of atomic layer-deposited TiN and electroplated Pt black (PtB) as candidate electrode materials to replace Au in a catechol-modified chitosan redox cycling system (Fig. 1) for the electrochemical detection of the antipsychotic clozapine (CLZ). In complex biological fluids like blood, interference from other electrochemically active species is a major challenge. The choice of electrode material is critical in addressing this challenge, as surface morphology and composition may produce a stronger and more reproducible CLZ signal, while shifting that signal away from potential interferents and improving the signal-to-noise ratio. Our electrochemical characterization results indicate that TiN is superior to Au as a sensor material, with a 2.6 times higher CLZ signal and a 3.2-fold lower variability.

Identifying electrode materials with high CLZ signal-to-noise ratio will greatly aid in translating our detection approach into a point-of-care monitoring system. Such a device will reduce the burden currently associated with CLZ due to safety and efficacy monitoring requirements [1], thereby improving the quality of life for people affected by schizophrenia. Our previous work [2] has relied on gold electrodes as a substrate for our catechol-modified chitosan films. These 5×5 mm² micro-fabricated planar gold electrodes serve as controls, which we further modified here with: TiN for its inert properties; and PtB for its high surface area and potential electrocatalytic activity (Fig. 2).

The fabricated electrodes were characterized using cyclic voltammetry. Bare Au yields an oxidative CLZ peak signal of 1.06 ± 0.20 μ A, compared to 5.20 ± 2.26 μ A when coated with chitosan-catechol (Fig. 3). TiN electrodes

produce a signal of 2.00 ± 0.26 μ A bare, and 13.7 ± 0.7 μ A when modified. The combination of higher signal and lower variability with the TiN is likely due to its inert chemical properties which also propagate more repeatable biomaterial modification. We observed a secondary peak with gold as well as bare TiN electrodes, likely due to interference related to chloride or oxygen. Modified TiN revealed only a single, CLZ-related peak. Results show that, as expected, signals from the bare PtB electrodes were 3370 times higher than from Au. However, they exhibited large variation between experiments, indicating the need for electroplating optimization. Testing the PtB electrodes with the chitosan-catechol film should increase both CLZ signal and resolution. Ongoing work is also focused on glassy carbon electrodes, which are expected to yield high repeatability by eliminating potential interfering oxygen signals in the redox cycling system.

9:00am **BI+AS+MN+NS-TuM4 Characterization of an Amperometric Glucose Sensor on a Flexible Polyimide Substrate for Continuous Glucose Monitoring and Insulin Delivery through Single Device**, *X. Du, J.R. Motley, A.K. Herman, Liney Arnadottir, G.S. Herman, X. Tan, J.F. Conley, Jr., Oregon State University, W.K. Ward, R.S. Cargill, J.R. Castle, P.G. Jacobs*, Pacific Diabetes Technologies

Type 1 diabetes affects over one million people and every year more than 30,000 children and adults are diagnosed with type 1 diabetes in the United States alone. Patients with type 1 diabetes cannot produce their own insulin and depend upon glucose sensors to monitor their blood glucose and adjust insulin levels either by injection or an insulin pump. The continuous monitoring of glucose blood levels and automatic insulin release by an artificial pancreas is a promising alternative to current treatment options, and can significantly improve the comfort and quality of life for the patient. Here we introduce a flexible catheter with an integrated glucose sensor capable of both continuously measuring glucose levels and deliver insulin through a single catheter. The amperometric glucose sensor includes multiple Pt indicating electrodes, Ag/AgCl reference electrode, electrohydrodynamic jet (e-jet) printed glucose oxidase enzyme layers, and permselective membrane for optimal glucose response from the interstitial tissue. The compact design is integrated on a flexible polyimide substrate and requires high durability for all the components due to the small radius of curvature of the catheter. The e-jet printing provides digital patterning flexibility and highly precise deposition of the enzyme layer, which allows improved uniformity and accuracy of the glucose sensor. Here we will discuss characterization and optimization of the indicating and reference electrodes using electrochemical methods, scanning electron microscopy, X-ray photoelectron spectroscopy (XPS), and time of flight secondary ion mass spectrometry. XPS was used to confirm full glucose oxidase coverage of the indicating electrode. Electrochemical testing indicates that e-jet printed glucose oxidase inks are still active towards glucose oxidation after printing and subsequent deposition of the permselective membrane. The operation and characterization of a fully functional glucose sensor integrated onto a catheter will also be discussed.

9:20am **BI+AS+MN+NS-TuM5 Chemically Modifying Graphene for Biosensing and Interfacing with Biology**, *Paul Sheehan*, Naval Research Laboratory, *S.C. Hernandez*, National Research Council, *N. Long*, Nova Research, *S.P. Mulvaney, J. Robinson*, Naval Research Laboratory, *R. Stine*, Nova Research, *C.R. Tamana, S.G. Walton*, Naval Research Laboratory

INVITED

Graphene has many properties that are highly suited for biological studies. For instance, its atomic thinness, high electrical conductivity, and simple production methods are ideal for biosensing. As another example, graphene can be attached to arbitrary substrates to lend them the chemical flexibility of carbon while adding only an ultrathin coating. For both biosensing and biofunctionalization, it is critical to produce high quality films that are precisely modified with the desired chemistry. For biosensing, the sensor must be functionalized for specific receptor-ligand recognition such as DNA-DNA or antibody-antigen binding. We will discuss our strategies for functionalization and the successful detection of specific DNA hybridization biologically-active field-effect transistors (BioFETs) based on chemically modified graphene. We will then discuss our use of graphene to interface biology with materials ranging from polymers to dielectrics to semiconductors. Graphene's incredible thinness enables its inclusion in more traditional sensing platforms as a non-intrusive functionalization layer, discreetly lending its chemical flexibility to other, more inert materials without otherwise impacting the sensing device.

11:00am **BI+AS+MN+NS-TuM10 Bioresorbable Sensors and Electronics**, *John Rogers*, University of Illinois at Urbana Champaign **INVITED**

A remarkable feature of the modern integrated circuit is its ability to operate in a stable fashion, with almost perfect reliability. Recently developed classes of electronic materials create an opportunity to engineer the opposite outcome, in the form of devices that dissolve completely in water, with harmless end products. The enabled applications range from 'green' consumer electronics to bio-resorbable medical implants – none of which would be possible with technologies that exist today. This talk summarizes recent work on this physically 'transient' type of electronics and sensors, from basic advances in materials chemistry, to fundamental studies of dissolution reactions, to engineering development of complete sets of device components, sensors and integrated systems.

11:40am **BI+AS+MN+NS-TuM12 Surface Chemistry Enhanced Microbial Bioelectrocatalysis**, *Kateryna Artyushkova, C. Santoro, S. Babanova, J. Cornejo, L. Ista, A. Schuler, P. Atanassov*, University of New Mexico

Bioelectrochemical oxidation carried out by bacteria attached on a solid electrode is capturing the attention of scientists all over the world. Different species of bacteria have been shown as electroactive and being able to oxidize organic compounds releasing electrons that can be transferred to a conductive solid support. If the oxidation reaction is coupled with the oxygen reduction reaction (ORR), the degradation of organics could lead to a production of useful electricity and water. Those related aspects are currently utilized in the development of alternative and cost effective bioelectrochemical systems (e.g. microbial fuel cell (MFC)) for simultaneous organics removal and electricity production. Understanding the bioelectrocatalytic nature of organics dissimilation by bacteria and the subsequent internal and external electron transfer is of a high importance for the further development of these systems and a key moment in their future application.

In this work, an artificial approach for enhanced microbial bioelectrocatalysis was explored along with study of the parameters promoting bacteria external electron transfer. This approach consisted of artificial modification of electrode surfaces having, as a result, different surface chemistries. Mixed bacterial culture development, biofilm growth and electrochemical performance have been studied. Smooth gold surfaces were modified with organic thiols to form self assembled monolayers (SAMs) with various functional groups (-CH₃, -OH, -N(CH₃)₃ and -COOH).

Power curves and single electrode polarization curves have been taken to evaluate the performance of the MFC as a whole and of the electrodes separately. XPS analysis of electrodes was used to study the effect of chemistry on the performance. Confocal and SEM microscopy was used to study the bacteria biomass and biofilm development was tracked over time.

Nanometer-scale Science and Technology

Room: 304 - Session NS+HI-TuM

Nanopatterning and Nanolithography

Moderator: Nancy Burnham, Worcester Polytechnic Institute, Leonidas Ocola, Argonne National Laboratory

8:00am **NS+HI-TuM1 Nanoetching and Characterization Towards sub-5 nm Patterning**, *Deirdre Olynick, D. Staaks, D. Tierno, S. Dallarto, S. Sassolini, B. Muddiman, Z. Lui, G. Calafiore*, Lawrence Berkeley National Laboratory, *X. Gu, T.P. Russell*, University of Massachusetts, Amherst, *M. Kocsis*, Inpria Corporation **INVITED**

Plasma etching is the ubiquitous method for high-resolution pattern transfer in semiconductor and related technologies. As lithographic techniques advance towards 5 nm half-pitch for applications in storage media, nanoelectronics, and plasmonic based devices, plasma etching processes must follow suit. This brings enormous and arguably insurmountable challenges using typical plasma hardware. For instance, very high etching selectivity must be achieved to accommodate mask heights (~1-2 times the feature size) which must shrink to mitigate pattern collapse in the lithographic and etching steps. In addition, line edge roughness at down to sub 1 nm levels must be achieved. To meet these enormous challenges we are investigating etching processes with temperatures down to -140 °C. Low temperature etching was first introduced by Tachi.¹ Lower etching temperatures can bring benefits such as higher selectivity processes, larger process windows, and reduced plasma damage which will be important for achieving sub-5 nm features.

We will discuss nanoscale cryogenic etching work in silicon, chromium, and silicon dioxide. With careful micron and deep nanoscale etching we

show that cryogenic temperature etching of silicon, previously studied in great detail at the micron scale,^{2,3} can provide extreme selectivity and anisotropy at the nanoscale even with soft masks derived from block copolymer lithography. Selectivity is enhanced while maintaining pattern verticality because resist etch rates decrease as temperature is lowered. Changing to a chromium hardmask increases selectivity towards deeper sub-10 nm features at 20:1 aspect ratios. Studies of chromium etching show a temperature dependent etch rate that can be used to enhance profile control and limit mask undercut, necessary when nanometer controlled is required. Finally, we will discuss investigations into reduced temperature silicon dioxide etching for applications in patterned media and vertical NAND.

References:

1. S. Tachi, K. Tsujimoto and S. Okudaira, *Appl. Phys. Lett.* (8), 616-618 (1988).
2. X. Mellhaoui, R. Dussart, T. Tillocher, P. Lefauchaux, P. Ranson, M. Boufnichel and L. J. Overzet, *J. Appl. Phys.* (10), 104901-104910 (2005).
3. J. Pereira, L. E. Pichon, R. Dussart, C. Cardinaud, C. Y. Dulaud, E. H. Oubensaid, P. Lefauchaux, M. Boufnichel and P. Ranson, *Appl. Phys. Lett.*, 071501-071501-071503 (2009).

Acknowledgements: This work was supported in part by the U.S. Department of Energy, Office of Basic Energy Sciences, under contract DE-FG02-96ER45612 (X. D. and T. R.) DE-AC02—05CH11231 (D.O. and S.C.). Z. Liu was supported by Oxford Instruments Plasma Science Division.

8:40am **NS+HI-TuM3 Cut Patterning Challenges for the 14nm-Node and Beyond**, *Ryan Jung, J.R. Sporre, F.L. Lie, S. Kanakasabapathy, S. Sieg, IBM Albany Nanotech Center, A. Ranjan, S. Voronin, A. Raley, V. Rastogi, A. Ko, TEL Technology Center, America, LLC, D. Lee, Samsung Electronics*

In order to satisfy certain device architecture, fabrication of certain levels such as channel and gate is typically done by first forming line and space arrays, followed by removing or cutting some lines or parts of lines to form the final pattern. For instance, the method of Sidewall Image Transfer (SIT) patterning generates pairs of lines that are structurally connected at the line ends. Accordingly, the line/space patterning must be supplemented with a companion cut mask pattern to remove these undesired features. The cut mask, in addition to removing undesired features, also facilitates orthogonal line end control and dense array tip-to-tip control, such as in memory device, that cannot be achieved solely from lithography side using mask optical proximity control (OPC) and negative tone developed resist. With channel and gate pitch being scaled down to below 80nm, the ability to precisely place the cut mask edge and to control the line end taper angle has a direct impact on defectivity and yield. The ability to control the critical dimension of the cut opening has a direct impact on the tip-to-tip CD and device density. This paper evaluates the advantages, technical challenges, and extendibility of various cut schemes for 14nm node and beyond, focusing on line edge profile and tip-to-tip control. This work was performed by the Research and Development Alliance Teams at various IBM Research and Development Facilities

9:00am **NS+HI-TuM4 Nanopore Memristors: Sub-10nm Devices Built on Membranes Milled with a Helium Ion Microscope**, *Douglas Ohlberg, J.P. Strachan, W. Thompson, Z.Y. Li, R.S. Williams*, Hewlett Packard

A novel platform has been developed to fabricate and study the performance of memristive devices smaller than 10 nm. The platform consists of free-standing silicon nitride membranes into which holes or pores with diameters ranging in size from 7nm – 50 nm have been milled with a helium ion microscope. In addition to serving as a substrate, the membrane also acts as an interlayer dielectric, and devices are fabricated by sequential deposition of materials above and below the membrane to fill the nanopore. Since deposition of the layers does not require intervening exposures to resists, developer solutions, or plasma cleans, all interfaces are clean and free of contaminants that would otherwise degrade device operation. This approach enables the compositional engineering of ideal device stacks at the nanometer scale decoupled from the problems often introduced by conventional lithographies. Working memristors are demonstrated that have been successfully fabricated around nanopores with diameters as small as 7nm. In addition, we demonstrate, how the sidewall profiles of the nanopores can be engineered in a variety of shapes from conical to hour glass by the deposition, prior to helium ion milling, of materials on the membrane that influence the scattering dynamics of the ions during milling.

9:20am **NS+HI-TuM5 Characterization of Cluster-Based High-Resolution Inorganic Resists**, *Rose Ruther, R.P. Oleksak, R. Frederick, B.T. Flynn, G.S. Herman*, Oregon State University

Both near- and long-term challenges for nanomanufacturing require significant advances in lithography to obtain sub-ten nanometer half-pitch. One approach to meet these challenges is through inorganic resists based on clusters and nanoparticles. Inorganic resists are of considerable interest due to the potential for both high resolution and low line width roughness (LWR), but generally suffer from low sensitivity. Recently, incorporation of radiation sensitive ligands into inorganic resists has enabled significantly improved sensitivity. For example, we have demonstrated the use of H_2O_2 as a radiation sensitive ligand for resists based on inorganic nano-clusters with the general formula, $\text{Hf}(\text{OH})_{4-2x-2y}(\text{O}_2)_x(\text{SO}_4)_y \cdot q\text{H}_2\text{O}$ (HafSOx). By including H_2O_2 the HafSOx has significantly improved sensitivity to extreme UV photons and electrons, while still displaying high-resolution and low LWR.

In this presentation we characterize key steps in the lithographic process to gain insight into the nanodimensional patterning of HafSOx. Dynamic light scattering (DLS) and transmission electron microscopy (TEM) confirm the presence of nanoscale particles in the precursor solutions. TEM is further used to characterize cross-sections of spin-coated HafSOx films before and after pattern exposure and development. Combined with energy dispersive X-ray spectroscopy (EDS) this allows for *in situ* investigations of the dynamic nature of both structural and compositional properties with electron exposure pertinent to the patterning process. In particular, oxygen species are found to be very mobile during TEM analysis and migrate to the Si interface with an associated densification of the HafSOx film. Cross-sectional TEM of patterned lines down to approximately 10 nm half-pitch provides unique information on pattern profiles and reveals the presence of inter-line residual material consisting of discrete structures consistent with solution species. Both temperature programmed desorption (TPD) and electron stimulated desorption (ESD) are used to characterize the key desorption species that occur during thermal and radiative processes during patterning. ESD indicates that the peroxy species have radiation sensitivity, where the primary desorption products are O_2 and H_2O . We find that the time evolution of the O_2 and H_2O desorption yields indicate much faster kinetics for O_2 desorption, suggesting that the formation of the insoluble oxide network is driven initially by desorption of peroxide groups as opposed to thermal dehydration. These data provide insight into the radiation-induced changes responsible for the contrast mechanism of this system.

9:40am **NS+HI-TuM6 Development Characteristics of PMMA in Alternative Alcohol:Water Mixtures**, *Leonidas Ocola*, Argonne National Laboratory

In the past decade there has been a shift from toxic solvents used in lithography processing towards more environmentally safer chemicals. The most widely used resist in electron beam lithography is polymethylmethacrylate (PMMA). The standard developer is a solution mixture of isopropanol (IPA) and methyl isobutyl ketone (MIBK) in a ratio of 3:1. The Globally Harmonized System (GHS) Classification for MIBK includes the following entries: Flammable liquids (category 2), Acute toxicity, Oral (Category 5) and Inhalation (Category 4). The most popular environmentally friendly alternative is an IPA and water (H_2O) solution in a ratio of 7:3. Excellent results have been published using this developer. The mechanism of why this solution works, given the fact that pure IPA and pure H_2O do not develop exposed PMMA is not well understood. Furthermore, the IPA GHS Classification the following entry: Specific target organ toxicity - single exposure (Category 3), central nervous system. Our research is focusing on shedding light onto what would be the interaction of water with similar alcohols, such as methanol and ethanol, and environmentally safer alternatives to IPA. This turns out to be Ethanol. The only Ethanol GHS Classification entry is: Flammable liquids (Category 2). We find that ethanol water mixtures exhibit excellent contrast, sensitivity, and resolution, and should be considered as one of the most environmentally safe viable developer solution for PMMA. We will present results pertaining on our best lithography results using Ethanol:water solutions, and a possible explanation on the role of the water:alcohol interaction with the exposed PMMA resist. We do not believe it is just an issue of cosolvency but more of a localized molecular interaction. The goal of better understanding of this interaction is to help find safer developers for other resists that rely on solvent based development.

This work was supported by the Department of Energy under Contract No. DE-AC02-06CH11357. Use of the Center for Nanoscale Materials was supported by the U. S. Department of Energy, Office of Basic Energy Sciences, under Contract No. DE-AC02-06CH11357.

11:00am **NS+HI-TuM10 Room Temperature Electron Beam Assisted Oxygen Purification of Electron Beam Induced Pt Deposits: Towards Pure and High-Fidelity Nanostructures**, *Brett Lewis, M.G. Stanford*, University of Tennessee, *H. Plank*, Graz University of Technology, Austria, *J.H. Noh*, University of Tennessee, *J. Fowlkes*, Oak Ridge National Laboratory, *P.D. Rack*, University of Tennessee

Electron Beam Induced Deposition (EBID) is a direct write mode capable of fabricating highly precise nanoscale structures by employing a scanning electron beam to disassociate adsorbed precursor molecules which subsequently condense on a substrate. The major drawback of the EBID process is that high purity metallic deposition is rarely achieved due to residual impurities attributed to the inadequate disassociation of the precursor molecule remaining in the final structure. Thus, purification strategies for nanoscale EBID deposits has been a critically important research area as EBID is poised to impact many nanoscale science and technology applications. To this end, our recent work has been focused on the post-deposition purification of EBID structures. We demonstrate a room temperature purification method in which platinum-carbon nanostructures deposited from MeCpPtIVMe_3 are purified by the presence of oxygen gas during a post-electron exposure treatment. Deposit thickness, oxygen pressure and oxygen temperature studies suggest that the dominant mechanism is the electron stimulated reaction of oxygen molecules adsorbed at the defective deposit surface. In this presentation we will overview the electron-stimulated reaction regimes as a function of oxygen partial pressure and temperature, and electron beam current and energy. We will overview electron stimulated reaction and adsorption/diffusive transport models to demonstrate that, for our experimental regime, we believe the rate-limiting mechanism is oxygen adsorption/transport. In addition to purification, the post-deposition electron stimulated oxygen purification process enhances the resolution of the EBID process due to the carbon removal of the as-deposited materials. Notably, pure platinum deposits with low resistivity and retain the original deposit fidelity were accomplished at room temperature.

11:20am **NS+HI-TuM11 Prospects for Nanofabrication using the Combination of STM-based Depassivation Lithography, Selective ALD, and Material Etch Processes**, *Joshua Ballard*, Zyvex Labs, *S. Anz, S. Sando*, Systine, Inc., *M. Bischof*, University of North Texas, *D. Dick*, University of Texas at Dallas, *J. Fu*, National Institute of Standards and Technology (NIST), *D. Jaeger*, University of North Texas, *R. Longo*, University of Texas at Dallas, *J. Owen*, *E. Fuchs*, Zyvex Labs, *S. McDonnell*, University of Texas at Dallas, *R. Reidy*, University of North Texas, *Y.J. Chabal*, *R.M. Wallace*, University of Texas at Dallas, *J. Randall*, Zyvex Labs, *A. Cherala*, *S. Singhal*, *S. Sreenivasan*, University of Texas at Austin

Attaining the capability to produce top-down designed nanostructures at sizes and precisions at the nanometer and atomic scales will enable new classes of research into material and device behavior. First demonstrated in the mid-1990s, Scanning Tunneling Microscopy (STM) based hydrogen depassivation lithography has been shown to allow selective functionalization of surfaces with many types of molecules and materials with near absolute precision. Recently, selective Atomic Layer Deposition (ALD) of titania has also been demonstrated on such a functionalized surface, with the deposited material behaving as an etch mask in 3-D nanostructure formation. This results in a process that combines the high precision of STM with standard processing techniques to produce 3-D structures.

Already, 3-D structures with arbitrary shapes with full-pitches down to 13 nm have been fabricated using this process. This work will describe this process as well as provide an overview of the problems that need to be addressed to further reduce the minimum feature size and improve precision. Given the current and near term limitations of the process, classes of devices that have been and are possible to be fabricated will be described, including designed quantum dots, photonic structures, and NEMS apparatuses. Finally, pathways for scalability will be discussed.

Nanostructured Thin Films and Coatings

Moderator: Robert Franz, Montanuniversität Leoben,
Andrey Voevodin, Air Force Research Laboratory

8:00am **SE+NS+TR-TuM1 Electrostatic Coating with Ligandless Copper Nanoparticles, Lance Hubbard, A.J. Muscat, University of Arizona**

Physical vapor deposition is currently used to deposit copper seed layers in through Si vias, but this approach is already close to its limit and may not be an option for future scaling of high performance integrated circuits. An alternative is electroless deposition (ELD) since it produces conformal, selective coatings at low temperature. ELD occurs by chemical reduction of metal ions without an externally applied potential. In the conventional approach, a metal catalyst such as Pt, Pd, or Ni is used that can be both expensive and increase the resistance of interconnect lines. Previous work was done in an aqueous phase using a complexing agent or polymer to protect the particles. Good film continuity was demonstrated, but the sheet resistance was low.^{1,2} In this study, we report on a nonaqueous ELD process that uses a charge compensator, but not a ligand or complexing agent. The weak electrostatic attachment of the charge compensator to the ions and particles in solution and the high pH conditions improve the driving force for metal deposition. Si(100) coupons were hydroxylated using sulfuric acid-hydrogen peroxide mixture. The surface was terminated with an amine adhesion layer by immersion in a 4 mM solution of either (3-aminopropyl)-trimethoxysilane (APTMS) or (3-mercaptopropyl)-trimethoxysilane (MPTMS) in methanol followed by a 150°C anneal. Metal films were deposited by suspending samples in a bath made by dissolving Cu(II) chloride in ethylene glycol, which also served as the reducing agent, and adding 1-butyl-3-methylimidazolium tetrafluoroborate as a charge compensator. The surface plasmon resonance (SPR) peak of the Cu nanoparticles in the bath and film was at 585 nm. Light scattering measurements and transmission electron microscopy (TEM) images yielded a size distribution of 3.1±1.6 nm. The complex consisting of the Cu particle core and ion shell is attracted to the positively charged amine groups at high pH, and a thin metal film is deposited that is both continuous and cohesive. Annealing the coupons at 200°C in nitrogen promoted the formation of an electrically conductive film. Electron microscopy images of the coated substrates show a 20-50 nm thick film of 3 nm dia. particles; spectroscopic ellipsometry shows both bulk and nanophase properties. Four-point probe measurements of the films yielded electrical conductivities in the range 10⁵-10⁶ S/m (bulk Cu conductivity 4-6x10⁷ S/m).

References

- 1) Armini and Caro, J. Electrochem. Soc. 2010, 157(1), D74-D80, doi: 10.1149/1.3258026.
- 2) Inoue et al. J. Electrochem. Soc. 2012, 159(7), D437-D441, doi: 10.1149/2.070207jes.

8:20am **SE+NS+TR-TuM2 Electrically Stable Pt-ZrB₂ Nanocomposite Thin Films for High Temperature Applications, Julia Sell, D.M. Stewart, G.P. Bernhardt, D.J. Frankel, R.J. Lad, University of Maine**

Considerable cost savings could be achieved by incorporating high temperature sensors into high temperature machinery to optimize processes and monitor materials degradation. However, in order to achieve reliable sensor operation, the thin film electrodes, sensing elements, and packaging materials must remain stable over long times at high temperature. Metallic thin films, such as Pt, agglomerate and lose conductive pathways quickly when exposed to temperatures exceeding 700°C. In this work, we show that Pt-ZrB₂ nanocomposite films retain a continuous morphology and remain electrically conductive up to at least 1100°C in air. Nanolaminate Pt-ZrB₂ films comprised of ten alternating layers of Pt and ZrB₂ were deposited to a total thickness of 200nm at ambient temperature onto sapphire substrates using e-beam evaporation. Annealing the nanolaminate films above 800°C in air causes intermixing, resulting in a nanocomposite Pt-ZrB₂ film architecture. Film electrical conductivities were measured using a 4-point probe as a function of time and temperature in air up to 1200°C. These results show that Pt-ZrB₂ nanocomposite films have conductivities in the 10⁶-10⁷ S/m range and remain stable above 1000°C, but that the overall conductivity and stability depends on the Pt-ZrB₂ layer thickness ratio. Analysis via x-ray photoelectron spectroscopy and x-ray diffraction indicates that both monoclinic and tetragonal ZrO₂ nanocrystallites are formed in the films during the annealing treatment, and they serve to hinder agglomeration of the Pt phase. Scanning electron microscopy shows highly conductive Pt-rich pathways in the films that coexist with the ZrO₂ phase. Some films were coated with an amorphous Al₂O₃ protective capping layer

using atomic layer deposition (ALD), and this capping layer helped to limit oxygen diffusion into the films, thereby increasing the long term stability of film conductivity.

8:40am **SE+NS+TR-TuM3 A Novel Reactive Plasma-Assisted Coating Technique (RePAC) for Thin BN/Crystalline-Si Structures and their Mechanical and Electrical Properties, Koji Eriguchi, Kyoto University, Japan, M. Noma, SHINKO SEIKI CO., LTD., Japan, S. Hasegawa, Osaka University, Japan, M. Yamashita, Hyogo Prefectural Institute of Tech., Japan, K. Ono, Kyoto University, Japan**

Cubic boron nitride (c-BN) has attracted much attention as a hard coating film on cutting tools, owing to its high oxidation resistance and hardness—the second hardest material to diamond. Although various methods of forming c-BN films on various substrates have been proposed, the interface between c-BN and the substrate material was unstable against delamination and oxidation [1] after long-time machining and air exposure. In this study, we propose a novel reactive plasma-assisted coating technique (RePAC) for forming sub-μm-thick BN film directly on crystalline Si substrates, where magnetically-confined high-density Ar/N₂ plasma was generated with a stable anodic current to promote the reaction between N radicals and B atoms evaporated onto a Si substrate placed on a sample stage [2]. Controlling substrate bias voltage V_{sub} in the RePAC, we fabricated various thin-BN/Si structures and identified a correlation among the properties such as mechanical hardness, friction coefficient, leakage current, and dielectric constants. TEM analyses revealed that nano-structures of the BN films were varied from bulk amorphous (a)-BN, layered hexagonal (h)-BN, to c-BN phase in turbostratic (t)-BN domain, in accordance with V_{sub} ($|V_{\text{sub}}|=10-120$ V). We speculate that bombardment of incident ions (Ar⁺ and/or N₂⁺) plays a key role in forming these characteristic features, in addition to stoichiometric N and B contents. Moreover, we clarified the high hardness (> 4000HK, by the Knoop indenter) and the dielectric constant higher than previously-reported values (10–20, by the electrical capacitance measurement) for the present thin c-BN/Si structure with anti-delamination feature after long-time air exposure. The obtained results suggest that the present BN film formed by the RePAC has wide applications not only as a hard coating film but also as a high dielectric-constant layer in electronic devices.

- [1] For example, P. B. Mirkarimi *et al.*, Mater. Sci. Engin., **R21**, 47 (1997).
- [2] M. Noma *et al.*, Jpn. J. Appl. Phys. **53**, 03DB02 (2014).

9:20am **SE+NS+TR-TuM5 Multifunctional Protective Coatings for Aerospace Applications, Etienne Bousser, L. Martinu, J. Klemberg-Sapieha, Ecole Polytechnique de Montreal, Canada** **INVITED**

Ever increasing technical, economic and environmental requirements give rise to situations where modern equipment and components are often pushed beyond the limits of their design capabilities. This frequently leads to tribological deficiencies, such as lubrication breakdown, excessive wear and tribo-corrosion, resulting in increased operational costs, decreased efficiency and premature failure. Therefore, appropriate material's selection for a given application must be guided by an accurate understanding of the intervening tribological processes while ensuring the maintained functionality of the surface for optimal application performance.

Solid Particle Erosion (SPE) occurs in situations where hard particles, present in the environment, are entrained in a fluid stream, and impact component surfaces such as in aircraft engines. It is well known that ductile materials erode predominantly by plastic cutting or ploughing of the surface, while brittle materials do so by dissipating the particle kinetic energy through crack nucleation and propagation. In the first part of this presentation, we examine the mechanisms by which surfaces dissipate the kinetic energy of impacting particles, and discuss the erosive response of hard protective coating systems. We investigate the means by which surface engineering can enhance erosion resistance, and correlate surface mechanical properties to the erosion behaviour. In addition, we will show that the architectural design of advanced coating systems is also well supported by finite element modelling of single particle impacts of the coated surfaces.

The second part of the talk will focus on the reparability of advanced coating systems. Indeed, because of the high fabrication costs of engine components, it is desirable to develop an effective and efficient industrially-viable technique to remove defective coatings with the aim of recycling the costly engine components. In particular, we will present our recent studies on the removal of TiN-based erosion resistant coatings using a non-line-of-sight reactive ion etching technique and a complementary laser ablation process.

11:00am **SE+NS+TR-TuM10 Hard Coatings with Designed Thermal Conductivity**, *P.H.M. Boettger*, Empa, ETH Zurich, Switzerland, *V. Shklover*, ETH Zurich, Switzerland, *M. Sobiech*, Oerlikon Balzers Coating AG, Liechtenstein, *Joerg Patscheider*, Empa, Switzerland

Hardness, thermal stability and oxidation resistance are often the main properties to optimize for most tool coatings developments for industrial applications. The thermal conductivity, however, has been regarded to a much lesser extent as property to improve tool life. So far, only little attention has been given to this fact and the explicit role of thermal conductivity in machining Ti and Ni-based alloys. These materials typically have low thermal conductivity, as well as modern tool coatings such as CrAlN and TiAlSiN. This unfavorable combination may lead to the formation of thermal hot spots during machining, which adds to the premature degradation of such coatings. For these reasons the thermal conductivity is an important process parameter.

This talk will discuss the relations between hardness, coatings architecture and thermal conductivity and how advanced coatings can be tuned to achieve significant anisotropy of the thermal conductivity. In arc-evaporated $\text{TiO}_x\text{N}_{1-x}$ and $\text{CrO}_x\text{N}_{1-x}$ thermal conductivity can be adjusted in a wide range between 2 and 35 W/m·K, while keeping hardness and oxidation resistance intact. The data for single phase oxynitrides as well as of multilayered coatings agree well with a newly developed model based on constant phonon scattering cross section of the introduced oxygen. It will be shown how temperature-mitigating multilayer coatings can be prepared using these materials by introducing highly anisotropic thermal conductivity.

11:20am **SE+NS+TR-TuM11 Microstructure and Hardness Gradients in Sputtered CrN Films**, *A. Riedl*, Materials Center Leoben, Austria, *R. Daniel*, Montanuniversität Leoben, Austria, *T. Schoeberl*, *M. Stefanelli*, Austrian Academy of Sciences, *B. Sartory*, Materials Center Leoben, Austria, *J. Keckes*, *Christian Mitterer*, Montanuniversität Leoben, Austria

Hardness and elastic modulus of a sputtered nanocrystalline CrN thin film, grown under varying ion bombardment conditions, were studied by nanoindentation using a depth-profiling technique and related to cross-sectional X-ray nanodiffraction data on the local microstructure. Changes in texture are shown to have almost no effect on the elastic modulus due to the isotropic response of the polycrystals. However, the locally varying growth conditions, which affect crystal size and number, determine the hardness values across the film thickness. Regions with highly distorted small crystals result in higher hardness in comparison to those with well-developed coarsened grains. This work confirms the notion of the existence of growth-related hardness gradients in single-phase nanocrystalline thin films.

11:40am **SE+NS+TR-TuM12 Development of Low Friction Nanocomposite Coatings for Diesel Engine Piston Rings**, *Jianliang Lin*, *R. Wei*, *K. Coulter*, *C. Bitsis*, *P.M. Lee*, Southwest Research Institute

Hard and thick (15-20 μm) TiSiCN nanocomposite coatings have been developed to improve the wear resistance and reduce the overall average friction for diesel engine piston rings. The coatings were deposited by sputtering Ti metal targets in a reactive atmosphere using a plasma enhanced magnetron sputtering (PEMS) process. The reactive mixture contains argon, nitrogen, acetylene gases, and hexamethyldisilazane vapor which were introduced into the chamber using a liquid evaporation/delivery system. The substrates were AISI 304 stainless steel coupons and piston rings. The TiSiCN coatings with different elemental compositions and microstructures were prepared by varying the hexamethyldisilazane and acetylene gas/vapor concentrations and the target power. The microstructure of the coatings was characterized using scanning electron microscopy, energy dispersive spectroscopy, and X-ray diffraction. The adhesion strength and mechanical and tribological properties of the coatings were measured using HRC tests, nanoindentation and ball-on-disk wear tests. By optimizing the composition and microstructure of the coatings, thick TiSiCN nanocomposite coatings with excellent adhesion and a dry sliding friction less than 0.2 have been obtained. The optimized coating systems were applied on the piston rings, which were evaluated on a Plint TE77 reciprocating bench rig and in the real diesel engine test. The principle for the increased wear resistance and the potential applications will be discussed in the paper.

Tuesday Afternoon, November 11, 2014

2D Materials Focus Topic

Room: 310 - Session 2D+AS+HI+MC+NS+PS+SP+SS-TuA

2D Materials Characterization including Microscopy and Spectroscopy

Moderator: Manish Chhowalla, Rutgers University

2:20pm **2D+AS+HI+MC+NS+PS+SP+SS-TuA1 Layer-Dependent Electronic and Physical Structure of 2D van der Waals Crystals, Richard Osgood, Columbia University** **INVITED**

Because of their weak Van der Waals interlayer bonding transition-metal dichalcogenide (TMDC) semiconductors can be fabricated into atomically thin two-dimensional (2D) crystals with substantial ~ 1-2 eV bandgaps. As one example, monolayer MoS₂ consists of a single layer of Mo atoms sandwiched between two layers of S atoms in a trigonal prismatic structure. The TMDC 2D system has attracted great interest because of its distinctive electronic and optical properties, such as (i) a transition from indirect-to-direct band gap in going from the multilayer to monolayer crystal due to a missing interlayer interaction in monolayer form and (ii) strong spin-orbit-coupling-induced split valence bands, i.e. 100's of meV, due to broken inversion symmetry, which makes TMDCs interesting for spin-physics physics and devices. Both properties have been predicted with density functional theory (DFT) calculations and indirectly demonstrated using photoluminescence and Raman spectroscopy.

Recently we have made a series of direct observations of the thickness-dependent electronic-band and crystal structure of TMDCs of both exfoliated and CVD grown sample. Because of the relatively modest sample sizes we have used micrometer-scale, angle-resolved photo-emission spectroscopy (micro-ARPES) of both the exfoliated and chemical-vapor-deposition-grown crystals; these measurements provide direct evidence for the shifting of the valence band maximum from gamma bar (Brillouin zone center) to kappa bar (Brillouin zone corner), as the sample thickness decreases from bulk to monolayer. Our initial results were with MoS₂ and are described in a preliminary way in Refs 1 and 2. Our TMDC experimental results are compared with rigorous DFT calculations of both the bands and the UV transitions matrix elements. The results show an evolution in band structure, which is consistent with an indirect-to-direct bandgap transition in going from few-layer to monolayer TMDC and can be attributed to changes in quantum confinement as the number of layer decreases. Our microARPES and, subsequently, higher resolution nanospectroscopy data provide clear measurements of the hole effective mass, the strain present in the monolayer crystal films, and the valence-band spin-orbit splitting. Our results explain the low hole mobility of monolayer MoS₂ compared to thicker MoS₂ and show clearly the strong orbit split energies. Our results, using nanoLEED and LEEM also provide insight into the structure and defects in monolayer films. Experiments using K-doping of single-crystal samples and resulting level shifts are also described.

1. W. Jin, P.-C. Yeh, N. Zaki, D. Zhang, J. T. Sadowski, A. Al-Mahboob, A. M. van der Zande, D. J. A. Chenet, J. I. Dadap, I. P. Herman, P. Sutter, J. Hone, R. M. Osgood, Jr., "Direct Measurement of the Thickness-Dependent Electronic Band Structure of MoS₂ Using Angle-Resolved Photoemission Spectroscopy." *Phys. Rev. Lett.* **111**, 106801 (2013)

2. Po-Chun Yeh, Wencan Jin, Nader Zaki, Datong Zhang, Jerzy T. Sadowski, Abdullah Al-Mahboob, Arend M. van der Zande, Daniel A. Chenet, Jerry I. Dadap, Irving P. Herman, Peter Sutter, James Hone, and Richard M. Osgood, Jr., "Probing substrate-dependent long-range surface structure of single-layer and multilayer MoS₂ by low-energy electron microscopy and microprobe diffraction," *Phys. Rev. B* **89**, 155408 (2014)

3:00pm **2D+AS+HI+MC+NS+PS+SP+SS-TuA3 X-ray Photoemission and Electron Energy Loss Spectroscopy Investigation of the Band Gap and Band Alignment for h-BN and MoS₂ Materials and Interfaces, Benjamin French, J. Brockman, M. French, M. Kuhn, J.D. Bielefeld, S.W. King, Intel Corporation, E. Bersker, G. Bersuker, SEMATECH, J. DiStefano, Y.C. Lin, J.A. Robinson, Penn State University**

Hexagonal boron nitride (h-BN) and molybdenum disulfide (MoS₂) are two dimensional (2D) materials of significant interest for future nano-electronic devices. Due to a wide band gap (~ 6 eV), close lattice matching (< 2%) and atomic planarity, hexagonal boron nitride (h-BN) is of primary interest as a potential substrate and gate dielectric in graphene channel transistor devices. In contrast, MoS₂ is a 2D semiconducting material with a band gap of ~ 1.8 eV that is attractive as a possible complement or alternative to

graphene for nano-electronic devices requiring a large band gap. A key property for the success of both h-BN and MoS₂ in such devices is the interfacial band alignment with graphene, the gate contact metallization and the surrounding insulating dielectric materials. In this regard, we have utilized x-ray photoelectron spectroscopy (XPS) to determine the Schottky barrier and valence band offsets present at the interfaces between plasma enhanced chemically vapor deposited amorphous h-BN:H and chemically vapor deposited MoS₂. In combination, we have utilized reflection electron energy loss spectroscopy (REELS) to investigate the band gap of both h-BN and MoS₂ materials to deduce the conduction band alignment. We show that in many instances the valence and conduction band offsets are significant and favorable for MoS₂/h-BN transistor devices.

3:20pm **2D+AS+HI+MC+NS+PS+SP+SS-TuA4 STM/STS Characterization of MoS₂ Monolayers and Nanostructures, A. Mills, C. Chen, Virginia Tech, Y. Yu, L. Cao, North Carolina State University, Chenggang Tao, Virginia Tech**

Atomically thin molybdenum disulfide (MoS₂) and nanostructures have been the subject of intense research efforts for their fascinating properties and potential applications in future electronic and optical devices. Especially, monolayer MoS₂, an atomically thin semiconductor with a direct band gap, as opposed to an indirect band gap in bulk MoS₂, has been demonstrated as field effect transistors, optoelectronic devices and chemical sensors. In our experimental study, Monolayer MoS₂ and MoS₂ triangular nanostructures are synthesized through a self-limiting chemical vapor deposition (CVD) approach. The precursor materials, MoCl₅ and sulfur, react at high temperatures to produce MoS₂ species and subsequently precipitate onto substrates to yield MoS₂ films and triangular nanostructures. Using scanning tunneling microscopy (STM), we have investigated the structural and electronic properties of monolayer MoS₂ grown on glassy carbon and triangular MoS₂ nanostructures on highly ordered pyrolytic graphite (HOPG). We will also discuss our scanning tunneling spectroscopy (STS) measurements on these structures.

4:40pm **2D+AS+HI+MC+NS+PS+SP+SS-TuA8 Surface Characterization of Metal Oxide Layers Grown on CVD Graphene and Spin Precession Measurements, Akitomo Matsubayashi, University at Albany-SUNY, W. Nolting, University of Albany-SUNY, D. Sinha, University at Albany-SUNY, A. Jayanthinarasimham, J.U. Lee, University of Albany-SUNY, V.P. LaBella, University at Albany-SUNY**

Ultra thin metal oxide films grown on graphene can be utilized as dielectric barriers between metals and graphene to help isolate a metal contact from the graphene channel for device applications. This is particularly important for graphene based spintronic devices as tunnel barriers between the ferromagnetic metal as a spin injector and graphene have been known to increase the spin relaxation time measured utilizing non-local detection technique of spin precession by avoiding the conductivity mismatch problem. However, simply depositing metal oxide layers such as aluminum oxide on graphene results in non-uniform film lowering the quality of the interface barrier. We will present a systematic study of aluminum oxide layers grown on CVD graphene under ultra-high vacuum conditions with and without titanium seed layers. The aluminum oxide layers with the 0.2 nm titanium seed layers showed reduced surface roughness. The chemical and structural composition determined by XPS will be also presented that shows full oxidation of the aluminum and partial oxidation of the titanium. The I-V characteristic study performed to electrically evaluate the metal oxide and the preliminary results of non-local spin precession measurements will be also addressed.

5:00pm **2D+AS+HI+MC+NS+PS+SP+SS-TuA9 Morphology of CVD-grown Hexagonal Boron Nitride on Cu Foils, Karthik Sridhara, W.G. Cullen, University of Maryland, College Park, J.K. Hite, Naval Research Laboratory, M.S. Fuhrer, Monash University, Australia, D.K. Gaskill, B.N. Feigelson, Naval Research Laboratory**

Hexagonal boron nitride (h-BN) has grown into prominence as a dielectric for graphene heterostructures. h-BN and graphene have been grown using chemical vapor deposition on various transition metal substrates. Compared to graphene, the morphology of CVD-grown h-BN on Cu has not been as widely studied. Here, we present a systematic study of the morphology of hexagonal boron nitride (h-BN) grown on polycrystalline Cu foils by chemical vapor deposition. The growth of h-BN is performed at ~1000°C in atmospheric pressure CVD using Ammonia Borane (H₃NBH₃) as the precursor. The copper foils, used as catalytic substrates, are thermally annealed at ~1030°C for >5 hours prior to growth and cooled slowly following growth termination. We utilized Ultra-high vacuum Scanning Tunneling Microscopy (STM), ambient AFM and SEM to assess the morphology of the CVD grown h-BN films. Highly symmetric single

crystallites of h-BN are observed for sub-monolayer growth, in agreement with recent reports. We consistently observe a corrugated topographic structure within the h-BN crystallites which is distinctly different from the surrounding copper surface, and this is consistently seen in STM, AFM, and high-resolution SEM. Our aim is to understand the nature of this difference and whether it might be due to effects of differential thermal contraction between h-BN and copper. However, complications arise due to possible changes in the copper substrate topography post-growth due to surface oxidation of the copper. Preliminary results with lateral force microscopy (LFM, frictional mode) show that these corrugations are unidirectional in a single Cu grain irrespective of the orientation of the h-BN crystal and generate frictional forces 200% greater than on the surrounding copper surface, reminiscent of earlier reports of unique frictional behavior in atomically-thin membranes [1]. STM and AFM are also used to study the twin crystal boundaries of h-BN. Preliminary STM observations indicate that merging h-BN crystals consistently have a gap of about 5 nm between them. The results of this study are independent of small variations of growth conditions.

References:

[1] C. Lee, Q. Li, W. Kalb, X.-Z. Liu, H. Berger, R. Carpick, and J. Hone, "Frictional characteristics of atomically thin sheets," *Science* (New York, N.Y.), vol. 328, no. 5974, pp. 76–80, 01-Apr-2010.

5:20pm **2D+AS+HI+MC+NS+PS+SP+SS-TuA10** **Influence of Chemisorbed Oxygen on the Growth of Graphene on Cu(100) and Cu(111) by Chemical Vapor Deposition**, *EngWen Ong*, University at Albany-SUNY, *Z.R. Robinson*, U.S. Naval Research Laboratory, *T.R. Mowll*, *P. Tyagi*, University at Albany-SUNY, *H. Geisler*, SUNY College at Oneonta, *C.A. Ventrice, Jr.*, University at Albany-SUNY

The influence of chemisorbed oxygen on the growth of graphene by catalytic decomposition of ethylene in an ultra-high vacuum (UHV) chamber on both the Cu(100) and Cu(111) surfaces has been studied. A custom UHV compatible heater stage was constructed that allows heating of a crystal to temperatures as high as 1000 °C at hydrocarbon pressures of up to 100 mTorr. System recovery to the low 10^{-10} Torr range is achieved within a few minutes of opening the gate valve to the turbo pump. The crystal structure of the graphene films was characterized with in-situ low energy electron diffraction (LEED), and the growth morphology was monitored by ex-situ scanning electron microscopy (SEM). For the clean Cu(100) substrate, heating from room temperature to the growth temperature while dosing with ethylene resulted in the formation of epitaxial graphene films. The crystal quality was found to depend strongly on the growth temperature. At 900 °C, well-ordered two-domain graphene films were formed. For the Cu(111) surface, heating from room temperature to the growth temperature while dosing with ethylene did not result in the formation of graphene. This is attributed to the lower catalytic activity of the (111) surface and the relatively high vapor pressure of the Cu surface. The use of an Ar overpressure to suppress Cu sublimation during the growth resulted in the formation of predominately single-domain epitaxial graphene films. Predosing either the Cu(100) or Cu(111) surface with a chemisorbed layer of oxygen before graphene growth was found to adversely affect the crystal quality of the graphene overlayers by inducing a much higher degree of rotational disorder of the graphene grains with respect to the substrate. The SEM analysis revealed that the nucleation rate of the graphene islands dropped by an order of magnitude after predosing either the Cu(100) or Cu(111) surface with a chemisorbed oxygen layer before growth. On the other hand, the average area of each graphene island was observed to increase by at least an order of magnitude. Therefore, the presence of oxygen during graphene growth affects both the relative orientation and average size of grains within the films grown on both substrates.

5:40pm **2D+AS+HI+MC+NS+PS+SP+SS-TuA11** **Novel Materials Properties at Atomically Thin Limit**, *Zhi-Xun Shen*, Stanford University **INVITED**

In this talk, I will discuss recent progresses in uncovering novel materials properties at ultra-thin limit, with focus on mono-unit-cell superconductor FeSe and semiconductor MoSe₂ respectively.

The observation of a large superconducting-like energy gap which opens at temperatures up to 65 K in single unit cell (1UC) thick iron selenide films on SrTiO₃(FeSe/STO) has generated tremendous interest. A challenge is to understand the cause of enhanced Cooper pairing strength in this system, and possibly increase superconducting T_c. In this talk, we show angle-resolved photoemission spectroscopy, mutual inductance, and other measurements on 1UC and multi-UC thick FeSe films grown on Nb-doped SrTiO₃. Our data provide clear evidence for strong cross-interface electron-phonon coupling in single UC, raising the possibility that large pairing gap are caused by the strong coupling between the FeSe electrons and certain

collective modes of SrTiO₃. This suggests a pathway of "integrated functional components" approach to boost superconducting properties.

The intense interest of quantum systems in confined geometries is further amplified by the recent discovery of large enhancement in photoluminescence quantum efficiency and a potential route to "valleytronics" in atomically thin layered transition metal dichalcogenides (TMDs) MX₂ (M = Mo, W; X = S, Se, Te), which are closely related to the indirect to direct band gap transition in the single layer limit. Using angle-resolved photoemission spectroscopy (ARPES) on high quality thin film samples of MoSe₂ grown by molecular beam epitaxy (MBE), we have made a direct observation of a distinct transition from indirect to direct band gap as the thickness of the sample is reduced to a monolayer. The experimental band structure indicates a stronger tendency of monolayer MoSe₂ towards direct band gap with larger gap size than theoretical prediction. A comparison of directly measured ARPES band gap and optical data led to important new insights on semiconductor physics in 2D. Moreover, our finding of a significant spin-splitting of ~180meV at the valence band maximum (VBM) of a monolayer MoSe₂ film could greatly expand its possible application in spintronic devices.

If time permits, I will also discuss the superconductivity in CaC₆ and its implication on a possible pathway for superconducting graphene.

Energy Frontiers Focus Topic
Room: 315 - Session EN+EM+NS-TuA

Charge Storage Materials and Devices
Moderator: Susanna Thon, Johns Hopkins University

2:20pm **EN+EM+NS-TuA1** **Spatiotemporal Investigation of Li-Air Battery under Operating Condition: Understanding the Cathodic and Anodic Electrochemical Processes and their Interdependence**, *Di-Jia Liu*, Argonne National Laboratory **INVITED**

Li-O₂ battery has generated a great deal of interests due to its high theoretical energy storage capacity for vehicular application. Many studies were carried out in attempt to understand the fundamental chemical processes inside of Li-O₂ battery. The reports so far have been segmented into the investigation on the individual regions of the battery, cathode, anode and separator, mostly at the post mortem state due to the limitation of the characterization methods used.

We adopted a holistic approach in studying electrochemical processes and mechanism of the Li-O₂ battery using operando methods. Particularly, we introduced the microfocused synchrotron X-ray diffraction (μ -XRD) and tomographic (μ -CT) techniques for the spatiotemporal study on the phase and structural changes in Li-O₂ battery. These tools offered some unique capabilities to probe battery properties under the actual discharge-charging condition. For example, the μ -XRD has a spatial resolution at the micron scale of with a complete side penetration to the battery, rendering it feasible to study battery's composition layer-by-layer without the interruption of battery operation. In this presentation, we will discuss our recent investigation of the Li-O₂ batteries under cycling condition in real time using the cells fabricated with the most representative design and materials. We were able not only to reveal individually the changes at anode, cathode and separator, but also to provide a comprehensive view between the regional chemical processes and their interdependence to the overall battery performance during the multiple discharge-charge cycles. More importantly, the finding of this study provides new insights on the catalytic process inside of Li-O₂ cell and calls for new design and materials which could lead to high capacity and longer battery life.

The work performed at Argonne is supported by DOE under Contract No. DE-AC02-06CH11357 by UChicago Argonne, LLC.

3:00pm **EN+EM+NS-TuA3** **Insights into Ionic vs. Electronic Transport in Nanostructured Battery Electrodes Enabled by Microfabrication and Spatially Resolved XPS**, *Alexander Pearse, E. Gillette, S.B. Lee, G.W. Rubloff*, University of Maryland, College Park

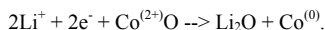
Nanostructured battery electrodes provide a design opportunity to achieve high power at high energy density, using thin active storage layers whose short ion diffusion pathways assure fast transport throughout the layers. However, this must be coupled with fast electron transport through current collectors to all regions of the ion storage layers, posing a design challenge in balancing and optimizing both charge transport components. Spatial inhomogeneity in the utilization of active material due to electronic or ionic transport limitations may lead to decreases in performance, but characterizing this effect with bulk electrochemical measurements is difficult. We address this challenge with a new state-of-charge (SOC) measurement scheme utilizing a patterned ultra-thin film battery electrode

and spatially resolved XPS, and focus on the case of limited electronic transport by examining SOC as a function of distance from the current collector.

We fabricate electrode test structures by evaporating metallic strips as current collectors on an electrically insulating substrate. A patterned thin film of active material (V_2O_5) is then deposited using atomic layer deposition (ALD) and mechanical masking so that only a small fraction of the active material is in contact with the current collector. The use of ALD allows for an ultrathin ($\leq 30\text{nm}$) pinhole-free film. We discharge these electrodes in a liquid electrolyte under different rates and conditions and directly measure the state of charge as a function of distance from the current collector using small spot XPS, achieving a lateral resolution of better than $20\mu\text{m}$. We find that a rate-dependent SOC gradient develops in the electrodes, with the SOC decreasing with distance from the current collector. Unlike microspot Raman or XRD, XPS provides a direct quantitative measurement of the SOC through the concentration of inserted ions and/or reduced vanadium ions. Additionally, in the ultrathin films relevant to nanostructured storage, XPS becomes a “quasi-bulk” measurement, because the escape depth of photoelectrons becomes a significant fraction of the film thickness. We also explore the depth dependence of the SOC using angle resolved XPS and ion beam depth profiling. We compare our observations with simulations using COMSOL Multiphysics, and attempt to resolve discrepancies between the two. We believe this approach can provide design guidance for heterogeneous nanostructures applied to electrical energy storage, and we anticipate it to be broadly applicable to other electrode materials and active ions.

3:20pm EN+EM+NS-TuA4 The Lithium-Induced Conversion Reaction of CoO Thin Film Battery Materials in Ultra-High Vacuum as Studied by ARXPS and STM, Ryan Thorpe, S. Rangan, A. Howansky, R.A. Bartynski, Rutgers, the State University of New Jersey

Li-ion conversion batteries can store 2-3 times more charge than intercalation batteries by utilizing the full range of oxidation states of their constituent divalent or trivalent transition metal compounds during discharge. A prototypical conversion compound is CoO, which follows the reaction



Cobalt oxide and other transition metal oxides are attractive for use as Li-ion anodes in portable electronics due to their high charge storage capacity and moderate voltage versus Li^+/Li^0 . However, the cycling stability of conversion electrodes is poor, and capacity losses have thus far prevented their implementation.

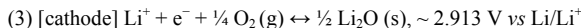
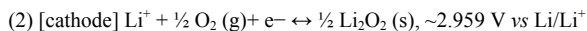
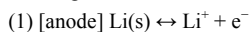
In order to understand phase progression during the conversion reaction of CoO, high-purity CoO thin films grown in UHV were sequentially exposed to atomic lithium. The electronic structure of the pristine films and of the products of lithiation was studied using x-ray photoemission spectroscopy (XPS), UV photoemission spectroscopy, and inverse photoemission spectroscopy. The crystal structure and film reorganization were probed in parallel with transmission electron microscopy (TEM) and scanning tunneling microscopy.

The amount of CoO reduction for a given Li dose was observed to be highly dependent upon the temperature at which lithiation was performed. At 150°C , Li mobility in the active material was sufficient to allow full reduction of the CoO film as confirmed by XPS. Consistent with electrochemically lithiated CoO electrodes, precipitation of Co nanoparticles in a Li_2O matrix was observed in TEM images. However, at room temperature, the Li-rich overlayers that formed on the CoO film after initial lithiations inhibited further Li diffusion. This could be due to the intrinsically poor kinetic properties of Li_2O or to the formation of Li_2O_2 and/or LiOH passivating films.

The reactivity of CoO films was also found to depend on the orientation of the film. CoO(100) films exhibited a higher degree of conversion for a given Li exposure than polycrystalline films. STM and angle-resolved XPS of these films have been used to investigate the differences between these two film morphologies upon exposure to Li.

4:20pm EN+EM+NS-TuA7 Controlled Cathode/Catalyst Architectures for Li-O₂ Batteries, Malakhi Noked, M.A. Schroeder, A.J. Pearce, C. Liu, A.C. Kozen, S.B. Lee, G.W. Rubloff, University of Maryland, College Park

Electrochemical power sources based on metal anodes have specific energy density much higher than conventional Li ion batteries, due to the high energy density of the metal anode (3842mAh/g^1 for Li). Rechargeable Li-O₂ batteries consume oxygen from the surrounding environment during discharge to form Li oxides on the cathode scaffold, using reactions



The cathode reaction requires large over-potentials for charging due to the mass transfer resistance of reagents to the active sites on its surface, decreasing the round trip efficiency, making recharge of the Li-O₂ cell difficult. To overcome these problems, the cathode needs good electrical conductivity and a porous structure that enables facile diffusion of oxygen and can accommodate the reduced oxygen species in the pores.

Two significant challenges exist in the use of the traditional activated carbon material as the cathode of the Li-O₂ system. First, in the presence of Li_2O_2 the carbon electrode becomes relatively unstable even at low voltages ($\sim 3\text{V}$). Second, cathode structures must be porous to accommodate a substantial amount of Li-peroxide (Li_2O_2) without blocking ion transport channels in the cathode. While a few studies have been reported on the effect of catalyst on the onset potentials for the oxygen evolution reaction (OER) and oxygen reduction reaction (ORR) in the Li-O₂ cell, the results were inconclusive due to the lack of systematic study in a single system and conditions.

We report here results from a model cathode system which enable determination of the effects of various catalysts on the OER/ORR reactions in the non-aqueous Li-O₂ cell. Mesoporous CNT sponge is used as the model cathode material, decorated with catalyst nanoparticles by nucleation-controlled atomic layer deposition (ALD) of Ru, RuO₂, MnO₂, and Pt catalyst components whose loading and composition are controlled by manipulating the ALD conditions. Using a custom Li-O₂ battery cell, we have studied the effect of different catalysts on the voltage of the OER and ORR, and on the cycling performances of the cell. We demonstrate a Li-O₂ cell that sustains $>3000 \text{mAh}_c^{-1}$ over more than 15 cycles at current density of $200 \text{mA}_c\text{g}^{-1}$. To our knowledge, this is the first comparison of a variety of catalysts with a well-defined morphology (controlled by ALD and monitored by TEM), and under the same electrochemical conditions.

4:40pm EN+EM+NS-TuA8 Vertically Aligned Carbon Nanotubes on Ni Foam as a 3D Li-O₂ Battery Cathode, Marshall Schroeder, M. Noked, A.J. Pearce, A.C. Kozen, S.B. Lee, G.W. Rubloff, University of Maryland, College Park

The Li-O₂ battery system is one of the prime candidates for next generation energy storage. Like other metal-O₂ systems, this technology is known for its impressive theoretical specific energy due to use of metallic anodes and because the cathode active material (oxygen) is not stored in the battery, but is available in the cell environment. A typical cell consists of a pure lithium metal anode, an organic electrolyte (in this study), and a porous positive electrode (usually made of carbon or oxides) which acts as a reaction scaffold for oxygen reduction to Li_2O_2 or Li_2O during discharge. Despite remarkable scientific challenges within every component of the cell, the positive electrode is particularly complicated by its role in the oxygen evolution (OER) and reduction (ORR) reactions, leading to strict requirements for electrode architecture and physicochemical stability for optimal performance. We present herein one of the first experimental realizations of a controlled macroscale 3D carbon nanotube architecture with a practical carbon loading of 1mg/cm^2 in an attempt to satisfy these requirements.

The O₂ cathode highlighted in this work features a macroporous nickel foam current collector coated with dense forests of vertically aligned carbon nanotubes (VACNT). This freestanding, hierarchically porous system is the first to feature VACNT robustly and electrically connected to a 3D current collector without a binder, and without requiring delamination of the CNT from the growth substrate. Grown via LPCVD with an Fe catalyst on a thin ALD interlayer, the micron-length VACNT provide a very promising electrode material due to their high electrical conductivity, physicochemical stability, and a high surface area architecture that is conducive to ionic mobility and storage of the reduced oxygen discharge product. As a result, this structure exhibits significant capacity ($>2\text{Ah/g-carbon}$) at high ORR voltages ($>2.76\text{V}$) without requiring a catalyst.

Electrochemical performance results as a scaffold for oxygen reduction in various non-aqueous electrolytes will be presented with SEM/TEM/XPS of pristine/discharged electrodes.

5:00pm EN+EM+NS-TuA9 Solid Micro-supercapacitor using Directed Self-Assembly of Tobacco Mosaic Virus and RuO₂, Markus Gnerlich, E.I. Tolstaya, J. Culver, D. Ketchum, R. Ghodssi, University of Maryland, College Park

The 3D micro-supercapacitor reported here utilizes a novel bottom-up assembly method that combines genetically modified Tobacco mosaic virus (TMV-1Cys) with deposition of RuO₂ on multi-metallic microelectrodes. The nanostructured RuO₂ coating is selectively deposited on the electrodes due their unique composition, which is a significant advantage for microfabrication process integration. Test results show electrode capacitance as high as 18mF/cm^2 in $1.0\text{M H}_2\text{SO}_4$ electrolyte and 7.2mF/cm^2 in solid Nafion electrolyte.

The device fabrication involves the photolithographic patterning of titanium nitride (TiN) microelectrodes with Au cap on top of polyimide micropillars supported by a silicon wafer. A schematic cross section of the device is shown in Figure 1 and a photograph of the fabricated chip in Figure 2. The complexity of the self-assembly process in multiple chemically reactive solutions required the development of a special kind of micro-electrode. The TiN functions as a chemically resistant current collector, the Au cap as an adhesion layer for the TMV-1cys, and the Ni pad as a sacrificial material during the RuO₂ deposition process. After microfabrication, each chip is submerged in TMV-1Cys solution for 24 hours and then transferred to a 0.5% solution of RuO₄. A nanostructured coating of RuO₂ forms on all exposed electrode areas as the Ni is sacrificed in a galvanic displacement reaction. EDX spectral imaging of the constituent elements on the electrode demonstrates selective RuO₂ coating (Figure 3), and SEM images of the electrodes before and after TMV/RuO₂ coating shows the TMV-1Cys/RuO₂ nanostructures (Figure 4).

Cyclic voltammetry (CV) was performed from 0-800mV versus Ag/AgCl at 10 mV/s in 1.0M H₂SO₄ electrolyte. Figure 5 shows the CV curves, and Figure 6 shows the associated capacity fading, which was insignificant after 100 cycles for electrodes annealed at 150°C. Separately prepared chips were coated with Nafion dispersion and tested in a controlled humidity environment. The measured capacitance drops from 18 to 7.2 mF/cm² per electrode due to ionic conductivity limitations, but 80% capacity is retained after 12,000 cycles (Figure 7). Associated rate capability (Figures 8-9) shows 60% capacity is retained when comparing 3 uA/cm² to 3000 uA/cm², and the low leakage current of only 5 nA (Figure 10) enables use in a wide variety of energy storage applications.

The primary challenge of nanomaterials is often integration into microfabrication processes. The RuO₂ electrode developed here is optimized for compatibility with standard microfabrication steps by using a novel bottom-up assembly approach for manufacturing micro-supercapacitors.

5:20pm **EN+EM+NS-TuA10 Characterization of Tobacco Mosaic Virus-templated Ni/NiO Electrodes for Solid Flexible Supercapacitors**, Sangwook Chu, K.D. Gerasopoulos, M. Gnerlich, J. Culver, R. Ghodssi, University of Maryland, College Park

Characterization of nickel oxide supercapacitor electrodes utilizing *Tobacco mosaic virus* (TMV) nanotemplates is presented. NiO was formed on Ni coated TMV nanotemplates by annealing at high temperatures (Figure 1). The resulting electrode showed excellent electrochemical performance with remarkable cycle stability. The TMV/Ni/NiO nanostructured electrodes were also integrated with a solid electrolyte to demonstrate their potential application as solid flexible supercapacitors.

NiO supercapacitor electrodes have been prepared in literature using various methods, and it has been found that the crystallinity of the NiO is critical for its electrochemical charge capacity [1]. The NiO electrode presented in this work was thermally grown on Ni coated TMVs. Gold electrodes (0.5cm²) were immersed in TMV solution for virus self-assembly followed by electroless deposition of Ni uniformly coating the TMV nanostructure [2]. TMV/Ni electrodes were annealed in a furnace at three different temperatures (200°C, 300°C, and 400°C) and the NiO formation on TMV/Ni surface was characterized by XPS (Figure 2). The results indicate that thermal growth of NiO layer on TMV/Ni electrodes starts at temperatures higher than 300°C, in good agreement with previously reported results.

Electrochemical testing was performed in aqueous 2M KOH electrolyte in a three-electrode configuration. The electrodes annealed at 300°C showed the highest areal capacitance (148mF/cm²) measured by a galvanostatic (2mA/cm²) charge/discharge test shown in Figure 3a. The redox charge storage mechanism was confirmed by cyclic voltammetry (CV) with good rate capability up to 100mV/s (Figure 3b). Excellent cycle stability was measured with little degradation over 500 cycles as shown in Figure 4. This is attributed to the conformal layers of Ni/NiO over the TMV nanostructure, and the stabilizing effect of KOH on NiO. The continuous electrical contact between the Ni and NiO layers ensures an optimized current collector configuration.

A PVA-KOH-H₂O polymer was prepared to study the performance of the nanostructured electrodes with a solid electrolyte. Polymer electrolyte solution was poured onto the nanostructured NiO electrodes and the Pt foil was assembled on top as an anode. The polymer electrolyte film formed after 24hours was flexible and strong enough to support both electrodes. Figure 5 shows CV curves measured with the assembled cell, verifying proper operation of the nanostructures in both liquid and solid electrolytes. The successful integration of TMV/Ni/NiO electrodes with polymer electrolytes highlights the potential of this approach to develop flexible solid-state supercapacitor devices.

5:40pm **EN+EM+NS-TuA11 Charged Particles Micro-Penning-Malmberg Trap: An Approach to Store High Densities with Substantially Lower End Barrier Potentials**, Alireza Narimannehad, J. Jennings, C. Minnal, M.H. Weber, K.G. Lynn, Washington State University
Among devices that have been used to store antimatter, Penning-Malmberg trap has become the device of choice because of its simplicity and versatility. However, the challenge involved in these traps is when the number of particles increases inside the trap to the densities of energy harvesting interest, the confining fields rise to unpractical values. One of the authors has proposed a design of microtube arrays with much lower end barrier potentials. The microtraps are designed for non-neutral plasma storage such as positrons. Here, we present fabrication, simulation studies, and trapping milestones so far. The fabrication involved advanced MEMS techniques including photolithography, deep reactive ion etching of silicon wafers, sidewalls smoothing, gold sputtering, wafers aligning, and thermo-compression gold bonding. Alignment of less than 2 microns was achieved using a micro-machined jig and precision ground sapphire rods. Simulation using a WARP Particle-In-Cell code showed that density of $1.6 \times 10^{11} \text{ cm}^{-3}$ is achievable with the new trap design while the end barrier potentials are several order of magnitudes smaller compared to the conventional traps. However, positron losses occur in experimentation by both trap imperfections such as misalignment of wafers, asymmetries, and physical imperfections on the surface, and also field misalignment and perturbations. The loss rates were also compared to the results from simulation in order to study and distinguish each effect. This project will open the door to a wide range of new and exciting research areas. The size of these traps along with the low confining potentials is a big step to make them portable. It could be used as a source of energy or in propulsion system where alternate sources are not feasible.

MEMS and NEMS

Room: 301 - Session MN+NS-TuA

Multi-Scale Phenomena and Bio-Inspired MEMS/NEMS
Moderator: Philip Feng, Case Western Reserve University, Meredith Metzler, Cornell University

2:20pm **MN+NS-TuA1 MEMS-Enabled Multiscale Nanolaminated Magnetics**, Mark Allen, University of Pennsylvania **INVITED**

The manufacture of materials with bulk volumes and precisely controlled nanostructure has led to the creation of materials with surprising and useful mechanical and electrical properties. Recently we have developed a 'top-down' fabrication technique that allows the creation of highly-structured multilayer metallic materials, with precisely designed characteristic lengths in the hundreds of nanometers scale, but volumes of manufactured material in the macro range. The fabrication relies on automated and repeated multilayer electrodeposition of multiple metallic materials, followed by sacrificial etching of one metal. The resultant structure consists of individualized high-lateral-aspect-ratio sub-micron metallic films. The application of these multiscale materials to ultracompact energy conversion is investigated. Metallic magnetic materials have desirable magnetic properties, including high permeability and high saturation flux density, when compared with their ferrite counterparts. However, eddy current losses preclude their use in many switching converter applications due to the challenge of simultaneously achieving sufficiently thin (100-500 nm) laminations such that eddy currents are suppressed while simultaneously achieving overall material thicknesses (0.1-1 mm) such that substantial power can be handled. Sequential electrodeposition of multiple nanoscale 'sheets', or laminations, of magnetic materials such as permalloy and NiFeCo offers an approach to fabricate the desired nanostructured magnetic core. Tests of toroidal inductors with nanolaminated cores showed negligible eddy current loss relative to total core loss even at a peak flux density of 0.5 T and a frequency of 10 MHz. The ability to operate at such high flux levels offers the possibility of dramatically shrinking the physical size of power inductors in energy converters. DC-DC converters with efficiencies of up to 93% and power handling of approximately 40W have been achieved in ultracompact form based on these materials.

3:00pm **MN+NS-TuA3 Fabrication and Electrical Performance of Through Silicon Via Interconnects Filled with a Copper/Carbon Nanotube Composite**, Y. Feng, Susan Burkett, The University of Alabama
Three-dimensional integrated circuit (3D-IC) technology has been developed using copper (Cu) filled through silicon vias (TSVs). The vertical interconnects pass through a set of stacked dies and enable many applications that benefit from increased bandwidth, reduced signal delay, and improved power management. However, the reliability of Cu interconnects is a serious concern since the performance is affected by

electromigration and stress associated with mismatch in thermal expansion coefficients. Carbon nanotubes (CNTs) are nanoscale materials which possess a high Young's modulus, a low coefficient of thermal expansion, and high thermal conductivity. Compared to Cu, CNTs exhibit low resistivity due to the existence of ballistic conduction and they are capable of carrying a higher current density. In this work, we fabricated TSVs using a novel materials system consisting of a composite of Cu and CNTs as a possible solution to the problems encountered in Cu-based interconnects. First, blind TSVs were fabricated using a Bosch process. After etching, an insulating layer, a metallic seed layer, and a catalyst layer were deposited previous to CNT growth. Vertically aligned CNTs were grown by chemical vapor deposition method. Finally, Cu was deposited by periodic reverse pulse electroplating inside the vias to form a Cu/CNT composite. Polishing completed the fabrication and allowed measurement of electrical performance for TSV interconnects. The experimental results were compared for interconnects filled with Cu and those filled with the Cu/CNT composite. The results are encouraging for the Cu/CNT composite having potential application as a TSV interconnect material.

3:20pm MN+NS-TuA4 Meso Scale MEMS Motion Transformer and Amplifier Electrostatically Actuated by Parallel Plate Electrodes, Y. Gerson, S. Krylov, Tel Aviv University, Israel, Tali (T.) Nahmias, R. Maimon, Microsystems Design Center, RAFAEL LTD, Israel

Meso scale microelectromechanical structures found on the upper scale of microelectromechanical systems (MEMS) can potentially replace conventional mechanical devices produced by common for the macro-engineering approaches such as machining and assembly of individual parts. When realized as a compliant mechanism containing a single flexible member rather than multiple parts attached by joints they provide smooth frictionless motion without backlash and exhibit improved reliability and robustness. Batch fabrication using micromachining processes established in MEMS allows improved yield and significantly lower cost. However, actuation of these devices remains challenging. Electrostatic actuation, which is the most widely used in smaller MEMS devices, is viewed to be less suitable for the actuation at the meso scale due to unfavorable scaling laws, namely quadratic reduction of the actuating force with the distance between the electrodes. For this reason, most of the meso scale micro devices are actuated by thermal transducers, distinguished by slow response and high power consumption or by piezoelectric or magnetic motors, which cannot be integrated within the device and require post-fabrication assembly.

In this work we report on the design, fabrication and characterization of an electrostatically actuated meso scale microelectromechanical motion transformer and amplifier. The actuator incorporate a transducer with multiple parallel plate electrodes and is realized as a compliant mechanism relying on flexible pseudo hinges. The $5000\ \mu\text{m} \times 4000\ \mu\text{m}$ device converts linear motion of the transducer into mechanically amplified angular motion of a rotating lever. By combining a highly efficient small-gap parallel plate electrode and a motion amplification the device is designed to provide a lever tip displacement of $60\ \mu\text{m}$, an initial blocking force of 0.001N at zero displacements and a blocking force of 0.012N in the maximal displacement configuration when the parallel plate actuator is in its closed position. The devices were fabricated using DRIE from a SOI wafer with (111) front surface orientation and a $150\ \mu\text{m}$ thick device layer. The devices were operated in ambient air conditions and the functionality of the device was demonstrated experimentally. The voltage-displacement dependence and resonant curves were built using image processing procedure implemented in Matlab. Excellent agreement between the results provided by the Finite Elements models and the experimental data was observed. The results of the work demonstrate an ability to achieve both large displacements and high blocking forces in an electrostatically actuated meso scale compliant mechanism.

4:20pm MN+NS-TuA7 Bio-Inspired Microlenses and Their Biomedical Applications, Hongrui Jiang, University of Wisconsin - Madison

INVITED

Optical detection and imaging have wide applications in biomedicine and biological and chemical analyses. With continuing miniaturization effort to realize integrated microsystems, micro-scale optical components become more and more important. For any optical system, lenses are critical elements. In this talk, I will present our work on liquid microlenses. I will first introduce a few types of microlenses and microlens arrays, including tunable liquid microlenses actuated by temperature-, pH- and infrared light-responsive hydrogels, microlens arrays for light-field imaging, microcamera arrays mimicking compound eyes, and artificial reflecting superposition compound eyes. Then, I will discuss about potential applications of these lenses in medical instruments. I will describe miniaturized cameras capable of multiple viewpoints, prototype flexible endoscopes implementing infrared-light responsive liquid microlenses at their distal ends, and prototype multiple-camera laparoscopes.

5:00pm MN+NS-TuA9 The Development of a Valve Based Microfluidic Biofilm Reactor for Biofilm Studies with Reliable Controls, Sowmya Subramanian, M.T. Meyer, Y.W. Kim, W.E. Bentley, R. Ghodssi, University of Maryland, College Park

We present a multi-experiment PDMS based biofilm analysis platform using a valve-actuated microfluidic system, designed to reduce growth variance of *in-vitro* biofilms to less than 10%. This was achieved by integrating hydraulic push-down valve actuators to section a uniform biofilm grown in a channel by maintaining a single source of bacterial suspension [1, 2]. In this work, we establish a simplified process flow for the fabrication of a multi-depth device mold and demonstrate the high throughput capability of the microfluidic biofilm reactor.

Bacterial biofilms are the primary cause of infections in medical implants and catheters. The widespread use of high doses of antibiotics to treat biofilm infections is leading to the emergence of antibiotic resistant strains, necessitating the development of alternative methods of treatment [3]. However, the experimental evaluation of new treatment techniques is strongly hindered by the stochastic nature of biofilm growth [1]. Therefore, it is required to develop a microsystem that can not only facilitate multi-experiment studies for new treatment evaluation but also enable the growth of uniform biofilms that can be used as reliable controls.

Figure 1 shows a single uniform biofilm grown in the horizontal center channel of the device is sectioned into multiple sections, by hydraulically actuating the push-down valves thereby enabling multi-experiment studies on the same biofilm. Figure 2 shows the schematic of the operation of a "push-down" valve [4], the schematic of the CAD layout of the two-level microfluidic device and its two modes of operation. The two-step photolithography of the molds (Figure 3) using negative photoresists, SU8-2015 and KMPR1050, allows for the patterning of the multi-depth microfluidic mold without the need for additional passivation of the first resist layer, thereby simplifying fabrication. The mold can be reused to produce multiple devices; a photograph of the valve region of a used multi-depth mold is shown in Figure 4. Photographs of the device operating in different modes are shown in Figure 5.

The unique capability of this valved microfluidic biofilm reactor to section uniform biofilms can facilitate high-throughput biofilm studies, including new drug discovery. The push-down valve configuration allows for easy integration of electrodes for the study of alternative treatment methods like electric fields. Furthermore, the integration of the biofilm reactor with a real-time measurement system will enable high-throughput continuous analyses on uniform biofilms while ensuring tight and reliable controls.

5:20pm MN+NS-TuA10 Multimode Silicon Carbide (SiC) Microdisk Resonator in Liquid, Hao Jia, P.X.-L. Feng, J. Lee, Case Western Reserve University

We experimentally demonstrate, for the first time to our knowledge, the operation of silicon carbide (SiC) microdisk resonators in fluidic and viscous environments (particularly in water) with robust multiple flexural-mode resonances in the high and very high frequency (HF/VHF) radio band. We observe ~ 8 resonance modes in a $20\ \mu\text{m}$ -in-diameter SiC microdisk resonator with resonance frequencies up to ~ 120 MHz and quality Q factors as high as ~ 40 in water.

SiC is a highly attractive material for microelectromechanical systems (MEMS) due to its superior mechanical (e.g. high elastic modulus, $E_V \sim 450$ GPa), optical (wide bandgap, $> 2.3\text{eV}$) and thermal properties (thermal conductivity of $320\text{--}490\ \text{W}/[\text{m}\times\text{K}]$)^[1]. These advantages make SiC especially suitable for sensing applications in liquid for its transparency from visible to mid-infrared light and high optical power handling ability, facilitating efficient laser actuation and detection. Meanwhile, two dimensional (2D) microdisk structure exhibits multiple flexural-mode resonance characteristics, which can enhance sensing performances in liquid with the additional degrees of freedom and larger sensing area. Further, the unique biocompatibility of SiC allows potential in-liquid biosensing applications be developed.

In this study, we demonstrate the operation of high frequency SiC microdisk resonators in liquid. The SiC microdisk resonators are completely immersed in water, and are optically driven by an amplitude-modulated 405nm laser. The multimode resonances are detected with optical interferometry using a 603nm He-Ne laser. We observe ~ 8 resonance modes up to ~ 120 MHz with Q_s as high as ~ 40 in water. To our best knowledge, both the number of resonance modes and Q_s measured are the highest among flexural-mode resonators operating in water reported to date^{[2],[3],[4],[5]}. Such high frequency SiC microdisk resonators with robust multimode resonances and high Q_s in water may provide an appealing platform for particle and biological sensing applications in liquid.

[1] X. Lu, J. Y. Lee, P. X.-L. Feng, and Q. Lin, *Opt. Lett.* **38**, 1304 (2013).

- [2] S. S. Verbridge, L. M. Bellan, J. M. Parpia, and H. G. Craighead, *Nano Lett.* **6**, 2109 (2006).
- [3] S. Sawano, T. Arie, and S. Akita, *Nano Lett.* **10**, 3395 (2010).
- [4] J. H. Park, T. Y. Kwon, D. S. Yoon, H. Kim, and T. S. Kim, *Adv. Func. Mater.* **15**, 2021 (2005).
- [5] C. Vancura, Y. Li, J. Lichtenberg, K.-U. Kirstein, A. Hierlemann, and F. Josse, *Anal. Chem.* **79**, 1646 (2007).

5:40pm **MN+NS-TuA11 Development of CMOS-based Capacitive Micromachined Ultrasonic Transducers Operated in Collapsed Mode**, **Wei-Cheng Chung**, *M.-C. Tsao, P.-C. Li, W.-C. Tian*, National Taiwan University, Taiwan, Republic of China

In this work, experimental results of complementary metal-oxide-semiconductor (CMOS)-based capacitive micromachined ultrasonic transducers (CMUTs) operated in the collapsed mode will be reported. Our CMUT is fabricated by TSMC 0.35 μ m two poly Si and four metal layer (2P4M) CMOS-MEMS standard process followed by a post customized wet etching. Conventionally, the applied DC bias is 80% of the collapse voltage during the CMUT operation. Compared to the conventional operation, the CMUT membrane will be snapped-down on the bottom electrode and this will change the center frequency of the transducers. The collapsed voltage of our CMUT is designed at approximately 40V. The center frequency (in immersion) of our CMUT in conventional mode operation is 2.89MHz while the frequency is shifted to 9.12MHz in collapsed-mode operation. The sensitivity is proved to be 4-times larger in the collapse-mode operation because the increased electrical-mechanical coupling efficiency.

The comparison of single-electrode and double-electrode design will be reported as well. With the double-electrode design, the collapse voltage is first applied to the center electrode while a separated DC bias is applied to the side electrode to actuate our CMUTs. The maximum displacement of the CMUT membrane will be appeared on the side electrode. It is proved that CMUTs with the double-electrode design can transmit a higher output pressure and receive signals with a higher sensitivity compared to CMUTs with the single-electrode design. It is believed that the our CMUTs with standard CMOS-based process will broaden the application spaces such as in biomedical imaging and nondestructive evaluation.

6:00pm **MN+NS-TuA12 Development of Micro Gas Preconcentrator Using Electroless Gold Deposition for Human Breath Analysis**, **ChunYen Kuo**, *C.-L. Hsu*, National Taiwan University, Taiwan, Republic of China, *H.-Y. Kuo, C.-J. Lu*, National Taiwan Normal University, Taiwan, Republic of China, *W.-C. Tian*, National Taiwan University, Taiwan, Republic of China

The detection of the volatile organic compounds (VOCs) in human breath can be analyzed by gas chromatograph (GC) as a non-invasive diagnosis for lung diseases. However, the gas concentration of the VOCs in human breath is low, approximating in the ppb to sub ppb range, and thus a gas preconcentrator (PCT) must be placed before a GC to collect and preconcentrate trace compounds. Early μ PCTs using commercially available adsorbents and microheaters were demonstrated. However, the heating efficiency of the device is limited either by a large thermal mass or a poor heat transfer.

In this study, we present a gas PCT using a simple one-photomask micromachined process and the electroless gold deposition method to form the gold film, serving as a thin film microheater, on the inner surface of the microchannel. An amorphous and porous carbon film that functions as an adsorbent is grown on microheaters inside the microfluidic channel followed by the electroless gold deposition. The developed gas PCT can be heated to >300°C by applying a constant electrical power of ~5W with a heating rate of 60°C/sec. Four suspected lung cancer biomarkers, acetone, benzene, toluene and xylene, are collected through the proposed gas PCTs and separated successfully using a 17-m-long gas chromatography (GC) column. Compared with previous works, the more simple fabrication process, more stable heating element, more uniform temperature distribution and more efficient heating rate of the micro gas preconcentrator are developed demonstrated.

Nanometer-scale Science and Technology Room: 304 - Session NS+AS+SS-TuA

Nanowires and Nanotubes: Advances in Growth and Characterization

Moderator: Lincoln Lauhon, Northwestern University

2:20pm **NS+AS+SS-TuA1 Surface Chemical Choreography of Nanowire Synthesis**, **Michael Filler**, *S.V. Sivaram, N. Shin, I.R. Musin*, Georgia Institute of Technology **INVITED**

This talk will provide an overview of our recent efforts to understand the chemical phenomena underlying semiconductor nanowire growth. The vapor-liquid-solid technique – where a liquid “catalyst” droplet collects atoms from the vapor and directs crystallization of individual solid layers – is a ubiquitous method for the synthesis of these quintessential nanoscale building blocks, but a lack of atomic-level design rules prevents robust programming of structure. Long-standing challenges in the control of heterostructure, dopant profile, atomic stacking sequence, kinking, and even simple axial growth restrict the accessible property space and highlight the pitfalls of an overreliance on empirical process optimization. We couple in-situ or operando infrared spectroscopy with post-growth high-resolution electron microscopy to connect specific surface chemical bonds present during synthesis with nanowire structure. Studies of Si and Ge nanowires demonstrate the fundamental, and previously unrecognized, role of adsorbed hydrogen atoms. The surface coverage of these precursor (e.g., Si₂H₆ or Ge₂H₆) decomposition intermediates, which we quantitatively determine as a function of pressure and temperature, can change over a narrow range and strongly influence growth. Our findings show, for example, that adsorbed hydrogen is essential for stabilizing the catalyst or driving elongation in new crystal directions for Ge and Si nanowires, respectively. We leverage these insights to rationally design precursors that choreograph nanowire structure on multiple length scales, permitting the fabrication of user-defined defect, kinking, and diameter-modulated superstructures.

3:00pm **NS+AS+SS-TuA3 Atom Probe Tomography Analysis of GaAs-AlGaAs Core-Shell Nanowire Heterostructures**, **Nari Jeon**, Northwestern University, *S. Morkötter, G. Koblmüller*, Technische Universität München, Germany, *L.J. Lauhon*, Northwestern University

GaAs-AlGaAs planar heterostructures have various electronic and optoelectronic applications such as solar cells and light-emitting diodes.^{1,2} This is due to a small lattice mismatch between GaAs and AlAs providing wider opportunities in bandgap tuning. Moreover, modulation doping scheme is well-known to be effective in enhancing electron mobility in the heterostructures by minimizing electron scattering from ionized impurities. Since growth of GaAs-AlGaAs core-shell nanowires was demonstrated in 2005,³ there has been a growing number of papers reporting novel (opto)electronic transport properties, which are originated from the nonparallel geometry of GaAs-AlGaAs interfaces and its related compositional fluctuations.⁴ In fact, compositional structures are more complex in the core-shell nanowires compared to the planar counterparts. For example, there are six Al-rich bands along the corners of {110} sidewall facets in the AlGaAs shell.⁵ While most of the previous studies were based on transmission electron microscopy on cross-sectioned samples, we exploited the atom probe tomography (APT) to explore compositional fluctuations in three dimensions. The focus of the presentation will be APT sample preparation and composition characterization of Si delta-doped GaAs-AlGaAs core-shell nanowires. Molecular beam epitaxy reactor was used to grow the core-shell nanowires and the GaAs-AlGaAs superlattice planar samples as a reference to the nanowires. Individual nanowires were mounted on tungsten tips using micromanipulator for APT and planar samples were fabricated into tip-shaped APT samples by the lift-out and sharpening method using focused ion beam (FIB). Carefully designed structures of the superlattice with varied thickness and spacing in planar samples enabled us to estimate the range of possible ion beam damage from FIB. The atom probe conditions such as laser pulse energy and target detection rate were also optimized to achieve high spectral and spatial resolutions, which are critical for APT of III-V compound semiconductors where preferential detection loss and surface diffusion for III and/or V group elements are possible depending on the APT conditions. Intermixing at GaAs-AlGaAs interface and stoichiometric fluctuation in AlGaAs shell were mainly studied along with the detection limit of Si dopants in the delta doping layer.

1 K. Takahashi et al. *Solar Energy Materials and Solar Cells* **66** 517-524 (2001).

2 D. Ban et al. *Journal of Applied Physics* **96** 5243-5248 (2004).

3 J. Naborisaka et al. *Applied Physics Letters* **87** 093109-3 (2005).

4 S. Funk et al. Nano Letters **13** 6189-6196 (2013).
5 M. Heiss et al. Nature Materials **12** 439-444 (2013).

3:20pm **NS+AS+SS-TuA4 Scanning Tunneling Microscopy of Semiconductor Nanowire Surfaces and Devices**, R. Timm, J. Knutsson, M. Hjort, S. McKibbin, O. Persson, J.L. Webb, Anders Mikkelsen, Lund University, Sweden

III-V semiconductor nanowires (NWs) offer tremendous possibilities for device application in solid-state lighting, energy conversion, and information technology [1]. With their small diameter and their very large surface-to-volume ratio, the NW device behavior is strongly determined by their surface structure. Thus, it is both essential and challenging to investigate their atomic surface structure and to combine this information with electrical measurements on individual NWs.

Recently, we have managed to clean InAs NWs from their native oxide and revealed the atomic arrangement of their side surfaces with scanning tunneling microscopy (STM). Here, we present STM images of various NW surfaces of both wurtzite and zincblende crystal structure [2], including InAs, GaAs, InP, and InSb NWs. By combining STM imaging with scanning tunneling spectroscopy (STS) measurements, we simultaneously study the surface structure and local electronic properties across the interfaces of NW heterostructures [3].

For correlating local structural and electronic characterization with transport measurements of NW devices, we have developed a novel STM-based setup: We are using combined atomic force microscopy (AFM) and STM/S on individually contacted NWs for mapping the surface structure and the local band alignment along the NW heterostructure under device performance. We show initial results of this unique approach on InAs-GaSb nanowire tunnel diodes, where we could prove Esaki behavior of a NW while it was investigated by STM/AFM. From a set of STS spectra we determined the position of the Fermi level along the nanowire for different applied biases, showing an abrupt drop directly at the material interface. In a reverse experiment, we used the STM/AFM tip as local gate and measured the resulting source-drain current through the nanowire for different biases [4].

In some cases it is desirable to measure the conductivity of individual as-grown nanowires in an upright-standing configuration without any sample processing. Here we have developed an alternative setup where the STM tip is used to first image free-standing nanowires from top and then form a point contact [5]. We will demonstrate the reproducibility of this method in establishing low-resistive Ohmic contacts to individual InP and InAs nanowires [6], and we will show initial results on the I-V properties of individual InP NW solar cells.

- [1] J. Wallentin *et al.*, Science **339**, 1057 (2013)
- [2] M. Hjort *et al.*, Nano Lett. **13**, 4492 (2013)
- [3] M. Hjort *et al.*, ACS Nano **6**, 9679 (2012)
- [4] J. L. Webb *et al.*, Nano Res., in print
- [5] D. B. Suyatin *et al.*, Nature Commun. **5**, 3221 (2013)
- [6] R. Timm *et al.*, Nano Lett. **13**, 5182 (2013)

4:20pm **NS+AS+SS-TuA7 Poly-Aromatic Hydrocarbon Nanostructure Growth on Single and Multi-Layer Graphene**, Alexander Yulaev, CNST/UMD Graduate Student Researcher, A. Kolmakov, NIST

Poly-aromatic hydrocarbons (PAH) are known as potential hazardous organic pollutants, which can be found in soil, air, meat, fish and etc. Carbon based materials are routinely used for environmental remediation. Graphene has ultrahigh surface area and can be seen therefore as an "ultimate carbon filter". In our communication we report PAH nanostructure nucleation and growth on a single and multi-layer graphene CVD grown on a copper substrate. The PAH deposition was performed by thermal evaporation in vacuum, and resultant morphology of a PAH was studied by means of SEM as a function of time, rate, substrate temperature and graphene thickness. We found that PAH predominantly grows in a form of nanowires which have a good vertical alignment with respect to a graphene plane. It was shown that temperature of a substrate, deposition rate of PAH, and number of graphene layers were the key parameters to control the PAH morphology such as a nucleation density and diameter of PAH nanowires. We relate the orthogonal growth of PAH nanowires to the discotic nature of PAH molecules forming weak VDW interactions with a graphene basal plane and lamella like structures due to favorable face-to-face intermolecular interaction. We envision PAH nanostructures grown on a graphene substrates may help optimize PAH filters.

4:40pm **NS+AS+SS-TuA8 Using Surface Chemistry to Direct the In Situ Synthesis and Placement of Nanowires**, A.A. Ellsworth, J. Yang, Z. Shi, Amy Walker, University of Texas at Dallas

Nanoscale one-dimensional materials, commonly called nanowires, have properties that differ significantly from their bulk counterpart materials, and thus have applications in areas including sensing, energy conversion, electronics and optoelectronics. One of the major challenges in the practical use of nanowires is their integration into complex functional structures in a predictable and controlled way. We have recently introduced two promising new techniques by which to direct the growth of metallic and semiconducting nanowires. ENDOM, or Electroless Nanowire Deposition On Micropatterned substrates, employs electroless deposition (ELD) to form metallic nanowires on substrates. SENDOM, or Semiconductor Nanowire Deposition on Micropatterned surfaces, uses chemical bath deposition (CBD) to deposit semiconductor nanowires. SENDOM and ENDOM are generally applicable to the preparation of metallic, semiconducting, and even insulating nanostructures on many technologically relevant substrates. These techniques have several advantages over existing *in situ* synthesis and placement methods: it is fast, and it does not require expensive lithographic equipment or a clean room.

Using ENDOM or SENDOM we are able to create nanowires that are ultralong (centimeters) and follow complex paths such as a right-angle or a curve. We illustrate ENDOM by deposition of Ni, Cu, Pd and other nanowires on patterned -OH/-CH₃ SAMs. We exploit the different deposition rates electroless deposition of metals using dimethylamine borane (DMAB) on -CH₃ and -OH terminated SAMs to deposit nanowires. We illustrate SENDOM by deposition of CuS nanowires on patterned -COOH/-CH₃ SAMs. In this case, the deposition is controlled by the interaction of thiourea (sulfur source) with the SAM surface. In this paper we discuss the reaction pathways involved in the formation of these nanowires including the nucleation sites and the dependence of the nanowire growth on pH and deposition temperature.

5:20pm **NS+AS+SS-TuA10 Development of New Nanocatalysts through Restructuring of Co₃O₄ Nanorods Anchored with Pt Atoms**, Shiran Zhang, University of Notre Dame, A. Frenkel, Brookhaven National Laboratory, F. Tao, University of Notre Dame

Low-temperature water-gas shift (WGS) reaction is crucial for low-temperature fuel cell technology as it provides a solution for on-board hydrogen purification near operational temperature. Design of catalysts with lower activation energy and higher activity is critical for a practical application. Significant effort has been devoted to development of new WGS catalysts with high activity at low temperatures. Most of them are metal nanoparticles supported on reducible oxides such as CeO₂ or TiO₂.

Here we reported two nanocatalysts, PtCo_n/Co₃O₄ and Pt_mCo_m/CoO_{1-x} that are highly active for low-temperature WGS reaction. They were prepared by restructuring singly dispersed Pt atoms supported on Co₃O₄ nanorods through a controlled reduction. The single dispersion of Pt atoms on cobalt oxide nanorods was confirmed with high-angle annular dark-field scanning transmission electron microscopy (HAADF-STEM). Photoemission features of Co2p and Pt 4d_{5/2} of these catalysts during catalysis were tracked with ambient pressure x-ray photoelectron spectroscopy (AP-XPS) using monochromated Al K α . Coordination environment of Pt atoms was tracked with in-situ extended x-ray absorption fine structure spectroscopy (EXAFS). These ex-situ and in-situ studies show that two new active phases, PtCo_n/Co₃O₄ and Pt_mCo_m/CoO_{1-x} were formed in the temperature ranges of 150 °C - 200 °C and 280 °C - 350 °C in the mixture of 3 Torr CO, 1 Torr H₂O, respectively. The formation of singly dispersed bimetallic sites PtCo_n anchored on Co₃O₄ was confirmed with in-situ EXAFS studies. The formed Pt_mCo_m nanoclusters supported on CoO_{1-x} in the temperature range of 280 °C - 350 °C was identified with HAADF-STEM. Kinetics studies in the gas mixture of carbon monoxide and water vapor with a ratio of 3:1 revealed that activation barriers for PtCo_n/Co₃O₄ at 150-200 °C and Pt_mCo_m/CoO_{1-x} at 150-250 °C are 50.1±5.0 kJ/mol and 29.6±4.0 kJ/mol, respectively. Turn-over frequencies (TOFs) of the two new catalysts PtCo_n/Co₃O₄ and Pt_mCo_m/CoO_{1-x} at 150 °C are larger than those of Pt and Au nanoparticles supported on CeO₂ and TiO₂ catalysts by one magnitude. The excellent activities of the new catalytic phases PtCo_n/Co₃O₄ and Pt_mCo_m/CoO_{1-x} formed through restructuring the singly dispersed Pt atoms on Co₃O₄ suggest a method of developing new catalysts through restructuring singly dispersed catalyst atoms such as noble metals on an oxide support.

5:40pm **NS+AS+SS-TuA11 A Study of Single-Walled Carbon Nanotubes Coated with Iron Oxide (Fe₂O₃) Nanoparticles for Enhanced Magnetic Properties**, Suman Neupane, D. Seifu, Morgan State University
Carbon nanotubes (CNTs) continue to attract significant interest due to their extraordinary thermal, electrical, optical, and mechanical properties. The preparation of CNTs coated with magnetically sensitive Fe₂O₃ nanoparticles

has implications to the development of advanced heat transfer nanofluids and high capacity lithium ion batteries. In this report, single-walled carbon nanotubes (SWNTs) were uniformly coated with Fe₂O₃ nanoparticles through solution mixture. Scanning and transmission electron microscopy were used to compare the surface morphology of pristine SWNTs and as-prepared SWNTs coated with Fe₂O₃ nanoparticles. Raman spectroscopy and thermo gravimetric analysis presented the extent of defects and the amount of Fe₂O₃ nanoparticles present in the sample. Near edge X-ray absorption fine structure spectroscopy was used to probe the electronic band structure of as-prepared core-shell structures. Magnetization measurements indicate that the coercive field of SWNTs coated with Fe₂O₃ nanoparticles was twice that of pristine SWNTs.

One of the authors, D. S., acknowledges funding from ARL W911NF-12-2-0041 and from NSF MRI-DMR-1337339

Surface Science

Room: 309 - Session SS+NS-TuA

Nanostructures: Growth, Reactivity and Catalysis

Moderator: Judith Harrison, United States Naval Academy, Greg Kimmel, Pacific Northwest National Laboratory

2:20pm **SS+NS-TuA1 Building Nanostructured Nanowires via Sequential Catalyst Reactions**, *Frances Ross*, IBM T.J. Watson Research Center **INVITED**

By exposing catalytic nanoparticles to reactive source gases, nanowires can be grown with excellent control over length, diameter, crystal structure and composition. Here we discuss the degree to which this vapour-liquid-solid growth mechanism can be augmented by “programming” a sequence of reactions in the catalyst. Our aim is to produce complex structures in which quantum dots and quantum wells of precise dimensions are incorporated into single nanowires. We supply different species to nanowire catalysts, either as reactive gases or by evaporation, triggering the formation of new phases that become incorporated into the nanowires as they grow. *In situ* transmission electron microscopy allows us to view this process, identify phases and measure kinetics. As an example, we discuss the formation of silicide quantum dots within Si nanowires. Supplying metals such as Co and Ni to catalysts composed of liquid AuSi results in the formation of faceted silicide nanocrystals. These floating nanocrystals subsequently attach at the AuSi/Si interface. Further growth of Si incorporates these quantum dots into the nanowire. We discuss the generality of this phenomenon and the control of silicide structure and dimensions. The formation of narrow quantum wells, such as Ge layers within Si nanowires, can also benefit from understanding the sequential changes in the catalyst. We describe the relationship between catalyst properties and quantum well compositional abruptness, strain and stability. We finally consider the possibilities of combining quantum dots and quantum wells in single nanowires. We suggest that control of reaction pathways within the catalyst provides exciting opportunities for the growth of complex nanostructures.

3:00pm **SS+NS-TuA3 Ar/O₂ and H₂O Plasma Modified SnO₂ Nanomaterials for Gas Sensing Applications**, *Erin Stuckert, E.R. Fisher*, Colorado State University

Tin oxide (SnO₂) is an excellent material for gas sensing applications. The sensing mechanism of SnO₂ is controlled through gas interactions with adsorbed oxygen, which alters the charge flow through the sensing material. By measuring changes in charge flow, sensitivity and selectivity of a gas sensor can be determined. Sensitivity is improved by increasing surface-gas interactions of high surface area materials, SnO₂ nanoparticles and nanowires, combined with surface modification. One surface modification method that can achieve greater oxygen adsorption is plasma treatment; with an expansive parameter space, plasmas allow for greater control of the modification process. In this work, commercial SnO₂ nanoparticles and chemical vapor deposition (CVD)-grown SnO₂ nanowires were plasma modified to create oxygen vacancies with the aim of increasing oxygen adsorption during sensing. Specifically, we employed Ar/O₂ and H₂O plasmas because they can etch materials like SnO₂ to increase oxygen adsorption by creating surface oxygen vacancies. Ar/O₂ plasma treatment of SnO₂ nanoparticles and nanowires showed increasing oxygen adsorption with increasing plasma power and treatment time without changing Sn oxidation state or morphology, as measured by X-ray photoelectron spectroscopy (XPS) and powder X-ray diffraction (PXRD). With low power H₂O plasma treatments, however, greater oxygen adsorption was observed with nearly complete Sn reduction as well as significant morphological changes evidenced in XPS, PXRD, and scanning electron microscopy (SEM). Plasma treated materials were evaluated for their sensitivity and selectivity for a variety of gases including ethanol, formaldehyde, and

benzene. Results for both Ar/O₂ and H₂O plasma treated SnO₂ nanoparticles and nanowires will be presented and discussed with respect to their sensing capabilities, including changes in selectivity and sensitivity.

Keywords:

Plasma treatment

Gas sensor

Tin oxide

Nanowire

Nanoparticle

3:20pm **SS+NS-TuA4 Interaction of D₂O on the Surface Grown ZnO(0001) Nanostructures**, *Xingyi Deng, D.C. Sorescu, J. Lee, C. Matranga*, National Energy Technology Laboratory

D₂O on the ZnO nanostructures grown on Au(111) has been investigated using a combination of experimental and theoretical methods as to probe the reactivity of model ZnO catalysts at the atomic level. We performed a series of D₂O temperature programmed desorption (TPD) experiments on two distinctive surfaces, one consisting of single layer Zn(0001) nanostructures, and the others consisting of mixtures of single and bilayer ZnO(0001) nanostructures. On the basis of our TPD data and in comparison with the ZnO structural characteristics, we are able to assign each D₂O TPD peak to a specific site existing on the ZnO nanostructures. Specifically, desorption peaks at 150 and 200 K are assigned to sublimation of D₂O multilayers and desorption of D₂O adsorbed directly on the ZnO surfaces, respectively; and D₂O adsorbed on the edges of either single or bilayer ZnO desorbs at a slightly higher temperature ~260 K. More importantly, we identify that D₂O binds to the steps between the single and bilayer ZnO much stronger than any other sites, desorbing around 400 K. Computational modeling based on density functional theory (DFT) calculations provides detailed adsorption geometry and energetics of the D₂O-ZnO(0001)/Au(111) system, further supporting our TPD assignments. Implications of our fundamental results for ZnO based catalysts will be discussed.

4:20pm **SS+NS-TuA7 2014 AVS Medard Welch Award Lecture: Quasicrystals to Nanoclusters: It's All on the Surface**, *Patricia Thiel**, Iowa State University **INVITED**

Surface science continues as an exciting frontier—perhaps more so now than in the past—for at least two reasons. First, powerful new tools are emerging, and second, a broad and robust body of knowledge has been established which is serving as a springboard for new breakthroughs, and is critically guiding other fields. In this talk I will present some of the contributions that I and my coworkers have been privileged to make in this field, particularly in the area of quasicrystal surfaces, and in the area of growth and stability of nanoclusters and thin films at surfaces. Metallic quasicrystals have a remarkable atomic structure that engenders unusual properties, including surface properties, and our goal has been to establish the structure-property relationship at the surface. One of our achievements was to show that quasicrystal surfaces are generally bulk-terminated. This laid the groundwork for showing that one of the characteristics of quasicrystals—low friction—derives (at least in part) from the quasiperiodic atomic structure. It also allowed us to understand unusual features of thin film nucleation and growth on these surfaces, and facilitated efforts of other groups to exploit quasicrystals and complex metallic alloys as catalysts. Nucleation and growth of nanoclusters and thin films also shows surprising features on more conventional (crystalline metal) surfaces, and has been a topic of investigation in my group for some time. We discovered that unusual smooth growth at low temperature, and associated non-monotonic temperature dependence of roughness, reflects a process now called “downward funneling”. In addition to non-equilibrium growth morphologies, we have also explored the relaxation of these morphologies towards equilibrium. We found that two-dimensional homoepitaxial metal nanoclusters can diffuse significant distances, leading to coarsening (a reduction in the cluster density) via agglomeration. Nanocluster destabilization and coarsening can also occur via Oswald ripening, but the identity of the mass carriers may not be obvious. The presence of even trace amounts of adsorbates can lead to formation of additive-metal complexes which more efficiently transport mass than metal atoms. We have searched for these complexes under conditions which have rarely been investigated in the past, i.e. very low temperature and very low coverage, with some surprising results.

* Medard W. Welch Award Winner

5:00pm **SS+NS-TuA9 Photodeposited Pt Nanoparticles on Iron Oxide Nanoparticles Supported on Highly Oriented Pyrolytic Graphite**, *Jayde Kwon, J.C. Hemminger*, University of California Irvine

Metal-semiconductor hybrid systems have been of great interest due to their unique photocatalytic properties. In metal-semiconductor hybrid systems, semiconductors are used as light absorbing components. They absorb photons and create electron holes localized at the semiconductor, which are formed by excited electrons that move through the heterointerface. Fe_2O_3 is a promising semiconductor photocatalyst due to its visible light absorption ($E_g = 2.2$ eV), abundance, non-toxicity, and stability against photo corrosion. However, Fe_2O_3 suffers from short hole diffusion length, low electrical conductivity and high rate of electron hole recombination. To overcome these barriers, different transition metals (e.g. Au, Si, Pt) have been deposited on Fe_2O_3 . Particularly, Pt on Fe_2O_3 is an ideal heterogeneous catalyst that has a variety of uses such as photoelectrochemical water splitting and CO oxidation. Importantly, Pt on Fe_2O_3 provides an improvement in photocatalytic properties on the degradation of dyes, such as methylene blue. Although many studies deposit Pt on various forms of Fe_2O_3 (e.g. films, nanorods, and coreshells), Pt nanoparticles on discrete Fe_2O_3 nanoparticles on highly oriented pyrolytic graphite (HOPG) has not been studied. The deposition of Pt on Fe_2O_3 has been studied using various methods such as electrodeposition and solution based synthesis. However, photodeposition of Pt on Fe_2O_3 has not yet been studied. In this work, we demonstrate photodeposition of Pt nanoparticles selectively on Fe_2O_3 nanoparticle arrays formed by physical vapor deposition on HOPG. We find that the Fe_2O_3 nanoparticles are in the range of 7-20 nm in diameter. Ongoing studies of the catalytic properties of these unique materials will be presented.

5:40pm **SS+NS-TuA11 Formation and Stability of and Surface Chemistry on Dense Arrays of Au Nanoclusters on Hexagonal Boron Nitride/Rh(111)**, *M.C. Patterson, Phillip Sprunger, J.R. Frick, Y. Xu*, Louisiana State University, *B.F. Habenicht*, University of California Merced, *R.L. Kurtz*, Louisiana State University, *L. Liu*, Texas A&M University

We have studied the nucleation and growth of Au clusters at sub-monolayer and greater coverages on the h-BN nanomesh grown on Rh(111) by means of scanning tunneling microscopy (STM), X-ray photoelectron spectroscopy (XPS), and density functional theory (DFT). STM reveals that sub-monolayer Au deposited at 115 K nucleates within the nanomesh pores and remains confined to the pores even after warming to room temperature. Whereas there is a propensity of mono-atomic high islands at low temperature, upon annealing, bi- and multilayer Au clusters emerge. Deposition of higher coverages of Au similarly results in Au confined to the nanomesh pores at both 115K and room temperature. XPS analysis of core-level electronic states in the deposited Au shows strong final-state effects induced by restricted particle size dominating for low Au coverage, with indications that larger Au clusters are negatively charged by interaction through the h-BN monolayer. DFT calculations suggest that the structure of the Au clusters transitions from monolayer to bilayer at a size between 30 and 37 atoms per cluster, in line with our experiment. Bader charge analysis supports the negative charge state of deposited Au. Using vibrational EELS, CO and O_2 are used to probe the activity of these gold model catalysts.

6:00pm **SS+NS-TuA12 Collective Multi-Atom Diffusion in Ag/Ge(110) 1D Nanoisland Growth**, *Shirley Chiang, C.H. Mullet*, University of California, Davis, *M.C. Tringides*, Iowa State University and Ames Lab-USDOE, *M.S. van Zijll, B.H. Stenger, E.S. Huffman, D.J. Lovinger, E.C. Poppenheimer*, University of California, Davis

The growth of Ag deposited on Ge(110) was studied with low energy electron microscopy (LEEM) and scanning tunneling microscopy (STM). The LEEM studies showed the formation of long, one-dimensional (1D) multi-height islands over the temperature range 430C-530C. During deposition, the length of the islands increases at a constant rate ($\sim 10^6$ atoms/sec reaching ~ 20 microns) and constant width (100-200nm) for 9ML total deposition. Stochastic diffusion cannot account for these very high island growth rates. When smaller islands decay, the rate is $\sim 2 \times 10^7$ atoms/sec, which is also exceedingly fast, based on the Ag diffusion and detachment barriers. These high rates are not consistent with independent adatom events and imply multi-atom correlated diffusion. Such collective mass transport must be related to the mobility of the wetting layer. STM images show the crystalline structure of the 1D Ag islands and also indicate that the reconstructed regions between the islands consist of bare Ge. These data are corroborated by LEEM IV curves. Together, they confirm that the wetting layer provides the material for the islands to grow at these high rates.

Wednesday Morning, November 12, 2014

2D Materials Focus Topic

Room: 310 - Session 2D+EM+NS+SS+TF-WeM

Novel 2D Materials

Moderator: Evan Reed, Stanford University

8:00am **2D+EM+NS+SS+TF-WeM1 Silicene and Germanene: Novel Graphene-like Artificial Silicon and Germanium Allotropes, Guy Le Lay, Aix-Marseille University, France** **INVITED**

Silicene, graphene's cousin, and germanene, a new born in Terra Plana, are predicted to combine the unique electronic properties of graphene associated to quasiparticles behaving as massless Dirac fermions to a character of two-dimensional topological insulators, and, even, possibly, high temperature superconductors. In this talk, I will present fundamental results on these novel synthetic 2D materials, which do not exist in nature, but which might open the way to practical applications, because of their expected direct compatibility with the current nano/micro electronic technologies.

8:40am **2D+EM+NS+SS+TF-WeM3 Silicon Growth at the Two-Dimensional Limit on Ag(111), Andrew Mannix, B.T. Kiraly, Northwestern University, B.L. Fisher, Argonne National Laboratory, M.C. Hersam, Northwestern University, N.P. Guisinger, Argonne National Laboratory**

Bulk silicon has played a dominant role in the growth of microelectronics over the past 50 years. Considering the immense interest in two-dimensional (2D) materials (e.g., graphene, MoS₂, phosphorene, etc.), the growth of Si in the 2D limit is of high relevance to the evolution of electronic materials. Utilizing atomic-scale, ultra-high vacuum (UHV) scanning tunneling microscopy (STM), we have investigated the 2D limits of Si growth on Ag(111). In agreement with previous reports of *sp*²-bonded silicene,^{1,2} we observe the evolution of ordered 2D phases, which we attribute to apparent Ag-Si surface alloys. At sufficiently high Si coverage, we observe the precipitation of crystalline, *sp*³-bonded Si(111) domains. These domains are capped with a $\sqrt{3}$ honeycomb phase that is indistinguishable from the $\sqrt{3}$ honeycomb-chained-trimer (HCT) reconstruction of Ag on Si(111).^{3,4,5} Additional evidence suggests that silicon intermixing with the Ag(111) substrate is followed by the precipitation of crystalline, *sp*³-bonded silicon nanosheets. These conclusions are supported by *ex-situ* atomic force microscopy (AFM), Raman spectroscopy, and X-ray photoelectron spectroscopy (XPS). Even at the 2D limit, scanning tunneling spectroscopy shows that the *sp*³-bonded silicon nanosheets exhibit semiconducting electronic characteristics.

[1] Vogt, P., *et al.* Silicene: Compelling Experimental Evidence for Graphene-like Two-Dimensional Silicon. *Phys. Rev. Lett.*, 108(15), 155501 (2012).

[2] Feng, B., *et al.* Evidence of silicene in honeycomb structures of silicon on Ag(111). *Nano Lett.*, 12(7), 3507–11 (2012)

[3] Le Lay, G. Physics and electronics of the noble-metal/elemental-semiconductor interface formation: A status report. *Surf. Sci.*, 132(1-3), 169–204 (1983).

[4] Aizawa, H., Tsukada, M., Sato, N., & Hasegawa, S. Asymmetric structure of the Si(111)- $\sqrt{3}\times\sqrt{3}$ -Ag surface. *Surf. Sci.*, 429 (0–5) (1999).

[5] Ding, Y., Chan, C., & Ho, K. Structure of the ($\sqrt{3}\times\sqrt{3}$) R30° Ag/Si(111) surface from first-principles calculations. *Phys. Rev. Lett.*, 67(11), 1454–1458 (1991).

9:00am **2D+EM+NS+SS+TF-WeM4 Growth, Structure, and Properties of 2D SiO₂ Polymorphs, Eric Altman, J. Götzén, X. Zhu, A. Sonnenfeld, U.D. Schwarz, Yale University**

Recently it has been shown that SiO₂ can form closed 2D bilayers; because the layers have no dangling bonds they are expected to interact solely through van der Waals interactions. Despite the expected weak interactions, hexagonal crystalline bilayers on Pd(100) are stretched 4% to match the lattice constant of the substrate. Both electron diffraction and STM reveal that the size of the crystalline domains is limited along Pd[011] and one of the other bilayer close-packed directions but was long along the third one. The formation of regular domain boundaries on the square Pd substrate is attributed to stress relief in the crystalline layer. *Ab initio* calculations indicate that much of the remaining strain energy can be relieved by allowing the film to relax along the incommensurate direction. In this way the square substrate actually aids the templating of the overlayer despite the severe geometric mismatch. The calculations also indicate that the bilayer is surprisingly compliant, explaining the lattice matching despite the weak

interaction and poor match. Amorphous bilayers could also be prepared on Pd(100). Atomic-scale features in STM images of the amorphous film could be associated with 4-9 membered rings of corner-sharing SiO₄ tetrahedra. In addition to the structural heterogeneity, spectroscopic STM imaging revealed electronic heterogeneity with oxygen sites joining larger rings of corner-sharing SiO₄ tetrahedra fading at low bias; spectra revealed two distinct electronic states responsible for this phenomenon. MBE growth of silica bilayers on graphene layers grown on epitaxial Ru on sapphire will also be discussed.

9:20am **2D+EM+NS+SS+TF-WeM5 Layer-dependent Electronic and Vibrational Properties of SnSe₂ and SnS₂ 2D Materials, Joseph Gonzales, R. Schlaf, I.I. Oleynik, University of South Florida**

Layered metal chalcogenides possess a wide range of unique electronic properties, which are currently explored for applications as novel two-dimensional electronic materials. SnS₂ and SnSe₂ layered materials consist of covalently bonded S-Sn-S (Se-Sn-Se) sheets bonded together by weak van der Waals interactions. The atomic, electronic and vibrational properties of SnS₂ and SnSe₂ thin films are investigated using first-principles density functional theory (DFT). The accurate prediction of electronic and optical properties of SnS₂ and SnSe₂ layered 2D materials is achieved by applying state of the art many-body perturbation theory in GW approximation followed by solving the Bethe-Salpeter equation (BSE) to take into account excitonic effects. The evolution of the thickness-dependent band structure, optical and Raman spectra are discussed. The strain effects due to interactions with the substrate are also considered. The first-principles results are compared with available experimental data.

9:40am **2D+EM+NS+SS+TF-WeM6 Synthesis and Properties of Large Scale, Atomically Thin Tungsten Diselenide (WSe₂), Sarah Eichfeld, Y.C. Lin, L. Hossain, The Pennsylvania State University, A. Piasecki, The Pennsylvania State University, A. Azcatti, University of Texas, Dallas, S. McDonnell, R.M. Wallace, University of Texas at Dallas, J.A. Robinson, The Pennsylvania State University**

Transition metal dichalcogenides (TMDs), such as tungsten diselenide (WSe₂) are of interest due to their intriguing properties including the transition from indirect gap to direct gap as the material is thinned to a single atomic layer. Stacking of these layered TMDs also allows for the possibility of bandgap tuning. These properties can suit a large range of flexible and low temperature electronic and optoelectronic devices. Current methods of WSe₂ research involve exfoliation or vaporization of WO₃ and Se powder, which limits industrial scalability. This work is focused on development of a metal-organic chemical vapor deposition process that can controllably produce highly-crystalline, atomically thin WSe₂ on large area substrates.

Growth of controlled monolayer tungsten diselenide (WSe₂) was carried out using chemical vapor deposition in a cold wall vertical reactor. Tungsten hexacarbonyl (W(CO)₆) and dimethylselenium (DMSe) served as the tungsten and selenium precursors, respectively. Use of MOCVD precursors provides a means to independently control the W and Se precursors allowing for more precise control of the individual species during growth. Process variables including temperature (500-950°C), pressure (100-700 Torr), and carrier gas, which were correlated with grain size, growth rate, and nucleation density of the WSe₂ to identify optimal parameters for atomically controlled synthesis. Increasing the growth pressure from 100-700 Torr results in a decrease in growth rate and nucleation density, leading to a >50x increase in grain size. Increased growth temperatures yield an increase in grain size, however, it was found that above temperatures of 800 °C the sapphire substrate begins to decompose in the growth environment, resulting in a degradation of WSe₂ above 800°C. Synthesis using 100% hydrogen, and also hydrogen/nitrogen mixtures was carried out. It was found that 100% hydrogen was necessary in order to achieve low carbon incorporation in the WSe₂ films. Characterization of these samples via Raman and photoluminescence spectroscopy verified that high quality, monolayer WSe₂ is readily achievable. Additional characterization (i.e. scanning electron microscopy, atomic force microscopy, etc.) verify the quality, grain size, and nucleation density of the atomic layers. Finally, we will discuss the impact of substrate choice on the quality of the WSe₂ atomic layers, as well as providing direct evidence that synthesis on graphene results in highly textured films, with nearly 100% commensurability to the underlying graphene.

11:00am **2D+EM+NS+SS+TF-WeM10 Growth of Transition Metal Dichalcogenides and their Alloys and on Flat and Patterned Substrates.** *E. Preciado, A. Nguyen, D. Barroso, V. Klee, S. Bobek, I. Lu, S. Naghibi, G. Von Son Palacio, T. Empante, K. Brown, K. Yang, A. Nguyen, J. Mann, Ludwig Bartels*, University of California - Riverside

The use of organic chalcogen precursors permits the CVD growth of $\text{MoS}_{2(1-x)}\text{Se}_{2x}$ alloys of any composition between pure MoS_2 and MoSe_2 on SiO_2 . Spatially resolved vibrational and photoluminescence (PL) spectroscopy is used to characterize our samples: while we observe a continuous transition of the PL maximum with S: Se ratio, the vibrational modes behave in a more complicated, 2-mode fashion. Depending on growth conditions, compositional homogeneous and heterogeneous films can be prepared.

We present details of our growth processes and show to which extend patterns on the substrates can affect the resultant structures. The patterns range from simple hole and pillar arrays to complex waveguide structures. We find that holes to an underlying reducing substrate (silicon) are effective in seeding growth. In contrast, protrusions on the substrate have little effect, so that complex devices can be overgrown.

Ref: Mann et al., 2-Dimensional Transition Metal Dichalcogenides with Tunable Direct Band Gaps: $\text{MoS}_{2(1-x)}\text{Se}_{2x}$ Monolayers, *Advanced Materials* 26, 1399 (2014)

11:20am **2D+EM+NS+SS+TF-WeM11 Synthesis, Characterization and Radiation Response of Boro-Carbon-Oxy-Nitride: A Heterogeneous 2D Material.** *GaneshRahul Bhimanapati, M. Wetherington, M. Kelly, J.A. Robinson*, The Pennsylvania State University

Since graphene, there have been many other two-dimensional materials systems (e.g., boron nitride (hBN), borocarbon nitride (BCN), transition-metal dichalcogenides) that provide an even wider array of unique chemistries and properties to explore future applications. In fact, these other 2D materials, are sometimes far better suited for many optoelectronic and mechanical applications. Specifically, tailoring graphene/boron nitride heterostructures, which retain the character of single-atom thick sheets that can withstand large physical strains, are easily functionalized, and have entirely different optical and mechanical properties compared to graphene can provide the foundation for entirely new research avenues. In recent years, it has been shown that because of the similar crystal structure, carbon, boron, and nitrogen can coexist as atomic sheets in a layered structure. Thus, combining these materials to form a new heterogeneous material system known as boro-carbon-oxy-nitride (BCON) for potential nano-mechanical and electronic applications and to study its fundamental property relations is necessary. Here, we present the fundamental property relations of BCON and its structural response to various radiation sources such as alpha, beta and gamma particles thereby providing a means for potential radiation sensing applications.

We have developed a facile method of integrating boron nitride and graphene oxide (GO) via chemical exfoliation. Chemical exfoliation of graphene oxide and boron nitride powders is accomplished via oxidation in strong acids, as we find previous methods of sonication in polar solvents does not yield stable solutions of hBN. Upon exfoliation, GO and hBN are mixed, and the resulting BCON material can be suspended in DI water, with suspension stability depending on the pH of the GO. The study of the stability of this material at different pH conditions indicates a stable and a uniform solution is achievable at pH 4-7. Fourier transform infrared spectroscopy (FTIR) indicates the B-N-B bending in the BCON is decreased as an effect of parent GO. Further, radiation response of this material to various radiation sources such as alpha, beta and gamma radiation are studied using In-Situ X-Ray Photoelectron Spectroscopy (XPS). The structural changes of carbon 1s peak in the BCON even for very low doses of radiation energy indicate potential applications in radiation sensing.

11:40am **2D+EM+NS+SS+TF-WeM12 The Structure of 2D Glass.** *Christin Büchner*, Fritz-Haber-Institut der Max-Planck-Gesellschaft, Germany, *L. Lichtenstein*, Lawrence Berkeley National Laboratory, *M. Heyde, H.-J. Freund*, Fritz-Haber-Institut der Max-Planck-Gesellschaft, Germany **INVITED**

For the first time, the structure of an amorphous network is imaged in real space.[1] Through a thin film approach, silica is made accessible for investigation with scanning tunneling microscopy (STM) and atomic force microscopy (AFM). Physical vapor deposition with subsequent annealing is employed to create an atomically flat bilayer of SiO_2 , supported on a Ru(0001) single crystal. Atomic positions of oxygen and silicon can be visualized, as well as ring structures with their distributions and local neighborhoods. All atomic species on the surface can be directly assigned with chemical sensitivity imaging.[2] This allows for statistical analysis of the building units, comparing amorphous to crystalline regions, as well as experiment to theory. Pair correlation functions of the 2D film structure are

set against diffraction data of bulk silica, revealing very similar bond distributions.

Coexisting crystalline and amorphous areas allow imaging of a topological transition region.[3] The understanding of glassy structures gained from these experiments is the starting point for more in-depth structural investigations[4], but also for investigating thin films with modified composition. Al-doping or Fe-doping can be employed to create 2D-Aluminosilicates or 2D-Clays, respectively.[5] Adsorption properties of the film can be probed using single metal atoms which migrate through the film, exhibiting ring-size-selectivity.[6]

[1] L. Lichtenstein, et al., *Angew. Chem., Int. Ed.* 51, 404 (2012)

[2] L. Lichtenstein, et al., *J. Phys. Chem. C* 116, 20426 (2012)

[3] L. Lichtenstein, et al., *Phys. Rev. Lett.* 109, 106101 (2012)

[4] C. Büchner, et al., *Z. Phys. Chem.*, DOI: 10.1515/zpch-2014-0438 (2014)

[5] J. A. Boscoboinik, et al., *Angew. Chem. Int. Ed.* 51, 6005 (2012)

[6] W. E. Kaden, et al., *Phys. Rev. B* 89, 115436 (2014)

Nanometer-scale Science and Technology

Room: 304 - Session NS-WeM

Nanoscale Catalysis and Surface Chemistry

Moderator: Jeremy Robinson, Naval Research Laboratory

8:00am **NS-WeM1 Single Atom Alloys as a Strategy for Selective Heterogeneous Hydrogenations.** *Charles Sykes*, Tufts University **INVITED**

Hydrogenation reactions are central to the petrochemical, fine chemical, pharmaceutical, and food industries and are of increasing interest in energy production and storage technologies. Typical heterogeneous catalysts often involve noble metals and alloys based on platinum, palladium, rhodium and ruthenium. While these metals are active at modest temperature and pressure, they are not always completely selective and are expensive. We have demonstrated that single palladium atoms can convert the otherwise catalytically inert surface of an inexpensive metal into an ultrasensitive catalyst. We used high resolution imaging to characterize the active sites and temperature programmed reaction spectroscopy to probe the chemistry. The mechanism involves facile dissociation of molecular hydrogen at individual palladium atoms followed by spillover onto the copper surface, where ultrasensitive catalysis occurs by virtue of weak binding. The reaction selectivity is in fact much higher than that measured on palladium alone, illustrating the unique synergy of the system.

8:40am **NS-WeM3 In Situ FTIR Spectroscopic Observation of the Formation of Gold Ketonylidene during Carboxylic Acid Oxidation on a Au/TiO₂ Nanoparticle Catalyst.** *Monica McEntee, W. Tang, M. Neurock, J.T. Yates, Jr.*, University of Virginia

Gold nanometer diameter particles supported on reducible oxide supports exhibit catalytic activity at temperatures as low as 90 K.[1] Numerous studies[2-4] have theorized that the catalytic activity occurs at the metal-support interfacial sites. In 2011, Green *et al.*[5] discovered, using infrared (IR) spectroscopy, a dual catalytic site for molecular oxygen adsorption and subsequent activation with one O atom bonded to the Au and the other O bonded to the Ti^{4+} site of the TiO_2 support. Here I show, using IR spectroscopy and density functional theory (DFT), the oxidation of three carboxylic acids (acetic, propionic and butyric acid) on a Au/TiO₂ catalyst with ~3 nm diameter Au nanoparticles producing gold ketonylidene, $\text{Au}_2\text{C}=\text{C}=\text{O}$, species. The initial step in all three acid oxidation processes is the dissociation of O_2 at the Au- Ti^{4+} dual site to form reactive O adatoms at the interface. Next, in sequential steps, α -CH and β -CH bonds specifically next to the COO group in each acid are oxidatively dehydrogenated to produce unsaturated, C=C, species. C-C and C-O bond scission occur next yielding adsorbed ketonylidene, $\text{Au}_2\text{C}=\text{C}=\text{O}$, an exotic species formed just before full oxidation. Control oxidation experiments on the TiO_2 support alone produce no $\text{Au}_2\text{C}=\text{C}=\text{O}$ species verifying the reaction occurs at the Au/TiO₂ interface. Also, isotopically-labelled O_2 and acid experiments confirm the $\text{Au}_2\text{C}=\text{C}=\text{O}$ is composed of specifically α -C and β -C atoms and O atoms from the acid.

References

1. Haruta, M.; Kobayashi, T.; Sano, H.; Yamada, N. Novel gold catalysts for the oxidation of carbon monoxide at a temperature far below 0 °C. *Chem. Lett.* **1987**, 405-408.

2. Rodriguez, J.; Ma, S.; Liu, P.; Hrbek, J.; Evans, J.; Perez, M. Activity of CeO_x and TiO_x nanoparticles grown on Au (111) in the water-gas shift reaction. *Science* **2007**, *318*, 1757-1760.
3. Molina, L.; Rasmussen, M.; Hammer, B. Adsorption of O₂ and oxidation of CO at Au nanoparticles supported by TiO₂(110). *J. Chem. Phys.* **2004**, *120*, 7673.
4. Camellone, M. F.; Zhao, J.; Jin, L.; Wang, Y.; Muhler, M.; Marx, D. Molecular Understanding of Reactivity and Selectivity for Methanol Oxidation at the Au/TiO₂ Interface. *Angew. Chem., Int. Ed.* **2013**, *52*, 5780 – 5784.
5. Green, I. X.; Tang, W.; Neurock, M.; Yates Jr., J. T. Spectroscopic observation of dual catalytic sites during oxidation of CO on a Au/TiO₂ catalyst. *Science* **2011**, *333*, 736-739.

9:00am NS-WeM4 Fabrication and Photocatalytic Activity of Metal-loaded TiO₂ Nanometer Scale Particles, Paolo Reyes, Y. Liu, J.C. Hemminger, University of California Irvine

We will describe methods to generate TiO₂ nanoparticles supported on HOPG substrates. We then utilize photoelectrochemical deposition to selectively decorate the TiO₂ particles with metal nanoparticles. These samples are easily amenable to characterization with SEM and TEM imaging as well as electron spectroscopy surface analysis methods. The introduction of noble metals adsorbed on TiO₂ substrates can affect the intrinsic catalytic properties of the metal oxide, however previous research has been focused on single species of adsorbed noble metals (e.g. Pt, Au, Co, etc.) and the result impact on the photocatalytic activity. Typical effects from noble metals include lowering the band-gap requirement of TiO₂ (3.2 eV) in order for electron excitation from the valence band to the conduction band to occur. Our current research focuses on the fabrication and study of two or more noble metal nanoparticle species loaded onto TiO₂ particle arrays and to observe the impact on the catalytic activity, chemistry, electromagnetic field enhancements. The presence of two or more noble metal species may affect the catalytic properties of TiO₂ in interesting ways, such as Au nanoparticles allowing visible light to be absorbed, and Pt particles allowing more efficient photo-chemistry in degrading pollutants. In this work, we photodeposit Pt and Au particles onto TiO₂ particles situated on highly oriented pyrolytic graphite (HOPG). Au and Pt particles are found to be on average 4.7 nm in diameter. Preliminary experiments on bi-metallic loaded particles have been conducted in order to study photocatalytic properties via pollutant degradation rate. Methylene Blue (MB), a common organic dye, is used to observe photocatalytic activity of these particles through UV-induced photo-degradation. Bare TiO₂ particles are known to be photoactive, however the introduction of noble metal species show an increase of MB degradation over time. We are currently observing MB degradation rates with dual-loaded TiO₂ nanoparticles. Previous work in our group has proven that polarized Raman spectroscopy performed on Ag nanoparticle arrays yields a significant increase in signal

1. Wei Luo, W. Van der Veer, P. Chu, D. L. Mills, R. M. Penner, and J.C. Hemminger, *Journal Of Physical Chemistry C*, 2008. : p. 11609-11613.

This work is supported by the U.S. Department of Energy, Office of Basic Energy Sciences through grant number: DE-FG02-96ER45576

9:20am NS-WeM5 Size-dependent Trends in CO and O₂ Adsorption on Pd Nanoparticle Catalysts, Hemma Mistry, L.K. Ono, University of Central Florida, B. Roldan Cuenya, Ruhr-University Bochum, Germany

Due to the striking dependence of many catalytic reactions on particle size and shape, a thorough understanding of structure-dependent reactivity trends in the interaction of adsorbates with model nanoparticles (NPs) is key to designing highly active and selective catalysts. Palladium NPs are highly active for important reactions such as CO oxidation and methane combustion. However, conflicting reports exist in the literature on the change in CO and O₂ adsorption strength on Pd NPs of different size. In this study, temperature programmed desorption (TPD) was used to investigate the binding strength of O and CO on Pd NPs supported on SiO₂/Si(111). A range of clusters with Pd deposition thicknesses between 1.5 and 15 Å were investigated and compared to Pd(111). Our results indicate that both O and CO binding strength increase dramatically with decreasing particle size, and the presence of distinct binding sites on the smaller NPs was revealed by CO TPD.

9:40am NS-WeM6 Mixed Structures of CO and H on Ru(0001) as Precursor States for Fischer-Tropsch Synthesis, Barbara Lechner, X. Feng, S. Carenco, Lawrence Berkeley National Laboratory, P.J. Feibelman, Sandia National Laboratories, M.B. Salmeron, Lawrence Berkeley National Laboratory

The Fischer-Tropsch reaction is of great importance in the industrial synthesis of hydrocarbon fuels and as such has motivated a large number of studies on the microscopic processes underlying the reaction. However,

while the adsorption and interaction of the two reactants, carbon monoxide and hydrogen, on model catalyst surfaces has been investigated in detail for decades, several fundamental questions still remain, in particular that of the nature of the precursor species [1]. In addition, CO and H have been shown to segregate into different domains on single crystal surfaces [2-4], raising the question whether the reaction only takes place at the interface of these domains.

Here we investigate the co-adsorption of CO and H on Ru(0001) using scanning tunneling microscopy (STM), X-ray photoelectron spectroscopy (XPS) and density functional theory calculations with the goal of a more detailed understanding of the forces driving the formation of the precursor state in the Fischer-Tropsch reaction. CO and H co-adsorbed at 77 K show a largely unordered structure in STM, while subsequent annealing to 150-300 K results in dense CO islands compressed and separated by H atom regions that decrease in size with increasing annealing temperature. Unexpectedly, further annealing to 300-350 K gives rise to a mixed phase of CO and H in a 1:1 ratio. XPS measurements confirm a change in bonding geometry upon annealing. We believe that studying the transition from a segregated to a mixed phase is an important step toward tracing the microscopic reaction pathway.

[1] R. A. van Santen, A. J. Markvoort, I. A. W. Filot, M. M. Ghouri, E. J. M. Hensen, *Phys.Chem. Chem. Phys.* **15**, 17038 (2013).

[2] D. E. Peebles, J. A. Schrefels, J. M. White, *Surf. Sci.* **116**, 117 (1982).

[3] B. Riedmuller, D. C. Papageorgopoulos, B. Berenbak, R. A. van Santen, A. W. Kleyn, *Surf. Sci.* **515**, 323 (2002).

[4] I. M. Ciobica, A. W. Kleyn, R. A. van Santen, *J. Phys. Chem. B* **107**, 164 (2003).

11:00am NS-WeM10 In Situ Investigation of Oxidation State and Reactivity of a Cu Model Catalyst by Simultaneous Mass Spectrometry and Indirect Nanoplasmonic Sensing, Hans Fredriksson, H.J.W. Niemantsverdriet, Eindhoven University of Technology, Netherlands

The activity of a catalyst depend on a wide range of factors such as elemental composition, particle dispersion and the oxidation state of the active material. All of these properties can change during operation, reversibly or irreversibly, thereby severely influencing the catalysts performance. It is therefore of great importance to learn how the fundamental properties of a catalyst change during use and to correlate these changes with changes in activity and selectivity. This requires simultaneous, in-situ measurements of both fundamental catalyst properties and activity, a far from trivial task. Here we present a novel quartz-tube micro flow-reactor in which optical spectroscopy and mass spectroscopy can be performed simultaneously. The optical setup is based on indirect nanoplasmonic sensing, which utilizes the localized surface plasmon resonances of Au-discs embedded in Si₃N₄ to detect subtle changes in the oxidation state of a material. We investigate CO-oxidation on a model catalyst consisting of Cu nanoparticles formed by thin film evaporation and subsequent annealing. From these measurements we demonstrate the correlation between oxidation state of the Cu-catalyst and onset temperature for CO₂ formation in gas mixtures with various CO/O₂ ratios. The changes in oxidation state were then confirmed by XPS.

11:20am NS-WeM11 Controlling Surface Reactivities of TiO₂ (110) by Nanoscale Strain Field, Zhisheng Li, D.V. Potapenko, R.M. Osgood, Columbia University

Strain is found to be an ubiquitous quantity in nanostructured surfaces and on supported catalysts. Therefore, understanding the influence of strain on surface properties is crucial for rational design of catalytic materials. The study of the interaction of nanoscale strain and adsorbate reactivity presents two experimental challenges, generating an intense strain field and differentiating strain effects from effects induced by change in other surface properties. In this work, we generate a patterned, nanoscale strain field on TiO₂ (110) surface by low energy bombardment of single crystal TiO₂ samples with argon ions at 1000°C. The interstitial argon diffuses so as to self-assemble into highly pressurized argon clusters and distort the surrounding lattice a few nanometers below the surface. As a result, the top surface layers of the crystal have a convex morphology while retaining their unstressed surface structures, thus introducing nanometer-size surface protrusions. The strain level obtained on the protrusions can be as large as ~4%. The locally varying strain field across the protrusion is ideal for strain effects study. By combining scanning tunneling spectroscopy (STM) imaging and continuum model, we show that the adsorption energy of hydrogen binding to surface bridge-bonded oxygen (BBO) is significantly altered by local lattice strain. In particular, strain causes oxygen vacancies (BBOv) to be absent from the strained area. Our results thus provide direct evidence of the influence of strain on atomic-scale surface properties and thus help guide future research in catalysis materials design

11:40am **NS-WeM12 NSTD Recognition Award Lecture: Probing Local Optoelectronic Properties of Porphyrin-Gold Molecular Interfaces with STM/STS**, *X. Chen, E.H. Morales, T.-H. Park*, University of Pennsylvania, *M.J. Therien*, Duke University, **Dawn Bonnell***, University of Pennsylvania

INVITED

Porphyrin molecules are a group of organic compounds that exist extensively in natural biological systems, and they manifest rich electronic and photonic properties, raising the possibility of optoelectronic device applications. In this research thiolated Zinc-porphyrin oligomer molecules were linked to Au(111) surface in a vertical device configuration, embedded within an alkanethiol self-assembled monolayer. Spectroscopic measurements were done to determine the electronic orbital structures of different Zinc-porphyrin oligomer single molecules via scanning tunneling microscope. With lasers of different wavelength coupled to the tunneling junction, both ground state and excited state electronic orbital structures of Zinc-porphyrin single molecule were measured.

* NSTD Recognition Award

Wednesday Afternoon, November 12, 2014

2D Materials Focus Topic

Room: 310 - Session 2D+AS+EM+MI+MN+NS+TF-WeA

Properties of 2D Materials

Moderator: Guy Le Lay, Aix-Marseille University

2:20pm **2D+AS+EM+MI+MN+NS+TF-WeA1 Tuning Excitons in Two-Dimensional Semiconductors**, Kirill Bolotin, Vanderbilt University
INVITED

Monolayer molybdenum disulfide (MoS₂) is a two-dimensional crystal comprising a single layer of molybdenum atoms sandwiched between two layers of sulfur atoms. Monolayer MoS₂ differs from its celebrated all-carbon cousin, graphene, by the presence of a direct band gap leading to robust light absorption and by strong electron-electron interactions leading to formation of rightly bound excitons. In this talk, we demonstrate that both electrical and optical properties of MoS₂ can be widely tuned via external influences.

In the first part of the talk, we study changes in the bandgap and phonon spectra in strained MoS₂. We investigate the transition from direct to indirect band gap in MoS₂ under uniaxial strain. The experimental signatures of this transition include strain-induced changes in the PL wavelength and intensity.

Second, we examine the influence of the environment of MoS₂ on its properties. We demonstrate substrate-induced scattering is suppressed in suspended MoS₂ specimens. We use photocurrent spectroscopy to study excitons in pristine suspended MoS₂. We observe band-edge and van Hove singularity excitons and estimate their binding energy. We study dissociation of these excitons and uncover the mechanism of their contribution to photoresponse of MoS₂.

3:00pm **2D+AS+EM+MI+MN+NS+TF-WeA3 Electron-Phonon Coupling and Photoluminescence in Single Layer Transition Metal Dichalcogenides**, Neha Nayyar, V. Turkowski, D.T. Le, T.S. Rahman, University of Central Florida

Single layer MoS₂ and other transition metal dichalcogenides have been the subject of numerous investigations because of their unusual optical, electronic and transport properties. To understand and thereby tune their photoluminescent properties, we have analyzed the role of electron-phonon interactions. Density functional perturbation theory is used to calculate the dispersion of system phonons, while electron-phonon coupling is obtained using the Eliashberg approach. Time-dependent density-functional theory based calculations using the density-matrix approach is employed to study the exciton and trion excitations which are found to appear as peaks in the absorption spectrum in the visible range with binding energy ~0.5 – 1 eV and ~0.02-0.03 eV, correspondingly. The emission peak is found to also lie in the visible spectrum and is sensitive to the value of the electron-phonon coupling, which depends on the nature and extent of doping. The position of the spectral peaks may thus be manipulated by doping. Calculations of the self-energy and spectral functions of doped systems show excitations to have 10-100 fs lifetime, which makes the system interesting for ultrafast applications. Comparison will be made of these optical properties of several single layer dichalcogenides and contact will be made with available experimental data. Work supported in part by DOE Grant No. DOE-DE-FG02-07ER46354

3:20pm **2D+AS+EM+MI+MN+NS+TF-WeA4 Temperature Dependent Photoluminescent Spectroscopy of MoS₂**, Michael Watson, J.R. Simpson, Towson University & NIST, R. Yan, H. Xing, University of Notre Dame, S. Bertolazzi, J. Brivio, A. Kis, EPFL, Switzerland, A.R. Hight-Walker, NIST

We report temperature and power dependent photoluminescence (PL) of molybdenum disulfide (MoS₂). Mechanical exfoliation of MoS₂, from bulk provides single-layer flakes which are then transferred either to sapphire substrates or suspended over holes in Si/SiO₂. We measure temperature dependence from ~100K to 400K and power dependence from ~6μW to ~7mW using an Argon laser at 514.5nm and a HeNe laser at 632.8 nm. The PL spectrum exhibits a main excitonic peak(A) at ~1.87eV which consist of both neutral excitons and charged trions (A⁻ or A⁺) [1]. The A exciton peak and the A⁻ exciton peak redshift and broaden with increasing temperature and power. Along with the A peak, we observe a lower energy bound exciton (BE) that is likely related to defects. The BE, a broad peak centred at ~1.7eV, linearly redshifts and narrows with increasing power. The power dependence of both the main and bound peak saturates above 0.5mW. Raman temperature and power dependence will also be discussed [2].

[1] K.F. Mak et al. Nat. Mat 12,207(2013)

[2] R.Yan and J.R.Simpson, S. Bertolazzi and J. Brivio, M. Watson, X.Wu and A. Kis, T.Luo, H.G.Xing, A.R. Hight Walker, ACS Nano 8,1 (2013)

4:20pm **2D+AS+EM+MI+MN+NS+TF-WeA7 Effects of Dimensionality on the Raman and Photoluminescence Spectra of and TaSe₂ and TaS₂ Dichalcogenides**, Danilo Romero, University of Maryland, College Park, M. Watson, J.R. Simpson, Towson University, H. Berger, Ecole Polytechnique Federale de Lausanne, Switzerland, A.R. Hight Walker, NIST

We investigate the effects dimensionality on the electronic properties through the optical spectra of the transition-metal dichalcogenides 2H-TaSe₂ and 1T-TaSe₂, and 1T-TaS₂. In bulk, these materials exhibit electronic states from Mott insulator, commensurate and incommensurate charge-density phases, and superconducting ground state as function of temperature. We explore the evolution of these properties as the materials approach a few layers, achieved via mechanical exfoliation of bulk single-crystals. Raman and photoluminescence spectroscopy of 2H-TaSe₂ and 1T-TaSe₂, and 1T-TaS₂, carried out over a wide-range of temperature, were used as a probe of the change of the electronic properties from the bulk to single-layer phases of the materials. Comparison of the phonon and excitonic transitions as a function of temperature and dimensionality will be presented.

4:40pm **2D+AS+EM+MI+MN+NS+TF-WeA8 Few-Layer and Symmetry-Breaking Effects on the Electrical Properties of Ordered CF₃Cl Phases on Graphene**, Josue Morales-Cifuentes, T.L. Einstein, Y. Wang, J. Reutt-Robey, University of Maryland, College Park

An effective potential mechanism for breaking the inherent sublattice symmetry of graphene has been studied using DFT calculations on hexagonal boron nitride.¹ Electrical detection of CF₃Cl phase transitions on graphene shows the existence of a commensurate ordered phase in which this can be tested.² We study the electronic properties of similar phases varying coverage and orientation of CF₃Cl with respect of the graphene substrate using VASP ver 5.3.3, with ab initio van der Waals density functionals (vdW-DF1, vdW-DF2).^{3,4} Consistent with a physisorbed phase, binding energies are calculated to be on the order of 280meV, and insensitive to coverage and orientation of the CF₃Cl molecules. Charge transfer was calculated to be sensitive with coverage, but not orientation, which is qualitatively consistent with experiment. For low coverages, sublattice symmetry breaking effects are responsible for gap openings in the order of 4meV, whereas for large coverages it is the formation of ordered overlayers that opens gaps of 15meV. Furthermore, in bilayer graphene at low coverage we estimate an enhanced gap of 20meV.

[1] Gianluca Giovannetti et al. , PRB **76**, 073103(2007)

[2] Yilin Wang et al. , APL **103**, 201606 (2013)

[3] Jiri Klimes et al. , PRB **83**, 195131 (2011)

[4] Kyuho Lee et al. , PRB **82**, 081101(R) (2010)

5:00pm **2D+AS+EM+MI+MN+NS+TF-WeA9 Optical Anisotropies in Layered Nanomaterials**, Jon Schuller, UC Santa Barbara
INVITED

In nanomaterials optical anisotropies reveal a fundamental relationship between structural and optical properties. In layered materials, optical anisotropies may result from in-plane and out-of-plane dipoles associated with intra- and inter-layer excitations respectively. In this talk, I describe a novel method wherein we resolve the orientation of luminescent excitons and isolate photoluminescence signatures from distinct intra- and inter-layer excitations, respectively. We compare photoluminescence anisotropies in materials with weak or strong interlayer coupling, MoS₂ and the organic semiconductor PTCDA respectively. We demonstrate that photoluminescence from MoS₂ mono-, bi- and trilayers originates solely from in-plane excitons, whereas PTCDA supports distinct in-plane and out-of-plane exciton species with different spectra, dipole strengths and temporal dynamics. The insights provided by this work are important for understanding fundamental excitonic properties in layered nanomaterials and designing optical systems that efficiently excite and collect light from exciton species with different orientations.

5:40pm **2D+AS+EM+MI+MN+NS+TF-WeA11 Mechanical Properties of 2D-Materials**, J.M. Gonzales, University of South Florida, R. Perriot, Los Alamos National Laboratory, Ivan Oleynik, University of South Florida

Graphene and other two-dimensional (2D) materials possess extraordinary mechanical properties, which are currently being explored in various novel applications. Atomic force microscopy (AFM) nanoindentation experiments

on both pristine and polycrystalline samples of 2D materials, while being successful in measuring overall mechanical performance of graphene, require some theoretical input to extract the important mechanical properties. Large-scale atomistic molecular dynamics simulations are used to predict the mechanical properties of 2D materials, such as the elastic moduli, breaking strength, stress/strain distributions, and mechanisms of fracture under conditions of AFM nanoindentation experiments. Perfect, defective, and polycrystalline samples are investigated using large-scale molecular dynamics simulations with a screened environment-dependent bond order (SED-REBO) potential. The mechanisms of crack propagation in both perfect and defective samples will also be presented.

6:00pm **2D+AS+EM+MI+MN+NS+TF-WeA12 Mechanical Control of Structural Phase Transitions in Two-Dimensional Mo- and W-Dichalcogenide Monolayers**, *Evan Reed, K.-A.N. Duerloo, Y. Li*, Stanford University

Mo- and W- dichalcogenide compounds have a two-dimensional monolayer form that differs from graphene in an important respect: it can potentially have more than one crystal structure. Some of these monolayers exhibit tantalizing hints of a poorly understood structural metal-to-insulator transition with the possibility of long metastable lifetimes. If controllable, such a transition could bring an exciting new application space to monolayer materials beyond graphene. Here we discover that mechanical deformations provide a route to switching the thermodynamic stability between a semiconducting and a metallic crystal structure in these monolayer materials. We employ density functional and hybrid Hartree-Fock/density functional calculations including vibrational energy corrections to discover that single layer MoTe₂ is an excellent candidate phase change material. We identify a range from 0.3% to 3% for the tensile strains required to transform MoTe₂ under uniaxial conditions at room temperature. We elucidate the appropriate thermodynamic constraints for monolayers, which can differ from bulk materials. The potential for mechanical phase transitions is predicted for all six studied compounds. The potential application space ranges from catalysis to information storage and nanoscale electronics.

In-Situ Spectroscopy and Microscopy Focus Topic
Room: 313 - Session IS+2D+MC+NS+SP+SS-WeA

In-Situ Scanning Microscopy

Moderator: Markus Ammann, Paul Scherrer Institut

2:20pm **IS+2D+MC+NS+SP+SS-WeA1 In Situ Studies of Model Fuel Cells**, *Zhi Liu*, Lawrence Berkeley National Laboratory **INVITED**

The ambient pressure x-ray photoelectron spectroscopy (AP-XPS) endstations based on differentially pumped electron energy analyzers have been recognized by scientific communities as an important in-situ tool to study water, environmental science, catalysis and many other important fields. Multiple new AP-XPS endstations are currently under planning or development at US and international synchrotron light sources. Recently we have installed a new hard x-ray AP-XPS endstation at ALS Beamline 9.3.1 (2.5keV- 5keV). By using X-ray up to 5KeV, we can perform AP-XPS at a pressure up to 110 torr. The probing depth of photoelectrons also increases to >10 nm, which will allow us to study not only the gas/solid interface but also the liquid/solid interface. In this talk, I will give an overview of science projects at ALS BL9.3.2 in heterogeneous catalysis and electro-chemistry using these new systems. Furthermore, I will present results of our in-situ study on the electrolyte/electrode interface of a working model electrochemical cell at ALS BL9.3.1. We believe the successful development of soft and hard X-ray APXPS endstations will provide energy research community a powerful in-situ tool to directly study the electrolyte/electrode interface of many important electrochemical devices.

3:00pm **IS+2D+MC+NS+SP+SS-WeA3 Probing of Nanoscale Objects in Reactive Liquids through Membranes using Near-Field Microwave Microscopy**, *Alexander Tselev*, Oak Ridge National Laboratory, *A. Komakov*, National Institute of Standards and Technology (NIST)

Many functional objects (and interfaces) have to be studied in situ when the object is immersed in liquid environment. In addition, for energy, chemical, (bio-) medical and other applications, there is a need to study the encapsulated objects, which otherwise can be chemically reactive or toxic. These samples are often mesoscopically small or exist in minuscule quantities. Recently, we have developed a process for preparation of liquid-filled cells sealed with ultrathin membranes. Such cells can be implemented for in-situ studies using, for example, electron or soft x-ray microscopy due to a high transparency of these membranes to electron beams. However, in many cases electron microscopy is an invasive technique due to various

electron beam induced parasitic effects (e.g. radiolysis or beam induced deposition). To overcome these impediments, we demonstrate the scanning microwave impedance microscopy (sMIM) to image different nanoscale objects immersed in the liquid environment through 30 nm SiN membranes. In the sMIM, microwaves of a frequency of 3 GHz are sent through a coaxial cable connected to a shielded cantilever probe fully compatible with an AMF microscope. The sharp probe tip provides "focusing effect" for the electric component of the microwave. For imaging, the tip is brought into gentle mechanical contact with a membrane. Amplitude and phase of microwaves reflected from the probe are monitored. Since the wave reflection is dependent on the tip-sample system impedance, reflected waves carry information about sample local properties. The effective distance into the sample depth, where the tip-induced field enhancement takes place, is approximately equal to the tip apex radius. Since the membrane thickness is smaller compared to the tip radius of a typical probe (about 50 nm for a fresh tip), the tip-sample impedance is dependent on the dielectric properties of the material beneath membrane, and therefore, it is possible to "see" through the membrane. We demonstrate imaging of different combinations of model liquids and nanoparticles: water and water-based solutions ($\epsilon \sim 80$), organic solvents ($\epsilon \sim 10-25$), and oils ($\epsilon \sim 2-3$) containing Ni metal, polystyrene ($\epsilon \sim 2.5$) and PbO ($\epsilon \sim 25$) particles. This technique can be further implemented for a broad range of objects in confined liquids, and can be used to monitor interfacial electrochemical reactions. Imaging with sMIM was performed at CNMS, which is sponsored at ORNL by the SUFD, BES, US DOE.

4:20pm **IS+2D+MC+NS+SP+SS-WeA7 Caught in the Act! Live Observations of Catalysts Using High-Pressure Scanning Probe Microscopy**, *Irene Groot*, Huygens-Kamerlingh Onnes Laboratory, Leiden University, Netherlands **INVITED**

Recently it has become clear that essential differences can exist between the behavior of catalysts under industrial conditions (high pressure and temperature) and the (ultra) high vacuum conditions of traditional laboratory experiments. Differences in structure, composition, reaction mechanism, activity, and selectivity have been observed. These observations indicated the presence of the so-called pressure gap, and made it clear that meaningful results can only be obtained at high pressures and temperatures. However, most of the techniques traditionally used to study catalysts and their reactions were designed to operate under (ultra) high vacuum conditions. To bridge the pressure gap, the last years have seen a tremendous effort in designing new instruments and adapting existing ones to be able to investigate catalysts *in situ* under industrially relevant conditions.

This talk focuses on the development of scanning probe microscopy for *operando* observations of active model catalysts. In our group, we have developed set-ups that combine an ultrahigh vacuum environment for model catalyst preparation and characterization with a high-pressure flow reactor cell, integrated with either a scanning tunneling microscope or an atomic force microscope. With these set-ups we are able to perform atomic-scale investigations of well-defined model catalysts under industrial conditions. Additionally, we combine the structural information from scanning probe microscopy with time-resolved mass spectrometry measurements on the gas mixture that leaves the reactor. In this way, we can correlate structural changes of the catalyst due to the gas composition with its catalytic performance.

This talk highlights a short overview of the instruments we developed and illustrates their performance with results obtained for different model catalysts and reactions. As a proof of principle, results for the fruit fly of surface science, *i.e.* CO oxidation, will be shown. But additionally, results for more complex reactions such as NO reduction, Fischer-Tropsch synthesis, desulphurization, and production of chlorine will be discussed.

5:00pm **IS+2D+MC+NS+SP+SS-WeA9 X-ray Photoelectron Spectroscopy Studies of H₂O Dissociation on Pre-oxidized Al (111) and Cu (111) Single Crystal Surface**, *Qianqian Liu*, SUNY, Binghamton University, *X. Tong*, Brookhaven National Laboratory, *G.W. Zhou*, SUNY, Binghamton University

Dissociation of H₂O molecules on ultrathin oxide overlayers formed on metal surfaces plays a critical role in many catalytic reactions. However, the effects of chemical states and thickness of oxide overlayers on the microscopic process of H₂O dissociation are still poorly understood. In this work, X-ray photoelectron spectroscopy (XPS) is employed to study H₂O dissociation on oxidized Al (111) and Cu (111) surfaces with controlled chemical states and thicknesses of the oxide films. For Al (111), the experiment was performed under two water vapor pressures (10⁻⁶ Torr and 5 Torr) on aluminum oxide films with the thicknesses varying from 2.47 Å to 5.14 Å; for Cu (111), the experiment was performed by varying the water vapor pressure from 10⁻⁷ Torr to 10⁻³ Torr and temperature from 100°C to 450°C on the oxide film with a constant thickness. Al (2p), Cu (2p), Cu (LMM) and O (1s) spectra were monitored by XPS after each oxygen

exposure followed by subsequent H₂O exposure. Upon exposing the oxide to water vapor, the O (1s) peak shifts to a higher energy and becomes broader. A detailed analysis of the spectra indicates that H₂O molecules dissociate into OH groups for both oxidized Al and Cu surfaces. However, the subsequent reaction of OH groups with the oxide films on Cu (111) and Al (111) surfaces are dramatically different. On the oxidized Al(111) surface, OH is further incorporated into the aluminum oxide that results in the thickening of the oxide film, whereas on the oxidized Cu (111) surface, OH works as a reducing agent to remove oxygen from the oxide film that results in the thinning of the Cu oxide film. The microscopic processes underlying the differences in H₂O dissociation on oxidized Al (111) and Cu (111) will be described in detail.

5:20pm **IS+2D+MC+NS+SP+SS-WeA10 Operando APXPS of the Liquid-Solid Interface: Au Oxidation, Ethan Crumlin, S.A. Axnanda, P.N.R. Ross, Z.L. Liu, Lawrence Berkeley National Laboratory**

Interfaces play an important role for many reaction processes and are essential for electrochemistry. Electrochemical systems ranging from high temperature solid oxide fuel cells (SOFC) to lithium ion batteries to capacitors have a wide range of important interfaces between solids, liquids, and gases which play a pivotal role in how energy is stored, transferred, and/or converted. Previous capabilities of ambient pressure X-ray Photoelectron Spectroscopy (APXPS) have primarily only been able to observe the gas-solid and gas-liquid interfaces. However, recent enhancements now enable new APXPS systems to work at pressures larger than 20 Torr, and utilize 'Tender' X-rays (2.5 – 7 keV). These features provide new capabilities and opportunities for probing the liquid-solid and solid-solid interfaces. Using synchrotron X-rays at Lawrence Berkeley National Laboratory, the Advanced Light Source and our 'Tender' X-ray APXPS endstation that is outfitted with various *in situ/operando* features such as electrical leads to apply electrical potentials and operates at pressures >20 Torr, to observe the liquid-solid interface of a gold foil electrode that has been immersed and partially removed from a liquid electrolyte. This talk will provide details on how we used this technique to probe liquid-solid interface and in real-time observe the oxidation of the gold foil electrode under varying applied potentials and different electrolyte solutions.

5:40pm **IS+2D+MC+NS+SP+SS-WeA11 Water on ZnO(10-10) Investigated by Ambient Pressure X-ray Photoelectron Spectroscopy, Chris Goodwin, University of Delaware, A. Boscoboinik, Brookhaven National Lab, C. Arble, J.T. Newberg, University of Delaware**

The extent to which ZnO hydroxylates under ambient conditions can significantly influence catalytic properties. Thus, it is critical to understand the composition of different ZnO terminations as a function of relative humidity (RH) in order to elucidate the true interfacial surface terminations. In this talk we present results of ambient pressure XPS (APXPS) for water exposures to a ZnO(10-10) single crystal. It will be shown that ZnO(10-10) extensively hydroxylates at the interface, and both molecular and dissociative water increase as the RH increases. These results are consistent with simulations in the literature that highlight the efficacy for ZnO(10-10) to dissociate water.

Nanometer-scale Science and Technology

Room: 304 - Session NS+AS-WeA

Nanoscale Imaging and Materials Characterization

Moderator: Craig Prater, Anasys Instruments, Paul Sheehan, Naval Research Laboratory

2:20pm **NS+AS-WeA1 2014 AVS Albert Nerken Mark Award Lecture - Brilliant Nanodiamond Particles, Olga Shenderova***, Adámas Nanotechnologies Inc., G.E. McGuire, International Technology Center **INVITED**

Despite that nanodiamond (ND) particles were discovered more than 50 years ago and were mass produced in the early 80s, for a long time they were in the shadow of their more famous sp² carbon cousins. Two recent major breakthroughs, production of individual 4-5nm particles and particles containing colour centres exhibiting stable luminescence and unique spin properties have brought ND particles to the forefront of materials research.¹ Nanometer size particles are produced by detonation of carbon-containing explosives or by grinding of microdiamond powders. Besides well-known outstanding mechanical and thermal properties, diamond particles have remarkable optical properties in combination with biocompatibility, high

specific surface area, and tuneable surface structure. Applications of ND which have captivated the imagination of scientist in areas which have broad societal impact, such as energy preservation and biomedical imaging, will be briefly illustrated and a more in-depth review of their optical properties provided.

The optical emission, scattering and attenuation of ND are finding unique applications. In life sciences nanoparticles are increasingly used as fluorescent probes to monitor cellular interactions and study cellular dynamics at the single molecular level. Foreign atoms can be incorporated into the lattice of ND particles providing photostable particles as well as systems for quantum sensing that may be used to probe the intracellular environment at the nanoscale. Development of multimodal imaging probes based on 5-10nm ND and doping of ND with different elements to generate photoluminescence at alternative wavelengths are future directions for this field. Carbon dot-decorated ND is another means of generating photoluminescent nanoparticles with tuneable emission over the visible to near-infrared portion of the electromagnetic spectrum. The photoluminescent ND is increasingly being viewed as a means of drug delivery. Encapsulating ND in a porous silica shell is a means of achieving stable fluorescent imaging with nanoparticles with a high loading capacity for bioactive molecules.

Due to its high refractive index, wide bandgap and crystalline lattice, ND highly attenuates and scatters ultraviolet radiation. High attenuation and scattering in combination with large surface area has been shown as a means of increasing the radiation resistance of polymer nanocomposites. This can be beneficial in sunscreens as well as in polymers used in the construction of satellites to be placed in low Earth orbit.

¹V.Mochalin, O.Shenderova, D.Ho and Y.Gogotsi, "The properties and applications of nanodiamonds", (2012) *Nature Nanotechnology*, 7 (1) 11-23.

3:00pm **NS+AS-WeA3 Oxidation State Sensitive Imaging of Ceria Nanoparticles, Aaron Johnston-Peck, National Institute of Standards and Technology (NIST)**

Scanning transmission electron microscopy (STEM) coupled with electron energy loss spectroscopy (EELS) has been successfully applied to track changes to composition as well as bonding environment with atomic resolution. These measurements impose exacting experimental and instrumentation requirements that include aberration-corrected optics, electron sources with narrow energy spreads, and extremely stable room environments. Therefore it seems prudent when possible that other techniques with less demanding experimental requirements supplement EELS measurements. Imaging or diffraction techniques greatly relax these aforementioned requirements as the need for corrective optics and narrow energy spreads can be eliminated. Moreover the possibility of beam induced artifacts is reduced because the total electron dose needed to form an image or diffraction pattern is less than an EELS spectrum image.

Low angle annular dark field (LAADF) STEM is presented as an alternative to EELS measurements to identify changes to local changes of oxidation state in ceria (CeO₂) nanoparticles. This relationship was established through the use of EELS, *in-situ* measurements, and image simulations. Ceria has numerous energy related applications due to the ability of ceria readily store and release oxygen. The formal charge of the cerium ions transition from 4+ to 3+ as oxygen vacancies are formed. These oxygen vacancies cause local distortions to the crystal and subsequently produces additional diffuse scattering to low angles. The LAADF STEM signal is sensitive to this change in scattering and contrast variations in the image become resolved. Additionally, preliminary experiments on other metal oxide nanoparticles suggest that this approach may be applied to other material systems and processes as well.

3:20pm **NS+AS-WeA4 Shape and support interaction of size-selected Pd and Pt NPs on TiO₂(110), Mahdi Ahmadi, F. Behafarid, University of Central Florida, B. Roldan Cuenya, Ruhr-University Bochum, Germany**

The shape and the support interaction of 3D palladium and platinum nanoparticles (NPs) deposited on TiO₂(110) was investigated using scanning tunneling microscopy (STM). The NPs were synthesized using inverse micelle encapsulation. In spite of the initial random location of the micelle-prepared NPs on the support, step edge decoration was observed after annealing at high temperature (>1000°C). In general, resolving the shape of 3D NPs using STM is very challenging due to the tip-convolution effects. However, a combination of ultra-sharp STM tips and samples containing structurally well-defined NPs allowed us to resolve the NP shape, with the highest features on the NPs being unaffected by tip artifacts. It was found that all NPs had a truncated octahedron shape, with {111} top and interfacial facets. Furthermore, the alignment of the NP edges (or symmetry axes) with the TiO₂(110)-[001] atomic rows evidenced the epitaxial relationship with support achieved after annealing. The STM data were analyzed following the Wulff-Kaischew theorem, and a MATLAB

* Albert Nerken Award Winner

code was used to reconstruct the NP shape, eliminating overestimations in the lateral size inherent to the STM technique due to tip effects. The surface energy ratio $\gamma_{100}/\gamma_{111}$ was calculated for each Pd NP with an average value of 1.12 ± 0.07 , which is in good agreement with theoretical values. Moreover, the adhesion energy was found to display a size-dependence, with larger NPs having smaller adhesion energy. This phenomenon can be explained based on the minimization of the interfacial strain by reducing the contact area. Following similar analysis of Pt NPs on $\text{TiO}_2(110)$, a higher $\gamma_{100}/\gamma_{111}$ ratio of 1.18 ± 0.1 was obtained as compared to Pd. Also, the rate of decrease in the adhesion energy with increasing NP height was lower for Pt as compared to Pd.

4:20pm NS+AS-WeA7 Nanoscale Imaging and Spectroscopy of Plasmonic Hot Spots and Dark Modes with the PTIR Technique, Andrea Centrone, National Institute of Standards and Technology (NIST)

INVITED

Localized surface plasmon resonances couple propagating light with nanoscale volumes of matter (hot-spots), enabling new applications in sensing and therapeutics. Surface-Enhanced Infrared Absorption (SEIRA) Spectroscopy exploits such hot-spots for sensitive chemical detection. Calculations predict large SEIRA enhancement factors but the diffraction of long IR wavelengths ($2 \mu\text{m} - 16 \mu\text{m}$) has hindered the experimental determination of SEIRA enhancements with nanoscale resolution.

Photo Thermal Induced Resonance (PTIR) combines the chemical specificity of IR spectroscopy with the lateral resolution of Atomic Force Microscopy (AFM). PTIR circumvents the limitations of light diffraction by employing an AFM tip as a local detector for measuring the transient thermal expansion induced by the absorption of light pulses in the sample. Local IR spectra and composition maps are obtained recording the amplitude of the tip deflection as a function of the laser wavelength and position, respectively. Notably, the PTIR signal is proportional to the absorbed energy (not scattering) and the PTIR spectra are directly comparable with IR spectral libraries, enabling materials identification.

In this work, the PTIR technique is applied to image the dark plasmonic resonance of gold Asymmetric Split Ring Resonators (A-SRRs) in the mid-IR with nanoscale resolution. Additionally, the chemically-specific PTIR signal is used to map the local absorption enhancement of PMMA coated A-SRRs, revealing hot-spots in the resonators' gaps with enhancement factors up to ≈ 30 .

The local information gathered with in the PTIR experiments can provide insightful information and possibly help to engineer nanomaterials for greatest efficacy. As an additional example the PTIR technique will be applied to image phase separated domains in Metal-Organic Frameworks single crystals, a novel class of materials that find application in catalysis, sensing and separation.

5:00pm NS+AS-WeA9 AFM-based Infrared Spectroscopy—Nanoscale Chemical Analysis with Sensitivity Down to Single Monolayers, Craig Prater, K. Kjoller, M. Lo, E. Dillon, R. Shetty, Anasys Instruments, C. Marcott, Light Light Solutions, F. Lu, M. Jin, M. Belkin, University of Texas at Austin, A. Dazzi, Université Paris-Sud, France

The ability to perform chemical analysis at the nanoscale has been considered one of the "holy grails" of the scanning probe microscope community. Many techniques have been developed to provide material contrast in SPM images based on a variety of properties (electronic, optical, mechanical, etc.), but there had not been the ability to perform broadly applicable chemical analysis on diverse samples. We have developed AFM-based infrared spectroscopy (AFM-IR)¹ that enables broadly applicable chemical analysis on samples with nanoscale spatial resolution and with sensitivity down to the scale of individual molecular monolayers. The AFM-IR technique illuminates a sample with light from a tunable infrared laser source and then uses the tip of an AFM to measure the sample's local photothermal expansion due to the absorption of infrared light at specific wavelengths.² Measuring absorption as a function of wavelength creates an IR absorption spectrum that acts as a chemical fingerprint to characterize and identify chemical components. Mapping IR absorption spatially over a sample at different wavelengths can be used to create maps of nanoscale chemical composition. Recently we have implemented two techniques to extend both the applicability and sensitivity of the AFM-IR technique. First, we implemented top side illumination to enable AFM-IR on a much wider array of samples and sample substrates. Second, we developed a resonance enhanced mode³ where the IR laser pulses are synchronized to a contact resonance of the AFM cantilever. Combined with "lightning rod" enhancement of the incident IR light, the resonance enhanced technique can achieve chemical analysis with single monolayer sensitivity⁴ and spatial resolution $\sim 25 \text{ nm}$. We will describe the AFM-IR technique, recent innovations and applications in materials, life sciences, photonics, and semiconductors.

References:

1. A. Dazzi, R. P., F. Glotin, and J. M. Ortega. *Opt. Lett.* 2005, 30, 2388-2390.
2. Dazzi, A.; Prater, C. B.; Hu, Q.; Chase, D. B.; Rabolt, J. F.; Marcott, C. *Appl. Spectrosc.* 2012, 66, (12), 1365-1384.
3. Lu, F.; Belkin, M. A. *Opt Express* 2011, 19, (21), 19942-19947.
4. Lu, F.; Jin, M.; Belkin, M. A. *Nat Photon* 2014, 8, (4), 307-312.

5:20pm NS+AS-WeA10 Schottky Barrier Height Mapping of Nanoengineered Metal/Semiconductor Interfaces, Robert Balsano, C. Durcan, University of Albany-SUNY, A. Matsubayashi, V.P. LaBella, University at Albany-SUNY

Metal/semiconductor junctions form rectifying contacts known as Schottky diodes, which have an energy barrier determined by charge transfer and bonding at the interface. Current-voltage and capacitance-voltage spectroscopy measurements yield a spatially averaged barrier height. Ballistic electron emission microscopy (BEEM) is a scanning tunneling microscopy (STM) technique that can measure transport of hot electrons through materials and interfaces locally with high spatial and energetic resolution due to the precise positioning of the STM tip. This presentation details work done to map the Schottky barrier height with nanoscale resolution at several metal/semiconductor interfaces. These maps can give insight into the homogeneity of the barrier height as well as the spatial distribution of individual metal species. Potentially this technique can be used to image nanoengineered interfaces.

5:40pm NS+AS-WeA11 Scanning Electron Microscopy to Probe Electron Transport of Working Nanodevices under Realistic Operation Conditions, Ana Stevanovic, A. Kolmakov, National Institute of Standards and Technology (NIST)

The interplay between the electron transport and chemical status of the surface of working nanodevices can be affected by local electroactive inhomogeneities (defects), presence of near surface depletion regions and Schottky contacts. In spite of tremendous progress achieved in understanding of semiconductor chemical sensors, very little experimental data are available on aforementioned interplay in working devices under realistic operation conditions. Ambient pressure electron microscopy is used in this work to address *in situ* imaging of a formation of electroactive inhomogeneities inside a model SnO_2 nanowire device as a function of gas environment and temperature under realistic operating conditions. In addition, using scanning photoelectron and Auger microscopy with the lateral resolution of ca 80 nm, we are able to access spectroscopically the fine changes in surface condition of an individual SnO_2 nanowire during their operation. It is possible to monitor the changes in a conductance of the SnO_2 nanodevice in operando mode upon exposures to different redox gases and relate them to the formation of the specific surface groups.

**Scanning Probe Microscopy Focus Topic
Room: 312 - Session SP+AS+BI+NS+SS-WeA**

Advances in Scanning Probe Microscopy

Moderator: Tae-Hwan Kim, Pohang University of Science and Technology, Jewook Park, Oak Ridge National Laboratory

2:20pm SP+AS+BI+NS+SS-WeA1 Majorana Mode in Vortex core of $\text{Bi}_2\text{Te}_3/\text{NbSe}_2$ Topological Insulator-Superconductor Heterostructure, Jinfeng Jia, Shanghai Jiao Tong University, China

INVITED

Majorana fermions have been intensively studied in recent years for their importance to both fundamental science and potential applications in topological quantum computing^{1,2}. Majorana fermions are predicted to exist in a vortex core of superconducting topological insulators³. However, they are extremely difficult to be distinguished experimentally from other quasiparticle states for the tiny energy difference between Majorana fermions and these states, which is beyond the energy resolution of most available techniques. Here, we overcome the problem by systematically investigating the spatial profile of the Majorana mode and the bound quasiparticle states within a vortex in $\text{Bi}_2\text{Te}_3/\text{NbSe}_2$ by using *in situ* ultra-low temperature STM/STS. While the zero bias peak in local conductance splits right off the vortex center in conventional superconductors, it splits off at a finite distance $\sim 20 \text{ nm}$ away from the vortex center in $\text{Bi}_2\text{Te}_3/\text{NbSe}_2$, primarily due to the Majorana fermion zero mode. While the Majorana mode is destroyed by reducing the distance between vortices, the zero bias peak splits as a conventional superconductor again. This work provides strong evidences of Majorana fermions and also suggests a possible route to manipulating them.

References:

1. J. Alicea, Rep. Prog. Phys.75, 076501 (2012).
2. C. W. J. Beenakker, Annu. Rev. Con. Mat. Phys. 4, 113 (2013).
3. L. Fu, C. L. Kane, Phys. Rev. Lett. 100, 096407 (2008).
4. M. X. Wang et al., Science 336, 52 (2012)

* In cooperation with Jin-Peng Xu, Mei-Xiao Wang, Zhi Long Liu, Jian-Feng Ge, Xiaojun Yang, Canhua Liu, Zhu An Xu, Dandan Guan, Chun Lei Gao, Dong Qian, Ying Liu, Qiang-Hua Wang, Fu-Chun Zhang, Qi-Kun Xue

3:00pm **SP+AS+BI+NS+SS-WeA3 Robust Protection from Backscattering in the Topological Insulator $\text{Bi}_{1.5}\text{Sb}_{0.5}\text{Te}_{1.7}\text{Se}_{1.3}$.** *Fumio Komori, S. Kim, S. Yoshizawa, Y. Ishida*, University of Tokyo, Japan, *K. Eto, K. Segawa*, Osaka University, Japan, *S. Shin*, University of Tokyo, Japan, *Y. Ando*, Osaka University, Japan

Three-dimensional (3D) topological insulators (TIs) are accompanied by gapless surface states due to a nontrivial Z_2 topology of the bulk wave functions. The topological surface state (TSS) of a 3D TI is helically spin polarized, which leads to a suppression of electron scatterings due to spin mismatch between the eigenstates before and after the scattering. The suppression has been inferred from the measurements of quasiparticle interference (QPI) using scanning tunneling microscopy. No QPI was observed for intraband scatterings within unwarped TSSs. However, it has not been clear to what extent the scattering is suppressed within TSS.

In the present study, we have elucidated how the elastic scattering is suppressed as a function of the scattering angle and electron energy in the helically-spin-polarized surface electrons in a single and unwarped upper Dirac cone of $\text{Bi}_{1.5}\text{Sb}_{0.5}\text{Te}_{1.7}\text{Se}_{1.3}$. In this material [1], E_F is located very close to the Dirac energy E_D . We compared the scattering wave vectors observed at 5 K with the diameters of the constant-energy contours of the unoccupied TSS which was measured by using time-resolved ARPES implementing a pump-probe method. Moreover, the inelastic scattering time of unoccupied TSS was directly obtained by this method.

At the energy above E_D , we found that there is a sharp threshold for the length of the scattering vector, above which the observed QPI intensity is abruptly diminished [2]. Such a threshold indicates the existence of a well-defined critical scattering angle beyond which elastic scattering is suddenly suppressed. The observed protection from backscattering in the TSS occurs not only for 180° but also for a wide range of angles between 100° and 180° . Such a wide angle range for the protection from backscattering is found to be essentially independent of the energy up to 300 meV above E_D until the Dirac cone becomes warped and/or the bulk scattering events intervene. At energies higher than 300 meV, we found hexagonal patterns in the FT-QPI images that come from warping of the TSS Dirac cone. In this energy range, the critical scattering vector was not clearly observed, indicating a different mechanism of the protection from backscattering in the warped Dirac cone. The observed inelastic scattering lifetime of TSS is longer than 10 psec just above E_F . The robust protection from the backscattering and long inelastic scattering in the TSS strongly support the possible applications for electronics and spintronics using weak electron scattering of TSS at E_F .

References

1. A. A. Taskin *et al.*, Phys. Rev. Lett. **109**, 066803 (2012).
2. S. Kim, *et al.*, Phys. Rev. Lett. **112**, 136802 (2014).

3:20pm **SP+AS+BI+NS+SS-WeA4 Measurements and Analysis of Sub Nanometer Stepped Surfaces Using a Traceable Atomic Force Microscope.** *Nabuisi Orji*, National Institute of Standards and Technology (NIST), *S. Gonda*, AIST, Japan, *R.G. Dixon*, National Institute of Standards and Technology (NIST)

Although scanning probe microscopes are used in a wide variety of nanoscale measurements, the issue of instrument characterization, accuracy and calibration, continue to be a limiting factor in interpreting the resulting data. In order to accurately characterize dimensional linearity and accuracy at the sub-nanometer range, samples and robust analysis techniques suited to measurements at this range should be used.

Using Al_2O_3 surfaces on the $c(0001)$, $a(110)$, and $r(102)$ planes, and robust analyses techniques, we evaluate stepped surfaces for linearity characterization at the nanoscale. Measurements were performed using a traceable atomic force microscope (T-AFM) with displacement interferometry in all three axes. The T-AFM, which has a metrology scanning stage monitored in six axes, is housed in a mini environment with a long term temperature range of less than 2 mK, and serves as a stable platform to develop calibration standards.

The smallest of the features Al_2O_3 $c(0001)$ with a height of 0.22 nm shows a combined uncertainty of 0.01 nm, with a linearity of 0.009%. The intrinsic

traceability of the T-AFM (through displacement interferometer to the SI meter) provides additional verification to the size naturally occurring steps of the Al_2O_3 and other samples used. The results show that robust and stable linearization and calibration procedures could be developed for sub nanometer SPM characterization with low uncertainty. This will enable and support accurate dimensional characterization of scientifically relevant surfaces.

4:20pm **SP+AS+BI+NS+SS-WeA7 Direct Observation of Edge States of 1D and 2D Topological Insulators.** *Han Woong Yeom*, Institute for Basic Science, Republic of Korea

INVITED

1D and 2D topological insulators (TIs) are characterized by 0D and 1D edge states of exotic spin-charge characteristics. In this talk, we introduce the first direct real space observations of such 0D and 1D edge channels of 1D and 2D TIs by scanning tunneling microscopy/spectroscopy. The 1D TI utilized is the charge density wave phase of In atomic wires formed on the Si(111) surface, which we discovered in 1999. We clearly identified, topographically and spectroscopically, two different soliton excitations along the wires. The unique features of these solitons, theoretically unraveled as chiral solitons of the Z_4 topology, are discussed. On the other hand, a Bi(111) bilayer was theoretically predicted as a 2D TI in 2005. We have grown Bi(111) bilayer nanoislands with zigzag edges on the surface of $\text{Bi}_2\text{Te}_2\text{Se}$. Along those edges, we identified the edge localized electronic state in accordance with first principle calculations. The unexpected electronic structures of the epitaxial Bi(111) bilayer and the Bi/ $\text{Bi}_2\text{Te}_2\text{Se}$ interface are discussed. These two findings pave the avenue towards the microscopic study and the nanoscale utilization of topological solitons and quantum spin Hall states.

5:00pm **SP+AS+BI+NS+SS-WeA9 Controlling Charges of the Dipole Layer at Metal-Semiconductor Interfaces.** *Tae-Hwan Kim*, Pohang University of Science and Technology, Republic of Korea, *H.W. Yeom*, Pohang University of Science and Technology and Institute for Basic Science, Republic of Korea

Metal-semiconductor interfaces have drawn a lot of interest in the field of semiconductor surface and interface science, and have been one of the most essential parts in semiconductor electronic and optoelectronic devices. For example, the Schottky-barrier height experimentally observed at the metal-semiconductor interface appears to be nearly independent of the work function of the metal. Since the time of Bardeen, interface gap states seem to have been a primary mechanism of the Schottky-barrier height causing Fermi level pinning at metal-semiconductor interfaces. Recently, polarized chemical bonds at metal-semiconductor interfaces have been recognised to lead to the apparent Fermi level pinning effect. When these interface bonds are formed underneath thin metal islands grown on a silicon substrate, a spontaneous charge transfer across the semiconductor-metal interfaces occurs as a result of the difference in the Fermi level positions between the metal and the semiconductor. These polarized chemical bonds can form a dipole layer. This dipole layer can play an important role in many areas of technology, for instance, in organic light emitting diodes. However, some of the fundamental aspects of the charge injection process into/from the interface dipole layer at the Schottky contact are yet not explored in any real detail.

In this work, we report the use of scanning tunneling microscopy (STM) to form a double-barrier tunneling junction (DBTJ) with thin metallic nanoislands grown on Si(111) and to control charges of the interface dipole layer formed between the metallic nanoislands and the Si(111) substrate. Reversible hysteric switchings in their $I-V$ and differential conductance spectra are observed due to the charging and discharging of the interface dipole layer in a similar fashion to molecular DBTJs. STM images clearly visualize the distinct charge states and scanning tunneling spectroscopy (STS) spectra reveal that quantum well states (QWSs) of the ultrathin islands act as the charging/discharging channels in analogy to the molecular orbitals in the case of the molecular DBTJs. This work demonstrates that the charges of the interface dipole layer at the nanoscale Schottky contact can be controlled by the electron transfer via the QWSs of the metallic islands.

5:20pm **SP+AS+BI+NS+SS-WeA10 Advances in Imaging and Quantification of Electrical Properties at the Nanoscale using Scanning Microwave Impedance Microscopy (sMIM).** *Stuart Friedman, Y. Yang, O. Amster*, PrimeNano, Inc, *S. Johnston*, Stanford University

Scanning Microwave Impedance Microscopy (sMIM) is a novel mode for AFM-enabling imaging of unique contrast mechanisms and measurement of local permittivity and conductivity at the 10's of nm length scale. Custom shielded AFM probes enable the system to use microwaves to probe the impedance of the tip sample interface and extract information on local electrical properties of the sample. After introducing the theory of operation, we will review the state of the art, including imaging studies of

microelectronic devices as well as novel materials and nanostructures, such as graphene and patterned optical crystals and ferro-electrics. These studies reveal novel information about doping distributions, domains, domain walls and other features. In addition to imaging, the technique is suited to a variety of metrology applications where specific physical properties are determined quantitatively. We will present research results on quantitative measurements of dielectric constant (permittivity) and conductivity (e.g. dopant concentration) for a range of materials. For samples where properties such as dielectric constant are known the technique can be used to measure film thickness.

5:40pm **SP+AS+BI+NS+SS-WeA11 Scanning Photocurrent Microscopy on MoS₂, MoS_{2(1-x)Se_{2x}}, and MoSe₂ Monolayer Islands and Films Grown by CVD.** *Velveth Klee, D. Barroso, E. Preciado*, University of California - Riverside, *K. Erickson*, Sandia National Laboratories, *M. Triplett*, University of California -Davis, *C. Lee, A. Nguyen, I. Lu, S. Bobek, J. Mann*, University of California - Riverside, *A. Talin, F. Leonard*, Sandia National Laboratories, *L. Bartels*, University of California - Riverside

We presents scanning photocurrent measurements on CVD-grown monolayer films of molybdenum disulfide, molybdenum diselenide and the alloys of these materials. Our experiments reveal a pronounced effect of the current on excitation in the gap region between contacts, as opposed to directly at the electrodes. Measurements at different irradiation intensity, irradiation position and bias shed light on the charge transfer processes in this material system. Thermal effects are ruled out by complementary measurements of thermal transport using infrared imaging.

2D Materials Focus Topic

Room: 310 - Session 2D+AS+HI+NS+SS-ThM

Nanostructures including 2D Heterostructures, Patterning of 2D Materials

Moderator: Kirill Bolotin, Vanderbilt University

8:00am 2D+AS+HI+NS+SS-ThM1 **Stitching and Stacking for Atomically Thin Circuitry**, Jiwoong Park, Cornell University **INVITED**

The development of large scale growth methods based on chemical vapor deposition (CVD) has enabled production of single-atom-thick films with diverse electrical properties, including graphene (conductor), h-BN (insulator), and MoS₂ (semiconductor). Precise vertical stacking and lateral stitching of these 2D materials will provide rational means for building ultrathin heterostructures with complex functionality. However, large scale production and control of these structures requires new characterization and fabrication approaches. In this talk, I will first discuss the structure and physical properties unique to CVD graphene in single and bilayers. Using the atomic-resolution imaging as well as a dark-field transmission electron microscopy (TEM) technique, our group investigated the structure of grain boundaries in CVD graphene and its impact on the mechanical, electrical, and chemical properties. This allowed us to produce CVD graphene with optimized electrical properties. We also reported a new patterned regrowth method to fabricate 2D lateral heterojunctions entirely made of graphene and h-BN, which enables the development of atomically thin integrated circuitry. If time allows, I will also discuss our recent results on the large scale growth of high quality single layer MoS₂ as well as graphene film with a uniform lattice orientation. Our characterization and growth approach would ultimately allow the fabrication of electrically isolated active and passive elements embedded in continuous, one-atom-thick sheets, which could be manipulated and stacked to form complex devices at the ultimate thickness limit.

8:40am 2D+AS+HI+NS+SS-ThM3 **Vertical and Lateral Heterostructures of Carbon Nanomembranes (CNMs) and Graphene**, Andreas Winter, University of Bielefeld, Germany, M. Woszczyzna, R. Stosch, T. Weimann, F. Ahrelrs, Physikalisches Bundesanstalt, Germany, A. Turchanin, University of Bielefeld, Germany

Heterostructures of graphene with other 2D materials are of great interest for nanoscience and nanotechnology. However, their fabrication is still not a trivial task. Here we present the engineering and characterization of (i) vertical and (ii) lateral heterostructures of molecular thin (~1 nm) dielectric carbon nanomembranes (CNMs) made of aromatic molecules [1] and single-layer (SLG) graphene sheets. (i) The vertical CNM/SLG heterostructures with terminal amino-groups (NH₂-) are assembled via the mechanical transfer onto oxidized silicon wafers. We show by complementary spectroscopy and microscopy techniques as well as by electric transport measurements that functional amino groups are brought into close vicinity of the SLG sheets and that electric transport of the SLG is not impaired by this assembly, leading to the non-destructive chemical functionalization of graphene [2]. (ii) *The lateral heterostructures* are engineered using electron-irradiation-induced crosslinking of SLG sheets with CNMs. We demonstrate reliable production of well-defined laterally patterned CNM-SLG heterostructures of various sized and architectures on solid substrates and as free-standing sheets, and characterize their properties by Raman spectroscopy and helium ion microscopy.

[1] A. Turchanin and A. Götzhäuser, Carbon nanomembranes from self-assembled monolayers: Functional surfaces without bulk. *Prog. Surf. Sci.* 87, 108-162 (2012)

[2] M. Woszczyzna et al., All-carbon vertical van der Waals heterostructures: Non-destructive functionalization of graphene for electronic applications. *Adv. Mater.* 26 (2014) DOI: 10.1002/adma.201400948

9:00am 2D+AS+HI+NS+SS-ThM4 **Gate Tunable Carbon Nanotube - Single Layer MoS₂ p-n Heterojunctions**, Deep Jariwala*, V.K. Sangwan, C.-C. Wu, P.L. Prabhumirashi, M.L. Geier, T.J. Marks, L.J. Lauhon, M.C. Hersam, Northwestern University

The isolation of graphene and the subsequent reports on its electronic properties have spurred tremendous interest in a variety of two dimensional (2D) materials for electronic device applications. Layered semiconducting transition metal dichalcogenides (TMDCs) of Mo and W have emerged as

promising alternatives to graphene for optoelectronic applications due to their finite band gap in the visible portion of the electromagnetic spectrum.¹ The atomically thin structure of these 2D materials coupled with van der Waals bonding between adjacent layers allows their stacking into atomically sharp heterostructures with defect-free interfaces, in contrast to epitaxially grown III-V semiconductor heterostructures where the material choices are constrained by lattice matching. Additionally, the few atom thickness of the individual layers enables doping modulation of the overlying layers in a heterostructure using a global back gate. While a large number of heterostructure devices employing graphene have been reported, it's gapless band structure prevents the formation of a large potential barrier for charge separation and current rectification. Consequently, a p-n heterojunction diode derived from ultrathin materials is notably absent and significantly constrains the fabrication of complex electronic and optoelectronic circuits. Here we demonstrate a gate-tunable p-n heterojunction diode using semiconducting single-walled carbon nanotubes (s-SWCNTs) and single-layer molybdenum disulphide (SL-MoS₂) as atomically thin p-type and n-type semiconductors, respectively. The vertical stacking of these two direct band gap semiconductors forms a heterojunction with electrical characteristics that can be tuned with an applied gate bias over a wide range of charge transport behavior, ranging from insulating to rectifying with forward-to-reverse bias current ratios exceeding 10⁴. In addition, the gate-dependent characteristics of this diode exhibit a unique 'anti-ambipolar' behavior with two off-states at either extremes of the gate voltage range and a maximum on-state current between them. This heterojunction diode also responds to optical irradiation with photoresponse time < 15 μs.² We anticipate that the novel properties and characteristics of this p-n heterojunction can be widely generalized to other atomically thin materials systems.

REFERENCES:

1. Jariwala, D. et al. Emerging Device Applications for Semiconducting Two-Dimensional Transition Metal Dichalcogenides. *ACS Nano* 2014 , 8, 1102–1120.
2. Jariwala, D. et al. Gate-Tunable Carbon Nanotube–MoS₂ Heterojunction p-n Diode. *Proc. Natl. Acad. Sci. U.S.A.* 2013 , 110, 18076–18080.

9:20am 2D+AS+HI+NS+SS-ThM5 **Graphene Transfer onto sub 1nm Al₂O₃/TiOPc/Graphene Gate Stacks**, Ijfo Kwak, J.H. Park, University of California at San Diego, H.C.P. Movva, University of Texas at Austin, E.K. Kinder, H.L. Lu, University of Notre Dame, A.C. Kummel, University of California at San Diego

A novel transfer method with chemically controlled interfacial adhesion is reported for the fabrication of novel logic devices. This method allows direct transfer onto gate stacks and eliminates the possibility of Au electrodes deposition could shorting the thin oxide prior to transfer. The top graphene layer was grown on a Cu layer on a SiO₂/Si substrate by CVD. Au electrodes were deposited on top of the graphene by e-beam evaporation. To transfer the graphene layer, PIB (Polyisobutylene) were drop cast on top of graphene prior to bonding of the Au/graphene/Cu to a PDMS (Polydimethylsiloxane) film. The PIB serves to moderate the adhesion between the PDMS (Polydimethylsiloxane) and the Au electrodes. The PDMS provides mechanical support. Afterwards, the PDMS/PIB/Au/graphene/Cu/SiO₂/Si stack was immersed in ammonium persulfate solution to dissolve the Cu, releasing the top graphene stack. The bottom gate stack was HOPG (highly ordered pyrolytic graphite) with a sub-nano Al₂O₃ film on a monolayer TiOPc(titanyl phthalocynine) film. The monolayer TiOPc was deposited via MBE at 100C and annealed to 250C to insure a monolayer film. The TiOPc acts as a nucleation layer for the oxide ALD. The Al₂O₃ layer was deposited by ALD using TMA (Trimethylaluminum) and H₂O at 100 C. The PDMS/PIB/Au/Graphene stack was placed on the gate stack, and PDMS was removed. Using hexane solution, the rePIB layer was dissolved, leaving clean graphene surface. To measure the oxide characteristics, an AFM was converted into a capacitance meter. This measurement allows non-destructive probing of Au/graphene/Al₂O₃/TiOPc/graphene structure while conventional probe station could damage the oxide or electrodes.

9:40am 2D+AS+HI+NS+SS-ThM6 **Effect of Monolayer Substrates on the Electronic Structure of Single-Layer MoS₂**, Alfredo Ramirez-Torres, D.T. Le, T.S. Rahman, University of Central Florida

We have performed first-principles calculations based on density functional theory (DFT) utilizing the optB88-vdW functional to study structural and electronic properties of a single layer of MoS₂ deposited on single-layer substrates of hexagonal boron nitride (BN), graphene and silicene. All have a honeycomb structure; hence the formation of heterostructures is expected. Since the lattice mismatch between MoS₂ and these substrates is large, we

* NSTD Student Award Finalist

have considered different periodicities among layers to reduce as far as possible the incommensurability between lattices. Our results show that BN barely affects the electronic structure of isolate single-layer MoS₂; the DFT gap remains proximately unchanged. Graphene and silicene severely modify the electronic structure introducing additional states within the optical gap. Adsorption on graphene produces that the system turns like a zero band gap semiconductor bringing the conduction bands of MoS₂ down to the Fermi level of graphene. Adsorption on silicene shifts both valence and conduction bands of MoS₂, towards the Fermi level of silicene, in addition to inducing a gap of about 50 meV in the silicene itself.

This work was partially supported by CONACYT (México) Postdoctoral Fellowship Program (number 204065) and DOE grant DE-FG02-07ER46354

11:00am **2D+AS+HI+NS+SS-ThM10 Ballistic Transport in Epitaxial Graphene Nanoribbons**, *Walt de Heer*, Georgia Institute of Technology
INVITED

Graphene nanoribbons are essential components in future graphene nanoelectronics. However, in typical nanoribbons produced from lithographically patterned exfoliated graphene, the charge carriers travel only about 10 nanometers between scattering events, resulting in minimum sheet resistances of about 1 kW In contrast 40 nm wide graphene nanoribbons that are epitaxially grown on silicon carbide are single channel room temperature ballistic conductors on greater than 10 μm length scale, similarly to metallic carbon nanotubes. This is equivalent to sheet resistances below 1W surpassing theoretical predictions for perfect graphene by at least an order of magnitude. In neutral graphene ribbons, we show that transport is dominated by two modes. One is ballistic and temperature independent; the other is thermally activated. Transport is protected from back-scattering, possibly reflecting ground state properties of neutral graphene. At room temperature the resistance of both modes abruptly increases non-linearly with increasing length, one at a length of 16 μm and the other at 160 nm. Besides their importance for fundamental science, since epitaxial graphene nanoribbons are readily produced by the thousands, their room temperature ballistic transport properties can be used in advanced nanoelectronics as well.

11:40am **2D+AS+HI+NS+SS-ThM12 Solution-Synthesized Graphene Nanoribbons**, *Alexander Siniitskii*, University of Nebraska - Lincoln

In this talk I will discuss a recently developed bottom-up approach for gram quantities of narrow graphene nanoribbons that are less than 2 nm wide and have atomically precise armchair edges. These graphene nanoribbons have been characterized by a number of microscopic (STM, AFM, SEM, TEM) and spectroscopic (XPS, UPS/IPES, UV-vis-NIR, IR and Raman spectroscopy) techniques. The properties of graphene nanoribbons could be tuned by incorporation of nitrogen atoms in their edges. Narrow graphene nanoribbons have a large electronic bandgap, which makes them promising for applications in field-effect transistors with high on-off ratios, as well as bulk applications, including coatings, composites and photovoltaic devices.

12:00pm **2D+AS+HI+NS+SS-ThM13 Graphene Silicon Interfaces at the Two-Dimensional Limit**, *Brian Kiraly, A.J. Mannix, M.C. Hersam*, Northwestern University, *N.P. Guisinger*, Argonne National Laboratory

Artificial van der Waals heterostructures have demonstrated both significant improvements of graphene's intrinsic properties and entirely new properties of their own. Early interest in these structures was based on nearly ideal carrier mobility in graphene on two-dimensional (2D) hexagonal boron nitride. Although exfoliation and reassembly of bulk vdW solids has yielded impressive initial results, this method inherently limits the geometry and constituent materials of these structures. Growth of 2D heterostructures has been demonstrated, but mainly limited to the prototypical graphene/hBN system. Adding new constituent materials, particularly those with electronic heterogeneity, to these 2D heterostructures allows them to be engineered with a variety of new properties.

We present the growth and characterization of interfaces between an atomically thin silicon layer and graphene. First, graphene is grown on Ag(111) via atomic carbon deposition at temperatures from 600°C -700°C. Following the growth of graphene, atomic silicon is evaporated on the graphene-covered Ag(111) substrate at 320°C-360°C. The resulting silicon growth results in faceted domains capped with a honeycomb lattice with periodicity 6.4 Å; Raman spectroscopy reveals peaks at 520 cm⁻¹ and 900-1000 cm⁻¹ that coincide precisely with bulk diamond cubic silicon, indicating these domains are comprised of *sp*³ bonded crystalline Si. These 2D sheets of silicon demonstrate both semiconducting character and a honeycomb lattice is attributed to a silver-based reconstruction of the Si(111) surface. The resulting silicon domains grow in two different configurations with respect to the dendritic graphene: (1) silicon domains appear to grow directly on the Ag(111) surface and terminate at the graphene boundaries.

These in-plane interfaces are atomically-precise and clearly resolved via scanning tunneling microscopy. Electronically, the density of states of both isolated constituent materials persist to these interfaces within the resolution of the measurement, indicating little interaction at the border. (2) The silicon growth is observed *underneath* the existing graphene flakes. The vertically stacked silicon graphene domains are identified via atomically resolved imaging *through* the graphene domains at larger biases where graphene is transparent under STM. Furthermore, the vertical materials interfaces demonstrate distinct electronic signatures from either constituent material. The resulting interfaces represent atomically pristine interfaces between graphene and a *sp*³ bonded semiconducting Si film, demonstrating a significant step forward in the diversification of van der Waals heterostructures.

Atom Probe Tomography Focus Topic
Room: 301 - Session AP+AS+MC+NS+SS-ThM

APT Analysis of Semiconductors, Magnetic and Oxide Materials

Moderator: Paul Bagot, Oxford University, UK, Daniel Perea, Pacific Northwest National Laboratory

8:00am **AP+AS+MC+NS+SS-ThM1 A Vision for Atom Probe Tomography**, *Thomas F. Kelly*, CAMECA Instruments Inc **INVITED**

Atom Probe Tomography has undergone revolutionary changes in the past two decades. It is tempting to think that these changes are likely to be followed by a period of adjustment and maturation but not continued innovation. However, there are still many active opportunities for development of atom probe tomography. Some of these new technologies are already upon us. There are recent major developments in data reconstruction, detector technology, data mining, and correlative microscopy. Furthermore, application areas are evolving at a rapid pace. The equipment needed to serve some applications will necessarily be developing alongside the more fundamental operating components of atom probes.

This talk with review some recent developments that are just emerging and will offer a vision for where the field is headed. Some of the unproven concepts needed to reach this vision will be highlighted.

8:40am **AP+AS+MC+NS+SS-ThM3 Interfaces in Semiconductors: Application to Photovoltaic Materials**, *Oana Cojocaru-Mirédin*, Max Planck Institut für Eisenforschung GmbH, Germany, *R. Würz*, Zentrum für Sonnenenergie- und Wasserstoff-Forschung Baden-Württemberg, Germany, *D. Raabe*, Max Planck Institut für Eisenforschung GmbH, Germany
INVITED

Cu(In,Ga)Se₂ (CIGS), Cu₂ZnSnSe₄ (CZTSe), and multicrystalline Si (mc-Si) solar cells possess a high efficiency [1], despite the polycrystalline structure of the absorber layer. One of the major factors controlling the cell efficiency is the diffusion of the impurities during the fabrication process into the absorber layer and to the p-n junction [2]. However, the interaction between the defects and the impurities at the internal interfaces is not completely understood. This is due to a lack of information on the local chemical changes across the internal interfaces at the nanoscale.

As a step towards a better understanding of the impurity redistribution at the internal interfaces, we have developed novel approaches of preparing site-specific atom probe specimens using combined focused ion beam (FIB), (scanning) transmission electron microscopy ((S)TEM) and electron backscattered diffraction (EBSD). These approaches allow selected GBs in polycrystalline CIGS, CZTSe and mc-Si layers to be studied by atom probe tomography (APT).

Several examples of correlative EBSD-TEM-APT (see Figure 1) and STEM-APT (see Figure 2) studies will be presented in this work. Using APT, segregation of impurities at the GBs was directly observed. APT data of various types of GBs will be presented and discussed with respect to the possible effects on the cell efficiency.

[1] Empa [Internet]. Empa.ch: A new world record for solar cell efficiency, 2013. Available from: <http://www.empa.ch/plugin/template/empa/3/131438/---/l=2> [cited 2013 January 18].

[2] J. L. Shay, S. Wagner, H. M. Kasper, Appl. Phys. Lett. 27 (1975) 89, S. Yip and I. Shih, Proceedings of the 1st World Conference on Photovoltaic Energy Conversion (IEEE, Piscataway, 1994), p.210.

9:20am **AP+AS+MC+NS+SS-ThM5 Analysis of Discontinuous InGaN Quantum Wells by Correlated Atom Probe Tomography, Micro-Photoluminescence, and X-ray Diffraction.** *J. Riley, X. Ren, Northwestern University, D. Koleske, Sandia National Laboratories, Lincoln Lauhon, Northwestern University*

In(x)Ga(1-x)N quantum wells are the foundation of solid-state lighting, with excellent quantum efficiencies despite high densities of defects. While there is as yet no universally accepted explanation for the high-efficiency, it is clear that carrier localization plays a role. Consistent with this picture, the quantum efficiencies of some samples can be improved by annealing and hydrogen gas to produce discontinuous quantum wells. However, the standard analysis of quantum well widths and composition by high-resolution x-ray diffraction is complicated by such complex morphologies. Specifically, the influence of surface roughness, and interfacial diffuseness, and planar continuity may be difficult to deconvolve. We will describe correlated analysis of continuous and discontinuous InGaN quantum wells by atom probe tomography, micro-photoluminescence, high-resolution x-ray diffraction, and atomic force microscopy. We find that precise composition profiles extracted from atom probe analysis enable refinement of x-ray diffraction peak fitting in the case of continuous quantum wells, and a better estimate of indium mole fraction and quantum well width. For discontinuous quantum wells, atom probe analysis enables simple models to be integrated into routine x-ray diffraction modeling to enable reliable extraction of indium mole fraction and better correlation with photoluminescence spectra. Correlation of atomic force microscopy tomographic images and micro-photoluminescence spectra over common sample areas, together with site-specific lift out techniques, will be presented to explore the surprising coexistence of high quantum efficiency and inhomogeneous broadening due to the complex underlying quantum well morphology.

9:40am **AP+AS+MC+NS+SS-ThM6 Atom Probe Tomography Characterization of Doped Epitaxial Oxide Multi-Layered Structures.** *Nitesh Madaan, A. Devaraj, Z. Xu, M.I. Nandasiri, S.A. Thevuthasan, Pacific Northwest National Laboratory*

Atom probe tomography is the state of the art 3D microscopy technique with sub-nanometer scale spatial resolution and ppm level mass sensitivity. For complex heterogeneous materials the accurate artifact-free reconstruction of collected data is quite a challenging task due to varying local evaporation fields leading to non-hemispherical evolution in the tip shape during the APT analysis. In this work we utilized laser assisted APT to analyze alternate multilayer oxide thin film structure of Samaria doped ceria (SDC) and Scandia stabilized zirconia (ScSZ), grown epitaxially on sapphire substrate, which is potentially useful for solid oxide fuel cells due to their high ionic conductivity. By analyzing the sample in different orientations (top-down, side-ways, and back-side) and comparing with dynamic tip shape evolution using level set simulations for similar geometries, an attempt was made to understand and decouple the APT evaporation artifacts from the real physical sample features. This study would help provide insights to improve the APT reconstruction process for complex multi-layered thin film materials.

11:00am **AP+AS+MC+NS+SS-ThM10 Atom Probe Tomography and Field Evaporation of Insulators and Semiconductors: Theoretical Issues.** *Hans Kreuzer, Dalhousie University, Canada* **INVITED**

After reviewing the physics and chemistry in high electrostatic fields and summarizing the theoretical results for Atom Probe Tomography of metallic tips, we turn to the new challenges associated with insulators and semiconductors with regard to local fields inside and on the surface of such materials. The recent (theoretical) discovery that in high fields the band gap in these materials is drastically reduced to the point where at the evaporation field strength it vanishes will be crucial in our discussion.

11:40am **AP+AS+MC+NS+SS-ThM12 Atom Probe Tomography Investigation of the Microstructure of Multistage Annealed Nanocrystalline SmCo₂Fe₂B Alloy with Enhanced Magnetic Properties.** *Xiujuan Jiang, A. Devaraj, Pacific Northwest National Laboratory, B. Balamurugan, University of Nebraska-Lincoln, J. Cui, Pacific Northwest National Laboratory, J. Shield, University of Nebraska-Lincoln*

Permanent magnets have garnered great research interest for energy applications. The microstructure and chemistry of a permanent magnet candidate—SmCo₂Fe₂B melt-spun alloy—after multistage annealing was investigated using high resolution transmission electron microscopy (HRTEM) and atom probe tomography. The multistage annealing resulted in an increase in both the coercivity and magnetization as is desired for permanent magnets design. The presence of Sm(Co,Fe)₂B (1:4:1) and Sm₂(Co,Fe)₁₇B_x (2:17:x) magnetic phases were confirmed using both techniques. Fe₂B at a scale of ~ 5 nm was found by HRTEM precipitating within the 1:4:1 phase after the second-stage annealing. Ordering within the 2:17:x phase was directly identified both by the presence of antiphase

boundaries observed by TEM and the interconnected isocomposition surface network found in 3D atom probe results in addition to radial distribution function analysis. These observed variations in the local chemistry after the secondary annealing were considered pivotal in improving the magnetic properties.

12:00pm **AP+AS+MC+NS+SS-ThM13 Detector Dead-time Effects on the Accurate Measurement of Boron in Atom Probe Tomography.** *Frederick Meisenkothen, National Institute of Standards and Technology (NIST), T.J. Prosa, CAMECA Instruments Inc., E.B. Steel, NIST, R.P. Koll, University of Maryland, College Park*

The atom probe tomography (APT) instrument uses a time-of-flight (TOF) mass spectrometer to identify ions that are field ionized and evaporated from the apex of a needle-like nano-tip specimen. A pulse event, either laser or voltage, is used to trigger field evaporation and to initiate the timing sequence for the mass spectrometer. Ideally, a single atom is field evaporated during a single pulse event. However, it is also common to have multi-hit detection events where more than one ion strikes the detector between pulses. For reasons not completely understood, some elements, such as boron, are prone to field evaporate in multi-hit detection events when compared to other elements, and a large fraction of the boron signal is reportedly lost during acquisition. Obtaining an improved understanding of the field evaporation behavior of boron at different concentration levels, in view of the limited ability of the detection system to resolve multi-hit detection events, may lead to new ways to compensate for the boron signal loss.

A nominally pure boron sample was chosen as a high boron concentration material while the boron implanted silicon, NIST-SRM2137, (1E15 atoms cm⁻² retained dose) was chosen as the low boron concentration material. A dual-beam FIB/SEM instrument, with an *in situ* lift-out system, was used to prepare the APT specimen tips from the bulk materials. A laser pulsed LEAP 4000X Si* instrument was used to acquire APT data sets for each of the specimen tips. Custom software scripts were used to filter the data sets and extract the ion information associated with specific search criteria, e.g. event multiplicity, which is the number of ions within a given multi-hit event. Ion correlation analysis was used to graphically demonstrate the detector dead-time effect. In the present work, more than 60% of the detected boron signal resided within the multi-hit detection events, for both the high and low boron concentration samples.

* Certain commercial equipment, instruments, or materials are identified in this paper in order to specify the experimental procedure adequately. Such identification is not intended to imply recommendation or endorsement by the National Institute of Standards and Technology, nor is it intended to imply that the materials or equipment identified are necessarily the best available for the purpose.

Scanning Probe Microscopy Focus Topic
Room: 312 - Session SP+2D+AS+EM+MC+NS+SS-ThM

Probing Electronic and Transport Properties
Moderator: An-Ping Li, ORNL, Corentin Durand, ORNL

8:00am **SP+2D+AS+EM+MC+NS+SS-ThM1 Investigation of the Electronic and Structural Properties of Metal Free Naphthalocyanine Vapor Deposited on Au(111).** *Bryan Wiggins, University of Chicago, K.W. Hipps, Washington State University*

Naphthalocyanines (Ncs) are promising candidates for future components in electronic devices and applications. To maximize the efficiency of Nc devices, it is critical to understand their structural and electronic properties and how these are impacted by deposition methods. The formation of a metal free naphthalocyanine (H₂Nc) self-assembled monolayer on a Au(111) crystal was investigated by scanning tunneling microscopy under ultra-high-vacuum conditions at room temperature. A rigorous purification and processing procedure was developed to produce high purity, low defect, and well-ordered monolayers. High-resolution STM images reveal epitaxial growth of H₂Nc on Au(111) with the observed structure having a molecular spacing of 1.6 ± 0.05 nm, with molecules orientated slightly off (roughly 2.5°) the low density packing direction of Au(111). A commensurate structure having 4 molecules per unit cell and unit cell parameters of $A = 3.25 \pm 0.05$ nm, $B = 3.17 \pm 0.05$ nm, and $\alpha = 87.5 \pm 2^\circ$ is proposed. Orbital-mediated tunneling spectroscopy was used to examine the electronic properties of individual molecules within the thin film. The first ionization potential and electron affinity of H₂Nc adsorbed on Au(111) were measured to be -0.68 ± 0.03 and 1.12 ± 0.02 eV, relative to the Fermi energy.

8:20am **SP+2D+AS+EM+MC+NS+SS-ThM2 The Fundamentals of Charge Transport at Oxide and Ferroelectric Interfaces**, *Ramsey Kraya, L.Y. Kraya*, University of Pennsylvania

Here we investigate how charge transport properties at metal-semiconductor interfaces scale down to the nanoscale regime, comparing the properties to macroscopic interfaces and providing a perspective on what it means to device manufacturing. Strontium titanate - the prototypical oxide material - has been widely studied for applications in thermoelectrics, nanoelectronics, catalysis, and other uses, and behaves as an n-type semiconductor when doped. We investigated how charge transport is effected at interfaces to strontium titanate under a wide range of conditions - by varying contact size, interface shape, dopant concentration, and surface structure and in various combinations. The results of the analysis have wide ranging implications, especially for ferroelectric oxide materials and serves as the basis for understanding and controlling switching effects - both polarization and oxygen migration based switching.

8:40am **SP+2D+AS+EM+MC+NS+SS-ThM3 Epitaxial Graphene on Nanostructured Silicon Carbide**, *Phillip First*, Georgia Institute of Technology **INVITED**

Graphene grown epitaxially on silicon carbide conforms to nanofaceted step edges, even for step heights of many nanometers. The "sidewall" nanoribbons that result show astounding transport characteristics (~15 um ballistic length at room temperature), as demonstrated by others,¹ but the physical basis for these results is still not certain. In our STM measurements of sidewall nanoribbons, we find an extended 1D region with electronic structure much different than 2D graphene. Spectroscopic results on graphene near nanofacet corners indicate a strain gradient and a rapid change in the doping. Such strong gradients may be key to understanding the ballistic transport in this system. P

¹J. Baringhaus, M. Ruan, F. Edler, A. Tejada, M. Sicot, Amina Taleb-Ibrahimi, A.-P. Li, Z. Jiang, E. H. Conrad, C. Berger, C. Tegenkamp and W. A. de Heer, "Exceptional ballistic transport in epitaxial graphene nanoribbons," *Nature*, **506**, 349 (2014).

9:20am **SP+2D+AS+EM+MC+NS+SS-ThM5 Conductivity of Si(111) - 7 × 7: The Role of a Single Atomic Step**, *B. Martins*, University of Alberta and The National Institute for Nanotechnology, Canada, *M. Smeu, H. Guo*, McGill University, Canada, *Robert Wolkow*, University of Alberta and The National Institute for Nanotechnology, Canada

The Si(111) - 7 × 7 surface is one of the most interesting semiconductor surfaces because of its

complex reconstruction and fascinating electronic properties. While it is known that the Si - 7 × 7 is

a conducting surface, the exact surface conductivity has eluded consensus for decades as measured

values differ by 7 orders of magnitude. Here we report a combined STM and transport measurement

with ultra-high spatial resolution and minimal interaction with the sample, and quantitatively determine the intrinsic conductivity of the Si - 7 × 7 surface. This is made possible by the capability of

measuring transport properties with or without a single atomic step between the measuring probes:

we found that even a single step can reduce the surface conductivity by two orders of magnitude.

Our first principles quantum transport calculations confirm and lend insight to the experimental observation.

9:40am **SP+2D+AS+EM+MC+NS+SS-ThM6 Asymmetric Electron Transport Revealed at Monolayer-Bilayer Graphene Junctions by Atomic-Scale Scanning Tunneling Potentiometry**, *K. Clark, X. Zhang, J. Park*, Oak Ridge National Laboratory, *G. Gu*, University of Tennessee, *G. He, R.M. Feenstra*, Carnegie Mellon University, *An-Ping Li*, Oak Ridge National Laboratory

The quest for novel two-dimensional (2D) materials has led to the discovery of hybrid heterostructures of graphene and other 2D atomic films [1]. These heterojunctions provide us fascinating playground for exploring electronic and transport properties in 2D materials. Even in graphene itself, there usually exist large amount of extended topological defects, such as grain boundaries, changes in layer thickness, and substrate steps, which divide graphene into grains and domains. These interfaces and boundaries can break the lattice symmetry and are believed to have a major impact on the electronic properties, especially the transport, in 2D materials.

Here, we present our recent study on an asymmetric electron transport upon bias polarity reversal at individual monolayer-bilayer (ML-BL) boundaries

in epitaxial graphene on SiC (0001), revealed by multi-probe scanning tunneling potentiometry [2,3]. A greater voltage drop is observed when the current flows from monolayer to bilayer graphene than in the reverse direction, and the difference remains nearly unchanged when bias exceeds a threshold. A thermovoltage is measured across the boundary due to the thermopower difference between the two sides, which however is too small to account for the observed asymmetry. Interestingly, this asymmetry is not from a typical nonlinear conductance due to electron transmission through an asymmetric potential. Rather, it indicates the opening of an energy gap at the Fermi energy. Our theoretical analysis finds that Friedel charge oscillation opens a gap for electrons with wave vectors perpendicular to the boundary. The Friedel gaps are different on the monolayer and bilayer sides, which can shift under bias and lead to asymmetric transport upon reversing the bias polarity. A quantitative agreement is seen between experiment and theory on both the sign and the magnitude of the asymmetry.

1 "Heteroepitaxial Growth of Two-Dimensional Hexagonal Boron Nitride Templated by Graphene Edges", L. Liu, J. Park, D. A. Siegel, K. F. McCarty, K. W. Clark, W. Deng, L. Basile, J.-C. Idrobo, A.-P. Li, G. Gu, *Science***343**, 163-167 (2014).

2 "Spatially Resolved Mapping of Electrical Conductance around Individual Domain (Grain) Boundaries in Graphene", K. W. Clark, X.-G. Zhang, I. V. Vlassiouk, G. He, R. M. Feenstra, and A.-P. Li, *ACS Nano*. **7** (9), 7956-7966 (2013).

3 "Friedel Oscillation-Induced Energy Gap Manifested as Transport Asymmetric at Monolayer-Bilayer Graphene Boundaries", K. W. Clark, X.-G. Zhang, G. Gu, G. He, R. M. Feenstra, and A.-P. Li, *arXiv*: 1401.1796, *Physical Review X***4** (1), 011021 (2014).

11:00am **SP+2D+AS+EM+MC+NS+SS-ThM10 Defect-mediated Transport in CVD-grown Monolayer MoS₂**, *Corentin Durand, J. Fowlkes*, Oak Ridge National Laboratory, *S. Najmaei, J. Lou*, Rice University, *A.P. Li*, Oak Ridge National Laboratory

Transition metal dichalcogenides like molybdenum disulphide (MoS₂) have attracted great interest as candidate to fill the need of 2 dimensional semiconductor materials. By controlling the thickness, the bandgap of MoS₂ thin films can be tuned from 1.2 eV (bulk material, indirect bandgap) to 1.8 eV (monolayer film, direct bandgap). Recently, researchers succeeded in growing monolayered MoS₂ by chemical vapor deposition (CVD) on silicon dioxide (SiO₂) substrate, showing the possibility of low cost scalable device fabrication. However, the mobility reported on exfoliated MoS₂ monolayers exceeds 200 cm².V⁻¹.s⁻¹, whereas the measurements realized on CVD growth MoS₂ monolayers reveal a mobility value that is usually 1-2 orders of magnitude lower. Here, we study the transport properties of CVD-grown monolayer on SiO₂/Si substrate. We directly measure the resistivity and the mobility of the material with a field-effect transistor architecture by using a cryogenic four-probe scanning tunneling microscope (STM), the Si substrate being used as back-gate. In order to ensure reliable electrical contacts, we fabricate platinum pads (4x4 μm²) on individual MoS₂ crystal domains by using an electron-beam induced deposition technique. The combination of the STM scanners and a scanning electron microscope (SEM) enables us to connect the STM tips on those pads and thereby establish the contacts on this material without any subsequent lithography process, avoiding contaminations introduced by other technological steps. An electron hopping process in localized charge trapping states appears to dominate the transport behavior. We performed temperature-dependent measurements in the range of 82 K to 315 K which demonstrate a variable range hopping (VRH) transport with a very low mobility. Furthermore, the effects of electronic irradiation are examined by exposing the film to electron beam in the SEM in an ultra-high vacuum environment. We found that the irradiation process affect the mobility and also the carrier concentration of the material, with conductance showing a peculiar time-dependent relaxation behavior. It is suggested that the presence of defects such as vacancies and antisites create charge trapping states, leading to the low mobility. This is consistent with recent density functional theory calculations where these defects are shown to create localized gap states that can act as scattering centers and thereby reduce the mobility.

11:20am **SP+2D+AS+EM+MC+NS+SS-ThM11 Coherent One Dimensional Boundaries in Graphene and Hexagonal Boron Nitride Heterostructures**, *Jewook Park*, Oak Ridge National Laboratory, *L. Liu*, The University of Tennessee Knoxville, *D.A. Siegel, K.F. McCarty*, Sandia National Laboratories, *L. Basile, J.-C. Idrobo, K. Clark*, ORNL, *W. Deng*, The Univ. of Tennessee Knoxville, *C.P. Durand*, ORNL, *G. Gu*, The Univ. of Tennessee Knoxville, *A.P. Li*, ORNL

The quest for novel two-dimensional (2D) materials has led to the discovery of hybrid heterostructures where graphene and other atomic layer films such as monolayer hexagonal boron nitride (hBN) form phase-separated domains or both materials grow epitaxially onto a common crystalline substrate. By

implementing the concept of epitaxy to 2D space, we developed and applied a new growth technique to hybrid isostructural but electrically dissimilar materials, such as the 2D epitaxial growth of hBN templated by graphene edge [1]. Scanning tunneling microscopy and spectroscopy measurements revealed a single-atomic-layer, in-plane heterostructure between graphene and hBN, as well as an abrupt 1D zigzag oriented boundary. In addition, the dI/dV conductance map unveiled the 1D interfacial states that are extended along, but localized at the boundary. We investigated spatial and energetic distributions of 1D boundary states. Also, low-energy electron microscopy and micro low-energy electron diffraction confirmed the heterostructure at mesoscopic scale and established that the graphene edge solely determines the crystallography of the hBN regardless of underlying the Cu(100) lattice. The Z-contrast scanning transmission electron microscopy further indicates an atomically sharp interface with a transition width of ~ 0.5 nm. We suggest that the graphene-hBN epitaxial heterostructure provides an excellent platform to explore heteroepitaxy in 2D space, and the unique functionalities at the 1D interface. [1] Lei Liu *et al. Science* **343** 163 (2014)

11:40am **SP+2D+AS+EM+MC+NS+SS-ThM12 Charge and Spin Density Waves in Quasi One-Dimensional Atomic Wires, Herbert Pfnür, Leibniz Universität, Germany INVITED**

Although free one-dimensional (1D) objects should exist only at $T=0$, atomic single wires or arrays embedded into a two- or three-dimensional environment exist even at room temperature and above, since they are stabilized by lateral interactions. These interactions not only stabilize, but also strongly modify the properties of the wires. Their 2D or 3D coupling, however, does not generally prevent observation of 1D properties with their complex variety of instabilities. Furthermore, these coupling can result in special 1D behavior not predicted by standard theories either in 1D or 2D. I will show several examples how atomic wires and wire arrays grown by self-assembly on semiconducting surfaces of Si and Ge acting as insulating substrates can be used to study in detail fundamental aspects of low-dimensional physics, such as charge density waves [1] and Luttinger liquid behavior [2], partially under explicit control of the atomic structure. Due to the low symmetry in these structures, large Rashba-type spin-orbit coupling is expected to lift the spin degeneracy of the metal-induced surface states. In this context new types of spin order were proposed, e.g. for Au/Si(553) [3] and found to be consistent with experiment. As a further example, the Pb/Si(557) system close to monolayer coverage turned out to be an intriguing model system that demonstrates the wealth of phenomena to be expected in quasi-1D physics. Adsorbate induced electronic stabilization leads to (223) refaceting of the (557) surface, to opening of a band gap, to Fermi nesting normal to the steps [4], and to the formation of a charge density wave. Rashba splitting is so large that it causes in-plane anti-ferromagnetic spin polarization along the steps with twice the step periodicity resulting in a combined spin-charge density wave. New superstructures are formed by an excess Pb coverage up to 0.1ML due to ordered step decoration indicating strong electron-electron correlation across steps. This leads to new long range ordered states and formation of a sequence of 1D charge density waves up to a concentration of 1.5 ML, but also, as very recent angular and spin resolved photoemission studies show, to new ordered spin states.

- [1] T. Tanikawa *et al.* Phys. Rev. Lett. 93, 016801 (2004).
- [2] C. Blumenstein *et al.* Nat. Phys. 7, 776 (2011).
- [3] S.C. Erwin, F. J. Himpsel, Nature Communications 1, 58 (2010); J. Aulbach *et al.* Phys. Rev. Lett. 111, 137203 (2013)
- [4] C. Tegenkamp, D. Lükermann, H. Pfnür, B. Slomski, G. Landolt H. Dil, Phys. Rev. Lett. 109, 266401 (2012).

Tribology Focus Topic

Room: 303 - Session TR+NS-ThM

Bridging Scales in Tribology

Moderator: J. David Schall, Oakland University

8:00am **TR+NS-ThM1 Temporal and Spatial Multiscale Simulations of Low-Velocity Frictional Sliding, Woo-Kyun Kim, University of Cincinnati INVITED**

As the size of mechanical systems of technological interest such as micro electro-mechanical systems (MEMS) decreases, the need to develop experimental and theoretical tools to investigate micro/nanometer scale phenomena has been growing rapidly. Since its invention in 1986, the Atomic Force Microscope (AFM) has been a primary tool to study the atomic-scale friction and wear and atomistic simulation methods such as molecular dynamics (MD) have also been widely used because these

simulations can provide direct access to atomic-scale mechanisms which cannot be observed experimentally. However, there is a great disparity in length and time scales between the simulated systems and the real experimental systems. One of the significant artifacts of these scale differences is that systems are loaded at by several orders of magnitudes larger rates in simulations than in experiments, which may completely distort the underlying mechanisms. Recently, a novel multiscale method, called hyper-QC, which can span both length and time scales simultaneously has been developed. Hyper-QC combines quasicontinuum (QC), a spatial multiscale method, and hyperdynamics, an accelerated MD scheme, in a single platform. In this talk, the hyper-QC simulation results of AFM experiments will be presented. Hyper-QC enables the reduction in the sliding rate by two or three orders of magnitudes from that of the conventional MD scheme as well as the reduced effective number of atoms that is achieved through the QC coarse-graining.

8:40am **TR+NS-ThM3 Crystal-Amorphous and Amorphous-Amorphous Transitions in Carbon under Tribological Load, Lars Pastewka, Karlsruhe Institute of Technology, Institute for Applied Materials IAM, Germany INVITED**

Diamond and amorphous carbon (aC) are prototypical examples of wear resistant materials. Yet, these materials wear down, but little is known about the atomic scale processes that cause wear. Molecular dynamics is ideally suited to gain a deeper understanding of the underlying wear processes [1]. Such atomic-scale simulations reveal that both, mechanical and oxidative wear actions are active. Mechanical action transforms the material to a weaker state that is then easily oxidized. For diamond, we find a transition to an aC, while we find a high-density—low-density aC-aC transition for amorphous thin films. The velocity of the diamond/aC interface depends crucially on the diamond surface orientation with the highest speed found for (110) surfaces that are rubbed in the (001) direction, while the lowest interface speed was observed for the diamond (111) surface. High-density aC itself transforms even faster to a low density state that then succumbs to wear [2]. We relate the aC-aC transition to shear-banding in plasticity of amorphous materials, and argue that the formation of shear-bands is crucial for the wear resistance of carbon based hard coating. These findings are in perfect agreement with a 600 years old experimental knowledge of diamond polishers, and with recent experiments comparing wear in diamond and amorphous carbon thin films.

- [1] L. Pastewka, S. Moser, P. Gumbsch, M. Moseler, Nat. Mater. 10, 34 (2011)
- [2] T. Kunze, M. Posselt, S. Gemming, G. Seifert, A.R. Konicek, R.W. Carpick, L. Pastewka, M. Moseler, Tribol. Lett. 53, 119 (2014)

9:20am **TR+NS-ThM5 A Molecular Dynamics Investigation of the Atomic-Scale Wear of Carbon-Based Materials Upon Repetitive Contact, Kathleen Ryan, United States Naval Academy, V. Vahdat, University of Pennsylvania, P.L. Keating, United States Naval Academy, Y. Jiang, K.T. Turner, R.W. Carpick, University of Pennsylvania, J.A. Harrison, United States Naval Academy**

Amplitude modulation atomic force microscopy (AM-AFM) involves hundreds of thousands of contacts between a tip and surface per second. Each contact can result in the formation and breakage of chemical bonds causing wear to the tip. Atomic-scale wear hinders the quality and reproducibility of structures created by tip-based nanomanufacturing processes. However, wear cannot be analyzed at the single-atom level using existing experimental methods. Continuum mechanics models can be used to estimate stresses, deformations, and the work of adhesion. However, these models can break down at the nanoscale as they rely upon assumptions about the tip shape and material properties, and ignore the discrete atomic structure of the materials. Molecular dynamics (MD) simulations allow the nanoscale behavior to be modeled by resolving the positions, velocities, and forces of all atoms in the system. Here, MD simulations are used to model the repeated contact of an axisymmetric, hydrogenated amorphous carbon (a-C:H) tip with a 3-dimensional ultrananocrystalline (3D UNCD) surface. Using a finite element method to select the smallest portion of the tip that should be modeled atomistically, the tip radius could be set at 15 nm, much larger than previous simulations of this type and in the range of experimental AFM tip sizes. Tip/surface material and tip shapes were also chosen to closely mimic those used in comparable experiments. The wear processes, including adhesive forces, material transfer, and changes to material hybridization are examined following multiple contact cycles. We observe discrete atomic bonding and transfer events, as opposed to plastic deformation or fracture of multi-atom clusters. This is consistent with interpretations of experimental wear behavior and adds significant new detail to the possible pathways for the wear process.

9:40am **TR+NS-ThM6 The Buried Interface: *In Situ* Methods for Tribology**, *Brandon Krick*, Lehigh University, *K.G. Rowe, A.I. Bennett, D.W. Hahn, W.G. Sawyer*, University of Florida

Tribological phenomena occur at interfaces which are often difficult to directly observe or access. *In situ* techniques are rapidly emerging to probe surfaces buried at an interface, illuminating the physical, mechanical and chemical interactions between two surfaces in intimate contact. In this presentation, we discuss several *in situ* techniques, including optical microscopy of the real area of contact, thermal imaging of contact temperature, and Surface Plasmon Resonance of molecular transfer of a solid lubricant during sliding.

Utilizing an optical *in situ* microtribometer, we can explore the real area of contact and near contact surface topography of contacting surfaces; this technique has been used to visualize adhesive-elastic contact between a rigid sphere and a thin elastic foundation as well as randomly rough elastomer surface in contact with an infinitely stiff and flat (by comparison) surface. Similarly, an forward looking infrared (FLIR) microscope camera can reveal interface temperatures with microscopic resolutions. Finally, an *in situ* Surface Plasmon Resonance (SPR) tribometer is used to measure molecular-scale transfer of solid lubricants during sliding. For some systems, such as PTFE, transfer is detected as early as the first cycle of sliding, while minimal transfer is observed in other systems such as UHMWPE.

11:00am **TR+NS-ThM10 Contact and Friction Between Rough Adhesive Surfaces: From Atomic to Micrometer Scales**, *Mark Robbins*, Johns Hopkins University, *L. Pastewka*, Fraunhofer Institute for Mechanics of Materials IWM, Germany **INVITED**

Experimental surfaces typically have roughness on a wide range of length scales. This roughness greatly reduces the fraction of the area that is in intimate molecular contact and thus can contribute to friction and adhesion. The talk will first describe recent numerical calculations of elastic contact between rough surfaces with nominally flat or spherical geometries on large scales. An efficient Greens function approach allows calculations for systems with roughness on nanometer to micrometer scales to be performed with atomic resolution in the contact. Results for a wide range of geometries can be collapsed using simple scaling relations that depend on the root mean squared surface slope, sphere radius, elastic modulus, and work of adhesion. The scaling relations explain why adhesive interactions have little effect unless the surfaces are extremely smooth or soft. The traditional Fuller-Tabor model for adhesion of rough surfaces is shown to be qualitatively inconsistent with the simulations. The effect of atomic scale plasticity on contact and adhesion is surprisingly small. The talk will conclude by considering how forces in the contact area give rise to friction at larger scales.

11:40am **TR+NS-ThM12 Scaling Properties of Measured Frictional Parameters in Microscale Contacts**, *Brian P. Borovsky*, St. Olaf College

We present a study of the frictional properties of microscopic contacts (radius $\sim 1 \mu\text{m}$) in the high-speed regime ($> 1 \text{ m/s}$) during the initiation of full slip. Energy dissipation, lateral contact stiffness, and amplitude of motion are measured for a transverse-shear quartz resonator in contact with a small spherical probe. Averaged values for the elastic and dissipative forces are derived as functions of shearing amplitude, at constant normal loads in the range from $10 \mu\text{N}$ to 8 mN . We observe a transition from partial to full slip at a threshold amplitude of motion, characterized by a maximum elastic force. Kinetic friction in the full-slip regime is observed to be about a factor of two smaller than this elastic force limit. Data from tests at various normal loads can be collapsed onto common curves by normalizing the forces and amplitudes according their characteristic values. We discuss the observed scaling of these frictional parameters with the size of the contact and the extent of agreement with current theories of microslip.

12:00pm **TR+NS-ThM13 Scale Effects in Single-Asperity Friction**, *Tristan Sharp*, Johns Hopkins University, *L. Pastewka*, Fraunhofer Institute for Mechanics of Materials IWM, Germany, *M.O. Robbins*, Johns Hopkins University

Simulations are used to examine the static friction in model single-asperity contacts between a rigid sphere and a flat elastic substrate. The sphere radius R and the contact radius a are varied from nanometers to micrometers. First the case of commensurate contact between identical aligned surfaces with repulsive interactions is considered. For small contacts all contacting atoms move coherently and the friction coefficient μ is independent of contact radius and load. In larger contacts, interfacial slip is mediated by localized dislocations. At first μ decreases with increasing contact radius: $\mu \sim (Ra_0)^{1/2}/a$, where a_0 is the nearest-neighbor spacing. At even larger contact sizes, μ begins to drop more slowly. The results are in sharp contrast to Cattaneo-Mindlin continuum theory where μ is independent of contact size. Separate simulations are performed to connect

the results to the dislocation-based models of contact-size effects due to Hurtado and Kim, and Gao, which assume adhesive interactions between surfaces and find $\mu \sim (a_0/a)^{1/2}$. The talk will conclude with discussions of the effect of changes in the relative alignment of crystalline axes.

Thursday Afternoon, November 13, 2014

2D Materials Focus Topic

Room: 310 - Session 2D+EM+MI+MN+NS+SS+TF-ThA

Novel Quantum Phenomena in 2D Materials

Moderator: Alexander Sinitskii, University of Nebraska-Lincoln

2:20pm **2D+EM+MI+MN+NS+SS+TF-ThA1 Optoelectronics of Two-Dimensional Semiconductors**, Xiaodong Xu, University of Washington
INVITED

Two dimensional transition metal dichalcogenides are a recent addition to the 2D electronic materials family. They have shown outstanding electrical and optical properties for new optoelectronic device concepts. In this talk, we will first discuss the unique interplay between spin, valley, and layer pseudospins in bilayer WSe₂. Such coupling effects lead to electrical control of spin states and optical generation of valley coherence through interlayer triions, where electrons and holes are localized in different layers. We will then talk about optoelectronic devices based on monolayer WSe₂, including p-n junctions as light emitting diodes and hybrid monolayer semiconductor/photonic crystal cavity devices. We will conclude the talk with a discussion of the optoelectronic properties of MoSe₂-WSe₂ heterostructures.

3:00pm **2D+EM+MI+MN+NS+SS+TF-ThA3 Theory of Graphene Transport Barriers in the Specular Limit**, Daniel Gunlycke, C.T. White, Naval Research Laboratory

Offering room-temperature ballistic electron transport well over one micron, while being atomically thin and planar, graphene is undeniably a promising material for future nanoelectronic devices. Presently, however, switchable devices have normally low on-off ratios, a reflection of the challenge of selectively blocking electron and hole carriers from propagating across the graphene surface. This has stimulated a lot of research on different methods for making graphene nanoribbons that exhibit suitable band gaps. An alternative way to obtain a controllable gap takes advantage of resonant tunneling across a pair of transport barriers. For the latter approach, the key is to find a barrier that is fairly reflective but not so much as to effectively cut off all transport across it.

In this presentation, we present a model for straight transport barriers in graphene in the specular limit. Using the Lippmann-Schwinger equation, we obtain the wave function, from which we derive the reflection and transmission probabilities, as well as the local density of itinerant states. This local density of states exhibits fluctuations arising from quantum interference between incoming and outgoing matter waves that allow the transport properties of a barrier to be estimated without explicitly probing the current across the barrier. Our model is tested against exact multi-channel, tight-binding quantum transport calculations for graphene with weak local potentials, local strain, local adsorption, and a locally defective structure. As the model parameters are related to observable quantities, they could be obtained from theory and/or experiment, allowing the model to be adopted even when the precise details of the barrier are unknown.

3:20pm **2D+EM+MI+MN+NS+SS+TF-ThA4 Tip-induced Potential Confinement on Graphene in Scanning Tunneling Microscopy Measurement**, Yue Zhao, J. Chae, J.E. Wyrick, NIST/CNST, F.D. Natterer, Ecole Polytechnique Fédérale de Lausanne (EPFL), France, S. Jung, Korea Research Institute of Standards and Science (KRISS), A.F. Young, C.R. Dean, L. Wang, Y. Gao, Columbia University, J.N. Rodrigues, Graphene Research Centre, NUS, Singapore, K. Watanabe, T. Taniguchi, National Institute for Materials Science (NIMS), Japan, S. Adam, Graphene Research Centre, NUS, Singapore, J.C. Hone, K. Shepard, P. Kim, Columbia University, N.B. Zhitenev, J.A. Stroscio, NIST/CNST

Graphene is a two-dimensional-electron-gas(2DEG) system with exposed surface, which allows scanning tunneling microscopy(STM) to investigate the electron-electron interaction associated with the Dirac nature on a local scale, with a variety of tuning knobs, such as carrier density, spatially varying disorder potential, and applied magnetic field. However, the electron-electron interaction in graphene is sensitive to the disorder details. Moreover, tip induced potential confinement can significantly complicate the interpretation of STM experiment. Utilizing a high mobility graphene device with low residual disorder, we can minimize the effect of local potential fluctuation, to better understand the role tip-induced potential plays in the measurement. We observed the emergency of large spectra gaps, modification to graphene Landau levels (LLs), and quantum dots with changing size due to the spatially inhomogeneous tip gating.

4:00pm **2D+EM+MI+MN+NS+SS+TF-ThA6 Topological Phase Transitions and Spin-orbit Density Waves**, Hugo Dil, Ecole Polytechnique Fédérale de Lausanne (EPFL), Switzerland
INVITED

In recent years systems where the spin-orbit interaction (SOI) is not just a perturbation but the main energy scale have received increasing attention. In combination with a broken inversion symmetry in the crystal structure or at interfaces, SOI will lift the spin degeneracy and induce a complex Fermi surfaces and spin textures with spin momentum locking [1,2]. Furthermore, the SOI can drive the system through a phase transition to a so-called topological insulator. Being an insulator in the bulk these systems are characterized by spin-polarized, topologically protected interface states.

After a short introduction to the role of topology in the band structure of solids I will give an overview of our main spin- and angle-resolved photoemission (SARPES) results on a variety of non-interacting topological insulators [3]. One of the questions is how the spin texture evolves around a topological transition. We explored the occurrence of spin polarized states around a SOI driven topological transition [4] and around a structure driven topological transition [5]. In both cases we observe spin-polarized precursor states, which indicate that although the topological transition is sharp, the response of the system is more gradual.

From a fundamental point of view the truly interesting aspect of non-trivial spin textures lies in their combination with other interactions. This can result in a variety of phenomena, cumulating in the creation of the elusive Majorana Fermion. An example of a combination of interactions is our recent verification with SARPES of SmB₆ as a topological Kondo insulator [6]. In topologically trivial systems, interactions can lead to the formation of a so-called spin-orbit density wave. I will show how the combination of a large spin-splitting and Fermi nesting leads to the formation of such a state and can explain the anisotropic behavior of Pb nanowires [7]. Furthermore, I will present our recent SARPES results for transition metal oxide surfaces where a subtle interplay between ferroelectricity and magnetic order results in the formation of a single spin-polarized energy contour. The occurrence of superconductivity in such systems could render it a 2D Majorana platform.

[1] J.H. Dil, J. Phys: Cond. Mat. 21, 403001 (2009)

[2] G. Landolt et al. Phys. Rev. Lett. 109, 116403 (2012)

[3] D. Hsieh et al. Science 323, 919 (2009); D. Hsieh et al. Nature 460, 1101 (2009); S.Y. Xu et al. Science 332, 560 (2011); S. Ereemeev et al. Nature Comm. 3, 635 (2012)

[4] S.Y. Xu et al. arXiv:1204.6518

[5] G. Landolt et al. Phys. Rev. Lett. 112, 057601 (2014)

[6] N. Xu et al. Nature Materials (2014)

[7] C. Tegenkamp et al. Phys. Rev. Lett. 109, 266401 (2012)

4:40pm **2D+EM+MI+MN+NS+SS+TF-ThA8 The Symmetry Dependent Band Structure of MoS₂**, Duy Le, University of Central Florida, T. Komesu, University of Nebraska-Lincoln, Q. Ma, University of California, Riverside, E.F. Schwier, H. Iwasawa, Hiroshima University, Japan, M. Shimada, Higashi-Hiroshima, Japan, T.S. Rahman, University of Central Florida, L. Bartles, University of California, Riverside, P.A. Dowben, University of Nebraska-Lincoln

We will present results of density functional theory (DFT) based calculations of symmetry dependent band structures of single crystal MoS₂(0001) surface together with symmetry-polarized angle resolved photoemission spectroscopy (ARPES) derived experimental band structure. The good agreement of the DFT band structure with the experimentally derived bands with even and odd symmetries, attests to the reliability of the results. We performed ARPES at the Hiroshima Synchrotron, determining the MoS₂ band structure separately for both p- and s-, polarized to distinguish even and odd symmetry, and the experimentally determined dispersion, in accordance with expectations and experimental confirmation of C_{3v} symmetry, argues in favor of an experimental band structure obtained from single domains. The comparison of theory and experiment provides strong indications that the bands at the top of the valence band are dominated by Mo 4d states. These states and indeed placement of the valence band can be perturbed by adsorbates. Indeed, we find that, under the effect of Na adsorption, the changing placement of the valence band structure of MoS₂ clearly indicate the Na atoms donate electrons to MoS₂ and that the Fermi energy level shifts as much as 0.5 eV with respect to the top of MoS₂'s valence band. Surprisingly, Na adsorption does not perturb the MoS₂ band dispersion significantly. We will discuss these results in the light of those obtained for single layer MoS₂ for insights and clarity.

5:00pm **2D+EM+MI+MN+NS+SS+TF-ThA9 CuIn_mP₂S₆ - Room Temperature Layered Ferroelectric**, Alex Belianinov, P. Maksymovych, Oak Ridge National Laboratory, A. Dziugys, Vilnius University, Lithuania, Q. He, Oak Ridge National Laboratory, E. Eliseev, National Academy of Sciences of Ukraine, A. Borisevich, Oak Ridge National Laboratory, A. Morozovska, NAS of Ukraine, J. Banys, Vilnius University, Lithuania, Y. Vysochanskii, Uzhgorod University, Ukraine, S.V. Kalinin, Oak Ridge National Laboratory

We have utilized ambient and Ultra High Vacuum Scanning Probe Microscopy tools to explore ferroelectric properties in cleaved 2D flakes of copper indium thiophosphate, CuIn_mP₂S₆ (CITP), and report on size effect and presently achievable limits of ferroelectric phase stability. CITP is an unusual example of a layered, anti-collinear, uncompensated, two-sublattice ferroelectric system. These are the only materials known to display “2-D” ferroelectric semiconductor behavior in a van-der-Waals crystal. The material exhibits a first-order phase transition of order–disorder type from the paraelectric to the ferroelectric phase at $T_c = 315$ K. Our observations suggest the presence of stable ferroelectric polarization as evidenced by domain structures, rewritable polarization, and hysteresis loops. These observations suggest that flakes above 100 nm have bulk-like polarization and domain structures, whereas below 50 nm polarization disappears. Furthermore, the materials have measurable ionic mobility, as evidenced both by macroscopic measurements and by formation of surface damage above tip bias of 4 V, likely due to copper reduction. We ascribe this behavior to well-known instability of polarization due to depolarization field, along with internal screening by mobile Cu ions, as suggested by their high ionic mobility.

Acknowledgement:

Research for (AB, PM, QH, AB, SVK) was supported by the US Department of Energy, Basic Energy Sciences, Materials Sciences and Engineering Division. Research was conducted at the Center for Nanophase Materials Sciences, which is sponsored at Oak Ridge National Laboratory by the Scientific User Facilities Division, Office of Basic Energy Sciences, US Department of Energy.

5:20pm **2D+EM+MI+MN+NS+SS+TF-ThA10 Doping Efficiency and Mechanisms of Single and Randomly Stacked Bilayer Graphene by Iodine Adsorption**, Hokwon Kim, A. Tyurnina, Univ. Grenoble Alpes/CEA, LETI, France, J.-F. Guillet, J.-P. Simonato, J. Dijon, Univ. Grenoble Alpes/CEA, LITEN, France, D. Rouchon, D. Mariolle, N. Chevalier, O.J. Renault, Univ. Grenoble Alpes/CEA, LETI, France

The precise control of graphene's conductivity and work function is crucial in developing practical applications of graphene based electronics. In order to enhance the conductivity of graphene, we employed a simple doping method where graphene films produced by chemical vapor deposition and transferred onto SiO₂, Al₂O₃, and WO₃ substrates are p-doped with iodine vapor through physisorption at temperature of ~ 100 °C [1-3]. The work function values and iodine to carbon ratios of the one-layer (1L) and two-layer (2L) folded regions were analyzed by high spatial- and energy resolution X-ray photoelectron emission microscopy (XPEEM) on a NanoESCA instrument. After the iodine doping, the work function values were significantly increased up to ~0.4 eV and ~0.5 eV, respectively, for 1L and 2L graphene on SiO₂/Si. This higher degree of doping by iodine was corroborated by I 3d_{5/2} core level imaging of the same area where the 2L graphene exhibited significantly larger concentration of iodine (2 at. % versus 1 at. %) likely due to the intercalation of iodine at the inter-layer space.

The main iodine species identified by high resolution core level X-ray photoemission spectroscopy and Raman spectroscopy were I₃⁻ and I₅⁻ polyiodide anionic complexes with slightly higher concentration of I₅⁻ in 2L than 1L graphene possibly due to different doping mechanisms. Temperature dependent ultra-high-vacuum, in-situ annealing of the doped films has demonstrated that most of iodine is removed above 300 °C for the both 1L and 2L regions, although a significant removal of iodine is observed for 2L graphene at temperature as low as 100 °C. Surprisingly, after the complete removal of iodine by annealing, the work function value did not return to the original one before the doping treatment and remained at a much higher value. This can be ascribed to the residual hydrocarbon contaminations interacting with the atomic defects within the graphene layer that lead to unintentional n-type doping in our samples[4].

Acknowledgement: The XPEEM and KFM measurements were performed at the Nanocharacterization Platform (PFNC).

References

- [1] L. Grigorian, K.A. Williams, S. Fang, G.U. Sumanasekera, A.L. Loper, E.C. Dickey, S.J. Pennycook, P.C. Eklund, Phys. Rev. Lett., (1998) 5560-5563.
- [2] A.B. Kaiser, Rep. Prog. Phys., (2001) 1.

[3] S.W. Chu, S.J. Baek, D.C. Kim, S. Seo, J.S. Kim, Y.W. Park, Synth. Met., (2012) 1689-1693.

[4] B.H. Kim, S.J. Hong, S.J. Baek, H.Y. Jeong, N. Park, M. Lee, S.W. Lee, M. Park, S.W. Chu, H.S. Shin, J. Lim, J.C. Lee, Y. Jun, Y.W. Park, Sci. Rep., (2012).

5:40pm **2D+EM+MI+MN+NS+SS+TF-ThA11 Use of XPS for Device Characterization**, P. Aydogan, E.O. Polat, C. Kocabas, Sefik Suzer, Bilkent University, Turkey

A noncontact chemical and electrical measurement technique of XPS is utilized to investigate a number of devices made of graphene. The main objective of the technique is to trace chemical and location specific surface potential variations as shifts of the XPS peak positions under operating conditions. Devices consisting of graphene; (i) acting as a simple resistive element between two gold electrodes, (ii) a semiconducting sheet controlled by a back-gate, and (iii) between the source and the drain metal electrodes in a full transistor geometry, have been analyzed by recording the Au4f of the metal electrodes, the C1s of the graphene layer, and the O1s (or N1s) peaks of the silicon oxide (or nitride) of the substrate. The advantage of this technique is its ability to assess element specific surface electrical potentials of devices under operation based on the deviations of the core level peak positions in surface domains/structures. Detection of the variations in electrical potentials and especially their responses to various stimuli gives unprecedented information about the chemical nature as well as the location of structural and/or other types of defects as a result of doping, oxidation, reduction, etc.

Atom Probe Tomography Focus Topic

Room: 301 - Session AP+AS+EN+NS+SS-ThA

APT and FIM Analysis of Catalysts and Nanomaterials

Moderator: David Diercks, Colorado School of Mines, David Larson, CAMECA Instruments Inc.

2:20pm **AP+AS+EN+NS+SS-ThA1 In Situ Study of Gas - Solid Reactions via Environmental APT**, Krishna Rajan, Iowa State University **INVITED**

In this presentation we describe the design and examples of applications of the use of an environmental cell integrated into a LEAP atom probe. The use of such a cell helps to open up the field of in-situ gas-solid reactions by permitting one to study surface and near surface reactions which are closer to ambient conditions than is possible in traditional surfaces science studies. The implications for this experimental approach in the context of the study of catalysts and nanomaterials are discussed.

3:00pm **AP+AS+EN+NS+SS-ThA3 Propagation of Chemical Waves: A Field Emission Microscopy Study**, Cédric Barroo, Y. De Decker, N. Kruse, T. Visart de Bocarmé, Université Libre de Bruxelles, Belgium

The catalytic hydrogenation of NO₂ over platinum field emitter tips has been investigated by means of field emission techniques. Field emission microscopy (FEM), as well as field ion microscopy (FIM), has been proved to be an efficient method to study the dynamics of catalytic reactions occurring at the surface of a nanosized metal tip, which represents a good model of a single catalytic nanoparticle. These studies are performed during the ongoing reaction which is imaged in real time and space. Nanoscale resolution allows for a local indication of the instantaneous surface composition.

The presence of adsorbates modifies the value of the local work function. These variations are expressed by modulations of the brightness of field emission patterns. A qualitative investigation of the local surface composition is then possible as function of time.

The microscope is run as an open nanoreactor, ensuring that the system is kept far from thermodynamic equilibrium. Under these conditions, chemical reactions can induce time and space symmetry breaking of the composition of a system, for which periodic oscillations and target patterns are well-known examples.

Self-sustained periodic oscillations have been reported for the NO₂ reduction. By increasing the time resolution of the system, it is now possible to study the emergence of these oscillations and to observe the propagation of chemical waves at the nanoscale, on a single facet of a nanocrystal. The velocity of wave propagation is estimated to be in the μm/s range, which is in accordance with previous studies of catalytic reaction at the mesoscale.

3:20pm **AP+AS+EN+NS+SS-ThA4 3D Nanoscale Chemical/Structure Analysis in Mineral Carbon Sequestration Study using Atom Probe Tomography**, *Jia Liu, D.E. Perea, R.J. Colby, L. Kovarik, B. Arey, O. Qafoku, A. Felmy*, Pacific Northwest National Laboratory

Mineral carbon sequestration is one of the important means to store CO₂ in order to mitigate the environmental concern regarding ever-growing anthropogenic CO₂ emissions. Olivines, X₂SiO₄ where X = Mg and Fe, hold promise as potential media to sequester carbon due to its broad availability in basalt deposits and reactivity to form stable metal carbonates. Site-specific reactivity of olivine with supercritical CO₂ is of great interest in understanding the fundamental elementary reaction mechanisms, where the presence of impurities within the bulk mineral may affect reaction kinetics. A combination of atom probe tomography (APT) and scanning transmission electron microscopy (STEM) is being used to map the complex composition and nanoscale structure across various site-specific regions. APT analysis of unreacted natural fayalite indicates the presence of 2-3-nm-thick hydrated iron oxide layers. In addition, Na impurities were found to concentrate within the hydrated layers while Mg and Mn were depleted from these regions. With the ability of APT to detect the chemical/structural heterogeneity at nanometer-scale, we find that APT will provide a means to correlate with ongoing experimental reaction studies and also provide guidance into models of the heterogeneous phase formation and reaction rates at precisely defined interfaces within minerals.

4:00pm **AP+AS+EN+NS+SS-ThA6 Catalyst Nanomaterials Analysis via Atom Probe Tomography**, *P.A.J. Bagot*, Oxford University, UK, *Q. Yang*, University of Oxford, UK, *K. Kruska*, Pacific Northwest National Laboratory, *D. Haley*, University of Oxford, UK, *E. Marceau, X. Carrier*, Université Pierre et Marie Curie, France, **Michael Moody**, UNIVERSITY OF OXFORD, UK

INVITED

Heterogeneous catalytic materials play an increasingly critical, yet largely unnoticed, role underpinning countless modern technologies. Their active components are generally transition group metals, each of which offers different catalytic properties in terms of selectivity, yield and stability under demanding operating conditions. The need to develop more efficient catalysts that meet industrial demands and comply with environmental legislation targets requires better understanding how different catalysts may alter at the atomic scale in terms of structure or surface composition under their respective operating environments. Further, many catalysts take the form of nanoparticles, the performance of which can be strongly correlated to size, shape, chemistry and structure. However, discerning the nature of nanoparticles scale poses significant challenges to conventional microscopy.

Recently, atom probe tomography (APT) techniques have been developed to provide unique insight into the behaviour of catalyst alloys subject to conditions like those experienced in service [1–3]. This study is aimed at more accurate and insightful analyses comprising unique 3D atomistic descriptions of the evolving alloy nanostructure which can then be correlated to catalyst performance. Here, APT results are presented for characterization of oxidation-induced segregation in a Pt-Pd-Rh gauze and Fe-Ni alloy catalysts. Progress in the development of new approaches for the analysis of nanoparticles via APT is also presented.

[1] T. Li et al., Atomic engineering of platinum alloy surfaces. *Ultramicroscopy* 132, 205 (2013).

[2] T. Li et al., Atomic Imaging of Carbon-Supported Pt, Pt/Co, and Ir@Pt Nanocatalysts by Atom-Probe Tomography. *ACS Catalysis* 4, 695 (2014).

[3] P. Felfer et al, Long-Chain Terminal Alcohols through Catalytic CO Hydrogenation. *Journal of the American Chemical Society* 135, 7114 (2013).

Scanning Probe Microscopy Focus Topic

Room: 312 - Session SP+AS+BI+NS+SS-ThA

Probing Chemical Reactions at the Nanoscale

Moderator: Carl Ventrice, Jr., University at Albany-SUNY, Jun Nogami, University of Toronto, Canada

2:20pm **SP+AS+BI+NS+SS-ThA1 Surface Structures of Catalysts in Reactive Environments with Scanning Tunneling Microscopy**, *Franklin (Feng) Tao, L.T. Nguyen*, University of Notre Dame

INVITED

Structure and chemistry of catalysts under a reaction condition or during catalysis are the key factors for understanding heterogeneous catalysis. Advance in ambient pressure photoelectron spectroscopy has taken place over the last decades, which can track surface chemistry of catalysts in gas environment of Torr or even tens of Torr pressure range. Environmental TEM has been developed for studying structures of catalysts while they are

in a gas or liquid phase. In terms of environmental TEM, images at a pressure up to bars have been obtained although 1-10 Torr to one bar is the typical pressure range of in-situ studies of catalysts by E-TEM. Compared to structural and chemical information of catalyst particles offered from environmental TEM, packing of adsorbed molecules on a catalyst surface and arrangement of catalyst atoms of catalyst surface are complementary for the structure information provided by environmental TEM. High pressure scanning tunneling microscopy (HP-STM) is the most appropriate technique to achieve these pieces of important information. With the HP-STM the structures of surfaces of model catalysts under a reaction condition or during catalysis can be visualized. Surface structures of catalysts only formed under a reaction condition or during catalysis can be tracked. Such information is significant for understanding catalysis performed at solid-gas interfaces.

In this talk, I will present the historical development of HP-STM. Then, I will review the pressure-dependent packing of chemisorbed molecules; one type of pressure dependence is the change of packing of adsorbates from site-specific binding in UHV or a gas phase with a low pressure to non-specific binding in a gas phase at a relatively high pressure; the other type is a switch from one specific binding site to another specific binding site along the increase of the pressure of gas phase of the reactant. In addition, restructuring of a catalyst surface is another consequence of the increase of the gas phase pressure. The threshold pressure at which a restructuring is performed depends on the original surface structure and the intrinsic electronic state of the metal. I will review the surface restructurings of metal model catalysts including different vicinal surfaces in different reactant gases. In addition, the in-situ studies of Pt(110) and Rh(110) during CO oxidation will be taken as two examples to illustrate the in-situ studies of surfaces of metal model catalysts under reaction conditions (in a gas phase of one reactant) and during catalysis (in a mixture of all reactants of a catalytic reaction).

3:00pm **SP+AS+BI+NS+SS-ThA3 Numerical Analysis of Amplitude Modulation Atomic Force Microscopy in Aqueous Salt Solutions**, *P. Karayaylali, Mehmet Z. Baykara*, Bilkent University, Turkey

We present a numerical analysis of amplitude modulation atomic force microscopy in aqueous salt solutions, by considering the interaction of the microscope tip with a model sample surface consisting of a hard substrate and soft biological material through Hertz and electrostatic double layer forces (P. Karayaylali and M.Z. Baykara, *Applied Surface Science*, 2014, DOI: [10.1016/j.apsusc.2014.02.016](https://doi.org/10.1016/j.apsusc.2014.02.016)). Despite the significant improvements reported in the literature concerning contact-mode atomic force microscopy measurements of biological material due to electrostatic interactions in aqueous solutions, our results reveal that only modest gains of ~15% in imaging contrast at high amplitude set-points are expected under typical experimental conditions for amplitude modulation atomic force microscopy, together with relatively unaffected sample indentation and maximum tip-sample interaction values.

3:20pm **SP+AS+BI+NS+SS-ThA4 Surface Potential Investigation of AlGaAs/GaAs Heterostructures by Kelvin Force Microscopy**, *S. Pouch, Nicolas Chevalier, D. Mariolle, F. Triozon, Y.M. Niquet, T. Melin, L. Borowik*, CEA, LETI, MINATEC Campus, France

The Kelvin force microscopy (KFM) provides a spatially resolved measurement of the surface potential, which is related to the energetic band structure of a material. However, it depends strongly on the physical properties of the tip, e.g. width of the apex, the geometric shape and the stiffness of the cantilever as well as the surface sample state. The goal of this work is to investigate the surface potential measured by KFM on AlGaAs/GaAs heterostructures. For this study, we used a certified reference sample (BAM-L200), which is a cross section of GaAs and Al_{0.7}Ga_{0.3}As epitaxially grown layers with a decreasing thickness (600 to 2 nm) and a uniform silicon doping (5 × 10¹⁷ cm⁻³). The resulting stripe patterns are commonly used for length calibration and testing of spatial resolution in imaging characterization tools (ToF-SIMS, SEM, XPEEM...) The surface potential measurement is performed under ultra-high vacuum with an Omicron system by using two acquisition modes: the amplitude modulation (AM-KFM), sensitive to the electrostatic force and the frequency modulation (FM-KFM), sensitive to its gradient. Three kinds of tips have been used for this study: platinum or gold nanoparticles coated silicon tips and super sharp silicon tips.

We will present the measurements obtained with these different tips for the narrowest layers (typ. < 40 nm). The surface potential mapping reveals a contrast around 300 meV between Al_{0.7}Ga_{0.3}As and GaAs layers. However, we observed that this contrast vanishes when layer thickness becomes thinner. This loss of contrast cannot be only explained by the resolution limit of the KFM technique. Indeed, we will discuss the effect of the band bending length scale at the AlGaAs/GaAs interface related to the dopant concentration. The contribution of band bending between the layers is evaluated by a self-consistent simulation of the electrostatic potential,

accounting for the free carriers distribution inside the sample and for the surface and interface dipoles. We will show that the electric fields of the narrowest layers recover each other, resulting in the partial or total loss of the contrast between $\text{Al}_{0.7}\text{Ga}_{0.3}\text{As}$ and GaAs layers. The simulation results will be compared to the experimental results in order to emphasize that the surface potential contrast is not only influenced by the resolution limit.

4:00pm **SP+AS+BI+NS+SS-ThA6 Probing the Quantum Nature of Hydrogen Bonds at Single Bond Limit in Interfacial Water**, *Ying Jiang*, Peking University, China **INVITED**

Quantum behaviors of protons in terms of tunneling and zero-point motion have significant effects on water properties, structure, and dynamics even at room and at higher temperature. In spite of tremendous theoretical and experimental efforts, accurate and quantitative description of the quantum nuclear effects (QNEs) in water is still challenging, due to the difficulty of accessing the internal degrees of freedom of water molecules. Using a low-temperature scanning tunneling microscope (STM), we are able to resolve in real space the internal structure, that is, the O-H directionality, of individual water molecules adsorbed on a solid surface [1,2]. The key steps are decoupling electronically the water from the metal substrate by inserting an insulating NaCl layer and enhancing the molecular density of states of water around the Fermi level via tip-water coupling. These techniques allow us not only to visualize the concerted quantum tunneling of protons within the H-bonded network, but also to determine the impact of proton delocalization on the strength of hydrogen bonds by resonantly enhanced inelastic electron tunneling spectroscopy (IETS).

Key words: STM, IETS, water, QNEs, proton transfer, H-bonding strength

[1] J. Guo, X. Z. Meng, J. Chen, J. B. Peng, J. M. Sheng, X. Z. Li, L. M. Xu, J. R. Shi, E. G. Wang*, and Y. Jiang*, "Real-space imaging of interfacial water with submolecular resolution", *Nature Materials* 13, 184 (2014).

[2] J. Chen, J. Guo, X. Z. Meng, J. B. Peng, J. M. Sheng, L. M. Xu, Y. Jiang*, X. Z. Li*, E. G. Wang, "An unconventional bilayer ice structure on a NaCl(001) film", *Nature Communications* 5, 4056 (2014).

4:40pm **SP+AS+BI+NS+SS-ThA8 Resonant Enhanced Spectroscopy of Molecular Rotations with the STM and Field Effect Control of Molecular Dynamics**, *Fabian Natterer*, F. Patthey, Ecole Polytechnique Fédérale de Lausanne (EPFL), Switzerland, *Y. Zhao*, J.E. Wyrick, J.A. Stroscio, NIST, *H. Brune*, Ecole Polytechnique Fédérale de Lausanne (EPFL), Switzerland

Inelastic electron tunneling spectroscopy (IETS) with the scanning tunneling microscope (STM) has vastly fueled the study of magnetic, electronic and vibrational properties of individual atoms and molecules due to its unmatched spatial and excellent energy resolution. Recently [1,2], rotational excitations could be characterized with IETS for the first time and yielded valuable insights into surface dynamics, bond lengths, and, notably about the nuclear spin state of homonuclear molecules. In particular, the two alike nuclei induce symmetry constraints in consequence of the Pauli principle and a certain alignment of nuclear spins requires a specific set of rotational levels J . We demonstrate rotational excitation spectroscopy (RES) with the STM for hydrogen, its isotopes, and mixtures thereof, physisorbed on metal supported graphene and hexagonal boron nitride, as well as on exfoliated graphene devices. We observe excitation energies that are equivalent with rotational transitions ($\Delta J = 2$) of molecules in the gas phase for hydrogen, hydrogen-deuteride, and deuterium, respectively. Notably, these values represent the nuclear spin isomers *para*- H_2 and *ortho*- D_2 . For HD, an additional $J = 0 \rightarrow 1$ transition is discerned, which is allowed for heteronuclear diatomics. We discuss the excitation mechanism in the light of resonant enhanced tunneling [3,4], and illustrate how the dynamics of molecules could be controlled by applying an electric field using a back gating graphene device geometry [5].

[1] F. D. Natterer, F. Patthey, H. Brune, *Phys. Rev. Lett.* **111**, 175303 (2013)

[2] Li *et al.*, *Phys. Rev. Lett.* **111**, 146102 (2013)

[3] F. D. Natterer, F. Patthey, H. Brune, *arXiv*:1403.1312 (2014)

[4] B. N. Persson, A. Baratoff, *Phys. Rev. Lett.* **59**, 339 (1987)

[5] J. Chae *et al.*, *Phys. Rev. Lett.* **109**, 116802 (2012)

Funding from the Swiss National Science Foundation under project number 148891 is greatly appreciated.

Surface Science

Room: 309 - Session SS+AS+NS-ThA

Semiconductor Surfaces and Interfaces 1

Moderator: Ludwig Bartels, University of California - Riverside, Kurt Kolasinski, West Chester University

2:20pm **SS+AS+NS-ThA1 A Study of the InAs(001) Surface Electronic Structure**, *Jacek Kolodziej*, *N. Tomaszewska*, *P. Ciochon*, Jagiellonian University, Poland

Angle-resolved photoelectron spectroscopy (ARPES) is used to study electronic bands at the n-type InAs(001) surfaces, having several different reconstructions. Indium-rich $(8 \times 2)/(4 \times 2)$ and arsenic-rich $c(2 \times 8)/(2 \times 4)$ surfaces as well as sulphur passivated (2×1) surface are prepared and investigated. Measured electronic bands are identified by analysis of their symmetries in the k-space.

In InAs crystal bulk the conduction band minimum (CBM) is located very close to the Fermi level (FL). Downward band bending, typical for the studied surfaces, causes formation of two dimensional electron gas, confined in a subsurface well, also known as the electron accumulation layer. This is indicated by characteristic quantized subband states visible in the ARPES spectra.

It is shown that the band bending magnitude and the quantization (of the accumulated electron energies associated with the coordinate normal to the surface) depend on the surface reconstruction as well as on the crystal doping. In most cases the electron accumulation bands are found at the Fermi level and close to the Γ_{1x1} symmetry point in the center of the surface Brillouin zone. The most clear picture is observed for the sulphur passivated (2×1) surface, where three distinct subbands with minima at $E_1 = -0,276\text{eV}$, $E_2 = -0,096\text{eV}$ and $E_3 = -0,039\text{eV}$ with reference to Fermi level are found. Unexpectedly, for the indium rich surface, occupied conduction states are found also at Γ_{4x2} symmetry points indicating that, for this case, surface resonances mix with the electron accumulation states.

It is also shown that the observed surface bands are sensitive to surface treatment. Two surface preparation techniques have been used: cycles of ion beam annealing (IBA) and *ex situ* wet chemical treatment (WCT). Although low electron energy diffraction (LEED) indicates no increased disorder on the IBA surfaces they yield considerably worse electronic band images. This is most likely due to scattering of photoelectrons on the electrically active antisite defects.

We acknowledge financial support by Polish NCN (contract 2011/03/B/ST3/02070). The research was carried out with the equipment purchased thanks to European Regional Development Fund in the framework of the Polish Innovation Economy Operational Program (contract no. POIG.02.01.00-12-023/08).

2:40pm **SS+AS+NS-ThA2 Control of Point Defect Behavior in Metal Oxides via Surface Band Bending**, *M. Li*, *P. Gorai*, *Edmund Seebauer*, University of Illinois at Urbana-Champaign

Point defects within metal oxide semiconductors such as ZnO affect the material's performance in applications for nanoelectronics, gas sensing, photonics and photocatalysis. Past work in this laboratory has shown that the presence of a nearby surface can influence the concentrations and spatial distributions of defects deep within the semiconductor – often in a controllable way. One mechanism for this influence involves band bending near the surface. The present work employs the optical modulation technique of photoreflectance to measure the magnitude V_s of band bending at polar c-axis ZnO surfaces, and demonstrates that V_s can be manipulated over a significant range (roughly 0.23-0.44 eV) through variations of both temperature and the ambient partial pressure of O_2 . Separate modeling of charged oxygen interstitial motion within the ZnO indicates that the near-surface concentration of these defects scales quadratically with V_s , thereby pointing to a novel general approach by which bulk point defect concentrations can be controlled.

3:00pm **SS+AS+NS-ThA3 Evolution of Surface-Assisted Oxidation of GaAs by Gas-Phase N_2O , NO and O_2** , *Xueqiang Zhang*, *S. Ptasinska*, University of Notre Dame

Interests in metal-insulator-semiconductor field effect transistors (MISFETs) have been re-ignited recently due to the approaching of the scaling limit of Si complementary metal-oxide-semiconductors (CMOS). The fate of the III-V semiconductors relies strongly on the availability of a suitable surface passivation technology for fabrication of high quality insulator/III-V semiconductor interface. Gallium oxides on GaAs represent one of contenders for suitable surface passivated oxide-based dielectrics that could produce device-quality electrical interfaces between the oxide

and semiconductor. However, there has been a debate on possible GaAs oxidation mechanisms over years. A comparisomal study between O₂ and other reactive but heteronuclear molecules (such as NO and N₂O) near realistic conditions would provide new insights for a better understanding of the GaAs oxidation process.

A near-ambient pressure X-ray photoelectron spectroscopy (NAP XPS) study of interfacial chemistry between GaAs (100) and three oxidizing gases, N₂O, NO and O₂, are carried out in a wide range of pressures and temperatures. At room temperature, surface oxidation, involving the formation of both Ga₂O and Ga₂O₃ is observed with the extent of oxidation in the order of NO>O₂>N₂O at elevated pressures. At elevated temperatures, the extent of oxidation is in the order of O₂>NO>N₂O. Our experimental results show that the oxidation of GaAs (100) by N₂O and NO is primarily determined by the probability and nature of interactions at the gas/semiconductor interface, whereas the limiting factor in the case of O₂ is the energy requirement for O-O bond dissociation.

3:20pm SS+AS+NS-ThA4 Morphology Dependence of Gas-Phase Molecule Interactions with GaAs Surfaces, *Sylwia Ptasinska, X.Q. Zhang*, University of Notre Dame

A great deal of progress has been made in understanding molecular interactions at the interface of two-dimensional GaAs systems under ultra-high vacuum (UHV) conditions. While research on understanding of such interactions with lower-dimensional GaAs-based structures, such as one-dimensional nanowires (NWs), has not been performed despite the potential importance of these structures for developing nano-electronic circuits. Moreover, surface characterization of GaAs under more realistic than the UHV studies, are critical in any attempt to correlate surface chemistry with device properties.

Nowadays, due to recent developments in the surface characterization techniques, and especially the development of Near Ambient Pressure X-ray Photoelectron Spectroscopy (NAP XPS) [1], we are able to track surface chemistry in-situ under elevated pressures and temperatures for different morphologies.

In our present study we used NAP XPS to investigate the interaction of a radically non-planar GaAs surface comprised of an ensemble of GaAs NWs with O₂ and H₂O molecules. In this study the evolution of O₂ and H₂O molecule dissociation on GaAs NWs is tracked under in-situ conditions as a function of temperature and gas pressure to establish whether these processes depend on surface morphology. In contrast to ideally flat GaAs single crystal surfaces that are previously studied [2], gas molecules experienced the enhanced dissociation on GaAs NW ensembles due to an increase in the surface area ratio and the presence of stepped edges, atom vacancies, and other defects on non-flat semiconductor surfaces [3].

[1] D. E. Starr, Z. Liu, M. Havecker, A. Knop-Gericke, and H. Bluhm, Investigation of solid/vapor interfaces using ambient pressure X-ray photoelectron spectroscopy, *Chem. Soc. Rev.* 42, 5833-5857 (2013)

[2] X. Zhang, S. Ptasinska, Dissociative Adsorption of Water on an H₂O/GaAs(100) Interface-in-Situ near Ambient Pressure XPS Studies, *J. Phys. Chem. C* 118, 4259-4266 (2014)

[3] X. Zhang, E. Lamere, X. Liu, J. K. Furdyna, S. Ptasinska, Morphology Dependence of Interfacial Oxidation States of Gallium Arsenide under near Ambient Conditions, *Appl. Phys. Lett.* DOI:10.1063/1.4874983 (2014)

4:00pm SS+AS+NS-ThA6 STM Imaging of the Buried Interface Structures at Ultra-thin Ag Films/Si(111) Substrates, *Y. Yoshiike, I. Kokubo, Y. Aoki, K. Nakatsuji, Hiroyuki Hirayama*, Tokyo Institute of Technology, Japan

The Schottky barrier height (SBH) has been reported to change sensitively to the variety of reconstructions at the Si substrates before depositing metal films in such systems as Pb/Si(111) and Ag/Si(111). Meanwhile, metal and Si do not mix, and the interfaces between the metals films and Si substrates are atomically abrupt in these systems. Thus, reconstructions at the Si(111) substrate are regarded to be preserved at buried interfaces under metal films, and have an influence on the SBH. In this respect, direct characterization of the buried interface structures in real space is required.

Scanning tunneling microscopy (STM) is a potentially promising method to achieve this, although it is conventionally considered to be useful only for exposed surfaces. Substantially, two different patterns, which were regarded to reflect the periodicity of the lattice at the buried interfaces, were observed on ultra-thin Pb films on the Si(111) substrates. However, the relation to the buried interface structures and the reason for the visualization were still not elucidated. With regard to these points, it is of significant interest to examine whether a different reconstruction on the Si(111) substrate could cause various periodic patterns in abrupt interface systems other than the Pb/Si(111). It is also of interest to investigate the origin of the new periodic pattern. From this perspective, we investigated the STM images of ultra-thin Ag films on Si(111) $\sqrt{3}\times\sqrt{3}$ -B and Si(111)7x7 substrates in this study.

As results, ripples were observed at the surface of ultra-thin Ag films on a Si(111) $\sqrt{3}\times\sqrt{3}$ -B substrate system in STM and dI/dV images. The ripples were faint, independent of the bias voltage, and had the 3x3 periodicity. These indicate that the ripples were geometric corrugations formed at the Ag film surface, which were induced by the commensuration of the Ag(111)1x1 and Si(111) $\sqrt{3}\times\sqrt{3}$ -B lattices at the buried interface. In the meantime, a different ripples were observed at the surface of ultra-thin Ag films on a Si(111)7x7 substrate. The ripples were less periodic, but the Fast Fourier Transform of the images revealed that they had the 7x7 periodicity. In contrast to the Pb/Si(111)7x7 system, the ripples were independent of the bias voltage. Thus, the 7x7 ripple was also regarded to reflect the interface commensuration-induced geometric corrugations at the Ag film surfaces. More detailed results and Synchrotron radiated X-ray diffraction data of these buried interfaces will be shown and discussed in the presentation.

4:20pm SS+AS+NS-ThA7 Ge on Si Epitaxy: Formation of 3D Ge Islands on Si(100)-2x1 by Annealing of Ge Wetting Layers, *Gopalakrishnan Ramalingam, P. Reinke*, University of Virginia

The epitaxial growth of Ge on Si(100)-(2x1) proceeds by Stranski-Krastanow (SK) mode where the formation of a wetting layer (WL) is followed by the emergence of quantum dots (QD). New growth modes have been reported recently which can lead to highly anisotropic Ge-wires and are achieved by annealing of the WL prior to the onset of QDs. The goal of the current work is to understand the atomistic processes involved in the transformation of the WL during annealing. We have investigated the WL structure during post-growth annealing at 400 to 600 C and report the transformation of epitaxial two dimensional Ge wetting layers into three dimensional islands, referred to here as pre-quantum dots (p-QDs). The p-QDs include hillocks with a stacked, wedding-cake type structure which show a progression to partial {105} faceting in case of thicker Ge WLs and longer anneal times. At low WL thickness (1-1.5 ML), the p-QDs have a stacked structure while thicker WLs (2-3.5 ML) lead to partial {105} faceted structures. All p-QDs, irrespective of the faceting or size, are characterized by an amorphous mound at the apex; this is strictly limited to p-QDs and not observed for regular QDs. The transition from the WL to p-QDs depends sensitively on the WL thickness (for a given annealing temperature): a six-fold increase in the island number density and a similar decrease in average island volume are observed when the initial WL thickness was increased from 1.2 to 3.5 ML. A small but notable increase in the island number density is observed when samples are annealed for longer durations (after the initial anneal to form the p-QDs) confirming that Ostwald ripening is not a dominant process in this system. Our observations will be integrated with a simulation of the growth process which will inform on the relevant mass transport and the role of strain on the WL transformation to p-QDs.

4:40pm SS+AS+NS-ThA8 In Search of Nanopatterns: STM Provides Mechanistic Insights into Silicon Functionalization, *Erik Skibinski*, Cornell University, *W.J.I. DeBenedetti, Y.J. Chabal*, University of Texas at Dallas, *M.A. Hines*, Cornell University

Functionalization reactions leave characteristic patterns on surfaces that can be read by STM, providing insight into reaction mechanisms. The functionalization of silicon surfaces with organic monolayers has attracted interest for applications ranging from chemical and biological sensing to renewable energy. A wide variety of surface functionalization reactions have been developed based on dehydration reactions that target surface -OH groups on oxidized silicon. Uniform functionalization therefore requires a uniform, high density of surface -OH groups. Hydroxylating silicon surfaces without concomitant oxidation of the substrate was long thought impossible; however, a novel three-step strategy was recently reported.¹ A hydrogen-terminated silicon surface is first methoxylated in methanol, and then the Si-OCH₃ sites are converted first to Si-F then to Si-OH by successive immersion in hydrofluoric acid and water. Original spectroscopic evidence suggested the creation of nanopatterned surface, in which every other site on the surface is functionalized. New STM and spectroscopic data show selective reaction at step edges and an unexpected functionalization pattern. The mechanistic implications of this pattern will be discussed.

¹ D. J. Michalak, S. R. Amy, D. Aureau, M. Dai, A. Estève, and Y. J. Chabal, *Nat. Materials* 9, 266 (2010).

5:00pm SS+AS+NS-ThA9 Benzene and Chlorobenzene Dissociation Pathways Involving Singlet-Triplet Crossing on the Si(100) Surface Modeled Using Small Clusters, *Nicholas Materer, E. Butson*, Oklahoma State University, *Q. Zhu*, University of Pittsburgh

The dimer rows in the Si(100) surface have di-radical character, which can be configured as a singlet or triplet. At the minimum energy crossing point of the singlet to triplet crossing for a single Si-dimer cluster, the spin-orbit coupling (SOC) coefficient was determined to be approximately 25 cm⁻¹.

Using this SOC, the Landau-Zener spin-crossing probability at room temperature was computed to be approximately 0.5%. Similar computational methods were used to investigate possible adsorption and dissociation processes for benzene and chlorobenzene. The 1,2 product (a tilted configuration) for benzene adsorption was proposed to undergo C-H bond cleavage to form lower-energy products. However, this process requires a spin-crossing of the initial 1,2 bond product, followed by a transition state with large activation barriers. Chlorobenzene can adsorb on the Si(100) by breaking one double bond on the phenyl ring and forming two new carbon-silicon bonds with the dimer cluster. Again, for dissociation to occur, the system must undergo a spin crossing process from the singlet to the triplet state. After this spin crossing event, the carbon-chlorine bond is cleaved and a new silicon-chloride bond is formed. The final product is a dissociation product with chlorine and a phenyl ring attached directly to the (100) surface of silicon. Both cases illustrate that spin crossing could be more common than realized in the adsorption and dissociation of organic molecules on Si(100).

5:20pm **SS+AS+NS-ThA10 Adsorption of Organic Triols on Ge(100)-2x1 Surface.** *Tania Sandoval, S.F. Bent*, Stanford University

Organic functionalization of semiconductor surfaces can provide tunable control of interfacial properties in organic-inorganic hybrid devices. The key step toward applications in this area is to understand the selectivity in the reactions of organic molecules on these surfaces.

In this work, adsorption of 1,3,5-benzenetriol and 2-hydroxymethyl-1,3-propanediol on Ge(100)-2x1 surface was studied. Both molecules have three hydroxyl groups available for reaction with the Ge surface. While the reactions of these molecules with the surface may be similar, differences in reactivity can be expected due to their different backbone structures. The aim of this study is to investigate whether a difference in reactivity exists and how the reaction with the surface is affected by the structure of the molecules.

Energy diagrams for both molecules were calculated by density functional theory. In both cases, proton transfer reactions from two or three hydroxyl groups to the Ge dimer atoms are suggested as thermodynamically favored pathways. However, the reaction through 3 OH groups in 2-hydroxymethyl-1,3-propanediol is more than 15 kcal/mol more stable than the same reaction in 1,3,5-benzenetriol. This difference can be associated with strain of the aromatic ring.

Infrared spectroscopy (IR) and X-ray photoelectron spectroscopy (XPS) were performed to investigate the adsorption products. IR results show the presence of a $\nu(\text{Ge-H})$ mode for both molecules, suggesting the proton transfer reaction as the main pathway. XPS spectra of each molecule both chemisorbed and physisorbed on the surface were obtained. The differences between these two spectra can be used to indicate the reaction products. For both molecules, no change in the C(1s) spectra is observed, suggesting that carbon does not form a bond directly with Ge. On the other hand, clear differences between the chemisorbed and physisorbed O(1s) spectra are observed for both molecules. A second peak with a lower binding energy only in the chemisorbed spectra, assigned to a Ge-O bond confirms that both molecules react with the Ge surface through O-H dissociation. The ratio between O(1s) peaks indicates that about 80% of the total hydroxyl groups are involved in reaction with Ge, suggesting that a significant fraction of the adsorbates react with the surface through all 3 of their hydroxyl groups.

In conclusion, both 1,3,5-benzenetriol and 2-hydroxymethyl-1,3-propanediol react with the Ge(100)-2x1 surface through O-H dissociative adsorption. Little difference in reactivity was observed between these triols, suggesting that other factors besides backbone structure are governing the reactivity in these systems.

5:40pm **SS+AS+NS-ThA11 The Chemistry of Adsorbed Water on Semiconductor Surfaces for Aqueous Photoelectrochemistry.** *Coleman Kronawitter, B. Koel*, Princeton University

The surface chemistry of water molecules adsorbed on single crystals, model structures relevant to photoelectrode-water interfaces in solar photoelectrochemical systems, is discussed. In heterogeneous processes relevant to photoelectrochemistry, the interaction of water with semiconductor and metal oxide surfaces is often a critical event whose character influences subsequent chemical pathways that ultimately dictate the reactions' efficiencies and selectivities. A surface science approach is used to characterize adsorbed water molecules on copper oxide and III-V semiconductor surfaces known to actively facilitate solar energy conversion in photoelectrochemical fuel synthesis devices. In this approach, ultrahigh vacuum conditions are used to facilitate the fabrication of highly characterizable adsorbate systems, and the use of single crystal substrates permits analysis of surface chemistry independent of sample grain boundaries and morphology. An understanding of the surface chemistry of

adsorbed water is developed through core-level spectroscopies and scanning probe microscopy.

Nanometer-scale Science and Technology

Room: Hall D - Session NS-ThP

Nanoscience Division Poster Session

NS-ThP1 Gallium Nitride Nanoparticle Synthesis using Non-Thermal Plasma with N₂ Gas and Ga Vapors, Jung-Hyung Kim, Korea Research Institute of Standards and Science, Republic of Korea, *K.H. You*, Korea Advanced Institute of Science and Technology, Republic of Korea, *S.J. You, D.J. Seong, Y.H. Shin*, Korea Research Institute of Standards and Science (KRISS), Republic of Korea

Compounds of Ga, such as gallium oxide(Ga₂O₃) and gallium nitride(GaN), are of interest due to its various properties in semiconductor application. In particular, GaN has the potentially application for optoelectronic device such as UV- to blue-light-emitting diodes(LEDs) and laser diodes(LDs).¹ Nanoparticle is an interesting material due to its unique properties compared to the bulk equivalents. While bulk-GaN exhibits a band gap of 3.3 eV to 3.5 eV, nanoparticles show a size-depending band gap if the particle size falls below 10.0 nm.²

In this report, we develop a synthesizing method for gallium nitride nanoparticle using non-thermal plasma. For gallium source, the gallium is evaporated by induction heating. Nitrogen radicals for GaN nanoparticle synthesis are supplied from inductively coupled plasma with N₂ gas. We use two plasma sources: one is for sufficient N radicals and the other is for in-situ plasma treatments. With this method, the post treatments such as annealing are not needed to get sufficient crystallinity. The synthesized nanoparticles are analyzed using field-emission scanning microscope(FESEM), transmission electron microscope(TEM) and x-ray photoelectron spectroscopy(XPS), and photo-luminescence(PL). The synthesized particles are investigated and discussed in wide range of experiment conditions such as flow rate, pressure and RF power.

References

1. D. Pile, Nat. Photonics 5, 394, 2011
2. H. Morkoc, S. Strite, G. B. Gao, M. E. Lin, B. Sverdlov and M. Burns, J. Appl. Phys., 76, 1363, Review. 1994

NS-ThP3 Imaging and Spectroscopy of Infrared Absorption Enhancement in the Near-Field of Plasmonic Array with the PTIR Technique, Jungseok Chae, B. Lahiri, G. Holland, A. Centrone, National Institute of Standards and Technology

Propagating light can interact efficiently with artificially fabricated metallic nanostructures through plasmonic excitations. In the infrared (IR) such light-matter interactions enables enhanced absorption in nanoscale volumes ("hot spots"), leading to sensitive IR detection. However, direct imaging of IR absorption hot spots is challenging because their size is several times smaller of the diffraction limit of the long IR wavelengths. Recently our group directly imaged and quantified the mid-IR absorption enhancement in polymer films coating asymmetric split ring resonators (ASSRs) using the photothermal induced resonance (PTIR) technique.[1] PTIR measures the transient thermal expansion caused by the absorption of light pulses in the sample with an atomic force microscope cantilever, leading to lateral resolution comparable to the AFM tip size. Plasmonic arrays of different shapes (ASRR, C-shaped, crescent-shaped and U-shaped) and different lattices (square, hexagonal and rhombic) were fabricated by e-beam lithography on top of zinc selenide right angle prisms to enable PTIR characterization. Here I'll show how the different shapes and arrangements of the resonators impact the shape, distribution and intensity of IR absorption hot spots in the near-field. The experimentally and directly measured enhancement factors in PMMA film coating the plasmonic structures will be compared for the different cases and with the enhancements measured for a single resonator of each shape.

[1]. B. Lahiri, G. Holland, V. Aksyuk and A. Centrone, NanoLetters. **13**, 3218 (2013).

NS-ThP5 A Novel Method for the Formation of Pt Metal Nanoparticle Array on Dimpled Ta using Nanosecond Pulsed Laser Dewetting, Ebenezer Owusu-Ansah, C. Horwood, University of Calgary, Canada, *H.A. El-Sayed*, Technische Universität, Germany, *V. I. Birss, Y. Shi*, University of Calgary, Canada

The unique properties of metal nanoparticle arrays (MNAs) depend on their sizes and geometries, and they differ considerably from the individual atoms and the bulk material. MNAs have been at the frontier in fabrication of materials with enhanced optical, magnetic, plasmonic, and mechanical properties, in biosensors as well as in catalysts with optimized selectivity.

Lithographic techniques are the major conventional methods used to generate MNAs, however, the processes are sophisticated and time consuming. The formation of sub-50-nm nanoparticle sizes has become increasingly difficult using lithography. Recently, thermal dewetting has been successfully used to form nanoparticle arrays of Au on dimpled Ta (DT) substrate, however, the major setback associated with this method is the deformation of the substrate when applied to high-melting point metals such as Pt. Pulsed laser dewetting is able to generate well-defined MNAs with the unique advantage of very little or no thermal damage to the substrate. Within the short width of the laser pulse, typically in the range of 7–12 ns, the laser energy is instantaneously converted into heat to dewet only the thin metal film with minimal or no heat transfer to the underlying substrate. We report here the results from our study on the formation of Pt MNAs using laser dewetting of Pt thin films on DT substrate under high vacuum condition. The DT substrate was fabricated using electrochemical anodization in highly concentrated H₂SO₄/HF solution. It has been demonstrated that dewetting occurs only at and beyond the threshold fluence. Beyond this threshold a single laser pulse was enough to achieve complete dewetting. The effect of several key parameters, including laser fluence, irradiation time, and film thickness, on the nanoparticle sizes and distribution was studied. To better characterize the MNA features, the percentage of dimples occupied by Pt nanoparticles was determined. As high as 80% of dimpled Ta occupancy can be achieved using pulsed laser dewetting. This study shows that laser dewetting is a novel method capable of annealing thin films of high-melting point Pt metal to achieve well-defined MNAs with narrow particle size distribution without subsequent damage to the DT substrate.

NS-ThP7 Dielectrophoretic Manipulation of Nickel Nanowires, Marcos Vinicius Puydinger dos Santos, R. Mayer, K.R. Pirota, F. Beron, S. Moshkalev, J.A. Diniz, University of Campinas, Brazil

Nanowires have received much attention because their high aspect ratio, shape anisotropy, relatively large surface area and particular electron transport properties. Furthermore, given to the low electrical current level usually present in the nanowires and their high sensitivity to the environment, they can be used as sensors devices. Dielectrophoresis (DEP) is a deposition method of electrically neutral particles based on the application of alternating electric field between electrodes. In this work, 80 nm-thick aluminum electrodes were deposited on a 300 nm-thick SiO₂ layer grown on n⁺-type silicon wafer using optical lithography and lift-off. After electrodes fabrication, nickel nanowires (NiNW) (length of 4 μm and diameter of 35 nm), obtained by electrodeposition, were manipulated and defined between the electrodes using DEP. Electrical parameters of DEP deposition – like frequency, electric potential, NiNW concentration and process time – as well as electrodes geometry were studied to investigate deposition efficiency. Preliminary results show best selection of electrical parameters and electrodes geometry that optimizes the nanowires deposition. For suitable parameters, the efficiency of DEP deposition is up to 90%. To characterize NiNW electrical properties, electrical current through the nanowires was measured as the voltage between electrodes. Initially, a Schottky-like contact is present and contact sintering under forming gas (92% of N₂ and 8% of H₂) at 450 °C was taken to reduce the electrodes-NiNW contact resistance down to the NiNW resistance (~ 1k Ω). Finally, this method for nanowire deposition and electrical contact reduction has a suitable throughput and is a key for electric characterization of nanowires and fabrication of nanowire-based devices.

NS-ThP9 Electron Tunneling in Weak Coupled Triple Quantum Dots: Sensitivity to Symmetry Violation, Igor Filikhin, B. Vlahovic, North Carolina Central University

The electron localization and tunneling in the triple quantum dots (TQD) is studied in relation to their spectral properties. Modeled are lateral InAs/GaAs TQDs using single sub-band effective mass approach with the effective potential simulating the strain effect [1]. As an approximation, two-dimension quantum wells (QW) are considered. Dynamics of electron localizations in TQD over whole spectrum is studied by varying the inter-dot distances. To consider tunneling between localized-delocalized states selected was a QD pair (DQD). In isolated DQD, such tunneling goes consecutively from high energy levels to the ground state when the inter-dot distance decreases [2]. The electron spectrum is separated by three parts: localized states, delocalized states, and states with different probability for localization in the left and right QDs. The electron localization demonstrates extreme sensitivity to small variations of DQD shape, which violate Left-Right symmetry. The effect of adding third quantum dot to DQD is considered for weak coupling triple system. We show that presence of the third dot increases tunneling in weakly coupled DQDs. The star and chain configurations of TQDs are considered. The effect of violation of

reflexing symmetry in TQD was studied. We found that the tunneling is highly sensitive to a small violation of the geometry symmetry.

This work is supported by the NSF (HRD-0833184) and NASA (NNX09AV07A).

[1] I. Filikhin, V. M. Suslov and B. Vlahovic, Phys. Rev. B 73, 205332 (2006).

[2] I. Filikhin, S. Matinyan and B. Vlahovic, Mathematical Modeling and Geometry, Vol. 2, No 2, 1 (2014).

Scanning Probe Microscopy Focus Topic

Room: Hall D - Session SP+AS+EM+NS+SS-ThP

Scanning Probe Microscopy Poster Session

SP+AS+EM+NS+SS-ThP2 Fabrication of Single-Walled Carbon Nanotube Probe and Processing of Single Nanometer Scale Pit with High-Aspect-Ratio of Highly Oriented Pyrolytic Graphite Using by STM, Syun Ohsumimoto, A. Matsumuro, Aichi Institute of Technology, Japan

Our unique fabrication methods of high-aspect-ratio nanometer scale three-dimensional structures of pits, lines and convex parts using a multi-wall carbon nanotube (MWNT) with diameter of about 50 nm as a STM probe have been developed successfully. It turns out that this method has been applicable to surfaces of various conducting materials, such as noble metal thin films, low-resistivity single crystalline silicon wafer and highly oriented pyrolytic graphite (HOPG). We also have clarified that the physical origin of this nanometer-scale pit processing using STM must be the field evaporation mechanism by the results of TEM *in-situ* observations during fabrication process. In order to realize further ultra-precise three dimensional structures with high aspect ratio, it is surely required that an innovative ultimate ultra-precision processing technology needs fabrication size below several nm, i.e. single nanometer scale.

This study paid great attention to realize the ultimate processing of single nanometer scale structures using a single-wall carbon nanotube (SWNT) probe as our original STM processing. The most important problem was to overcome too much difficulty in synthesis of SWNT probes with high probability. Then, the application of mixed dispersion liquid containing both MWNTs and SWNTs could be devised at the process of producing SWNT probes. In this process, it was clarified that the SWNT easily attached to the point of the MWNT, which was easily adhered to the apex of the conventional tungsten needle through the pulling method that we developed originally. The success rate for synthesis of the SWNT probes with diameters of about 2 nm and 10 nm were drastically increased up to about 10 % and 14 %, respectively. As compared with the case where the dispersion liquid of only SWNT is used, success fabrication rate has been nearly equal to 0 %. Single nanometer scale pits were actually fabricated on HOPG in atmosphere and room temperature condition. The SWNT probe with diameter of about 2 nm under the conditions of a bias voltage of 5 V, tunnel current of 1 nA and fabrication time of 60 s could realize a single nanometer scale pit with the diameter of 9 nm and the depth of 13 nm. The aspect ratio with SWNT probes increased up to about 5 times in the case of MWNT probes. These demonstrate that these STM fabrications by using SWNT probes with several diameters must give a remarkable effect in fabricating three-dimensional high-aspect-ratio structures with single nanometer-scale.

SP+AS+EM+NS+SS-ThP3 Probing the Electronic Structure of the Layered Electride Ca₂N, Jeonghoon Ha, NIST/Maryland Nano Center, University of Maryland, H. Baek, NIST & Seoul National University, Republic of Korea, D. Zhang, NIST/Maryland Nano Center, University of Maryland, Y. Kim, S. Kim, Y.J. Song, Sungkyunkwan University, Republic of Korea, Y. Kuk, Seoul National University, Republic of Korea, J.A. Stroscio, NIST

Electrides are electronic materials in which excessive electrons are confined into cavities defined by the crystal structure. These excessive electrons take the place of negatively charged ions in an ionic crystal. The geometry of the cavities confining these anionic electrons determines the electronic properties of the material and provides a platform to study various interaction physics [1]. A previous study reported the inorganic electride Ca₂N to have a layered structure with anionic electrons confined to 2-dimensional cavities between the cationic crystal layers [2]. In this previous study, transport measurements showed high electron mobility and long mean scattering time, and magneto-resistance measurements confirmed diffusive 2-dimensional transport in the electron layers.

In the present work, we use an ultra-low temperature scanning tunneling microscope to investigate the local electronic structure of a cleaved surface

of a Ca₂N single crystal. An energy gap was observed in the tunneling spectrum with a gap size of 0.4 meV. The spectra contain multiple coherence-like peaks which are equally spaced in energy, suggestive of possible multi-band superconductivity or quantum confinement in the electron layers. Temperature-dependent tunneling spectroscopy measurements show a gradual suppression of the energy gap up to 2.5 K. An interesting observation is that the gap structure and the peak features do not get suppressed in the presence of a perpendicular magnetic field up to 14.5 T, suggesting if the crystal is in a superconducting state, then the critical field is extremely large compared to the transition temperature. These observations and further discussion of possible unconventional superconductivity will be discussed in this presentation.

[1] J. Dye, Science 301, 607 (2003)

[2] K. Lee *et al*, Nature 494, 336 (2013)

SP+AS+EM+NS+SS-ThP5 Improving the Accuracy of Atomic Force Microscopy in Nanometrology for Linewidth Measurements, James Su, N.N. Chu, M.H. Shiao, C.N. Hsiao, Instrument Technology Research Center, National Applied Research Laboratories, Taiwan, Republic of China

Atomic force microscopy (AFM) has an important role in dimensional metrology especially in the nanoscale. The morphology image processed by the AFM is the interaction between the tip and the sample surface. The result of the interaction may cause broadening of peaks and shrinking of valleys in the scanning process caused by tip effects. It would be impossible to differentiate the portion due to the tip and the portion due to the sample surface without determining the tip geometry which is a key role in AFM-image quality. As a case study, AFM measurements of nanowires (NW), carbon nanotubes (CNT) and nano-honeycombs fabricated by nanosphere lithography (NSL) technology are examined. Line width measurement results may expand up to 39.5% by adopting a conventional pyramid-shaped probe and 17.5% by using a conical-shaped one as the dimensions of the scanned features approaches to the order of magnitude of the tip apex. The uncertainty of measurement would expand if tip wear occurs during image scan. Calculation for surface reconstruction has been developed to extract the part related to the tip from the SPM image. The SPM used for these measurements is equipped with a highly accurate scanning system, which employs closed-loop capacitive feedback control to ensure outstanding linearity and position accuracy. To identify the geometry of the tip, a silicon tip characterization grating was imaged between the measurements. Deconvolution process were carried out for topography image corrections, and the results were further compared with the ones measured from the scanning electron microscope (SEM). This process is essential to derive accurate measurement results in the nanoscale region.

SP+AS+EM+NS+SS-ThP8 The Effect of Electrochemical Potential on Single Molecule Conductance, Esteban Sanchez, R. Aguilar, BUAP, Mexico, S. Afsari, Temple University, Z. Li, Ball State University, E. Borguet, Temple University

Porphyrins have been widely studied for their electrochemical properties to understand charge transfer. The related property of charge transport can be accessed by single molecule conductance (SMC) measurements. The most common SMC studies involve transport between different anchor groups at transversal positions in the molecule [1]. Few investigations have been made using porphyrins lying flat on the substrate in electrochemical environment [2]. Recent studies have shown that the templating effect of self-assembly can be exploited to orient molecules in metal-molecule-metal junctions, so that transport perpendicular to the molecular plane can also be easily accessed [3].

This goal research is to use self assembly, verified by scanning tunneling microscopy (STM), to measure charge transport in single porphyrins adsorbed flat on the Au (111) surface. 5,10,15,20-Tetra(4-pyridyl)porphyrin (TPyP) is a good candidate for this research because it has been demonstrated that this porphyrin has a strong interaction with, and can form ordered layers on, Au (111) in electrochemical environment [4]. This control of the orientation of the porphyrin by electrochemical potential enables us to make SMC measurements perpendicular to the molecular plane.

[1] Zhihai Li, Manuel Smeu, Mark A. Ratner, and Eric Borguet, Effect of Anchoring Groups on Single Molecule Charge Transport through Porphyrins, J. Phys. Chem. C, 117, 14890–14898 (2013).

[2] Quirina Ferreira, Ana M. Braganca, Luis Alcacer, and Jorge Morgado, Conductance of Well-Defined Porphyrin Self-Assembled Molecular Wires up to 14 nm in Length, J. Phys. Chem. C, 118, 7229–7234 (2014)

[3] Sepideh Afsari, Zhihai Li, and Eric Borguet, Orientation-Controlled Single-Molecule Junctions, Angew. Chem. Int. Ed. 53, 9771–9774 (2014).

[4] Tao Ye, Yufan He, and Eric Borguet, Adsorption and Electrochemical Activity: An In Situ Electrochemical Scanning Tunneling Microscopy

Study of Electrode Reactions and Potential-Induced Adsorption of Porphyrins, *J. Phys. Chem. B*, 110, 6141-6147 (2006).

Friday Morning, November 14, 2014

2D Materials Focus Topic

Room: 310 - Session 2D+EM+MS+NS-FrM

2D Materials: Device Physics and Applications

Moderator: Daniel Gunlycke, Naval Research Laboratory

8:20am **2D+EM+MS+NS-FrM1 1, 2, 3... Ripples, Gaps and Transport in Few-layer Graphene Membranes, ChunNing(Jeanie) Lau**, University of California, Riverside **INVITED**

Graphene, a two - dimensional single atomic layer of carbon, has recently emerged as a new model system for condensed matter physics, as well as a promising candidate for electronic materials. Though single layer graphene is gapless, bilayer and trilayer graphene have tunable band gaps that may be induced by out-of-plane electric fields or arise from collective excitation of electrons. Here I will present our results on mechanical manipulation and transport measurements in bilayer and trilayer graphene devices with mobility as high as 400,000 cm²/Vs. We demonstrate ripple formation due to thermally or mechanically induced strain, the presence of an intrinsic gapped state in bilayer and trilayer graphene at the charge neutrality point and evidence for quantum phase transition. Our results underscore the fascinating physics in these 2D membranes, and have implications for band gap engineering for graphene electronics and optoelectronic applications.

9:00am **2D+EM+MS+NS-FrM3 Photoinduced Doping in Heterostructures of Graphene and Boron Nitride, Jairo Velasco Jr., L. Ju**, UC Berkeley, *E. Huang*, Stanford University, *S. Kahn, C. Nosiola, H.-Z. Tsai*, UC Berkeley, *W. Yang*, Beijing National Laboratory for Condensed Matter Physics, Republic of China, *T. Taniguchi, K. Wantanabe*, National Institute for Materials Science (NIMS), Japan, *Y. Zhang*, Fudan University, Republic of China, *G. Zhang*, Beijing National Laboratory for Condensed Matter Physics, Republic of China, *M.F. Crommie, A. Zettl, F. Wang*, UC Berkeley

Van der Waals heterostructures (VDH) provide an exciting new platform for materials engineering, where a variety of layered materials with different electrical, optical and mechanical responses can be stacked together to enable new physics and novel functionalities. Here we report an emerging optoelectronic phenomenon (i.e. photo-induced modulation doping) in the graphene-boron nitride VDH (G/BN heterostructure). We find it enables flexible and repeatable writing and erasing of charge doping in graphene with visible light. We demonstrate that the photo-induced modulation doping maintains the remarkable carrier mobility of the G/BN heterostructure, and it can be used to generate spatially varying doping profiles like *pn* junctions. Our work contributes towards understanding light-matter interactions in VDHs, and innovates a simple technique for creating inhomogeneous doping in high mobility graphene devices. This opens the door for new scientific studies and applications.

9:20am **2D+EM+MS+NS-FrM4 Two-dimensional Resistance Map of Graphene p-n Junction in the Quantum Hall Regime, Nikolai N. Klimov, S. Le, C.A. Richter**, National Institute of Standards and Technology (NIST), *J. Yan*, University of Massachusetts, Amherst, *E. Comfort, J.U. Lee*, SUNY-University of Albany, *D.B. Newell*, National Institute of Standards and Technology (NIST)

Graphene, a two dimensional (2D) electronic system with a unique band structure, is a promising material for future electronic devices, especially for electrical metrology [1]. Currently, devices based upon GaAs heterostructures 2D electron gases (GaAs-2DEG) are used to realize a single quantum resistance standard value of $(\frac{1}{2})h/e^2 = 12,906.4035 \Omega$ with metrological accuracy. It is important to realize resistance values over a wider resistance scale to expand the technical relevance of quantum resistance standards.

In the past, attempts have been made by using parallel or series GaAs-2DEG Hall bars to achieve multiple or fractional resistance values of h/e^2 . However, the difficulties of fabricating ideal contacts and metal interconnects between the Hall bars severely limit the yield of properly operating devices. Graphene, with its ability to create both electron and hole 2D gases on a single Hall bar device without metal interconnects, is an ideal platform to overcome this difficulty [2].

We have fabricated a graphene FET p-n junction device in a Hall bar geometry and experimentally characterized it at large magnetic fields to determine the range of quantized resistance values that can be obtained. The device features two doped polysilicon split gates that are buried in a SiO₂ substrate within 100 nm-150 nm from the surface of graphene. The fabrication process achieves an atomically smooth dielectric surface, which is needed to preserve the intrinsic band structure of graphene. Independent

voltage control on these gates allows separate tuning of both type and concentration of charge carriers in the two parts of graphene conducting channel. In addition, a very narrow 150 nm gap between split gates gives a very sharp junction. Measurement of the sample's resistance at different gate values and measurement configurations in the quantum Hall regime allows us to fully characterize the device and to obtain multiples or fractions of the resistance value h/e^2 . We will show that our experimental results can be explained by the Landauer-Büttiker edge-state transport model with the assumption of a partial mixing at the p-n interface. Potential application of graphene p-n junction devices for resistance standards with a wide range of resistance values other than $h/2e^2$ will be discussed.

References:

[1] A. Tzalenchuk, *et al.*, Nature Nanotech., 5, 186 (2010)

[2] M. Woszczyzna, *et al.*, APL, 99, 022112 (2011)

9:40am **2D+EM+MS+NS-FrM5 Electrical Breakdown and Current Carrying Ability of Multilayer MoS₂ Transistors, Philip Feng, R. Yang, Z. Wang**, Case Western Reserve University

We report the first study of electrical breakdown of multilayer molybdenum disulphide (MoS₂) transistors through precision electrical measurements and simulation that shows the effect of varying the device size and conductivities on the breakdown limit. We demonstrate that the multilayer devices have better current carrying capabilities compared to thin layer devices. We also study the effect of varying MoS₂ thickness upon electron mobility in the channel.

MoS₂ has recently emerged as a new two-dimensional (2D) semiconducting crystal with attractive properties, such as the absence of dangling bonds, high thermal stability, and having a thickness-dependent bandgap [#_edn1]. While prototype single- and few-layer MoS₂ FETs and circuits have been demonstrated, in practice multilayer (up to 10s of nanometers) devices may be more desirable for certain applications: they can have higher carrier mobility and density of states under the same dielectric environment, greater mechanical strength, higher current limit and better manufacturability [#_edn2] [#_edn3]. While the breakdown of single layer MoS₂ transistors has been demonstrated [#_edn4], breakdown of multilayer devices has not been studied.

In this work, we study the electrical breakdown of devices with different thicknesses through experimental demonstration and simulation with finite element method (FEM). We observe that the breakdown process happens gradually with multiple voltage sweeping cycles, and thicker devices generally show higher breakdown current, which is also demonstrated in the simulation. The highest breakdown current in the measurement is 1.2mA, which is one of the highest current reported results so far for MoS₂ transistors. Simulation also shows that with higher conductivity channel, the breakdown current and breakdown current density both increase. The high field transport characteristics of multilayer MoS₂ transistors demonstrate that the devices could drive high loads in circuits and could be used for circuits that require high power or current. The thickness dependence of mobility shows that the device performance can be further improved by carefully tuning the device parameters.

[i] [#_ednref1] Q. H. Wang, *et al.*, Nat. Nanotechnol. 7, 699 (2012).

[ii] [#_ednref2] D. Jariwala, *et al.*, ACS Nano 8, 1102 (2014).

[iii] [#_ednref3] R. Ganatra, Q. Zhang, ACS Nano (2014), DOI: 10.1021/nn405938z.

[iv] [#_ednref4] D. Lembke, A. Kis, ACS Nano 6, 10070 (2012).

10:00am **2D+EM+MS+NS-FrM6 Lithography-free Fabrication of Graphene Devices, Nick Thissen, R.H.J. Vervuurt**, Eindhoven University of Technology, Netherlands, *J.J.L. Mulders*, FEI Electron Optics, Netherlands, *J.W. Weber, A.J.M. Mackus, W.M.M. Kessels, A.A. Bol*, Eindhoven University of Technology, Netherlands

Graphene device fabrication on large-area graphene typically involves several patterning steps using electron beam or optical lithography, followed by graphene etching and metallization for application of metallic contacts. However, the resist films and lift-off chemicals used in lithography introduce compatibility issues, such as the difficulty of removing the resist from the graphene. This resist residue has a negative influence on the thermal and electrical properties of the graphene and interferes with functionalization of the graphene. This motivates the development of a 'bottom-up', direct-write, lithography-free fabrication method.

In this work, a lithography-free fabrication method for graphene-based devices was developed. As a first step, the method involves direct

patterning of large-area graphene by focused ion beam (FIB) in order to isolate graphene from the bulk. The patterning of the graphene is performed in a DualBeam (SEM / FIB) system, in which a 30 kV FIB is used to locally remove graphene from the substrate. An *in situ* Raman microscope allows for direct observation of the graphene quality before and after FIB processing, from which it was determined that a low Ga-ion dose of 10 C/m² is sufficient for complete graphene removal. By optimizing the pattern design, the ion beam current and the background pressure in the DualBeam system, unintentional damage of the graphene by scattered ions is almost completely prevented.

After FIB patterning, as a second step a direct-write atomic layer deposition (ALD) technique is applied in the same system to locally deposit contacts to the isolated graphene. In the direct-write ALD technique, the patterning capability of electron beam induced deposition (EBID) is combined with the material quality of ALD. A thin seed layer consisting of small Pt grains in amorphous carbon is deposited on the graphene by EBID in the desired contact pattern. Subsequently, a selective ALD process purifies the seed layers and builds them into high-quality Pt contacts. This combined approach yields virtually 100% pure Pt (resistivity of 12 μΩcm) with a lateral resolution of 10 nm¹¹. This chemical approach to contact deposition is expected to yield lower contact resistances compared to conventional physical deposition techniques.

By combining patterning and direct contact deposition in the same system, graphene devices were fabricated from large-area graphene without the use of lithography. First results from sub-optimal devices demonstrate field-effect mobilities approaching 500 cm²/Vs and contact resistances as low as (40 ± 30) Ω.

[1] A.J.M. Mackus et al., *Nanoscale* **4**, 4477 (2012)

10:40am 2D+EM+MS+NS-FrM8 Electronic Transport in Transition Metal Dichalcogenides, Joerg Appenzeller, Purdue University INVITED

Since the discovery of graphene for electronic applications, there has been a substantial worldwide effort to explore other layered materials. Transition metal dichalcogenides (TMDs) like MoS₂, MoSe₂, or WSe₂, to just name a few, not only offer the desired ultra-thin body structure that translates into superior electrostatics as desirable for nanoelectronics applications, but also exhibit a sizable band gap. While to date the ideal application space for these materials has not been identified, it is obvious that only through a detailed understanding of the underlying transport in these layered materials intrinsic properties that lend themselves to particular applications can be uncovered.

In my presentation I will first discuss the benefits of an ultra-thin body structure for scaled tunneling FET applications including tunneling devices. Contacts play a particularly crucial role in this context and can easily mask the intrinsic performance of TMDs as will be discussed based on experimental Schottky barrier tunneling data obtained from MoS₂, MoSe₂ and WSe₂ field-effect transistors. A careful analysis of all these material systems reveals details about Schottky barrier heights for electron and hole injection as well as the band gap. These findings are then put into the context of channel length scaling and layer thickness dependence of three-terminal TMD devices based on MoS₂ transistors. Last, experimental data on the band-to-band tunneling in partially gated WSe₂ device structures will be discussed and projections about the potential usefulness of TMDs for tunneling device applications will be made.

11:20am 2D+EM+MS+NS-FrM10 Controlled Synthesis and Fuel Cell Application of Carbon Nanowalls, Hiroki Kondo, S. Imai, K. Ishikawa, M. Sekine, M. Hori, Nagoya University, Japan, M. Hiramatsu, Meiji University, Japan

Carbon nanowalls (CNWs) are one of carbon nanomaterials and contain stacks of graphene sheets vertically standing on a substrate. Each wall with the top edge is continuous crystallographically through bending or branching and composed of nanographite domains. Recently, we have developed the formation method of the ultra-high-density over 10¹³ cm⁻² Pt nanoparticles on the whole surface area of the CNWs with a diameter of 2-3 nm employing metal-organic chemical fluid deposition (MOCFD) method in supercritical fluid (SCF). They are promising as a catalytic electrodes for a polymer electrolyte fuel cell because of its high-specific-surface-area and high aspect ratio. On the other hand, while it is known that Pt nanoparticles are poisoned by CO below 100°C, it is reported that Pt-Au nanoparticles are excellent candidate for a low-temperature anode electrocatalyst. In this study, supporting processes of Pt-Au nanoparticles on the CNWs using the SCF-MOCFD method and their catalytic properties were investigated.

We used the SCF-MOCFD system to support Pt and Au nanoparticles on the CNWs. Firstly, Pt nanoparticles were supported using 1wt% (CH₃C₃H₄)(CH₃)₃Pt solution (2 ml). Then, Au nanoparticles were subsequently supported using (CH₃)₂Au(CH₃COCHCOCH₃) solution (1 ml). Both precursors were diluted by n-hexane [CH₃(CH₂)₄CH₃].

According to the SEM images of the CNWs after the supporting processes of only Pt nanoparticles and, both Pt and Au ones, the nanoparticles are supported on the entire surface area of each CNWs in the both cases. It is also found that the diameter and its distribution of the nanoparticles decrease after the second Au supporting process, while its density increases. This means that the relatively large Pt nanoparticles are effectively removed and small Au nanoparticles are simultaneously supported at the second supporting process. On the other hand, we evaluated cyclic voltammetry (CV) characteristics using CNWs with different-density Pt nanoparticles, in which density of 3.0×10¹² cm⁻² and diameter of 1.1 nm obtained for 10 min supporting and, density of 8.3×10¹² and diameter of 1.5 nm obtained for 30 min supporting. Peaks related to adsorption and desorption of hydrogen were found in both cases. With increasing the supporting time, the specific surface area of Pt evaluated from the CV about twofold increased. However, according to the TEM images, the ratio of surface area of Pt nanoparticles are about fivefold. It is deduced that some parts of Pt nanoparticles are inactive. Therefore, these results indicate that not the crystallinity control of CNWs are essential to improve the catalytic performance.

Atom Probe Tomography Focus Topic

Room: 301 - Session AP+AS+NS+SS-FrM

Correlative Surface and Interface Analysis with APT

Moderator: Arun Devaraj, Pacific Northwest National Laboratory

8:20am AP+AS+NS+SS-FrM1 Correlative Transmission Electron Microscopy and Atom Probe Tomography of Interfaces in CdTe, David Diercks, J.J. Li, C.A. Wolden, B.P. Gorman, Colorado School of Mines INVITED

CdTe solar cells are a promising thin film technology, yet the highest reported efficiencies [1] remain well below the theoretical efficiency for such materials. For polycrystalline CdTe, interface contacts and grain boundaries along with impurities likely account for the majority of this underperformance.

Atomic scale analysis is an important feedback mechanism to relate the structure to both the device performance and the processing conditions. Through this, the atomic scale factors which improve or limit the performance can be ascertained. This then enables the development of materials and processing methods which best eliminate or mitigate the detrimental effects.

With these goals, atom probe tomography (APT) in conjunction with transmission electron microscopy (TEM) was used to study the contact interfaces and grain boundaries in CdTe devices. With the combination of time-of-flight mass spectrometry and point projection microscopy by controlled field evaporation, APT has the ability to obtain tens of ppm composition sensitivity along with near atomic-level spatial resolution. TEM provides crystallographic information along with other correlative information for guiding the reconstruction of the APT data.

It is demonstrated that the compositions measured for CdTe by APT are sensitive to the analysis conditions. Therefore, the APT analysis conditions for obtaining accurate measurements of the specimen stoichiometry were first ascertained. Following that, TEM and APT analyses of thin film devices consisting of a fluorine-doped tin oxide coated glass substrate subsequently coated with CdS, CdTe, Cu-doped ZnTe, and Au were performed. Using optimized values, APT analyses on the absorber layers and contact interfaces after different deposition and processing conditions were performed. These show significant changes in copper and sodium distributions as a result of the thermal processing.

[1] M. A. Green, K. Emery, Y. Hishikawa, W. Warta, and E. D. Dunlop, "Solar cell efficiency tables (version 42)," *Progress in Photovoltaics*, vol. 21, pp. 827-837, Aug 2013.

9:00am AP+AS+NS+SS-FrM3 Atom Probe Compositional Analysis of Nanoscale Precipitates in Nb-Ti Micro-alloyed Steels, Monica Kapoor, G.B. Thompson, University of Alabama, R.M. O'Malley, Nucor Steel

Composition of complex carbide and carbo-nitride precipitates in Ti-Nb micro-alloyed 80-ksi (0.06 wt. % Nb; 0.06 wt. % Ti) and 100-ksi (0.03 wt. % Nb; 0.12 wt. % Ti) steels was studied using atom probe tomography. Fine (~2 nm) and coarse (~8 nm) NbTiC precipitates were identified in the 100 ksi steel with the Fe content decreasing with increasing precipitate size. Both steels had coarse NbTiCN precipitates (~80 nm) having ~7 at. % and ~30 at. % Nb in the precipitates for the 100 ksi and 80 ksi steels respectively. Star-shaped TiC precipitates and parallel rows of interphase NbTiC clusters on and near grain boundaries were also identified in the 100

ksi steel. In the 80 ksi steels, uniformly distributed disk-shaped and spherical NbTiC clusters were observed along dislocations. The composition and phase stability of these precipitates are discussed in terms of Thermo-Calc solution thermodynamic modeling.

9:20am **AP+AS+NS+SS-FrM4 Nanoscale Imaging of Li and B in Glass Samples, a Comparison of ToF-SIMS, NanoSIMS, and APT**, *Zihua Zhu, Z.Y. Wang, J. Liu, J. Crum, J.V. Ryan, D.K. Schreiber, J.J. Neeway*, Pacific Northwest National Laboratory

A widely used method to immobilize nuclear wastes is fusing them into glasses. These proposed glass waste forms are multicomponent complex material with the common components of Li and B compounds. It is difficult for commonly-used surface analysis tools (e.g., X-ray photoelectron spectroscopy (XPS), Auger electron spectroscopy, scanning electron microscope/energy dispersive spectroscopy (SEM/EDX), and transmission electron microscope/energy dispersive spectroscopy (TEM/EDX)) to image the distributions of ultra-light elements like Li and B with sub-micron lateral resolutions. Time-of-flight secondary ion mass spectrometry (ToF-SIMS), NanoSIMS, and atom probe tomography (APT) were used to image Li and B distributions in several representative glass samples. ToF-SIMS can provide ~100 nm lateral resolutions if using Li^+ and BO_2^- images. However, both positive ion mode and negative ion mode are needed because neither B signals in positive ion mode nor Li signals in negative ion mode can provide adequate intensity to form qualified images. NanoSIMS can provide ~100 nm lateral resolutions if using Li^- and BO_2^- images, while the lateral resolution of positive ion mode of NanoSIMS is poor (~400 nm). APT can provide ~2 nm lateral resolution for Li^+ and B^+ in a 3-D mode and quantification of APT is better than that of SIMS. While APT can provide much better ultimate lateral resolution than ToF-SIMS and NanoSIMS, it has three drawbacks: limited field-of-view, time-consuming sample preparation, and frequent/unpredicted sample damage during measurement. As a comparison, field-of-view of SIMS is flexible, sample preparation is simple, and little unpredicted sample damage occurs during SIMS measurement. Therefore, SIMS and APT can be regarded as complimentary techniques in nanoscale imaging of Li and B in glass samples.

9:40am **AP+AS+NS+SS-FrM5 Application of (S)TEM and Related Techniques to Atom Probe Specimens**, *William Lefebvre, D. Hernandez-Maldonado, F. Cuvilly, F. Moyon*, University of Rouen, France **INVITED**

The geometry of atom probe tomography (APT) specimens strongly differs from standard scanning transmission electron microscopy (STEM) foils. Whereas the later are rather flat and thin, APT tips display a curved surface and a significantly larger thickness. As far as a correlative approach aims at analysing the same specimen by STEM and APT, it is mandatory to explore the limits and advantages imposed by the particular geometry of APT specimens to STEM.

High angle annular dark field (HAADF) in STEM provides a contrast related to atomic number and to the amount of atoms in a column. A complete analysis of a high resolution HAADF STEM image requires the identification of projected column positions, the calculation of integrated HAADF intensity for each column and, eventually, the estimation of a "background level" generated by the amorphous carbon or oxide layer present on the specimen surface. Then, by of a statistical analysis [1], the possibility of atomic counting in an APT specimen can be explored. For this purpose, we propose an image processing method which provides a complete analysis of HAADF STEM images, that was applied here to APT specimens. In order to estimate the advantages and limitations of the method for such a particular specimen geometry, simulations have been applied and confronted to experimental results. Illustrations will be given for specimens before and after field evaporation in APT.

[1] S. Van Aert et al. Phys. Rev. B 87 (2013) 064107

10:40am **AP+AS+NS+SS-FrM8 APT Analysis of Biological Materials**, *Daniel Perea, J. Liu, J.A. Bartrand, N.D. Browning, J.E. Evans*, Pacific Northwest National Laboratory **INVITED**

Biointerfaces play an essential role for the function of many biological materials and organisms. The behaviors of complex macromolecular systems at materials interfaces are important in the fields of biology, environmental biology, biotechnology, and medicine. An understanding of the chemical processes and physics, and ultimate the ability to engineer biomaterials and microorganisms with specific properties and functions, is aided by an atomic level understanding of the composition and morphology of biointerfaces. However, a great challenge exists to map the atomic level composition and morphology of biointerfaces using APT, precluding a complete understanding of the structure properties relationship. At the Environmental Molecular Sciences Laboratory (EMSL), the application of APT is being developed in combination with other microscopy and spectroscopic techniques to study interfaces in biologic materials. We are

developing methodologies and analyses that are allowing us to probe the ultimate limits of what APT analysis can confidently provide despite the complex thermally-assisted field evaporation behavior of soft materials. Advanced sample preparation techniques will also be discussed that further advance the application of APT into field of biology.

Electronic Materials and Processing
Room: 314 - Session EM+NS+TF-FrM

Transparent Electronics

Moderator: Lisa M. Porter, Carnegie Mellon University

9:00am **EM+NS+TF-FrM3 Transparent Amorphous Oxide Semiconductors: Interfacial Chemistries and New Applications**, *Gregory Herman*, Oregon State University **INVITED**

During the past decade research in the area of transparent amorphous oxide semiconductors (TAOS) has increased substantially due to the ability to fabricate thin film transistors (TFT) at relatively low processing temperatures while still maintaining large electron mobilities. The primary applications for these materials include active matrix displays with the possibility for integration onto flexible polymeric substrates. More recently potential applications have expanded to include non-volatile memory, sensing, and memristive neurological networks. We have studied amorphous zinc tin oxide (ZTO) and indium gallium zinc oxide (IGZO) that have been deposited by both vacuum and solution based approaches. The electrical characteristics of the films have been evaluated in both TFT and metal-insulator-metal memristive devices. Excellent device characteristics have been obtained, however we have found that surface impurities can strongly affect device stabilities. We have found that the chemistry of absorbed species on the back-channel strongly influences the bias stress stabilities of ZTO and IGZO TFTs, while reactions at the Al/ZTO interface leads to the resistive switching characteristics of memristors, and post annealing leads to interfacial reactions and modifies the Schottky barrier for Pt/IGZO diode structures. To better understand the role of interfacial reactions on TFT and memristive devices we have developed methods to prepare clean well defined surfaces for ZTO and IGZO, and further characterized there surface and interface properties with X-ray photoelectron spectroscopy and secondary ion mass spectrometry.

9:40am **EM+NS+TF-FrM5 HMDSO/O₂-Plasma-Deposited Organic-Inorganic-Hybrid Materials as Gate Dielectrics for MgZnO Thin Film Transistors and Encapsulation Layers for Solar Cells**, *Y.S. Li, C.H. Tsai, I.C. Cheng, Jian-Zhang Chen*, National Taiwan University, Taiwan, Republic of China

Organic-inorganic hybrid materials can be deposited from hexamethyldisiloxane (HMDSO) diluted with oxidants using plasmas technology. The properties of the deposited material can be controlled by varying the dilution ratio of the oxidants. The chemical compositions can vary from polymer-like (organic-like) to SiO₂-like (inorganic-like) depending on the oxidant dilution ratio and the process power. In this paper, we report two applications of HMDSO/O₂-plasma-deposited organic-inorganic-hybrid materials developed in our group: (1) as gate dielectrics of MgZnO TFTs, and (2) as the encapsulation layers for organic-inorganic hybrid solar cells.

The inorganic/organic component ratios in hybrid films were tailored by varying the process power and the O₂/HMDSO flow rate ratio. The FTIR analysis and contact angle measurement show that higher deposition power and/or larger O₂/HMDSO flow rate ratio result in more SiO₂-like films. For rf-sputtered MgZnO TFTs, a more organic-like film affords a better interface to the MgZnO active layer and higher dielectric constant, leading to a smaller threshold voltage and a steeper subthreshold slope; while an inorganic-like film has lower leakage currents, resulting in a larger on/off current ratio in the transistors. The TFT with an organic-inorganic-hybrid gate dielectric deposited at an O₂/HMDSO ratio of 40 and process power of 30 W exhibits a threshold voltage of 6.8 V, a subthreshold slope of 0.48 V/dec, an on/off current ratio of >10⁷ and a linear mobility of ~60 cm²V⁻¹s⁻¹, respectively. We also have demonstrated that this O₂/HMDSO-plasma-deposited organic-inorganic material can be used as an efficient single-layer encapsulation technique for organic photovoltaic cells. Calcium test was used to evaluate the water vapor transmission rate (WVTR) of the barrier film deposited on a polyimide foil. A water vapor transmission rate of 3.6×10⁻⁶ g/m²-day was obtained for a 1.5 um-thick single permeation layer. Inverted type organic photovoltaic passivated by the hybrid material was used to evaluate the effectiveness of this encapsulation. Efficiency decay was not observed in the cell coated with this encapsulation layer after 3000-hour exposure to the air; on the contrary, the un-encapsulated counterpart cell degraded rapidly and completely failed after 120-hour exposure to the

air. The result shows that this single-layer hybrid material encapsulation can enhance the stability of organic photovoltaic cell. The cell life time is greatly improved.

10:00am **EM+NS+TF-FrM6 Solution Processed Oxide Semiconductor and Dielectric Thin Films: Towards High Performance, Low Temperature ZnO Field-effect Transistors with Low Operation Voltage.** *Yu Liu, H. Katz*, Johns Hopkins University

Solution processing is a preferred method for manufacturing large-area low-cost electronic devices. High performance metal oxide semiconductor-based field-effect transistors can be fabricated in this manner. For applications of flexible electronics, a low processing temperature is required to avoid overheating of the substrate material. It is a challenge to fabricate a dense impurity-free oxide semiconductor film at low temperature. A water-based ZnO precursor with ammine-hydroxo complex was introduced to decrease the processing temperature. However, repeated time-consuming centrifugation and decantation steps are required in this process.

To simplify the processing steps we discovered a new strategy to prepare aqueous ZnO precursor. Based on this precursor, ZnO FETs with a benchmark dielectric SiO₂ have been fabricated at 200 °C. The transistors exhibited promising performance with a saturation field-effect mobility of 0.7 cm²·V⁻¹·s⁻¹ and a typical on/off current ratio on the order of 10⁴. To prepare the precursor, zinc nitrate hexahydrate and acetylacetone were dissolved in ammonium hydroxide with a concentration of 0.6 M. As prepared precursor was then filtered and dilute it with DI water. A similar strategy was applied in the preparation of aqueous zinc tin oxide precursor with tin fluoride as tin source.

Based on a redox chemical reaction between fuel and highly exothermic oxidizer, a combustion processing method has been found to be promising for decreasing the annealing temperature of oxide semiconductor thin films. In this study, combustion processing strategy was used in preparing high capacitance ion-incorporated alumina dielectrics at 200 °C by using urea as the fuel and aluminum nitrate nonahydrate as oxidizer.

Both zinc tin oxide and sodium-incorporated alumina low temperature precursors showed strong exothermic reaction peaks at temperatures lower than 200 °C. This suggests a conversion from ammine-hydroxo/combustion precursor to solid zinc tin oxide/sodium incorporated alumina thin films at a temperature lower than 200 °C. A sharp (002) peak is shown in the XRD pattern of 200 °C processed ZnO thin film, which demonstrates a wurtzite crystal structure.

The high-k dielectrics exhibited a good compatibility with our low temperature ZnO precursor and excellent transistor performance has been achieved in these devices. With this, we are able to fabricate low temperature low voltage transistors on plastic substrates such as polyimide. This low temperature ZnO precursor could also be applied to fabricate flexible inverters in combination with p-type solution processed polymer semiconductors, such as PBTTT and TIPS-pentacene.

10:40am **EM+NS+TF-FrM8 Metal Oxide Conductors and Semiconductors: From Materials to Device Applications.** *Elvira Fortunato, R. Martins*, FCT-UNL and CEMOP-UNINOVA, Portugal
INVITED

Transparent electronics has arrived and is contributing for generating a free real state electronics that is able to add new electronic functionalities onto surfaces, which currently are not used in this manner and where silicon cannot contribute [1,2]. The already high performance developed n- and p-type TFTs have been processed by physical vapour deposition (PVD) techniques like rf magnetron sputtering at room temperature which is already compatible with the use of low cost and flexible substrates (polymers, cellulose paper, among others). Besides that a tremendous development is coming through solution-based technologies very exciting for ink-jet printing, where the theoretical limitations are becoming practical evidences. In this presentation we will review some of the most promising new technologies for n- and p-type thin film transistors based on oxide semiconductors and its currently and future applications.

[1] E. Fortunato, P. Barquinha, and R. Martins, "Oxide Semiconductor Thin-Film Transistors: A Review of Recent Advances," *Advanced Materials*, vol. 24, pp. 2945-2986, Jun 2012.

[2] P. Barquinha, R. Martins, L. Pereira and E. Fortunato, *Transparent Oxide Electronics: From Materials to Devices*. West Sussex: Wiley & Sons (March 2012). ISBN 9780470683736.

11:20am **EM+NS+TF-FrM10 Influence of Oxygen Diffusion in Transparent In_{0.9}Sn_{0.1}O_x Film on Effective Work Function Change.** *Toshihide Nabatame*, NIMS, Japan, *H. Yamada*, Shibaura Institute of Technology, Japan, *A. Ohi*, NIMS, Japan, *T. Oishi*, Shibaura Institute of Technology, Japan, *T. Chikyo*, NIMS, Japan

The In_{0.9}Sn_{0.1}O_x (ITO) films is widely used as transparent electrodes in optical and optoelectronic devices. The work function (WF) of the ITO film was generally evaluated by optical measurements such as ultraviolet photoemission spectroscopy and Kelvin probe. However, the optically measured WF differs from the effective work function (EWF) estimated by electrical measurement. The influence of oxygen diffusion in ITO film on EWF change has not been also understood. In this paper, we systematically investigate EWF change of ITO film by oxidation and reduction annealing. We also examine oxygen diffusion coefficient (D) of ITO film, using isotope ¹⁸O tracer, to discuss influence of oxygen diffusion of ITO film on EWF change.

The ITO films were prepared under an Ar/O₂ by sputtering using an In_{0.9}Sn_{0.1}O_x target. The ITO-gated metal-oxide-semiconductor (MOS) capacitors with HfO₂ and SiO₂ gate insulators were fabricated to estimate EWF value of ITO film. The ITO (150 nm)/SiO₂/Si films were annealed at 300 – 500 °C for 30 min under 10⁴ Pa of ¹⁸O isotope (99%) gas to obtain D value.

The resistivity of ITO film, which consists of cubic structure, shows an almost same value regardless of oxidation and reduction annealing temperatures. The EWF of ITO-gated MOS capacitors significantly changes from 4.4 to 5.2 eV as the oxidation annealing temperature increases from 250 to 350 °C. The EWF change is saturated at 350 °C. On the other hand, the EWF value decreases in reduction annealing temperature ranging from 200 to 350 °C. This must be due to oxygen introduction and removal in ITO film during oxidation and reduction annealing, respectively. To understand the mechanism of oxygen transfer in the ITO film, we examine D behavior of ITO film. The ITO film has a large D value of about a 1.1X10⁻²⁰cm²/s at 300 °C and a small activation energy (E_a) of about 1.4 eV. We found that the D and E_a values are similar to those of grain boundary in monoclinic ZrO₂. This results indicate that oxygen diffusion of ITO film occurs even at low temperature of 300 °C and affects to the EWF change during oxidation and reduction annealing at around 300 °C.

11:40am **EM+NS+TF-FrM11 Transparent Conducting Films from Ultraporous Aerogels of Single-Walled Carbon Nanotubes / PEDOT:PSS Composites.** *Xi Liu, L.M. Porter, M.F. Islam*, Carnegie Mellon University

In this study we report on the fabrication and characterization of ultralight (>99% porosity) aerogels based on single-walled carbon nanotubes (SWCNTs) and poly(ethylene dioxythiophene) : poly(styrene sulfonate) (PEDOT:PSS), that are electrically conducting and highly stretchable. The aerogels were created by critical-point drying of aqueous elastic co-gels of individually dispersed SWCNTs mixed with PEDOT:PSS to yield either free-standing films or thin films supported on flexible (PET) or glass substrates; the nanotubes substantially reduce the percolation threshold of PEDOT:PSS. These transparent conductors with sheet resistance of 35 ohm/sq and 60% transparency (at 550 nm) also proved to be highly flexible – they can be repeatedly stretched to 20% with < 1% change in resistivity. The electrical, optical, mechanical, and microstructural properties of these materials will be presented, along with their application in devices.

Scanning Probe Microscopy Focus Topic

Room: 312 - Session SP+AS+BI+EM+NS+SE+SS-FrM

Probe-Sample Interactions and Emerging Instrument Formats

Moderator: Carl Ventrice, Jr., University at Albany-SUNY

8:40am **SP+AS+BI+EM+NS+SE+SS-FrM2 2013 ASSD Student Award Talk: New Insights into Nanoscale Adhesion from *In Situ* TEM Studies.** *Tevis Jacobs, J.A. Lefever*, University of Pennsylvania, *J. Liu*, University of Wisconsin-Madison, *D.S. Grierson*, SysteMECH LLC, *K.E. Ryan, P.L. Keating, J.A. Harrison*, United States Naval Academy, *K.T. Turner, R.W. Carpick*, University of Pennsylvania

A fundamental understanding of adhesion is important for applications at all length scales, but is particularly critical in nanoscale devices and applications due to their high surface-to-volume ratio. Advancements in studying such tribological phenomena are typically hindered by the inaccessibility of the sliding interface. We will present nanoscale adhesion measurements conducted inside of a transmission electron microscope (TEM), using a modified *in situ* nanoindentation apparatus that makes

contact with atomic force microscope (AFM) cantilever tips. This tool provides new opportunities to observe, identify, and quantify tribological processes with unprecedented access and resolution. First, using ultra-strong carbon-based tip materials, we find that roughness of tips can greatly reduce the pull off force and lead to severe underestimation of the work of adhesion [1]. Furthermore, we have quantified adhesion by making and breaking contact between nanoscale silicon asperities and a flat diamond substrate. The snap-in distance and the pull-off force are measured with sub-nanometer and sub-nanonewton resolution, respectively. The shape of the Si asperity is determined with sub-nanometer resolution immediately before and after contact to verify that elastic conditions were maintained. From this, we independently determine the work of adhesion and range of adhesion. The results show that accounting for roughness has a strong effect on both parameters. These two results demonstrate the importance of applying in situ approaches to studies of adhesion. --- 1. Jacobs, T.D.B., Ryan, K.E., Keating, P.L., Grierson, D.S., Lefever, J.A., Turner, K.T., Harrison, J.A. and Carpick, R.W. The Effect of Atomic-Scale Roughness on the Adhesion of Nanoscale Asperities: A Combined Simulation and Experimental Investigation. *Tribol. Lett.* 50, 81-93 (2013).

9:40am **SP+AS+BI+EM+NS+SE+SS-FrM5 Nanoscale Mapping of the W/Si(001) Schottky Barrier using Ballistic Electron Emission Microscopy**, *Christopher Durcan*, University of Albany-SUNY, *V.P. LaBella*, University at Albany-SUNY

The W/Si(001) Schottky barrier was spatially mapped using ballistic electron emission microscopy (BEEM) and ballistic hole emission microscopy (BHEM) using high resistivity *n*-type and *p*-type silicon substrates. A thin tungsten silicide is observed upon deposition utilizing transmission electron microscopy (TEM) and Rutherford backscattering spectrometry (RBS). The sum of the Schottky barrier heights from *n*-type and *p*-type silicon substrates agree with the silicon band gap. The BEEM and BHEM spectra are fit utilizing a linearization method to the power law of the BEEM model. Spatially resolved Schottky barrier maps are generated over a 1 μ m x 1 μ m area and provide insight into the spatial homogeneity of the barrier height. Histograms of the barrier heights show a Gaussian distribution, consistent with an interface dipole model.

10:00am **SP+AS+BI+EM+NS+SE+SS-FrM6 Local Probing of Superconductivity in Half Heusler Compounds**, *Hongwoo Baek*, NIST & Seoul National University, Republic of Korea, *J. Ha*, *D. Zhang*, NIST/Maryland Nano Center, University of Maryland, *Y. Nakajima*, *P.S. Syers*, *X. Wang*, *K. Wang*, *J. Paglione*, University of Maryland, *Y. Kuk*, Seoul National University, Republic of Korea, *J.A. Stroscio*, NIST

Heusler alloys have attracted interest as multifunctional experimental platforms for topological quantum phenomena ranging from magnetism to superconductivity and heavy fermion behavior. The rare-earth chalcogenide ternary half Heusler compounds were theoretically predicted to have topologically nontrivial surface states due to band inversion [1]. The lack of inversion symmetry of the crystal lattice makes unconventional pairing symmetry feasible. The superconductivity in the non-centrosymmetric half Heusler compound YPtBi was recently reported as a promising system for the investigation of topological superconductivity [2]. In this work, we use ultra low temperature scanning tunneling micro scopy to investigate the superconducting properties of the ternary half Heusler compounds YPdBi and YPtBi. Both were theoretically proposed to have topological states with different band inversion strength [1], and experimentally reported as a topological insulator [3]. Strong spin-orbit coupling and the lack of inversion symmetry present the possibility of spin-triplet superconductivity in these materials. The tunneling spectra of YPdBi show two different superconducting gaps of 0.36 meV and 0.16 meV depending on the measurement location. The variation in gaps might originate from inhomogeneity in the crystal. The superconducting gap of 0.36 meV is completely suppressed above a critical magnetic field of $B=2.5$ T, in agreement with bulk transport measurements. A superconducting gap of 0.21 meV and an upper critical field of 1.25 T were measured in a circular superconducting domain of diameter ≈ 180 nm in YPtBi. Sequential addition of single vortices to the superconducting YPtBi domain could be observed with increasing magnetic field, with vortices occupying the perimeter of the island. These observations will be discussed in terms of island confinement and pairing symmetry of YPtBi.

[1] S. Chadov, X. Qi, J. Kubler, G. H. Fecher, C. Felser, and S. C. Zhang, *Nat. Mater.* **9**, 541 (2010).

[2] N. P. Butch, P. Syers, K. Kirshenbaum, A. P. Hope, and J. Paglione, *Phys. Rev. B* **84**, 220504(R) (2011).

[3] W. Wang, Y. Du, G. Xu, X. Zhang, E. Liu, Z. Liu, Y. Shi, J. Chen, G. Wu, and X. Zhang, *Scientific Reports* **3** (2013).

10:40am **SP+AS+BI+EM+NS+SE+SS-FrM8 Multimodal Intermittent Contact Atomic Force Microscopy: Topographical Imaging, Compositional Mapping, Subsurface Visualization and Beyond**, *Santiago Solares*, George Washington University

Multifrequency atomic force microscopy (AFM) refers to a family of techniques that involve excitation of the microcantilever probe at more than one frequency [R. Garcia and E.T. Herruzo, *Nature Nanotechnology* **7**, 217 (2012)]. This can be carried out in a sequential manner, varying the excitation frequency over time, as in chirp band excitation methods, or simultaneously supplying drive signals containing more than one frequency to the cantilever shaker. The latter mode of operation commonly involves the simultaneous excitation of more than one cantilever eigenmode, such that each eigenmode is used to carry out different functions. For example, in a recently developed trimodal imaging scheme for soft sample characterization [D. Ebeling, B. Eslami and S.D. Solares, *ACS Nano*, **7**, 10387 (2013)], the fundamental eigenmode is used for topographical acquisition, as in standard tapping-mode AFM, while two higher eigenmodes are used for compositional mapping and subsurface visualization, respectively. This talk presents experimental and computational results for validated multimodal imaging schemes involving one to three eigenmodes, and discusses the expected benefits and complexities of including more than three eigenmodes.

Authors Index

Bold page numbers indicate the presenter

— A —

Abriago, M.: BI+AS+NS-MoA9, **9**
Adam, S.: 2D+EM+MI+MN+NS+SS+TF-ThA4, **43**
Afsari, S.: SP+AS+EM+NS+SS-ThP8, **50**
Aguilar, R.: SP+AS+EM+NS+SS-ThP8, **50**
Ahmadi, M.: NS+AS-WeA4, **33**
Ahrelrs, F.: 2D+AS+HI+NS+SS-ThM3, **37**
Aihara, T.: EN+EM+MN+NS+TR-MoA11, **10**
Albertini, D.: EM+MI+NS-MoM8, **3**
Allen, M.G.: MN+NS-TuA1, **21**
Altman, E.I.: 2D+EM+NS+SS+TF-WeM4, **27**
Amster, O.: SP+AS+BI+NS+SS-WeA10, **35**
Anand, B.: EN+EM+MN+NS+TR-MoA3, **9**
Ando, Y.: SP+AS+BI+NS+SS-WeA3, **35**
Anz, S.: NS+HI-TuM11, **15**
Aoki, T.: EM+MI+NS-MoM3, **2**
Aoki, Y.: SS+AS+NS-ThA6, **47**
Appenzeller, J.: 2D+EM+MS+NS-FrM8, **53**
Arble, C.: IS+2D+MC+NS+SP+SS-WeA11, **33**
Arey, B.: AP+AS+EN+NS+SS-ThA4, **45**
Armadottir, L.: BI+AS+MN+NS-TuM4, **13**
Artyushkova, K.: BI+AS+MN+NS-TuM12, **14**
Asensio, M.C.: 2D+AS+EM+NS+SS-MoA6, **6**
Atanassov, P.: BI+AS+MN+NS-TuM12, **14**
Atwater, H.: NS+EN-MoA1, **11**
Avila, J.: 2D+AS+EM+NS+SS-MoA6, **6**
Axnanda, S.A.: IS+2D+MC+NS+SP+SS-WeA10, **33**
Aydogan, P.: 2D+EM+MI+MN+NS+SS+TF-ThA11, **44**
Azad, Z.: BI+AS+NS-MoA11, **9**
Azcati, A.: 2D+EM+NS+SS+TF-WeM6, **27**

— B —

Babanova, S.: BI+AS+MN+NS-TuM12, **14**
Bachelet, R.: EM+MI+NS-MoM8, **3**
Baek, H.: SP+AS+BI+EM+NS+SE+SS-FrM6, **56**;
SP+AS+EM+NS+SS-ThP3, **50**
Baer, D.R.: BI+AS+NS-MoA7, **8**
Bagot, P.A.J.: AP+AS+EN+NS+SS-ThA6, **45**
Balamurugan, B.: AP+AS+MC+NS+SS-ThM12, **39**
Ballard, J.: NS+HI-TuM11, **15**
Balsano, R.: NS+AS-WeA10, **34**
Banys, J.: 2D+EM+MI+MN+NS+SS+TF-ThA9, **44**
Barback, C.: BI+AS+NS-MoA2, **7**
Barroo, C.: AP+AS+EN+NS+SS-ThA3, **44**
Barroso, D.: 2D+EM+NS+SS+TF-WeM10, **28**;
SP+AS+BI+NS+SS-WeA11, **36**
Bartels, L.: 2D+EM+NS+SS+TF-WeM10, **28**;
SP+AS+BI+NS+SS-WeA11, **36**
Bartles, L.: 2D+EM+MI+MN+NS+SS+TF-ThA8, **43**
Bartrand, J.A.: AP+AS+NS+SS-FrM8, **54**
Bartynski, R.A.: EN+EM+NS-TuA4, **20**
Basile, L.: SP+2D+AS+EM+MC+NS+SS-ThM11, **40**
Batzill, M.: 2D+AS+EM+NS+SS-MoA6, **6**
Baykara, M.Z.: SP+AS+BI+NS+SS-ThA3, **45**
Behafarid, F.: NS+AS-WeA4, **33**
Belianinov, A.: 2D+EM+MI+MN+NS+SS+TF-ThA9, **44**
Belkin, M.: NS+AS-WeA9, **34**
Belsey, N.A.: BI+AS+NS-MoA8, **8**
Bennett, A.I.: TR+NS-ThM6, **42**
Bent, S.F.: SS+AS+NS-ThA10, **48**
Bentley, W.E.: BI+AS+MN+NS-TuM2, **13**;
MN+NS-TuA9, **22**
Ben-Yoav, H.: BI+AS+MN+NS-TuM3, **13**
Berger, H.: 2D+AS+EM+MI+MN+NS+TF-WeA7, **31**
Bernhardt, G.P.: SE+NS+TR-TuM2, **16**
Beron, F.: NS-ThP7, **49**

Bersch, E.: 2D+AS+HI+MC+NS+PS+SP+SS-TuA3, **18**
Bersuker, G.: 2D+AS+HI+MC+NS+PS+SP+SS-TuA3, **18**
Bertolazzi, S.: 2D+AS+EM+MI+MN+NS+TF-WeA4, **31**
Bhimanapati, G.R.: 2D+EM+NS+SS+TF-WeM11, **28**
Bielefeld, J.D.: 2D+AS+HI+MC+NS+PS+SP+SS-TuA3, **18**
Birss, V. I.: NS-ThP5, **49**
Bischof, M.: NS+HI-TuM11, **15**
Bitsis, C.: SE+NS+TR-TuM12, **17**
Blair, S.L.: BI+AS+NS-MoA2, **7**
Bobek, S.: 2D+EM+NS+SS+TF-WeM10, **28**;
SP+AS+BI+NS+SS-WeA11, **36**
Boettger, P.H.M.: SE+NS+TR-TuM10, **17**
Bol, A.A.: 2D+EM+MS+NS-FrM6, **52**
Bolotin, K.I.: 2D+AS+EM+MI+MN+NS+TF-WeA1, **31**
Bonnell, D.A.: NS+EN-MoA10, **11**; NS-WeM12, **30**
Bonner, J.: BI+AS+NS-MoA1, **7**
Borguet, E.: SP+AS+EM+NS+SS-ThP8, **50**
Borisevich, A.: 2D+EM+MI+MN+NS+SS+TF-ThA9, **44**
Borovsky, B.P.: TR+NS-ThM12, **42**
Borowik, L.: SP+AS+BI+NS+SS-ThA4, **45**
Boscoboinik, A.: IS+2D+MC+NS+SP+SS-WeA11, **33**
Bousser, E.: SE+NS+TR-TuM5, **16**
Braun, P.: NS+SE-MoM8, **4**
Brivio, J.: 2D+AS+EM+MI+MN+NS+TF-WeA4, **31**
Brockman, J.: 2D+AS+HI+MC+NS+PS+SP+SS-TuA3, **18**
Brown, K.: 2D+EM+NS+SS+TF-WeM10, **28**
Brown, K.A.: NS+SE-MoM11, **4**
Browning, J.: EN+EM+MN+NS+TR-MoA9, **10**
Browning, N.D.: AP+AS+NS+SS-FrM8, **54**
Brune, H.: SP+AS+BI+NS+SS-ThA8, **46**
Büchner, C.: 2D+EM+NS+SS+TF-WeM12, **28**
Bultman, J.E.: 2D+EM+NS+PS+SS+TF-MoM5, **1**
Burger, A.: EM+MI+NS-MoM4, **2**
Burkett, S.L.: MN+NS-TuA3, **21**
Burnham, N.A.: NS+SE-MoM3, **4**
Butson, E.: SS+AS+NS-ThA9, **47**

— C —

Cahill, D.G.: NS+SE-MoM8, **4**
Calafiore, G.: NS+HI-TuM1, **14**
Cao, L.: 2D+AS+HI+MC+NS+PS+SP+SS-TuA4, **18**
Cao, S.: EM+MI+NS-MoM10, **3**
Carencio, S.: NS-WeM6, **29**
Cargill, R.S.: BI+AS+MN+NS-TuM4, **13**
Carpick, R.W.: SP+AS+BI+EM+NS+SE+SS-FrM2, **55**; TR+NS-ThM5, **41**
Carrier, X.: AP+AS+EN+NS+SS-ThA6, **45**
Castle, J.R.: BI+AS+MN+NS-TuM4, **13**
Centrone, A.: NS+AS-WeA7, **34**; NS-ThP3, **49**
Chabal, Y.J.: EN+EM+MN+NS+TR-MoA3, **9**;
NS+HI-TuM11, **15**; SS+AS+NS-ThA8, **47**
Chae, J.: 2D+EM+MI+MN+NS+SS+TF-ThA4, **43**;
NS-ThP3, **49**
Chakraborty, D.: NS+SE-MoM5, **4**
Chen, C.: 2D+AS+HI+MC+NS+PS+SP+SS-TuA4, **18**
Chen, J.Z.: EM+NS+TF-FrM5, **54**
Chen, S.: BI+AS+NS-MoA7, **8**
Chen, X.: NS-WeM12, **30**
Cheng, I.C.: EM+NS+TF-FrM5, **54**
Cherala, A.: NS+HI-TuM11, **15**
Chevalier, N.: 2D+EM+MI+MN+NS+SS+TF-ThA10, **44**; SP+AS+BI+NS+SS-ThA4, **45**
Chiang, S.: SS+NS-TuA12, **26**

Chikyo, T.: EM+NS+TF-FrM10, **55**
Chocron, S.E.: BI+AS+MN+NS-TuM3, **13**
Choi, H.K.: NS+EN-MoA4, **11**
Choi, J.S.: NS+EN-MoA4, **11**
Chopra, S.N.: EM+MI+NS-MoM11, **3**
Chu, N.N.: SP+AS+EM+NS+SS-ThP5, **50**
Chu, S.: BI+AS+MN+NS-TuM2, **13**;
EN+EM+NS-TuA10, **21**
Chung, W.-C.: MN+NS-TuA11, **23**
Ciobanu, C.V.: 2D+EM+NS+PS+SS+TF-MoM10, **2**
Ciochon, P.: SS+AS+NS-ThA1, **46**
Clark, K.: SP+2D+AS+EM+MC+NS+SS-ThM11, **40**; SP+2D+AS+EM+MC+NS+SS-ThM6, **40**
Cohen, H.: EN+EM+MN+NS+TR-MoA8, **10**
Cojocaru-Mirédin, O.: AP+AS+MC+NS+SS-ThM3, **38**
Colby, R.J.: AP+AS+EN+NS+SS-ThA4, **45**
Comfort, E.: 2D+EM+MS+NS-FrM4, **52**
Conley, Jr., J.F.: BI+AS+MN+NS-TuM4, **13**
Cornejo, J.: BI+AS+MN+NS-TuM12, **14**
Coulter, K.: SE+NS+TR-TuM12, **17**
Coy-Diaz, H.: 2D+AS+EM+NS+SS-MoA6, **6**
Craighead, H.G.: BI+AS+NS-MoA10, **9**
Crommie, M.F.: 2D+EM+MS+NS-FrM3, **52**
Crum, J.: AP+AS+NS+SS-FrM4, **54**
Crumlin, E.J.C.: IS+2D+MC+NS+SP+SS-WeA10, **33**
Cui, J.: AP+AS+MC+NS+SS-ThM12, **39**
Culbertson, J.: 2D+AS+EM+NS+SS-MoA3, **6**
Cullen, W.G.: 2D+AS+HI+MC+NS+PS+SP+SS-TuA9, **18**
Culver, J.: EN+EM+NS-TuA10, **21**; EN+EM+NS-TuA9, **20**
Cun, H.Y.: 2D+AS+EM+NS+SS-MoA1, **6**
Cuvilly, F.: AP+AS+NS+SS-FrM5, **54**

— D —

Dallarto, S.: NS+HI-TuM1, **14**
Dandley, E.C.: BI+AS+NS-MoA1, **7**
Daniel, R.: SE+NS+TR-TuM11, **17**
Dazzi, A.: NS+AS-WeA9, **34**
De Decker, Y.: AP+AS+EN+NS+SS-ThA3, **44**
de Heer, W.A.: 2D+AS+HI+NS+SS-ThM10, **38**
Dean, C.R.: 2D+EM+MI+MN+NS+SS+TF-ThA4, **43**
DeBenedetti, W.J.I.: SS+AS+NS-ThA8, **47**
Demkov, A.A.: EM+MI+NS-MoM11, **3**;
EM+MI+NS-MoM3, **2**
Deng, W.: SP+2D+AS+EM+MC+NS+SS-ThM11, **40**
Deng, X.: SS+NS-TuA4, **25**
Devaraj, A.: AP+AS+MC+NS+SS-ThM12, **39**;
AP+AS+MC+NS+SS-ThM6, **39**
Dick, D.: NS+HI-TuM11, **15**
Diercks, D.R.: AP+AS+NS+SS-FrM1, **53**
Dietrich, R.: BI+AS+MN+NS-TuM3, **13**
Dijon, J.: 2D+EM+MI+MN+NS+SS+TF-ThA10, **44**
Dil, J.H.: 2D+EM+MI+MN+NS+SS+TF-ThA6, **43**
Dillon, E.: NS+AS-WeA9, **34**
Diniz, J.A.: NS-ThP7, **49**
DiStefano, J.: 2D+AS+HI+MC+NS+PS+SP+SS-TuA3, **18**
Dixson, R.G.: SP+AS+BI+NS+SS-WeA4, **35**
Dorman, J.: EN+EM+MN+NS+TR-MoA10, **10**
Dowben, P.A.: 2D+EM+MI+MN+NS+SS+TF-ThA8, **43**; EM+MI+NS-MoM10, **3**
Du, S.X.: 2D+AS+EM+NS+SS-MoA10, **7**
Du, X.: BI+AS+MN+NS-TuM4, **13**
Dubourdieu, C.: EM+MI+NS-MoM8, **3**
Duerloo, K.-A.N.: 2D+AS+EM+MI+MN+NS+TF-WeA12, **32**
Durand, C.P.: SP+2D+AS+EM+MC+NS+SS-ThM10, **40**; SP+2D+AS+EM+MC+NS+SS-ThM11, **40**

Durcan, C.: NS+AS-WeA10, 34;
 SP+AS+BI+EM+NS+SE+SS-FrM5, **56**
 Dziaugys, A.: 2D+EM+MI+MN+NS+SS+TF-
 ThA9, 44
 — **E** —
 Ebnounasir, A.: 2D+EM+NS+PS+SS+TF-MoM10,
 2
 Eichelsdoerfer, D.J.: NS+SE-MoM11, 4
 Eichfeld, S.M.: 2D+EM+NS+SS+TF-WeM6, **27**
 Einstein, T.L.: 2D+AS+EM+MI+MN+NS+TF-
 WeA8, 31
 Ekerdt, J.G.: EM+MI+NS-MoM11, 3
 El Zubir, O.: BI+AS+NS-MoA6, 8
 Eliseev, E.: 2D+EM+MI+MN+NS+SS+TF-ThA9,
 44
 Ellsworth, A.A.: NS+AS+SS-TuA8, 24
 El-Sayed, H.A.: NS-ThP5, 49
 Empante, T.: 2D+EM+NS+SS+TF-WeM10, 28
 Engelhard, M.H.: BI+AS+NS-MoA7, 8
 Erickson, K.: SP+AS+BI+NS+SS-WeA11, 36
 Eriguchi, K.: SE+NS+TR-TuM3, **16**
 Eto, K.: SP+AS+BI+NS+SS-WeA3, 35
 Evans, J.E.: AP+AS+NS+SS-FrM8, 54
 — **F** —
 Feenstra, R.M.: 2D+EM+NS+PS+SS+TF-MoM6,
 1; SP+2D+AS+EM+MC+NS+SS-ThM6, 40
 Feibelman, P.J.: NS-WeM6, 29
 Feigelson, B.N.:
 2D+AS+HI+MC+NS+PS+SP+SS-TuA9, 18
 Felmy, A.: AP+AS+EN+NS+SS-ThA4, 45
 Feng, P.X.-L.: 2D+EM+MS+NS-FrM5, **52**;
 MN+NS-TuA10, 22
 Feng, X.: NS-WeM6, 29
 Feng, Y.: MN+NS-TuA3, 21
 Filikhin, I.N.: NS-ThP9, **49**
 Filler, M.A.: NS+AS+SS-TuA1, **23**
 First, P.N.: SP+2D+AS+EM+MC+NS+SS-ThM3,
 40
 Fisher, B.L.: 2D+EM+NS+SS+TF-WeM3, 27
 Fisher, E.R.: SS+NS-TuA3, 25
 Flynn, B.T.: NS+HI-TuM5, 15
 Fortunato, E.: EM+NS+TF-FrM8, **55**
 Fowlkes, J.: NS+HI-TuM10, 15;
 SP+2D+AS+EM+MC+NS+SS-ThM10, 40
 Frank, M.M.: EM+MI+NS-MoM8, 3
 Frankel, D.J.: SE+NS+TR-TuM2, 16
 Frederick, R.: NS+HI-TuM5, 15
 Fredrickson, K.D.: EM+MI+NS-MoM3, **2**
 Fredriksson, H.: NS-WeM10, **29**
 French, B.: 2D+AS+HI+MC+NS+PS+SP+SS-
 TuA3, **18**
 French, M.: 2D+AS+HI+MC+NS+PS+SP+SS-
 TuA3, 18
 Frenkel, A.: NS+AS+SS-TuA10, 24
 Freund, H.-J.: 2D+EM+NS+SS+TF-WeM12, 28
 Frick, J.R.: SS+NS-TuA11, 26
 Friedman, A.: 2D+AS+EM+NS+SS-MoA3, 6
 Friedman, S.: SP+AS+BI+NS+SS-WeA10, **35**
 Fu, J.: NS+HI-TuM11, 15
 Fuchs, E.: NS+HI-TuM11, 15
 Fuhrer, M.S.: 2D+AS+HI+MC+NS+PS+SP+SS-
 TuA9, 18
 Fujii, H.: EN+EM+MN+NS+TR-MoA11, 10
 Fukuyama, A.: EN+EM+MN+NS+TR-MoA11, **10**
 — **G** —
 Gao, H.-J.: 2D+AS+EM+NS+SS-MoA10, 7
 Gao, Y.: 2D+EM+MI+MN+NS+SS+TF-ThA4, 43
 Gartstein, Y.: EN+EM+MN+NS+TR-MoA3, 9
 Gaskill, D.K.: 2D+AS+HI+MC+NS+PS+SP+SS-
 TuA9, 18
 Gautier, B.: EM+MI+NS-MoM8, 3
 Geier, M.L.: 2D+AS+HI+NS+SS-ThM4, 37
 Geisler, H.: 2D+AS+HI+MC+NS+PS+SP+SS-
 TuA10, 19
 Gerasopoulos, K.D.: BI+AS+MN+NS-TuM2, 13;
 EN+EM+NS-TuA10, 21
 Gerson, Y.: MN+NS-TuA4, 22

Ghodssi, R.: BI+AS+MN+NS-TuM2, 13;
 BI+AS+MN+NS-TuM3, 13; EN+EM+NS-
 TuA10, 21; EN+EM+NS-TuA9, 20; MN+NS-
 TuA9, 22
 Gillette, E.: EN+EM+NS-TuA3, 19
 Gnerlich, M.: EN+EM+NS-TuA10, 21;
 EN+EM+NS-TuA9, **20**
 Gonda, S.: SP+AS+BI+NS+SS-WeA4, 35
 Gonzales, J.M.: 2D+AS+EM+MI+MN+NS+TF-
 WeA11, 31; 2D+EM+NS+SS+TF-WeM5, **27**
 Goodwin, C.: IS+2D+MC+NS+SP+SS-WeA11, **33**
 Gorai, P.: SS+AS+NS-ThA2, 46
 Gorman, B.P.: AP+AS+NS+SS-FrM1, 53
 Götzten, J.: 2D+EM+NS+SS+TF-WeM4, 27
 Grady, M.: NS+SE-MoM8, 4
 Greber, T.: 2D+AS+EM+NS+SS-MoA1, **6**;
 2D+EM+NS+PS+SS+TF-MoM8, 2
 Grierson, D.S.: SP+AS+BI+EM+NS+SE+SS-
 FrM2, 55
 Groot, I.M.N.: IS+2D+MC+NS+SP+SS-WeA7, **32**
 Gu, G.: SP+2D+AS+EM+MC+NS+SS-ThM11,
 40; SP+2D+AS+EM+MC+NS+SS-ThM6, 40
 Gu, X.: NS+HI-TuM1, 14
 Guillet, J.-F.: 2D+EM+MI+MN+NS+SS+TF-
 ThA10, 44
 Guisinger, N.P.: 2D+AS+EM+NS+SS-MoA7, **6**;
 2D+AS+HI+NS+SS-ThM13, 38;
 2D+EM+NS+SS+TF-WeM3, 27
 Gunlycke, D.: 2D+EM+MI+MN+NS+SS+TF-
 ThA3, **43**
 Guo, H.: SP+2D+AS+EM+MC+NS+SS-ThM5, 40
 Guyot-Sionnest, P.: NS+SE-MoM5, 4
 — **H** —
 Ha, J.: SP+AS+BI+EM+NS+SE+SS-FrM6, 56;
 SP+AS+EM+NS+SS-ThP3, **50**
 Habenicht, B.F.: SS+NS-TuA11, 26
 Hahn, D.W.: TR+NS-ThM6, 42
 Haley, D.: AP+AS+EN+NS+SS-ThA6, 45
 Hanbicki, A.T.: 2D+EM+NS+PS+SS+TF-MoM4,
 1
 Haque, M.A.: 2D+EM+NS+PS+SS+TF-MoM5, 1
 Harrison, J.A.: SP+AS+BI+EM+NS+SE+SS-
 FrM2, 55; TR+NS-ThM5, 41
 Hart, C.: EM+MI+NS-MoM4, 2
 Hasegawa, S.: SE+NS+TR-TuM3, 16
 He, G.: 2D+EM+NS+PS+SS+TF-MoM6, 1;
 SP+2D+AS+EM+MC+NS+SS-ThM6, 40
 He, Q.: 2D+EM+MI+MN+NS+SS+TF-ThA9, 44
 Helms, B.A.: NS+SE-MoM10, 4
 Hemmi, A.: 2D+AS+EM+NS+SS-MoA1, 6;
 2D+EM+NS+PS+SS+TF-MoM8, 2
 Hemminger, J.C.: NS-WeM4, 29; SS+NS-TuA9,
 26
 Herath, N.: EN+EM+MN+NS+TR-MoA9, **10**
 Herman, A.K.: BI+AS+MN+NS-TuM4, 13
 Herman, G.S.: BI+AS+MN+NS-TuM4, 13;
 EM+NS+TF-FrM3, **54**; NS+HI-TuM5, 15
 Hernandez, S.C.: BI+AS+MN+NS-TuM5, 13
 Hernandez-Maldonado, D.: AP+AS+NS+SS-
 FrM5, 54
 Hersam, M.C.: 2D+AS+EM+NS+SS-MoA7, 6;
 2D+AS+HI+NS+SS-ThM13, 38;
 2D+AS+HI+NS+SS-ThM4, 37;
 2D+EM+NS+SS+TF-WeM3, 27
 Heyde, M.: 2D+EM+NS+SS+TF-WeM12, 28
 Hight Walker, A.R.:
 2D+AS+EM+MI+MN+NS+TF-WeA7, 31
 Hight-Walker, A.R.:
 2D+AS+EM+MI+MN+NS+TF-WeA4, 31
 Hines, M.A.: SS+AS+NS-ThA8, 47
 Hipps, K.W.: SP+2D+AS+EM+MC+NS+SS-
 ThM1, 39
 Hiramatsu, M.: 2D+EM+MS+NS-FrM10, 53
 Hirayama, H.: SS+AS+NS-ThA6, **47**
 Hite, J.K.: 2D+AS+HI+MC+NS+PS+SP+SS-
 TuA9, 18
 Hjort, M.: NS+AS+SS-TuA4, 24
 Hofer, W.: 2D+AS+EM+NS+SS-MoA10, 7
 Holland, G.: NS-ThP3, 49

Hone, J.C.: 2D+EM+MI+MN+NS+SS+TF-ThA4,
 43
 Hori, M.: 2D+EM+MS+NS-FrM10, 53
 Horwood, C.: NS-ThP5, 49
 Hossain, L.: 2D+EM+NS+SS+TF-WeM6, 27
 Hou, J.: NS+EN-MoA10, **11**
 Howansky, A.: EN+EM+NS-TuA4, 20
 Hsiao, C.N.: SP+AS+EM+NS+SS-ThP5, 50
 Hsu, C.-L.: MN+NS-TuA12, 23
 Hu, J.J.: 2D+EM+NS+PS+SS+TF-MoM5, 1
 Huang, E.: 2D+EM+MS+NS-FrM3, 52
 Hubbard, L.R.: SE+NS+TR-TuM1, **16**
 Huffman, E.S.: SS+NS-TuA12, 26
 Hwang, E.: NS+EN-MoA4, 11
 Hytch, M.: EM+MI+NS-MoM8, 3
 — **I** —
 Iannuzzi, M.: 2D+AS+EM+NS+SS-MoA1, 6
 Idrobo, J.-C.: SP+2D+AS+EM+MC+NS+SS-
 ThM11, 40
 Ikari, T.: EN+EM+MN+NS+TR-MoA11, 10
 Imai, S.: 2D+EM+MS+NS-FrM10, 53
 Ishida, Y.: SP+AS+BI+NS+SS-WeA3, 35
 Ishikawa, K.: 2D+EM+MS+NS-FrM10, 53
 Islam, M.F.: EM+NS+TF-FrM11, 55
 Ista, L.: BI+AS+MN+NS-TuM12, 14
 Iwasawa, H.: 2D+EM+MI+MN+NS+SS+TF-
 ThA8, 43
 — **J** —
 Jacobs, P.G.: BI+AS+MN+NS-TuM4, 13
 Jacobs, T.D.B.: SP+AS+BI+EM+NS+SE+SS-
 FrM2, **55**
 Jaeger, D.: NS+HI-TuM11, 15
 Jariwala, D.: 2D+AS+HI+NS+SS-ThM4, **37**
 Jayanthinarasimham, A.:
 2D+AS+HI+MC+NS+PS+SP+SS-TuA8, 18
 Jennings, J.: EN+EM+NS-TuA11, 21
 Jeon, M.H.: 2D+AS+EM+NS+SS-MoA8, 7
 Jeon, N.: NS+AS+SS-TuA3, **23**
 Jespersen, M.L.: 2D+EM+NS+PS+SS+TF-MoM5,
 1
 Jia, H.: MN+NS-TuA10, **22**
 Jia, J.F.: SP+AS+BI+NS+SS-WeA1, **34**
 Jiang, H.: MN+NS-TuA7, **22**
 Jiang, X.: AP+AS+MC+NS+SS-ThM12, **39**
 Jiang, Y.: SP+AS+BI+NS+SS-ThA6, **46**; TR+NS-
 ThM5, 41
 Jin, M.: NS+AS-WeA9, 34
 Johnston, S.: SP+AS+BI+NS+SS-WeA10, 35
 Johnston-Peck, A.C.: NS+AS-WeA3, **33**
 Jonker, B.T.: 2D+EM+NS+PS+SS+TF-MoM4, 1
 Jordan-Sweet, J.: EM+MI+NS-MoM8, 3
 Ju, L.: 2D+EM+MS+NS-FrM3, 52
 Jung, R.: NS+HI-TuM3, **14**
 Jung, S.: 2D+EM+MI+MN+NS+SS+TF-ThA4, 43
 Junkermier, C.: 2D+AS+EM+NS+SS-MoA3, 6
 — **K** —
 Kahn, S.: 2D+EM+MS+NS-FrM3, 52
 Kalinin, S.V.: 2D+EM+MI+MN+NS+SS+TF-
 ThA9, 44
 Kanakasabapathy, S.: NS+HI-TuM3, 14
 Kapoor, M.: AP+AS+NS+SS-FrM3, **53**
 Karayaylali, P.: SP+AS+BI+NS+SS-ThA3, 45
 Katz, H.: EM+NS+TF-FrM6, 55
 Kaur, S.: NS+SE-MoM10, 4
 Keating, P.L.: SP+AS+BI+EM+NS+SE+SS-FrM2,
 55; TR+NS-ThM5, 41
 Keckes, J.: SE+NS+TR-TuM11, 17
 Kelly, D.L.: BI+AS+MN+NS-TuM3, 13
 Kelly, M.: 2D+EM+NS+SS+TF-WeM11, 28
 Kelly, T.F.: AP+AS+MC+NS+SS-ThM1, **38**
 Kessels, W.M.M.: 2D+EM+MS+NS-FrM6, 52
 Ketchum, D.: EN+EM+NS-TuA9, 20
 Kim, E.: BI+AS+MN+NS-TuM3, 13
 Kim, H.: 2D+EM+MI+MN+NS+SS+TF-ThA10,
 44
 Kim, J.H.: NS-ThP1, **49**
 Kim, K.N.: 2D+AS+EM+NS+SS-MoA8, 7

- Kim, K.S.: 2D+AS+EM+NS+SS-MoA4, **6**;
2D+AS+EM+NS+SS-MoA8, **7**
- Kim, P.: 2D+EM+MI+MN+NS+SS+TF-ThA4, **43**
- Kim, S.: SP+AS+BI+NS+SS-WeA3, **35**;
SP+AS+EM+NS+SS-ThP3, **50**
- Kim, T.-H.: SP+AS+BI+NS+SS-WeA9, **35**
- Kim, W.-K.: TR+NS-ThM1, **41**
- Kim, Y.: SP+AS+EM+NS+SS-ThP3, **50**
- Kim, Y.W.: BI+AS+MN+NS-TuM2, **13**; MN+NS-TuA9, **22**
- Kinder, E.K.: 2D+AS+HI+NS+SS-ThM5, **37**
- King, S.W.: 2D+AS+HI+MC+NS+PS+SP+SS-TuA3, **18**
- Kingshott, P.: BI+AS+NS-MoA9, **9**
- Kiraly, B.T.: 2D+AS+EM+NS+SS-MoA7, **6**;
2D+AS+HI+NS+SS-ThM13, **38**;
2D+EM+NS+SS+TF-WeM3, **27**
- Kis, A.: 2D+AS+EM+MI+MN+NS+TF-WeA4, **31**
- Kjoller, K.: NS+AS-WeA9, **34**
- Klee, V.: 2D+EM+NS+SS+TF-WeM10, **28**;
SP+AS+BI+NS+SS-WeA11, **36**
- Klemborg-Sapieha, J.: SE+NS+TR-TuM5, **16**
- Klimov, N.N.: 2D+EM+MS+NS-FrM4, **52**
- Knutsson, J.: NS+AS+SS-TuA4, **24**
- Ko, A.: NS+HI-TuM3, **14**
- Kobl Müller, G.: NS+AS+SS-TuA3, **23**
- Kocbas, C.: 2D+EM+MI+MN+NS+SS+TF-ThA11, **44**
- Kocsis, M.: NS+HI-TuM1, **14**
- Kodambaka, S.: 2D+EM+NS+PS+SS+TF-MoM10, **2**
- Koel, B.: SS+AS+NS-ThA11, **48**
- Kokubo, I.: SS+AS+NS-ThA6, **47**
- Kolagani, R.: EM+MI+NS-MoM4, **2**
- Koleske, D.: AP+AS+MC+NS+SS-ThM5, **39**
- Kolli, R.P.: AP+AS+MC+NS+SS-ThM13, **39**
- Kolmakov, A.: NS+AS+SS-TuA7, **24**; NS+AS-WeA11, **34**
- Kolodziej, J.: SS+AS+NS-ThA1, **46**
- Komakov, A.: IS+2D+MC+NS+SP+SS-WeA3, **32**
- Komesu, T.: 2D+EM+MI+MN+NS+SS+TF-ThA8, **43**
- Komorí, F.: SP+AS+BI+NS+SS-WeA3, **35**
- Kondo, H.: 2D+EM+MS+NS-FrM10, **53**
- Kovarik, L.: AP+AS+EN+NS+SS-ThA4, **45**
- Kozen, A.C.: EN+EM+NS-TuA7, **20**;
EN+EM+NS-TuA8, **20**
- Kraya, L.Y.: SP+2D+AS+EM+MC+NS+SS-ThM2, **40**
- Kraya, R.: SP+2D+AS+EM+MC+NS+SS-ThM2, **40**
- Kreuzer, H.J.: AP+AS+MC+NS+SS-ThM10, **39**
- Krick, B.A.: TR+NS-ThM6, **42**
- Krieg, U.: NS+EN-MoA6, **11**
- Kronawitter, C.: SS+AS+NS-ThA11, **48**
- Kruse, N.: AP+AS+EN+NS+SS-ThA3, **44**
- Kruska, K.: AP+AS+EN+NS+SS-ThA6, **45**
- Krylov, S.: MN+NS-TuA4, **22**
- Kuhn, M.: 2D+AS+HI+MC+NS+PS+SP+SS-TuA3, **18**
- Kuk, Y.: SP+AS+BI+EM+NS+SE+SS-FrM6, **56**;
SP+AS+EM+NS+SS-ThP3, **50**
- Kummel, A.C.: 2D+AS+HI+NS+SS-ThM5, **37**;
BI+AS+NS-MoA2, **7**
- Kuo, C.-Y.: MN+NS-TuA12, **23**
- Kuo, H.-Y.: MN+NS-TuA12, **23**
- Kurtz, R.L.: SS+NS-TuA11, **26**
- Kwak, I.J.: 2D+AS+HI+NS+SS-ThM5, **37**
- Kwon, J.Y.: SS+NS-TuA9, **26**
- **L** —
- LaBella, V.P.: 2D+AS+HI+MC+NS+PS+SP+SS-TuA8, **18**; NS+AS-WeA10, **34**;
SP+AS+BI+EM+NS+SE+SS-FrM5, **56**
- Lad, R.J.: SE+NS+TR-TuM2, **16**
- Lahiri, B.: NS-ThP3, **49**
- Lau, C.N.: 2D+EM+MS+NS-FrM1, **52**
- Lauer, I.: EM+MI+NS-MoM8, **3**
- Laumon, L.J.: 2D+AS+HI+NS+SS-ThM4, **37**;
AP+AS+MC+NS+SS-ThM5, **39**; NS+AS+SS-TuA3, **23**
- Lauter, V.: EN+EM+MN+NS+TR-MoA9, **10**
- Lawson, A.P.: NS+EN-MoA3, **11**
- Le Lay, G.: 2D+EM+NS+SS+TF-WeM1, **27**
- Le, D.T.: 2D+AS+EM+MI+MN+NS+TF-WeA3, **31**;
2D+AS+HI+NS+SS-ThM6, **37**;
2D+EM+MI+MN+NS+SS+TF-ThA8, **43**
- Le, S.: 2D+EM+MS+NS-FrM4, **52**
- Lechner, B.A.J.: NS-WeM6, **29**
- Lee, C.: SP+AS+BI+NS+SS-WeA11, **36**
- Lee, D.: NS+HI-TuM3, **14**
- Lee, H.: NS+EN-MoA4, **11**
- Lee, J.: MN+NS-TuA10, **22**; SS+NS-TuA4, **25**
- Lee, J.U.: 2D+AS+HI+MC+NS+PS+SP+SS-TuA8, **18**;
2D+EM+MS+NS-FrM4, **52**
- Lee, P.M.: SE+NS+TR-TuM12, **17**
- Lee, S.B.: EN+EM+NS-TuA3, **19**; EN+EM+NS-TuA7, **20**; EN+EM+NS-TuA8, **20**
- Lee, Y.K.: NS+EN-MoA4, **11**
- Lefebvre, W.: AP+AS+NS+SS-FrM5, **54**
- Lefever, J.A.: SP+AS+BI+EM+NS+SE+SS-FrM2, **55**
- Leggett, G.J.: BI+AS+NS-MoA6, **8**
- Leonard, F.: SP+AS+BI+NS+SS-WeA11, **36**
- Lepkowski, D.L.: NS+EN-MoA11, **12**
- Lewis, B.B.: NS+HI-TuM10, **15**
- Li, A.P.: SP+2D+AS+EM+MC+NS+SS-ThM10, **40**;
SP+2D+AS+EM+MC+NS+SS-ThM11, **40**;
SP+2D+AS+EM+MC+NS+SS-ThM6, **40**
- Li, J.: 2D+EM+NS+PS+SS+TF-MoM6, **1**
- Li, J.J.: AP+AS+NS+SS-FrM1, **53**
- Li, M.: SS+AS+NS-ThA2, **46**
- Li, P.-C.: MN+NS-TuA11, **23**
- Li, Y.: 2D+AS+EM+MI+MN+NS+TF-WeA12, **32**
- Li, Y.S.: EM+NS+TF-FrM5, **54**
- Li, Z.: NS-WeM11, **29**; SP+AS+EM+NS+SS-ThP8, **50**
- Li, Z.Y.: NS+HI-TuM4, **14**
- Liao, X.: NS+SE-MoM11, **4**
- Lieberman, A.: BI+AS+NS-MoA2, **7**
- Lichtenstein, L.: 2D+EM+NS+SS+TF-WeM12, **28**
- Lichtenstein, T.: NS+EN-MoA6, **11**
- Lie, F.L.: NS+HI-TuM3, **14**
- Lin, J.: SE+NS+TR-TuM12, **17**
- Lin, Y.C.: 2D+AS+HI+MC+NS+PS+SP+SS-TuA3, **18**;
2D+EM+NS+SS+TF-WeM6, **27**
- Liu, C.: BI+AS+NS-MoA7, **8**; EN+EM+NS-TuA7, **20**
- Liu, D.-J.: EN+EM+NS-TuA1, **19**
- Liu, J.: AP+AS+EN+NS+SS-ThA4, **45**;
AP+AS+NS+SS-FrM4, **54**; AP+AS+NS+SS-FrM8, **54**;
SP+AS+BI+EM+NS+SE+SS-FrM2, **55**
- Liu, L.: SP+2D+AS+EM+MC+NS+SS-ThM11, **40**;
SS+NS-TuA11, **26**
- Liu, Q.Q.: IS+2D+MC+NS+SP+SS-WeA9, **32**
- Liu, X.: EM+NS+TF-FrM11, **55**
- Liu, Y.: EM+NS+TF-FrM6, **55**; NS-WeM4, **29**
- Liu, Z.: IS+2D+MC+NS+SP+SS-WeA1, **32**
- Liu, Z.L.: IS+2D+MC+NS+SP+SS-WeA10, **33**
- Lo, M.: NS+AS-WeA9, **34**
- Long, N.: BI+AS+MN+NS-TuM5, **13**
- Longo, R.: NS+HI-TuM11, **15**
- Losego, M.: NS+SE-MoM8, **4**
- Lou, J.: 2D+EM+NS+PS+SS+TF-MoM1, **1**;
SP+2D+AS+EM+MC+NS+SS-ThM10, **40**
- Lovinger, D.J.: SS+NS-TuA12, **26**
- Lu, C.-J.: MN+NS-TuA12, **23**
- Lu, F.: NS+AS-WeA9, **34**
- Lu, H.L.: 2D+AS+HI+NS+SS-ThM5, **37**
- Lu, I.: 2D+EM+NS+SS+TF-WeM10, **28**;
SP+AS+BI+NS+SS-WeA11, **36**
- Lui, Z.: NS+HI-TuM1, **14**
- Lynn, K.G.: EN+EM+NS-TuA11, **21**
- **M** —
- Ma, Q.: 2D+EM+MI+MN+NS+SS+TF-ThA8, **43**
- Mackus, A.J.M.: 2D+EM+MS+NS-FrM6, **52**
- Madaan, N.: AP+AS+MC+NS+SS-ThM6, **39**
- Maimon, R.: MN+NS-TuA4, **22**
- Maksymovych, P.: 2D+EM+MI+MN+NS+SS+TF-ThA9, **44**
- Malachosky, E.: NS+SE-MoM5, **4**
- Malko, A.: EN+EM+MN+NS+TR-MoA3, **9**
- Mann, J.: 2D+EM+NS+SS+TF-WeM10, **28**;
SP+AS+BI+NS+SS-WeA11, **36**
- Mannix, A.J.: 2D+AS+EM+NS+SS-MoA7, **6**;
2D+AS+HI+NS+SS-ThM13, **38**;
2D+EM+NS+SS+TF-WeM3, **27**
- Marceau, E.: AP+AS+EN+NS+SS-ThA6, **45**
- Marcott, C.: NS+AS-WeA9, **34**
- Mariolle, D.: 2D+EM+MI+MN+NS+SS+TF-ThA10, **44**;
SP+AS+BI+NS+SS-ThA4, **45**
- Marks, T.J.: 2D+AS+HI+NS+SS-ThM4, **37**
- Martin, L.W.: EM+MI+NS-MoM5, **2**
- Martins, B.: SP+2D+AS+EM+MC+NS+SS-ThM5, **40**
- Martins, R.: EM+NS+TF-FrM8, **55**
- Martins, L.: SE+NS+TR-TuM5, **16**
- Materer, N.: SS+AS+NS-ThA9, **47**
- Matranga, C.: SS+NS-TuA4, **25**
- Matsubayashi, A.:
2D+AS+HI+MC+NS+PS+SP+SS-TuA8, **18**;
NS+AS-WeA10, **34**
- Matsui, F.: 2D+EM+NS+PS+SS+TF-MoM8, **2**
- Matsumuro, A.: SP+AS+EM+NS+SS-ThP2, **50**
- Mattrey, R.: BI+AS+NS-MoA2, **7**
- Mayer, R.: NS-ThP7, **49**
- Mayergoyz, I.D.: NS+EN-MoA3, **11**
- Mazet, L.: EM+MI+NS-MoM8, **3**
- McArthur, S.L.: BI+AS+NS-MoA9, **9**
- McAvoy, P.C.: NS+EN-MoA3, **11**
- McCartney, M.R.: EM+MI+NS-MoM3, **2**
- McCarty, K.F.: 2D+EM+NS+PS+SS+TF-MoM10, **2**;
SP+2D+AS+EM+MC+NS+SS-ThM11, **40**
- McConney, M.E.: 2D+EM+NS+PS+SS+TF-MoM5, **1**
- McCreary, K.M.: 2D+EM+NS+PS+SS+TF-MoM4, **1**
- McDaniel, M.D.: EM+MI+NS-MoM11, **3**
- McDonnell, S.: 2D+EM+NS+SS+TF-WeM6, **27**;
NS+HI-TuM11, **15**
- McEntee, M.: NS-WeM3, **28**
- McGuire, G.E.: NS+AS-WeA1, **33**
- McKibbin, S.: NS+AS+SS-TuA4, **24**
- Meisenkothen, F.: AP+AS+MC+NS+SS-ThM13, **39**
- Melin, T.: SP+AS+BI+NS+SS-ThA4, **45**
- Meyer, M.T.: MN+NS-TuA9, **22**
- Meyers, G.F.: NS+SE-MoM1, **3**
- Mikkelsen, A.: NS+AS+SS-TuA4, **24**
- Mills, A.: 2D+AS+HI+MC+NS+PS+SP+SS-TuA4, **18**
- Minelli, C.: BI+AS+NS-MoA8, **8**
- Minnal, C.: EN+EM+NS-TuA11, **21**
- Mirkin, C.A.: NS+SE-MoM11, **4**
- Mistry, H.: NS-WeM5, **29**
- Mitterer, C.: SE+NS+TR-TuM11, **17**
- Mok, H.S.: 2D+EM+NS+PS+SS+TF-MoM10, **2**
- Moody, M.P.: AP+AS+EN+NS+SS-ThA6, **45**
- Morales, E.H.: NS-WeM12, **30**
- Morales-Cifuentes, J.R.:
2D+AS+EM+MI+MN+NS+TF-WeA8, **31**
- Morkötter, S.: NS+AS+SS-TuA3, **23**
- Morozovska, A.: 2D+EM+MI+MN+NS+SS+TF-ThA9, **44**
- Moshkalev, S.: NS-ThP7, **49**
- Motley, J.R.: BI+AS+MN+NS-TuM4, **13**
- Movva, H.C.P.: 2D+AS+HI+NS+SS-ThM5, **37**
- Mowll, T.R.: 2D+AS+HI+MC+NS+PS+SP+SS-TuA10, **19**;
2D+EM+NS+PS+SS+TF-MoM3, **1**
- Moyon, F.: AP+AS+NS+SS-FrM5, **54**
- Muddiman, B.: NS+HI-TuM1, **14**
- Mulders, J.J.L.: 2D+EM+MS+NS-FrM6, **52**
- Mullet, C.H.: SS+NS-TuA12, **26**
- Mulvaney, S.P.: BI+AS+MN+NS-TuM5, **13**
- Mundle, R.M.: NS+EN-MoA11, **12**

Munusamy, P.: BI+AS+NS-MoA7, 8
Murata, Y.: 2D+EM+NS+PS+SS+TF-MoM10, 2
Muratore, C.: 2D+EM+NS+PS+SS+TF-MoM5, 1
Muscat, A.J.: SE+NS+TR-TuM1, 16
Musin, I.R.: NS+AS+SS-TuA1, 23

— N —

Nabatame, T.: EM+NS+TF-FrM10, 55
Naghibi, S.: 2D+EM+NS+SS+TF-WeM10, 28
Nahmias: MN+NS-TuA4, 22
Najmaei, S.: SP+2D+AS+EM+MC+NS+SS-
ThM10, 40
Nakajima, Y.: SP+AS+BI+EM+NS+SE+SS-FrM6,
56
Nakano, Y.: EN+EM+MN+NS+TR-MoA11, 10
Nakatsujii, K.: SS+AS+NS-ThA6, 47
Nandasarri, M.L.: AP+AS+MC+NS+SS-ThM6, 39
Narayanan, V.: EM+MI+NS-MoM8, 3
Narimannezhad, A.: EN+EM+NS-TuA11, 21
Natterer, F.D.: 2D+EM+MI+MN+NS+SS+TF-
ThA4, 43; SP+AS+BI+NS+SS-ThA8, 46
Nayyar, N.: 2D+AS+EM+MI+MN+NS+TF-
WeA3, 31
Neeway, J.J.: AP+AS+NS+SS-FrM4, 54
Neupane, S.: NS+AS+SS-TuA11, 24
Neurock, M.: NS-WeM3, 28
Newberg, J.T.: IS+2D+MC+NS+SP+SS-WeA11,
33
Newell, D.B.: 2D+EM+MS+NS-FrM4, 52
Ngo, T.Q.: EM+MI+NS-MoM11, 3
Nguyen, A.: 2D+EM+NS+SS+TF-WeM10, 28;
SP+AS+BI+NS+SS-WeA11, 36
Nguyen, H.: EN+EM+MN+NS+TR-MoA3, 9
Nguyen, L.T.: SP+AS+BI+NS+SS-ThA1, 45
Nie, S.: 2D+EM+NS+PS+SS+TF-MoM10, 2
Niemantsverdriet, H.J.W.: NS-WeM10, 29
Niquet, Y.M.: SP+AS+BI+NS+SS-ThA4, 45
Nishioka, K.: EN+EM+MN+NS+TR-MoA11, 10
Noebels, M.: EN+EM+MN+NS+TR-MoA10, 10
Noh, J.H.: NS+HI-TuM10, 15
Noked, M.: EN+EM+NS-TuA7, 20; EN+EM+NS-
TuA8, 20
Nolting, W.: 2D+AS+HI+MC+NS+PS+SP+SS-
TuA8, 18
Noma, M.: SE+NS+TR-TuM3, 16
Nosiglia, C.: 2D+EM+MS+NS-FrM3, 52

— O —

Ocola, L.E.: NS+HI-TuM6, 15
Odom, T.W.: NS+EN-MoA8, 11
Ogletree, D.F.: NS+SE-MoM10, 4
Ohi, A.: EM+NS+TF-FrM10, 55
Ohlberg, D.A.A.: NS+HI-TuM4, 14
Ohsumimoto, S.: SP+AS+EM+NS+SS-ThP2, 50
Oishi, T.: EM+NS+TF-FrM10, 55
Okada, T.: 2D+AS+EM+NS+SS-MoA9, 7
Oleksak, R.P.: NS+HI-TuM5, 15
Olynyk, I.I.: 2D+AS+EM+MI+MN+NS+TF-
WeA11, 31; 2D+EM+NS+SS+TF-WeM5, 27
Olynyk, D.L.: NS+HI-TuM1, 14
O'Malley, R.M.: AP+AS+NS+SS-FrM3, 53
Ong, E.W.: 2D+AS+HI+MC+NS+PS+SP+SS-
TuA10, 19; 2D+EM+NS+PS+SS+TF-MoM3, 1
Ono, K.: SE+NS+TR-TuM3, 16
Ono, L.K.: NS-WeM5, 29
Orji, N.G.: SP+AS+BI+NS+SS-WeA4, 35
Osgood, R.M.: 2D+AS+HI+MC+NS+PS+SP+SS-
TuA1, 18; NS-WeM11, 29
Osterwalder, J.: 2D+AS+EM+NS+SS-MoA1, 6;
2D+EM+NS+PS+SS+TF-MoM8, 2
Owen, J.: NS+HI-TuM11, 15
Owusu-Ansah, E.: NS-ThP5, 49

— P —

Paglione, J.: SP+AS+BI+EM+NS+SE+SS-FrM6,
56
Park, J.: 2D+AS+HI+NS+SS-ThM1, 37;
SP+2D+AS+EM+MC+NS+SS-ThM11, 40;
SP+2D+AS+EM+MC+NS+SS-ThM6, 40
Park, J.H.: 2D+AS+HI+NS+SS-ThM5, 37
Park, J.Y.: NS+EN-MoA4, 11

Park, T.-H.: NS-WeM12, 30
Parsons, G.N.: BI+AS+NS-MoA1, 7
Pastewka, L.: TR+NS-ThM10, 42; TR+NS-
ThM13, 42; TR+NS-ThM3, 41
Patscheider, J.: SE+NS+TR-TuM10, 17
Patterson, M.C.: SS+NS-TuA11, 26
Patthey, F.: SP+AS+BI+NS+SS-ThA8, 46
Paudel, T.: EM+MI+NS-MoM10, 3
Payne, G.F.: BI+AS+MN+NS-TuM3, 13
Pearse, A.J.: EN+EM+NS-TuA3, 19;
EN+EM+NS-TuA7, 20; EN+EM+NS-TuA8,
20
Pelton, M.: NS+SE-MoM5, 4
Peng, W.: EN+EM+MN+NS+TR-MoA3, 9
Perea, D.E.: AP+AS+EN+NS+SS-ThA4, 45;
AP+AS+NS+SS-FrM8, 54
Perriot, R.: 2D+AS+EM+MI+MN+NS+TF-
WeA11, 31
Persson, O.: NS+AS+SS-TuA4, 24
Pfadler, T.: EN+EM+MN+NS+TR-MoA10, 10
Pfnür, H.: NS+EN-MoA6, 11;
SP+2D+AS+EM+MC+NS+SS-ThM12, 41
Phuong, P.V.: 2D+AS+EM+NS+SS-MoA8, 7
Piasecki, A.: 2D+EM+NS+SS+TF-WeM6, 27
Pirota, K.R.: NS-ThP7, 49
Plank, H.: NS+HI-TuM10, 15
Polat, E.O.: 2D+EM+MI+MN+NS+SS+TF-
ThA11, 44
Ponath, P.: EM+MI+NS-MoM3, 2
Poppenheimer, E.C.: SS+NS-TuA12, 26
Porter, A.E.: BI+AS+NS-MoA7, 8
Porter, L.M.: EM+NS+TF-FrM11, 55
Posadas, A.B.: EM+MI+NS-MoM11, 3;
EM+MI+NS-MoM3, 2
Potapenko, D.V.: NS-WeM11, 29
Pouch, S.: SP+AS+BI+NS+SS-ThA4, 45
Prabhumirashi, P.L.: 2D+AS+HI+NS+SS-ThM4,
37
Pradhan, A.K.: NS+EN-MoA11, 12
Prasher, R.: NS+SE-MoM10, 4
Prater, C.B.: NS+AS-WeA9, 34
Preciado, E.: 2D+EM+NS+SS+TF-WeM10, 28;
SP+AS+BI+NS+SS-WeA11, 36
Prosa, T.J.: AP+AS+MC+NS+SS-ThM13, 39
Ptasinska, S.: SS+AS+NS-ThA3, 46; SS+AS+NS-
ThA4, 47
Putnik, M.: EN+EM+MN+NS+TR-MoA10, 10
Puydinger dos Santos, M.V.: NS-ThP7, 49

— Q —

Qafoku, O.: AP+AS+EN+NS+SS-ThA4, 45
Qiu, J.: NS+EN-MoA7, 11

— R —

Raabe, D.: AP+AS+MC+NS+SS-ThM3, 38
Rabin, O.: NS+EN-MoA3, 11
Rack, P.D.: NS+HI-TuM10, 15
Rahman, T.S.: 2D+AS+EM+MI+MN+NS+TF-
WeA3, 31; 2D+AS+HI+NS+SS-ThM6, 37;
2D+EM+MI+MN+NS+SS+TF-ThA8, 43
Rajan, K.: AP+AS+EN+NS+SS-ThA1, 44
Raley, A.: NS+HI-TuM3, 14
Ramalingam, G.: SS+AS+NS-ThA7, 47
Ramirez-Torres, A.: 2D+AS+HI+NS+SS-ThM6,
37
Randall, J.: NS+HI-TuM11, 15
Rangan, S.: EN+EM+NS-TuA4, 20
Ranjan, A.: NS+HI-TuM3, 14
Raravikar, N.: NS+SE-MoM10, 4
Rastogi, V.: NS+HI-TuM3, 14
Reed, E.J.: 2D+AS+EM+MI+MN+NS+TF-
WeA12, 32
Reidy, R.: NS+HI-TuM11, 15
Reinecke, T.: 2D+AS+EM+NS+SS-MoA3, 6
Reinke, P.: SS+AS+NS-ThA7, 47
Ren, X.: AP+AS+MC+NS+SS-ThM5, 39
Renault, O.J.: 2D+EM+MI+MN+NS+SS+TF-
ThA10, 44
Reutt-Robey, J.: 2D+AS+EM+MI+MN+NS+TF-
WeA8, 31

Reyes, P.: NS-WeM4, 29
Richter, C.A.: 2D+EM+MS+NS-FrM4, 52
Riedl, A.: SE+NS+TR-TuM11, 17
Riehn, R.: BI+AS+NS-MoA11, 9
Riley, J.: AP+AS+MC+NS+SS-ThM5, 39
Robbins, M.O.: TR+NS-ThM10, 42; TR+NS-
ThM13, 42
Robinson, J.: 2D+AS+EM+NS+SS-MoA3, 6;
2D+EM+NS+PS+SS+TF-MoM4, 1;
BI+AS+MN+NS-TuM5, 13
Robinson, J.A.: 2D+AS+HI+MC+NS+PS+SP+SS-
TuA3, 18; 2D+EM+NS+SS+TF-WeM11, 28;
2D+EM+NS+SS+TF-WeM6, 27
Robinson, Z.R.: 2D+AS+HI+MC+NS+PS+SP+SS-
TuA10, 19; 2D+EM+NS+PS+SS+TF-MoM3, 1
Rodrigues, J.N.: 2D+EM+MI+MN+NS+SS+TF-
ThA4, 43
Rogers, J.A.: BI+AS+MN+NS-TuM10, 14
Roldan Cuenya, B.: NS+AS-WeA4, 33; NS-
WeM5, 29
Romero, D.: 2D+AS+EM+MI+MN+NS+TF-
WeA7, 31
Ross, F.M.: SS+NS-TuA1, 25
Ross, P.N.R.: IS+2D+MC+NS+SP+SS-WeA10, 33
Roth, S.: 2D+EM+NS+PS+SS+TF-MoM8, 2
Rouchon, D.: 2D+EM+MI+MN+NS+SS+TF-
ThA10, 44
Roushan, M.: BI+AS+NS-MoA11, 9
Rowe, K.G.: TR+NS-ThM6, 42
Rubloff, G.W.: EN+EM+NS-TuA3, 19;
EN+EM+NS-TuA7, 20; EN+EM+NS-TuA8,
20
Rupich, S.: EN+EM+MN+NS+TR-MoA3, 9
Russell, T.P.: NS+HI-TuM1, 14
Rutherford, R.: NS+HI-TuM5, 15
Ryan, J.V.: AP+AS+NS+SS-FrM4, 54
Ryan, K.E.: SP+AS+BI+EM+NS+SE+SS-FrM2,
55; TR+NS-ThM5, 41
Ryan, M.P.: BI+AS+NS-MoA7, 8

— S —

Sader, J.E.: NS+SE-MoM5, 4
Saint-Girons, G.: EM+MI+NS-MoM8, 3
Salmeron, M.B.: NS-WeM6, 29
Sampat, S.: EN+EM+MN+NS+TR-MoA3, 9
Samukawa, S.: 2D+AS+EM+NS+SS-MoA9, 7
Sanchez, E.: SP+AS+EM+NS+SS-ThP8, 50
Sando, S.: NS+HI-TuM11, 15
Sandoval, T.: SS+AS+NS-ThA10, 48
Sangwan, V.K.: 2D+AS+HI+NS+SS-ThM4, 37
Santiago, K.C.: NS+EN-MoA11, 12
Santoro, C.: BI+AS+MN+NS-TuM12, 14
Sartory, B.: SE+NS+TR-TuM11, 17
Sassolini, S.: NS+HI-TuM1, 14
Sawyer, W.G.: TR+NS-ThM6, 42
Schaefer, D.: EM+MI+NS-MoM4, 2
Schamm-Chardon, S.: EM+MI+NS-MoM8, 3
Scheu, C.: EN+EM+MN+NS+TR-MoA10, 10
Schlaf, R.: 2D+EM+NS+SS+TF-WeM5, 27
Schmidt-Mende, L.: EN+EM+MN+NS+TR-
MoA10, 10
Schoeberl, T.: SE+NS+TR-TuM11, 17
Schreiber, D.K.: AP+AS+NS+SS-FrM4, 54
Schroeder, M.A.: EN+EM+NS-TuA7, 20;
EN+EM+NS-TuA8, 20
Schuler, A.: BI+AS+MN+NS-TuM12, 14
Schuller, J.: 2D+AS+EM+MI+MN+NS+TF-
WeA9, 31
Schwarz, U.D.: 2D+EM+NS+SS+TF-WeM4, 27
Schwier, E.F.: 2D+EM+MI+MN+NS+SS+TF-
ThA8, 43
Seebauer, E.G.: SS+AS+NS-ThA2, 46
Segawa, K.: SP+AS+BI+NS+SS-WeA3, 35
Seifu, D.: NS+AS+SS-TuA11, 24
Sekine, M.: 2D+EM+MS+NS-FrM10, 53
Sell, J.C.: SE+NS+TR-TuM2, 16
Seong, D.J.: NS-ThP1, 49
Shamberger, P.J.: 2D+EM+NS+PS+SS+TF-
MoM5, 1
Shard, A.G.: BI+AS+NS-MoA8, 8

- Sharma, P.: EM+MI+NS-MoM4, 2
 Sharp, T.: TR+NS-ThM13, **42**
 Sheehan, P.E.: 2D+AS+EM+NS+SS-MoA3, 6;
 BI+AS+MN+NS-TuM5, **13**
 Shen, Z.-X.: 2D+AS+HI+MC+NS+PS+SP+SS-
 TuA11, **19**
 Shenderova, O.A.: NS+AS-WeA1, **33**
 Shepard, K.: 2D+EM+MI+MN+NS+SS+TF-ThA4,
 43
 Shetty, R.: NS+AS-WeA9, 34
 Shi, Y.: NS-ThP5, 49
 Shi, Z.: NS+AS+SS-TuA8, 24
 Shiao, M.H.: SP+AS+EM+NS+SS-ThP5, 50
 Shield, J.: AP+AS+MC+NS+SS-ThM12, 39
 Shimada, M.: 2D+EM+MI+MN+NS+SS+TF-
 ThA8, 43
 Shin, N.: NS+AS+SS-TuA1, 23
 Shin, S.: SP+AS+BI+NS+SS-WeA3, 35
 Shin, Y.H.: NS-ThP1, 49
 Shklover, V.: SE+NS+TR-TuM10, 17
 Sieg, S.: NS+HI-TuM3, 14
 Siegel, D.A.: SP+2D+AS+EM+MC+NS+SS-
 ThM11, 40
 Simonato, J.-P.: 2D+EM+MI+MN+NS+SS+TF-
 ThA10, 44
 Simpson, J.R.: 2D+AS+EM+MI+MN+NS+TF-
 WeA4, 31; 2D+AS+EM+MI+MN+NS+TF-
 WeA7, 31
 Singhal, S.: NS+HI-TuM11, 15
 Sinha, D.: 2D+AS+HI+MC+NS+PS+SP+SS-
 TuA8, 18
 Sinitskii, A.: 2D+AS+HI+NS+SS-ThM12, **38**
 Sivaram, S.V.: NS+AS+SS-TuA1, 23
 Skibinski, E.S.: SS+AS+NS-ThA8, **47**
 Skuza, J.R.: NS+EN-MoA11, **12**
 Smeu, M.: SP+2D+AS+EM+MC+NS+SS-ThM5,
 40
 Smith, D.J.: EM+MI+NS-MoM3, 2
 Smith, J.N.: BI+AS+NS-MoA7, 8
 Smith, R.: 2D+EM+NS+PS+SS+TF-MoM5, 1
 Snee, P.: BI+AS+NS-MoA3, **8**
 Sobiech, M.: SE+NS+TR-TuM10, 17
 Solares, S.D.: SP+AS+BI+EM+NS+SE+SS-FrM8,
56
 Song, Y.J.: SP+AS+EM+NS+SS-ThP3, 50
 Sonnenfeld, A.: 2D+EM+NS+SS+TF-WeM4, 27
 Sorescu, D.C.: SS+NS-TuA4, 25
 Sottos, N.: NS+SE-MoM8, 4
 Sporre, J.R.: NS+HI-TuM3, 14
 Sprunger, P.T.: SS+NS-TuA11, **26**
 Sreenivasan, S.: NS+HI-TuM11, 15
 Sridhara, K.: 2D+AS+HI+MC+NS+PS+SP+SS-
 TuA9, **18**
 Staaks, D.: NS+HI-TuM1, 14
 Stanford, M.G.: NS+HI-TuM10, 15
 Steel, E.B.: AP+AS+MC+NS+SS-ThM13, 39
 Stefanelli, M.: SE+NS+TR-TuM11, 17
 Stemmer, S.: EM+MI+NS-MoM1, **2**
 Stenger, B.H.: SS+NS-TuA12, 26
 Stevanovic, A.: NS+AS-WeA11, **34**
 Stevenson, R.: 2D+EM+NS+PS+SS+TF-MoM5, 1
 Stewart, D.M.: SE+NS+TR-TuM2, 16
 Stine, R.: BI+AS+MN+NS-TuM5, 13
 Stollenwerk, A.J.: NS+SE-MoM6, **4**
 Stosch, R.: 2D+AS+HI+NS+SS-ThM3, 37
 Strachan, J.P.: NS+HI-TuM4, 14
 Stroschio, J.A.: 2D+EM+MI+MN+NS+SS+TF-
 ThA4, 43; SP+AS+BI+EM+NS+SE+SS-FrM6,
 56; SP+AS+BI+NS+SS-ThA8, 46;
 SP+AS+EM+NS+SS-ThP3, 20
 Stuckert, E.P.: SS+NS-TuA3, **25**
 Stumpf, C.: EM+MI+NS-MoM4, 2
 Su, J.Y.: SP+AS+EM+NS+SS-ThP5, **50**
 Subramanian, S.: MN+NS-TuA9, **22**
 Sugiyama, M.: EN+EM+MN+NS+TR-MoA11, 30
 Suzer, S.: 2D+EM+MI+MN+NS+SS+TF-ThA11,
44
 Suzuki, H.: EN+EM+MN+NS+TR-MoA11, 10
- Syers, P.S.: SP+AS+BI+EM+NS+SE+SS-FrM6,
 56
 Sykes, E.C.H.: NS-WeM1, **28**
 Szeto, K.: BI+AS+NS-MoA10, 9
 — **T** —
 Talin, A.: SP+AS+BI+NS+SS-WeA11, 36
 Tamanaha, C.R.: BI+AS+MN+NS-TuM5, 13
 Tan, X.: BI+AS+MN+NS-TuM4, 13
 Tang, W.: NS-WeM3, 28
 Taniguchi, T.: 2D+EM+MI+MN+NS+SS+TF-
 ThA4, 43; 2D+EM+MS+NS-FrM3, 52
 Tao, C.: 2D+AS+HI+MC+NS+PS+SP+SS-TuA4,
18
 Tao, F.: NS+AS+SS-TuA10, 24;
 SP+AS+BI+NS+SS-ThA1, **45**
 Tao, M.: NS+SE-MoM3, 4
 Taylor, A.: BI+AS+NS-MoA1, 7
 Taylor, D.: EN+EM+MN+NS+TR-MoA3, 9
 Tegenkamp, C.: NS+EN-MoA6, 11
 Therien, M.J.: NS-WeM12, 30
 Thevuthasan, S.A.: AP+AS+MC+NS+SS-ThM6,
 39
 Thiel, P.A.: SS+NS-TuA7, **25**
 Thissen, N.F.W.: 2D+EM+MS+NS-FrM6, **52**
 Thompson, G.B.: AP+AS+NS+SS-FrM3, 53
 Thompson, W.: NS+HI-TuM4, 14
 Thon, S.M.: EN+EM+MN+NS+TR-MoA1, **9**
 Thorpe, R.: EN+EM+NS-TuA4, **20**
 Tian, W.-C.: MN+NS-TuA11, 23; MN+NS-
 TuA12, 23
 Tierno, D.: NS+HI-TuM1, 14
 Timm, R.: NS+AS+SS-TuA4, 24
 Tolstaya, E.I.: BI+AS+MN+NS-TuM2, **13**;
 EN+EM+NS-TuA9, 20
 Tomaszewska, N.: SS+AS+NS-ThA1, 46
 Tong, X.: IS+2D+MC+NS+SP+SS-WeA9, 32
 Tringides, M.C.: SS+NS-TuA12, 26
 Triozon, F.: SP+AS+BI+NS+SS-ThA4, 45
 Triplett, M.: SP+AS+BI+NS+SS-WeA11, 36
 Trogler, W.: BI+AS+NS-MoA2, 7
 Tsai, C.H.: EM+NS+TF-FrM5, 54
 Tsai, H.-Z.: 2D+EM+MS+NS-FrM3, 52
 Tsao, M.-C.: MN+NS-TuA11, 23
 Tsargorodska, A.: BI+AS+NS-MoA6, 8
 Tselev, A.: IS+2D+MC+NS+SP+SS-WeA3, **32**
 Tsymbal, E.Y.: EM+MI+NS-MoM10, 3
 Turchanin, A.: 2D+AS+HI+NS+SS-ThM3, 37
 Turkowski, V.: 2D+AS+EM+MI+MN+NS+TF-
 WeA3, 31
 Turner, K.T.: SP+AS+BI+EM+NS+SE+SS-FrM2,
 55; TR+NS-ThM5, 41
 Tyagi, P.: 2D+AS+HI+MC+NS+PS+SP+SS-
 TuA10, 19; 2D+EM+NS+PS+SS+TF-MoM3, 1
 Tyurnina, A.: 2D+EM+MI+MN+NS+SS+TF-
 ThA10, 44
 — **V** —
 Vahdat, V.: TR+NS-ThM5, 41
 van Zijll, M.S.: SS+NS-TuA12, 26
 Velasco Jr., J.: 2D+EM+MS+NS-FrM3, **52**
 Ventrice, Jr., C.A.:
 2D+AS+HI+MC+NS+PS+SP+SS-TuA10, 19;
 2D+EM+NS+PS+SS+TF-MoM3, 1
 Vervuurt, R.H.J.: 2D+EM+MS+NS-FrM6, 52
 Visart de Bocarmé, T.: AP+AS+EN+NS+SS-
 ThA3, 44
 Viveros, R.: BI+AS+NS-MoA2, 7
 Vlahovic, B.: NS-ThP9, 49
 Voevodin, A.A.: 2D+EM+NS+PS+SS+TF-MoM5,
1
 Von Son Palacio, G.: 2D+EM+NS+SS+TF-
 WeM10, 28
 Voronin, S.: NS+HI-TuM3, 14
 Vysochanskii, Y.: 2D+EM+MI+MN+NS+SS+TF-
 ThA9, 44
 — **W** —
 Waite, A.: 2D+EM+NS+PS+SS+TF-MoM5, 1
 Walker, A.V.: NS+AS+SS-TuA8, **24**
- Wallace, R.M.: 2D+EM+NS+SS+TF-WeM6, 27;
 NS+HI-TuM11, 15
 Walton, S.G.: BI+AS+MN+NS-TuM5, 13
 Wang, B.: 2D+EM+NS+PS+SS+TF-MoM5, 1
 Wang, C.-M.: BI+AS+NS-MoA7, 8
 Wang, F.: 2D+EM+MS+NS-FrM3, 52
 Wang, H.: BI+AS+NS-MoA11, 9
 Wang, J.: BI+AS+NS-MoA2, **7**
 Wang, K.: SP+AS+BI+EM+NS+SE+SS-FrM6, 56
 Wang, L.: 2D+EM+MI+MN+NS+SS+TF-ThA4,
 43
 Wang, X.: SP+AS+BI+EM+NS+SE+SS-FrM6, 56
 Wang, Y.: 2D+AS+EM+MI+MN+NS+TF-WeA8,
 31
 Wang, Z.: 2D+EM+MS+NS-FrM5, 52
 Wang, Z.L.: EN+EM+MN+NS+TR-MoA6, **9**
 Wang, Z.Y.: AP+AS+NS+SS-FrM4, 54
 Wantanabe, K.: 2D+EM+MS+NS-FrM3, 52
 Ward, W.K.: BI+AS+MN+NS-TuM4, 13
 Warecki, Z.: EM+MI+NS-MoM4, 2
 Watanabe, K.: 2D+EM+MI+MN+NS+SS+TF-
 ThA4, 43
 Watson, M.: 2D+AS+EM+MI+MN+NS+TF-
 WeA4, **31**; 2D+AS+EM+MI+MN+NS+TF-
 WeA7, 31
 Webb, J.L.: NS+AS+SS-TuA4, 24
 Weber, J.W.: 2D+EM+MS+NS-FrM6, 52
 Weber, M.H.: EN+EM+NS-TuA11, 21
 Wei, R.: SE+NS+TR-TuM12, 17
 Wei, W.D.: NS+EN-MoA7, 11
 Weickert, J.: EN+EM+MN+NS+TR-MoA10, **10**
 Weimann, T.: 2D+AS+HI+NS+SS-ThM3, 37
 Wetherington, M.: 2D+EM+NS+SS+TF-WeM11,
 28
 White, C.T.: 2D+EM+MI+MN+NS+SS+TF-ThA3,
 43
 Widom, M.: 2D+EM+NS+PS+SS+TF-MoM6, 1
 Wiggins, B.C.: SP+2D+AS+EM+MC+NS+SS-
 ThM1, **39**
 Williams, R.S.: NS+HI-TuM4, 14
 Winkler, T.E.: BI+AS+MN+NS-TuM3, 13
 Winter, A.: 2D+AS+HI+NS+SS-ThM3, **37**
 Wisnet, A.: EN+EM+MN+NS+TR-MoA10, 10
 Wolden, C.A.: AP+AS+NS+SS-FrM1, 53
 Wolkow, R.: SP+2D+AS+EM+MC+NS+SS-
 ThM5, **40**
 Woszczyna, M.: 2D+AS+HI+NS+SS-ThM3, 37
 Wu, C.-C.: 2D+AS+HI+NS+SS-ThM4, 37
 Wu, Z.: BI+AS+NS-MoA2, 7
 Würz, R.: AP+AS+MC+NS+SS-ThM3, 38
 Wyrick, J.E.: 2D+EM+MI+MN+NS+SS+TF-
 ThA4, 43; SP+AS+BI+NS+SS-ThA8, 46
 — **X** —
 Xing, H.: 2D+AS+EM+MI+MN+NS+TF-WeA4,
 31
 Xu, X.D.: 2D+EM+MI+MN+NS+SS+TF-ThA1,
43
 Xu, X.S.: EM+MI+NS-MoM10, 3
 Xu, Y.: SS+NS-TuA11, 26
 Xu, Z.: AP+AS+MC+NS+SS-ThM6, 39
 — **Y** —
 Yamada, H.: EM+NS+TF-FrM10, 55
 Yamashita, M.: SE+NS+TR-TuM3, 16
 Yan, J.: 2D+EM+MS+NS-FrM4, 52
 Yan, R.: 2D+AS+EM+MI+MN+NS+TF-WeA4,
 31
 Yang, J.: NS+AS+SS-TuA8, 24
 Yang, K.: 2D+EM+NS+SS+TF-WeM10, 28
 Yang, Q.: AP+AS+EN+NS+SS-ThA6, 45
 Yang, R.: 2D+EM+MS+NS-FrM5, 52
 Yang, W.: 2D+EM+MS+NS-FrM3, 52
 Yang, Y.: SP+AS+BI+NS+SS-WeA10, 35
 Yates, Jr., J.T.: NS-WeM3, 28
 Yeh, J.W.: BI+AS+NS-MoA10, **9**
 Yeom, G.: 2D+AS+EM+NS+SS-MoA4, 6;
 2D+AS+EM+NS+SS-MoA8, 7
 Yeom, H.W.: SP+AS+BI+NS+SS-WeA7, **35**;
 SP+AS+BI+NS+SS-WeA9, 35

Yong, G.: EM+MI+NS-MoM4, 2
Yoshiike, Y.: SS+AS+NS-ThA6, 47
Yoshizawa, S.: SP+AS+BI+NS+SS-WeA3, 35
You, K.H.: NS-ThP1, 49
You, S.J.: NS-ThP1, 49
Young, A.F.: 2D+EM+MI+MN+NS+SS+TF-ThA4, 43
Yu, X.: NS+SE-MoM3, 4
Yu, Y.: 2D+AS+HI+MC+NS+PS+SP+SS-TuA4, 18
Yulaev, A.: NS+AS+SS-TuA7, 24

— Z —

Zalalutdinov, M.: 2D+AS+EM+NS+SS-MoA3, 6
Zettl, A.: 2D+EM+MS+NS-FrM3, 52
Zhang, D.: SP+AS+BI+EM+NS+SE+SS-FrM6, 56; SP+AS+EM+NS+SS-ThP3, 50
Zhang, G.: 2D+EM+MS+NS-FrM3, 52
Zhang, L.Z.: 2D+AS+EM+NS+SS-MoA10, 7
Zhang, S.: NS+AS+SS-TuA10, 24
Zhang, X.: SP+2D+AS+EM+MC+NS+SS-ThM6, 40

Zhang, X.Q.: SS+AS+NS-ThA3, 46; SS+AS+NS-ThA4, 47
Zhang, Y.: 2D+EM+MS+NS-FrM3, 52
Zhao, Y.: 2D+EM+MI+MN+NS+SS+TF-ThA4, 43; SP+AS+BI+NS+SS-ThA8, 46
Zhitenev, N.B.: 2D+EM+MI+MN+NS+SS+TF-ThA4, 43
Zhou, G.W.: IS+2D+MC+NS+SP+SS-WeA9, 32
Zhu, Q.: SS+AS+NS-ThA9, 47
Zhu, X.: 2D+EM+NS+SS+TF-WeM4, 27
Zhu, Z.: AP+AS+NS+SS-FrM4, 54